Cross Section for Residual Nuclide Production by Proton–Induced Reaction with Heavy Target Elements at Medium Energies

As Ph.D. Thesis in Experimental Nuclear Physics

Submitted to Physics Department

Al-Azhar University

Faculty of Science

Assiut, Egypt

by

Shamselden Abdelrasoul Azobir Mohamed Issa

Supervised by

Prof. Dr. Rolf Michel

Center for Radiation

Protection and Radioecology (ZSR)

Leibniz University Hanover, Germany

2009

ABSTRACT

There is no doubt that fission is the most important nuclear reaction for society at large today due to its use in energy production. However, this has raised the problem of how to treat the long-lived radioactive waste from nuclear reactors. Besides the option of waste depositories in deep geological formations hiding the waste from the biosphere for millions of years, a radical other solution would be to transmute the long-lived radionuclides of the waste into stable or short-lived nuclides. This could be done through nuclear transmutation. Such a transmutation concept requires accelerator-driven systems to be designed, in which an accelerator with a spallation target serves as an external neutron source for an under-critical reactor. In such hybrid reactors, the neutrons could provide the required nuclear reactions for the transmutation of long-lived waste.

Integral excitation functions for the production of residual nuclides are basic quantities for the calculation of radioactive inventories of spallation targets in spallation neutron sources and in accelerator-driven devices for energy amplification or for transmutation of nuclear waste. For accelerator technologies, production of residual nuclides has to be described to model the radioactive inventories of the spallation targets, the activation of accelerating structures, of the beam pipes and windows and of shielding materials, cooling materials and ambient air. Radionuclide inventories will determine the final disposal costs of spallation targets and will decide whether the burn-up of nuclear waste can be counterweighted or not by the creation of other activation products. Due to the large range of relevant target elements and the vast amount of product nuclides it will not be possible to measure all the cross sections needed. Consequently, one will have to rely widely on models and codes to calculate the required cross sections and validation of such calculations is a high priority issue. Since previous experiences with predictions of such excitation functions were not satisfying, two new code systems (TALYS and INCL4+ABLA) were developed within the HINDAS (High and Intermediate Energy Nuclear Data for Accelerator-Driven Systems) project. The validation of theoretical predictions is only possible if highly reliable experimental data are available which allow for systematic tests of the respective codes. During the last decade, substantial progress has also

been made with respect to the experimental data base, and in particular the HINDAS project improved the experimental data base considerably.

In this thesis, the production of residual nuclides by proton-induced reactions on rhenium and uranium is investigated using activated targets from irradiation experiments at the cyclotron of the University of Uppsala and at the Saturne accelerator at Saclay. Experimental cross sections are derived from gamma-spectrometric measurements. For the target element rhenium practically no earlier experimental data exist. For Uranium, the new data allow to close gaps in our knowledge and to derive some complete excitation functions. The new cross sections for residual nuclide production are compared with actual theoretical calculations. This thesis contributes to ongoing efforts of the European NUDATRA (Nuclear Data for Transmutation) project within the European IP EUROTRANS.

In this work, comprehensive measurements for the proton-induced residual nuclei distribution for rhenium and uranium targets are performed. A total of 7146 cross-sections was determined for 363 residual nuclides for an energy range between 78.2 MeV and 2590 MeV for rhenium and between 211 MeV and 2530 MeV for uranium. The dependencies of the cross sections on incident proton energy and target nuclei were studied. This resulted in a systematics that may make it possible to give certain estimates for unmeasured nuclides. The experimental data are discussed via a comparison with theoretical excitation functions calculated by the INCL4+ABLA and the newly developed TALYS codes.

CONTENTS

CHAPTER 1
INTRODUCTION

1.1 NUCLEAR PHYSICS:

Nuclear techniques play an important role in many facets of our daily life and are an integral part of our socioeconomic development. Be it in medical diagnostics and treatment, in food security, in industrial process control or in luggage screening at airports, these techniques serve basic human needs, strengthen industrial competitiveness or increase our understanding of nature and its processes. However, triggered in part by accidents in the field of nuclear power, a segment of the general public perceives anything nuclear as inherently unsafe, ignoring the great number of nuclear applications beneficial for health, welfare and the environment. Most of these sentiments are caused by a lack of information and by a misconception. This situation can only be rectified by showing the many opportunities and advantages provided by nuclear applications [1].

Besides of a general interest in basic nuclear physics, cross section for the productions of nuclides in nuclear reactions induced by medium energy protons and neutrons are of increasing importance for a wide variety of applications. These applications range from astro- and cosmophysics over space and environmental sciences, medicine (radionuclide production, dosimetry in mixed nucleon fields, radiation therapy), accelerator technology (activation of detectors, radiation protection, on-line mass separation), space and aviation technology to accelerator-based nuclear waste transmutation and energy amplification [2].

1.1.1 Nuclear Reactions:

The term “nuclear reaction” is quite generic. It is used to refer to interaction of nuclei with nuclei, individual nucleons with nuclei, nucleons with one another and even the interactions of photons and electrons with nuclei. Nuclear reactions are the fundamental means by which we probe the nature of the nuclear force, the structure of complex nuclei, and the means by which we produce radioactive nuclei for study or application [3].

The nature of the experimental observation is the following: A beam of particles, such as protons, deuterons, alpha particles, or heavier nuclei (referred to as heavy ions), is accelerated to a desired energy and then deflected so as to strike a target of known isotopic composition. The energy and scattering angle of some of the products of the collision are measured. For example, in a reaction initiated by protons, the proton itself will sometimes emerge, deflected in angle but having the some energy in the centre-of- mass system. This is elastic scattering, the measurement of the cross section is important because its analysis yields the parameters of the optical potential.

Sometimes the proton will excite the target nucleus from its ground to some higher-energy state, thus losing some energy and at the same time being deflected in angle. This is an inelastic event. The cross section for such an event yields information on the spin and parity of the nuclear transition and is sensitive to the wave functions of the nucleons that are excited [4].

In order that a nuclear reaction might occur, the nucleons in the incident particle, or projectile, must interact with the nucleus in the target. Thus, the energy must be higher than the natural electromagnetic repulsion between the interaction partners. This energy barrier is called the Coulomb barrier. If the energy is below the barrier, the nuclei will bounce off each other. The energy barrier, E_c, depends on the atomic numbers of the target nucleus Z_1 and atomic number of the projectile nucleus Z_2. It can be calculated according to the following equation [5].

$$E_c = \frac{1}{4\pi\varepsilon_\circ} \cdot \frac{Z_1 \cdot e \cdot Z_2 \cdot e}{r} \tag{1.1}$$

When E_c is in MeV and r in cm

$$E_c = 1.44 \cdot 10^{-13} \cdot \frac{Z_1 \cdot Z_2}{r} \tag{1.2}$$

Where r represents the distance between the two nucleons and within this distance nuclear forces become operative. It can be calculated lated as follows:

$$r = r_0(A_1^{1/3} + A_2^{1/3}) \tag{1.3}$$

Nuclear reactions give us much information about nuclei and nuclear energy. From nucleon-nucleon scattering we obtained information about the fundamental nuclear force. With elastic scattering of nuclei, we can calculate nuclear sizes and investigate the interaction potential. By inelastic scattering to excited states, we get information about energy levels and quantum numbers. Transfer and knockout reactions gave us details of the shell model of the nucleus. Fusion reactions help us to understand many of the astrophysical processes in the sun and different anther stars. The fission reactions as collective processes gave us good understanding of properties of the liquid-drop model. From compound nucleus reactions, we know the statistical properties of the nucleus, and by studying electron scattering, we can learn about the quark structure of nuclei.

1.1.2 Nuclear Fission:

The discovery of nuclear fission in 1939 by Otto Hahn and Fritz Strassmann, following years of collaborative work with Lisa Meinter, opened a wide field of scientific endeavors and new technological possibilities. Within less than five years, the nuclear fission was applied to the production and successful deployment of a prototype of a weapon of mass destruction tens of thousands of times more powerful than anything that had ever been known. Within less than fifteen years the door was opened to the development of weaponry that could literally destroy a large fraction of the surface of the earth, and the era of the nuclear terror know as the Cold war was opened.

From the beginning, the use of fission as a power source was discussed, and by 1941 Enrico Fermi and co-workers had demonstrated the first controlled chain reaction based on neutron-induced fission. Following several decades of design and construction of various types of demonstration plants of relatively small size, the nuclear power industry began to grow rapidly during the period 1960-1970. In the United State today something greater than 100 commercial nuclear reactors supply about 20% of the nation's electric power. In Japan, roughly 40% of the electric power production is form nuclear plants, and in France, more than 70% of electricity is generated by nuclear fission. The discovery of the neutron by Chadwick was perhaps the most important key that opened the door to fission [3].

Since two or three neutrons are released in every neutron-induced fission reaction, the possibility of a sustain neutron chain reaction is obvious, as illustrated in Fig. (1.1). To sustain a fission chain reaction, one or more of the neutrons produced in the fission event must, on average, survive to produce another fission event. There is competition for the fission neutrons in any assembly-some will be absorbed in fuel nuclides as radioactive capture events rather than fission events, some will be absorbed by nonfuel nuclides, and some will leak out of the assembly. A scattering event dose not compete for a neutron because the scattered neutron remains in the assembly and available for causing a fission event, but a scattering event dose change a neutron's energy and thus, because the various cross sections are energy dependent, dose change the relative likelihood of the next collision being a fission event [6].

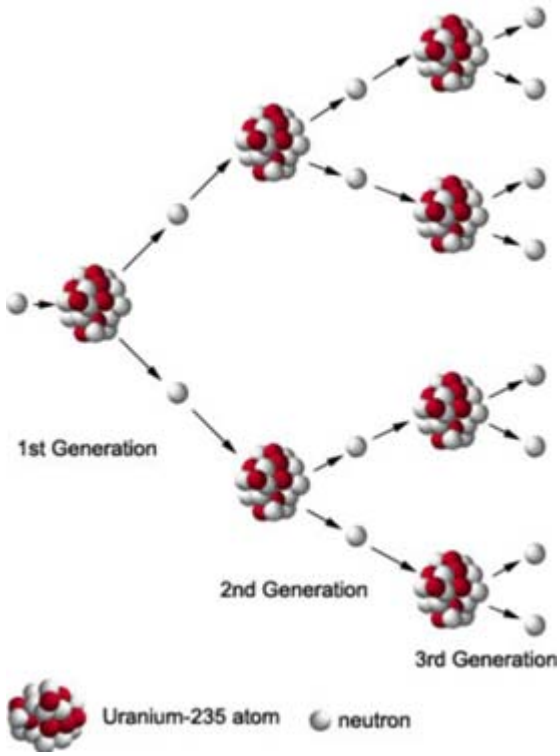

Fig. (1.1): *Schematic of a fission chain reaction.*

Fission is the most important nuclear reaction for society today due to its use in nuclear power plants. In these reactors, ^{235}U is used as a source of energy, which is released through neutron chain reactions. The uranium reactors were driven by fission neutrons of low energy (E < 2 meV) and the corresponding research field of neutrons

is very well studied. Intermediate-energy neutrons and protons can also induce fission reactions. These are also of interest, either for the purpose of providing basic knowledge of nuclear physics or for the applied purpose of applications in transmutation of nuclear waste using accelerator driven systems. More general, nuclear reactions at intermediate energies are also of importance for beam monitoring or dosimetry, for radiation protection, cancer therapy, studies of particle-induced effects in electronics, etc. Very heavy nuclei ($Z \geq 92$) are subject to spontaneous fission. They can break apart into two nuclei spontaneously without external energy or interaction. We can understand this by considering the analogy of a charged liquid drop. If the drop is not too large, surface tension can overcome the repulsive forces of the charges and hold the drop together. There is, however, a certain maximum size beyond which the drop will be unstable and will spontaneously break apart. Spontaneous fission puts an upper limit on the size of the nucleus and therefore on the number of elements that are possible.

1.1.3 Mechanics of Fission:

Nuclear fission is unique among nuclear reactions since the nucleus divides into roughly equal parts with the release of a large amount of energy, about 200 MeV per fission. It is probably no overstatement to say that fission is the most important nuclear process, both for its potential to destroy civilization through the use of weapons and its potential through reactors to supply abundant power for all people.

An aspect of fission which has been studied extensively is the distribution of mass, charge and kinetic energy among the fragments formed in fission. No matter how nuclei are made to undergo fission, fragments of various masses are formed which result in production of chemical elements as light as zinc (atomic number 30) and as heavy as gadolinium (atomic number 64), with half-lives from fractions of seconds to millions of years. Approximately 400 different nuclides have been identified as products in the fission of ^{235}U by neutrons. Study of these fission products has required extensive radiochemical work and continues as a very active field of research for example, in the measurement of very short-lived products. Although fission is an extremely complicated process, and still challenges theorists, satisfactory models for most of the fission phenomena have been developed [7].

The binding energy per nucleon for heavy elements decreases as the atomic mass number increases. Thus, when heavy nuclei are split into smaller pieces, energy is released. Nuclear fission can be induced in certain nuclei as a result of absorbing a neutron. With ^{235}U, ^{239}Pu and ^{233}U absorption of a thermal neutron can set up vibrations in the nucleus which cause it to become so distended that it splits apart under the mutual electrostatic repulsion of its parts. The thermal neutron fission cross sections for these isotopes are 580, 747 and 525 barns respectively. Greater activation energy is required to cause other nuclei to fission. An example is ^{238}U, which requires a neutron with a kinetic energy in excess of 1 MeV to fission. Cross sections for such "fast-fission" reactions are much smaller than those for thermal fission. Also, fission does not always result when a neutron is absorbed by a fissionable nucleus. ^{235}U fissions only 85% of the time after thermal-neutron absorption.

Nuclei with an odd number of nucleons fission more readily following neutron absorption than do nuclei with an even number of nucleons. This fact is related to the greater binding energy per nucleon found in even-even nuclei, as mentioned in Section 3.2. The ^{235}U nucleus is even-odd in terms of its proton and neutron numbers. Addition of a neutron transforms it into an even-even nucleus with a larger energy release than that following neutron absorption by ^{238}U. Fissionable nuclei break up in a number of different ways. The ^{235}U nucleus splits in some 40 or so modes following the absorption of a thermal neutron. One typical example is the following [8]:

$$ {}^{1}_{0}n + {}^{235}_{92}U \rightarrow {}^{147}_{57}La + {}^{87}_{35}Br + 2{}^{1}_{0}n \qquad (1.4) $$

The surface tension of a liquid causes a droplet to assume a spherical shape, but if energy is supplied in some fashion, this shape is distorted. If the attractive surface tension force is greater than the distorting force, the drop oscillates between spherical and elongated shapes. If, however, the distorting force becomes larger than the attractive force, the drop elongates past a threshold point and splits (fission). The repulsive Coulomb force tends to distort the nucleus in the same way a distorting force does a droplet, while the surface tension tries to bring it in to a spherical form. The ratio between the two opposing energies should measure the instability to fission of the nucleus. The liquid drop model predicts that the probability of fission should increase with increasing Z^2/A. Of all naturally occurring nuclides only ^{235}U can be fission by thermal neutrons, while ^{238}U fission requires energetic neutrons ($\geq$ 2

MeV). With increasing Z (> 92) the fission probability with thermal neutrons increases and the half-life of radioactive decay by spontaneous fission decreases. Both of these processes are more probable for even Z-elements than for odd Z-elements.

If N and Z are kept constant and the potential energy of the nuclear liquid drop is calculated as a function of deformation from spherical to prolate, the curve in Figure (1.2a) is obtained. The nucleus exists normally in the ground state level of the potential well. In order to undergo fission it must be excited above the fission barrier which is about 5 - 6 MeV. As the diagram shows, this means excitation of the nucleus into the continuum level region if the nucleus retains the shape associated with the potential well. However, if the nucleus deforms, some excitation energy goes into deformation energy. At the top of the barrier, the nucleus is highly deformed and has relatively little internal excitation energy. It exists in well-defined vibrational levels, and fission occurs from such a level. This is known as the "saddle point" (the top of the barrier) of fission. It has long been recognized that the liquid-drop model semi-empirical mass equation cannot calculate the correct masses in the vicinity of neutron and proton magic numbers. More recently it was realized that it is less successful also for very deformed nuclei midway between closed nucleon shells. Introduction of magic numbers and deformations in the liquid drop model improved its predictions for deformed nuclei and of fission barrier heights. However, an additional complication with the liquid-drop model arose when isomers were discovered which decayed by spontaneous fission. Between uranium and californium a number of nuclides were found to decay by spontaneous fission with half-lives of 10^{-2} to 10^{-9} s, millions of times slower than prompt fission which occurs within 10^{-14} s but millions of times faster than normal spontaneous fission. For example, ^{242}Cm has a ground state half-life to spontaneous fission of 106 years, while an isomeric state of ^{242}Cm has been found to fission with $t_{1/2}$ of 10^{-7} s.

Strutinsky developed an extension of the liquid drop model which satisfactorily explains the fission isomers and asymmetric fission. For such short half-lives the barrier must be only 2 -3 MeV. Strutinsky added shell corrections to the basic liquid-drop model and obtained the "double-well" potential energy curve in Figure (1.2b). In the first well the nucleus is a spheroid with the major axis about 25%

larger than the minor. In the second well, the deformation is much larger, the axis ratio being about 1.8 A nucleus in the second well is metastable (i.e. in isomeric state)

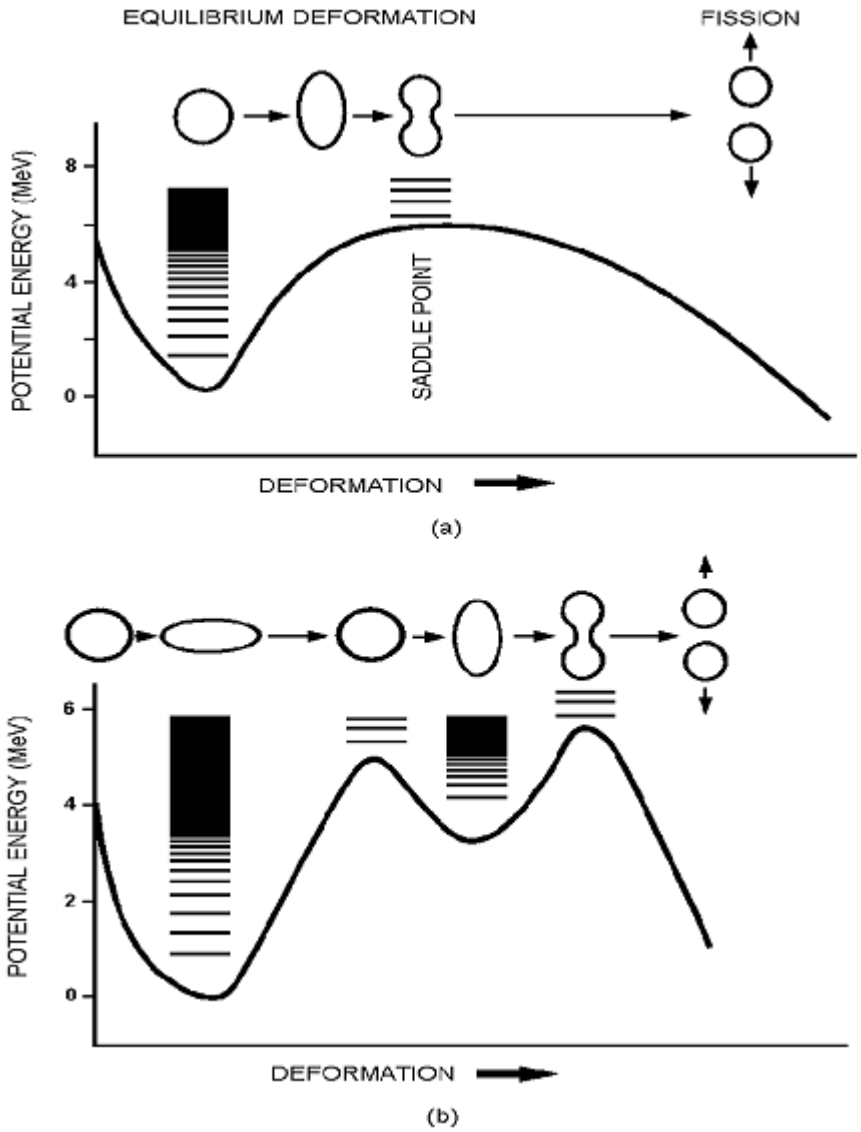

Fig. (1.2): *(a) The liquid drop model. (b) Same, but modified by shell correction*

as it is unstable to decay to the first well or to fission. Fission from the second well is hindered by a 2-3 MeV barrier, while from the first well the barrier is 5-6 MeV, accounting for the difference in half-lives. The single-well curve in Figure (1.2a) predicts symmetric fission whereas the double-well curve in Figure (1.2b) leads to the correct prediction of asymmetric fission and a thin neck. Incorporation of shell effects in the fission model also leads to the prediction that the half-lives of very heavy

nuclides ($Z \geq 106$) must be longer than the simple liquid-drop model would indicate. This has led to a search for "super heavy" elements with Z=110–118 [7].

1.1.4 Fission Products:

When a nucleus undergoes fission, a number of products are formed. There are, of course, the fission fragments, but in addition, neutrons, γ-rays, β-rays and neutrinos are emitted [9].

Many different atomic nuclei have been produced by the fission of uranium and thorium as a result of bombarding them with neutrons. The fact that so many different fission products have been produced indicates that the excited uranium or thorium nucleus can split up in many different ways. All of the presently known fission products are elements in the middle of the periodic table with atomic numbers ranging from Z=30 to Z=66.

The relative distribution of the different nucleus among fission products depends on the energy of excitation available for the fission process. Figure (1.3) is a graph showing the fission yield (in percentages) plotted against the mass number of the fission fragment for the fission ^{235}U. From this graph it is seen that the most probable values for the mass numbers of the two fission fragments are about 95 and 139 when two prompt neutrons are emitted simultaneously. It will be observed that the yield passes through a minimum at mass number 117, corresponding the fragments of equal mass. The yield curve drops rapidly at mass numbers 72 and 162.

The ratio of the number of the neutrons to the number of protons that is N/Z for uranium is about 1.6. For stable elements in the range of atomic numbers 30 to 63 the range maximum values of N/Z is 1.3 to 1.5; hence the fission fragment will have an excess of neutrons. The fission products will therefore be unstable; they will thus go to more from either by beta disintegration or by the emission of one or more excess neutrons. Neutrons emitted a metastable time after the fission process is called delayed neutrons; they play an important role in the control of nuclear reactors.

The isobaric yield shown in Fig. (1.3) only indicate that how many nuclide with a given A are formed per fission, the total fission yield is 200%. From Fig. (1.3) one can observe that when the nucleon number of fission nuclei increases, the fission

yield distribution changes. The right hump of curve remain at the same position while the left shifts to higher nucleon number as a result of which the fission yield percent

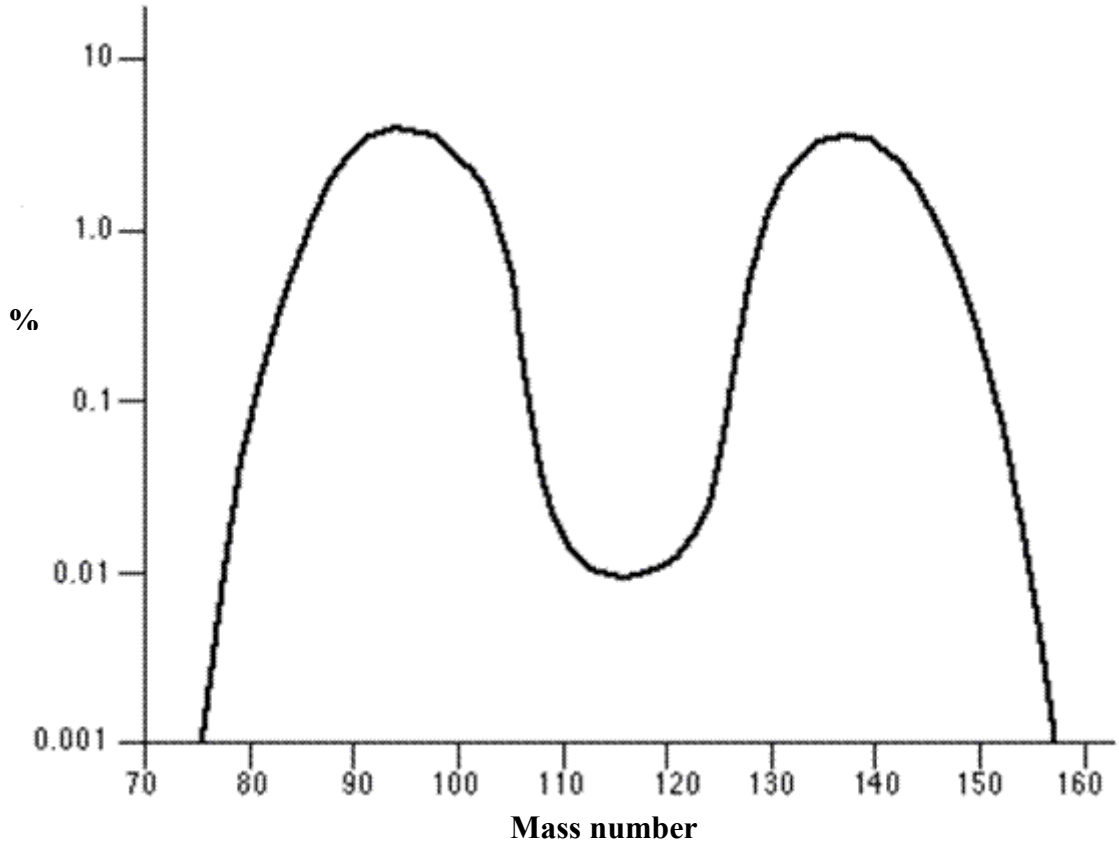

Fig. (1.3): *Distribution of fission products form Uranium*

become less. While with increasing incident particle energy the trough become shallower. Many heavy nuclei can be fissioned with fast neutrons while few with slow neutrons. It means that nuclei with some exceptions like ^{240}Pu, only can undergo fission with slow neutrons which can be used for sustaining chain reaction [10].

1.1.5 Uranium's Scientific History:

On the 24th September 1789 a German chemist Martin Heinrich Klaproth announced the discovery of uranium in an address to the Prussian Academy of Science in Berlin. He named this element as the same after the discovery of recently planet Uranus. Klaproth made his discovery while analyzing an ore known as pitchblinde from the mines at Jachimsthal in Bohemia, which nowadays is known as Jachymov in Czech Republic. Round about 50 years later a Frenchman Eugene

Peligot succeeded in getting pure uranium from the ore. In nineteenth century, uranium ore was mined along with other minerals at Joachimsthal and a few minerals in Cornwall, England. In U.S uranium was discovered in 1870s. With the discovery of radioactivity, Henery Becquerel also did experiments over uranium. One of his students obtained the results which were interpreted correctly and radioactivity was named for the new phenomenon [11].

Henri Becquerel first observed uranium's radioactivity in 1896, although he did not realize the full significance of his discovery. However, one of his students did correctly interpret his results and chose the name 'radioactivity' for the new phenomenon [12].

Uranium is an element with the atomic number 92. Natural occurrences of uranium contain three isotopes in the following relative abundances; ^{238}U 99.28%, ^{235}U 0.71%, ^{234}U 0.0055%. Uranium exploration activities are taking place in Canada, USA, Australia, India, Russia, Uzbekistan, and in lesser extent in Egypt, Ukraine, France, and Romania [13].

1.1.6 Cross Section:

Although in principle an approach similar to that employed in deriving the transition probability could be used for expressing the likelihood that a reaction will take place under given circumstances, a more direct means of expressing this probability is offered by the elementary concept of a reaction cross section, which has the dimension cm^2 rather than sec^{-1} and thus is represented by an area [14].

The concept of cross section is based upon a consideration of the physical situation encountered in determining reaction probability in the laboratory. An incident collimated beam of particles impinges upon target nuclei in a suitable specimen of material and interacts with these through the processes of scattering, absorption and/or reaction, thereby becoming attenuated it may be in intensity or energy, or both by an amount which can be determined by measurements effected on the emergent beam. The most naive way of picturing the likelihood of interaction is to visualize the incident beam as made up of point particles which if they directly strike some part of a target nucleus, set up an interaction, whereas if they miss the target

nucleus, they produced unaffected. However, this naive conception overlooks both the finite extension of the impinging particles and the finite interaction radius which may be presumed to extend quite some way beyond the immediate confines of the target nucleus. Hence rather than treating the geometrical cross sectional area of nucleus πr^2 as a measure of interaction probability, it is meaningful to ascribe to each nucleus an effective area σ perpendicular to the incident beam such that if a bombarding particle impinges upon any part of such an imaginary disk, a reaction will occur, but otherwise no interaction takes place if the particle's path falls outside the target zone. The magnitude of the disk's cross section σ depends upon the reaction and upon the energy; its size is suitably expressed in units of:

$$1b = 1barn = 10^{-28}\ m^2 = 10^{-24}\ cm^2 \qquad (1.5)$$

1.2 ACCELERATOR DRIVEN SESTEM:

In 1996, at GSI, Darmstadt, an European Collaboration started a dedicated experimental program, devoted to reaching full comprehension of proton-induced spallation reactions. Accurate knowledge of proton-induced spallation reactions is relevant both for fundamental research and for technical applications. Among the latter, the design of accelerator driven system (ADS) and radioactive ion beam (RIB) facilities relies strongly on knowledge of the formation cross section of residual nuclei produced in such reactions. This information is needed to calculate the short term and long term radioactivity building up in these facilities and thus is crucial for designing the shielding and estimating the residual activation of such devices [15].

Accelerators with high beam intensities (10-25 mA) make it possible to envisage accelerator driven system for energy production and nuclear waste incineration. In such systems, the large numbers of neutrons that result from the interaction of high energy ions (e.g. protons) with massive targets such as lead can be used to operate sub-critical nuclear assemblies. The chain reaction in an accelerator driven system is sustained by continuous operation of the driving accelerator and system remains sub-critical at all time. This cub-critical is the key issue and is the main advantage of accelerator driven system over conventional nuclear system that operates only in critical conditions. A sub-critical accelerator driven system provides the opportunity to use the excess neutrons foe other purposes such as nuclear waste

transmutation as well as for breeding of fissile material from fertile isotopes such as ^{232}Th [16].

The technical working group that develops common European research and development programme on ADS system proposes liquid-lead or liquid-bismuth as suitable spallation materials and coolant. For fast system fuel used is normally in solid form and is dissolved in salt for thermal system. Though we use also He-gas and molten salt as coolants in the sub-critical and thermal reactor. But the advantage of liquid-lead or liquid-bismuth as coolants are, their neutron physical characteristics of the lead alloys. For example the low absorption cross section for both thermal and fast neutrons and the high neutron gain of the spallation reaction. Lead alloys also shows excellent heat transport capacities which allow their applicability even if high surface heat fluxes present [17].

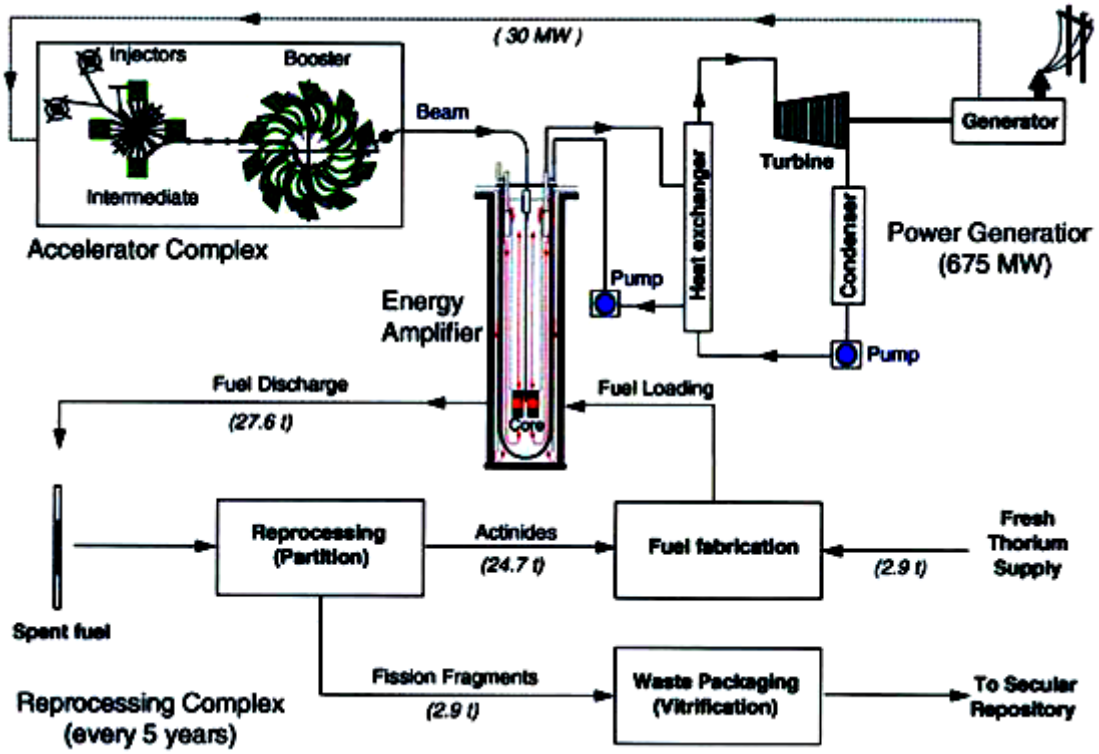

Fig. (1.4): *Closing the nuclear cycle with the energy amplifier, a sub-critical device with a Th-^{233}U fissile core fed with a supply of spallation neutrons. There is no critical, no plutonium and no problem of actinide waste. At the end of the cycle, ^{233}U and other uranium isotopes are recycled to serve as the initial fissile part of new load of fuel. Thorium is an abundant resource (mach more than uranium) and supplies could last thousands of centuries.*

Adding that ADS techniques involves the breeding of ^{235}U or ^{239}Pu from the most dominant isotopes in natural thorium (^{232}Th 100%) and uranium (^{238}U 99.3%) respectively. So human needs for energy can be produced by these natural resources for a very long time. It has been observed that a 1000 MeV proton beam can produce 20 to 30 spallation neutrons per proton. In these produced neutron some are captures while others are used for fission [18]. The spallation neutron flux could be in the range of $10^{14} - 10^{15}$ $cm^{-2}s^{-1}$ which depends on the actual power of the proton beam. We need 10^{16} $cm^{-2}s^{-1}$ neutron/proton flux for the incineration of nuclear waste, but actually there are certain deficiencies that this value of flux is impossible to get and we are restricted with flux value $<10^{14}$ $cm^{-2}s^{-1}$. Detailed simulations showed the necessity of discarding some schemes and of introducing new ideas as shown in Fig. (1.4) [19].

1.2.1 Accelerator Driven System Properties:

The important issue in designing an ADS is its inherent sub-criticality and stability of reactivity. This feature can significantly improve the safety of an ADS. Contrary to a critical reactor (Figure 1.5), an ADS operates in a non self-sustained

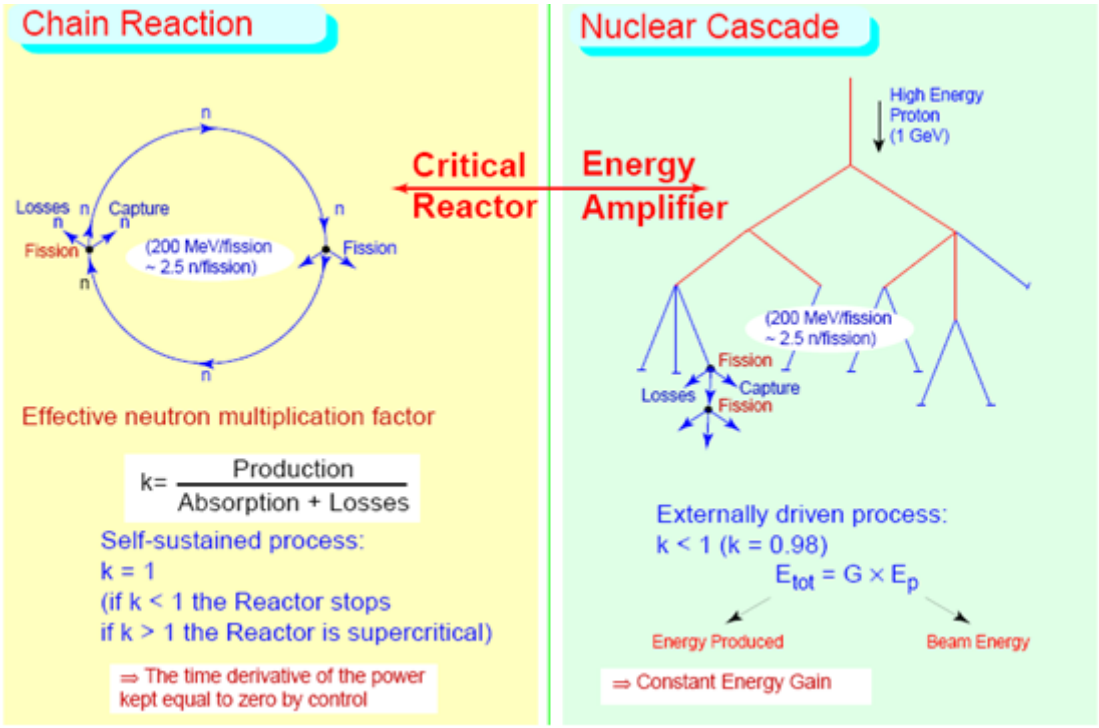

Fig. (1.5): *Illustration of the nuclear cascade that drives an ADS as opposed to the self sustained chain reaction driving a critical fission reactor.*

chain reaction mode, which minimizes criticality and power excursions. The ADS is operated in a sub-critical mode and remains sub-critical whether the accelerator is on or off, providing thus an extra level of safety against criticality accidents. The accelerator provides a control mechanism for sub-critical systems, which is by far more convenient than control rods in critical reactors. Control rods are not only a safety concern, they degrade the neutron economy of the system as well. Good neutron economy is crucial for ADS since it determines the power and consequently the cost of the accelerator. The ADS provides a decoupling of the neutron source (spallation source) from the fissile fuel (fission neutrons). It accepts fuels that would not be acceptable in critical reactors, such as Minor Actinides, fuels with a high Pu content, and even long-lived fission fragments (e.g. ^{99}Tc and ^{129}I) [20].

1.2.2 Nuclear Waste:

Transuranic elements (TRU) and fission products (FP) are the two main components of nuclear waste, representing respectively 1.1% and 4% of spent nuclear fuel. TRU, which are produced by neutron capture in the fuel eventually followed by decay, can only be destroyed by fission, while FP can only be destroyed by neutron capture; therefore, different methods will have to be used to eliminate them. As the long-term radio-toxicity of waste (Figure 1.6) is clearly dominated by TRU, the EA has been designed to destroy them with the highest efficiency.

At present most of the nuclear waste is kept under surveillance in shallow depth storage facilities (e.g. cooling ponds in nuclear power plants). However, concerns about leaks in the biosphere and proliferation risks implies that this can only be a standby solution to be followed either by permanent storage in deep geological repositories and/or transmutation into “harmless” nuclear species [20].

1.2.3 Transmutation of Nuclear Waste by ADS:

The transmutation of problematic fission products for waste disposal has motivated the research of numerous scientists since the 1960s. In the early 1990s the international community began to consider the concept of ADSs as a suitable alternative for the elimination of high-level waste (HLW). Several research programs were launched and led to the definition of several technological alternatives. Among

the alternatives garnering international attention was the energy amplifier (EA) [21]. The idea of using dedicated sub-critical reactors for transmuting actinides was first mentioned in open literature by Foster (1974). This idea gained renewed interest when Carminati et al. (1993) published their work on the energy amplifier (EA), an accelerator-driven system (ADS) with the potential both to generate electricity in significant quantities and to transmute high-level nuclear waste [22].

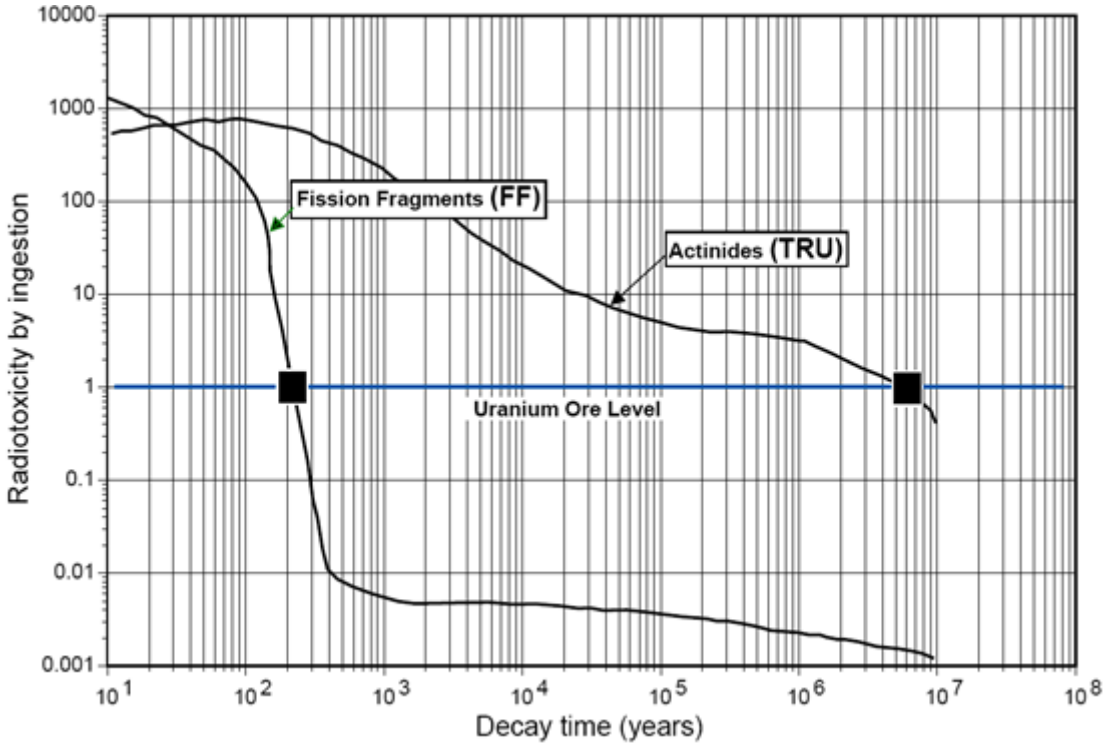

Fig. (1.6): *Time evolution of the potential radio-toxicity (relative to uranium ore) of the two main components of nuclear waste for PWR spent fuel [20].*

Transmutation of plutonium and minor actinides and long-lived fission products is a promising concept to reduce the radioactive waste and its long-term radiotoxicity. Partitioning and transmutation are considered as ways of reducing the burden on a geological disposal. Since plutonium and the minor actinides are mainly responsible for the long-term radiotoxicity, when these nuclides are removed from the waste (partitioning) and fissioned (transmutation), the remaining waste loses most of its long-term radiotoxicity. Transmutation is the process of bombarding a material with particles to form new atoms with higher masses and/ or to fission the material into atoms with smaller masses. It can reduce the mass, volume, activity, heatload, and/or raditoxicity of waste that must be sent to repository. Many different

technologies have been examined for transmutation, including a variety of reactors and ADSs. These systems are primarily distinguished by whether they have fast or thermal neutron spectrums. Transuranics transmutation can be planned in both thermal and fast reactors. However, a critical reactor with solid fuel and liquid coolant, thermal and fast, in which neutron production and neutron losses are in balance, may contain a quite limited amount of particular TRU mixture components like Np, Am or Cm isotopes, due to safety constraints. This is one of the mains reasons why the accelerator-driven systems are currently studied worldwide for nuclear waste burning. Accelerator-driven subcritical reactors have been proposed for many applications such as energy production, fertile-to-fissile transmutation and conversion of long-lived radioisotopes into stable or much shorter-lived isotopes. The transmutation technology to incinerate the longlived radioactive isotopes using an accelerator-driven subcritical reactor is one of the best solutions. ADS can be designed to have a fast neutron energy spectrum, and they are subcritical so safety issues can be considered less significant than in a fast reactor. Another advantage of ADS is that they can burn mixtures of material that would not maintain criticality in a reactor [23].

Transmutation of one radionuclide into another is achieved by neutron bombardment in a nuclear reactor or by an accelerator driven device. A high-energy proton beam hitting a heavy metal target produces shower of neutrons by spallation. The neutrons can cause fission in a subcritical fuel assembly, but unlike a conventional reactor, fission ceases when the accelerator is turned off. The fuel may be uranium, plutonium or thorium, possibly mixed with long-lived wastes from conventional reactors. The objective is to change the long-lived actinides and fission products into significantly shorter-lived nuclides. The goal is to have wastes which become radiologically innocuous in only a few hundred years. Some radiotoxic nuclides, such as ^{239}Pu and the long-lived fission products ^{99}Tc and ^{129}I, can be transmuted (fissioned, in the case of ^{239}Pu) with thermal (slow) neutrons.

The minor actinides Np, Am and Cm (as well as the higher isotopes of plutonium) are all highly radiotoxic and much more readily destroyed by fissioning in a fast neutron energy spectrum, where they can also contribute to the generation of power. With repeated recycle in a transmutation system, the radiotoxicity of the spent

nuclear fuel can be reduced to the point that after a decay period of less than 1000 years, it is less toxic than the uranium that is originally used to produce the fuel. The need for a waste repository is certainly not eliminated but the hazard posed by the disposed waste materials is greatly reduced.

There is an approach for commercial nuclear energy production without a long term high level waste stream and for transmutation of both fission product and higher actinide commercial waste using a thermal flux of neutrons in the 10_{16} n/cm$_{2}$s range which can be produced using high-current radio-frequency proton accelerators in the 0.8 to 1.6 GeV energy range. With the recent advances in the proton accelerator technology it is possible to get such high flux, which is approximately 100 times larger than that produced in the typically available thermal reactor. When these protons strike a target of a heavy nuclide with a large radius such as lead, approximately 55 neutrons are generated per proton. The energy deposited for this process is about 30 MeV of proton energy per neutron compared with about 200 MeV of fission energy deposited per useful neutron from a chain reaction in fissile material such as $_{235}$U. This large flux of thermal neutrons makes a possible waste inventory in the transmutation system which is smaller by about a factor of 100 than the competing concepts. The accelerator allows the system to operate well below criticality so that the possibility for a criticality accident is eliminated. The elimination of the use of control rods makes this process more convenient.

The main constraint on any practical reactor is the use of the available neutrons per fission primarily for maintaining the chain reaction and secondarily for other purposes. The extra neutron produced per fission with an accelerator can be used to transmute waste in addition to keeping the chain reaction on and also for breeding. Consider the case of ^{237}Np. In a high neutron flux, with the capture of two neutrons the target nucleus ^{237}Np produces ^{239}Np by fission which is accompanied the emission of about 2.7 neutrons. So that ^{237}Np behaves as a fuel in high flux. In a lower flux the nucleus ^{238}Np decay to non-fissile ^{238}Np before the second neutron can be captured. The nucleus may be destroyed by the fission of ^{239}Np with the release of 2.9 neutrons. On average about four neutrons are needed for destruction in the lower flux. Therefore the ^{237}Np waste is a poison in the low flux but a fuel in the high flux [24].

1.2.4 Spallation Process:

Spallations a type of nuclear reaction in which the high energy level of incident particles causes the nucleus to eject many particles, thus changing both its mass number and its atomic number. Also, nuclear spallation has to be slightly specified in the context of accelerator driven system or high intense neutron sources. Here spallation is the disintegration of a nucleus by means of high energetic proton-induced reactions. Typically approximately 20 neutrons are created per incident 1GeV proton on lead [25].

The term spallation covers the interaction of high-energy hadrons (e.g. protons, neutrons, pions, muons, etc.) or light nuclei (deuterons, tritons, etc.), from few hundreds of MeV to few GeV, with target nuclei. It corresponds to the reaction mechanism by which this high-energy projectile knocks out of the target some nucleons and/or light nuclei, leaving a highly excited residual nuclei which may excite via particle evaporation or fission leading to the final spallation product. Depending upon the conditions, the number of emitted light particles, and especially neutrons, may be quite large. This is, of course, the feature of utmost importance for ADS. For thick targets, high-energy secondary particles can undergo further spallation reactions (inter-nuclear cascade). For some target materials, low-energy spallation neutrons can enhance neutron production through low-energy (n, xn) reactions. For heavier nuclei, high-energy fission can compete with evaporation (e.g. tungsten or lead). Some spallation targets such as thorium and uranium can be further fissioned by low-energy spallation neutrons (41 MeV) [26].

The concept of spallation covers the interaction of high-energy (from a few tens of MeV to a few GeV) hadrons or light nuclei with nuclear targets. In other words, it corresponds to the reaction mechanism by which a high-energy hadronic projectile knocks out of the nuclear target some nucleons and/or light particles, leaving a residual nucleus (spallation product). Depending upon the conditions, the number of emitted light particles, and especially neutrons, may be quite large. This is, of course, a feature of utmost importance for an ADS. Figure (1.7) describes the spallation reactions produced by a 1 GeV proton in heavy nuclei.

At such a high projectile energy high compared to the most probable energy of thermal neutrons (the peak in the Maxwell distribution of energies) of 0.0253 eV it is no longer correct to think of the nuclear reaction as proceeding through the formation of a compound nucleus. As shown in Figure (1.7), high-energy protons produce a wide range of reactions through the interactions with the nuclei. At first, the fast direct process induced is an Intra- Nuclear Cascade (nucleon-nucleon collisions inside the nucleus); this reaction depends on the geometrical cross-section of the different elements rather than the common reaction cross sections used at lower energies. Pre-Compound Stage (including pre-equilibrium, multifragmentation, Fermi break-up) and Compound Nuclei (evaporation of neutrons mostly and high-energy fissions) are subsequent models of interactions between the secondary particles and the nuclei of the spallation source. Finally, Low-Energy Inelastic Reactions (n, xn), (n, α), (n, γ), etc. are produced once the energy of the secondary particles has decreased below a certain threshold (assumed to be around 20 MeV for neutrons).

The relevant aspects of the spallation process are mainly characterised by:

- Spallation Neutron Yield (i.e. multiplicity of emitted neutrons), which determines the requirement in terms of the accelerator power (current and energy of incident proton beam).

- Spallation Neutron Spectrum (i.e. energy distribution of emitted neutrons), which determines the damage to and activation of the structural materials (design of the beam window and spallation target) and the kind of materials to be transmuted by the source. The spectrum of spallation neutrons evaporated from an excited heavy nucleus bombarded by high-energy particles is similar to the fission neutron spectrum slightly shifting to higher energies. The average neutron energy $\langle En \rangle \approx$ 3-4 MeV, higher than the ~2 MeV of the fission neutrons due to the contribution of direct knockout neutrons. This higher average energy makes these source neutrons more suitable transmuting elements with different resonance spectra, although the damage to the structural materials is also more intense.

- Spallation Product Distribution, determining the radiotoxicity of the residues (radioprotection requirements).

- Energy Deposition, which determines the thermal-hydraulic requirements (cooling capabilities and nature of the spallation target and beam-windows) [27].

1.2.5 Energy Amplifier:

The energy amplifier (EA) is the result of a 'cross-fertilisation' between the technologies of modern particle accelerators and of nuclear power, in particular the development of fast-neutron breeder reactors and fuel reprocessing. The underlying physical principles of energy amplification and the transmutation possibilities of the device were demonstrated in the FEAT and TARC experiments performed at CERN [21].

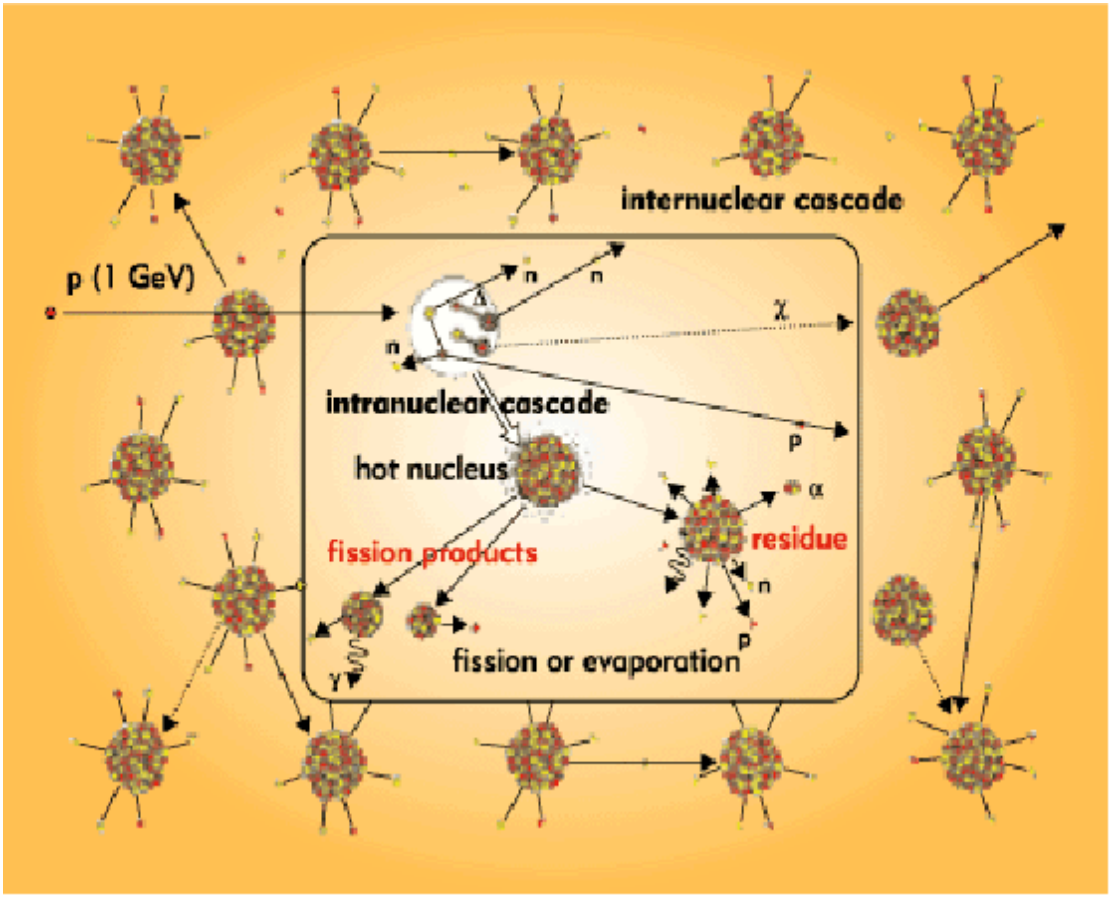

Fig. (1.7): *Representation of the spallation process caused by a proton interacting with heavy nuclei.*

The EAs are sub-critical, fast neutron systems, driven by a proton accelerator. The accelerator bombards a target with high-energy protons, which produces a very intense neutron source through the spallation process. These neutrons are subsequently multiplied in the sub-critical core which surrounds the spallation target [26].

In a sub-critical reactor, the number of neutrons originating from fission is not sufficient to overcome the losses (due to leaks and absorption of neutrons by some materials). Therefore, under no circumstances can a chain reaction be self-sustained and in order for the reaction to proceed, one needs to continuously supply neutrons from an external source. In an Accelerator Driven System, this external source consists of neutrons created by spallation when a medium energy proton beam reacts with a heavy target (usually Lead). The supply of neutrons is proportional to the proton intensity, which can be modified precisely and with a very short time constant. The proton beam plays the role of the control bars in a reactor, the difference being that it is proactive rather than reactive: if it fails, the reaction stops and it can never lead to an overheating.

In contrast to fission, spallation costs energy and the ability to steer the fission process will come at a cost, coming from the accelerator beam power needed, and that cost has to be minimized for the proposal to remain economical. The energy of an incoming proton results - because it initiates nuclear fission cascades - in the production of a much larger energy. We say it is amplified (by fission) and call the device an Energy Amplifier (EA). The ratio between the incoming energy and the total energy is called the gain G of the amplifier. G is related to the neutron multiplication factor k [26].

$$K = \frac{\text{Production}}{\text{Absorption} + \text{Losses}} \tag{1.6}$$

For an efficient control of the reaction, it is enough for the EA to be weakly sub-critical. We see that k=0.98 is sufficient to ensure that the EA is sufficiently far from criticality conditions. Setting k=0.98, the neutron deficit, to be supplied by spallation is s=0.02. For each 100 neutrons, there will be 98 fission and 2 spallation neutrons (each costing 30 MeV), in the mix. Only part of the neutrons (40%) will

induce fission and bring 200 MeV of energy, the rest will be captured or leaked out. Therefore:

$$G = \frac{\text{Return}}{\text{Cost}} = \frac{200 \times 0.4 \times 98}{2 \times 30} = 130 \qquad (1.7)$$

The gain will be smaller (G≈50) if 5% of the neutrons come from spallation and more generally, it can be shown to be:

$$G = G_o \frac{1}{1-k} \qquad (1.8)$$

The energy gain was measured as a function of the proton energy Figure (1.8) and shown to be constant at energies larger than 1 GeV . As shown in Figure (1.9), only a small proportion of the energy produced by the Energy Amplifier (4 to 6%) will have to be recirculated into running the accelerator.

Neutrons are created by spallation when a beam of protons coming from the accelerator interacts with a Lead target. Neutrons lose their energy and diffuse to interact with a sub-critical fissile core. The heat created by fission is evacuated from

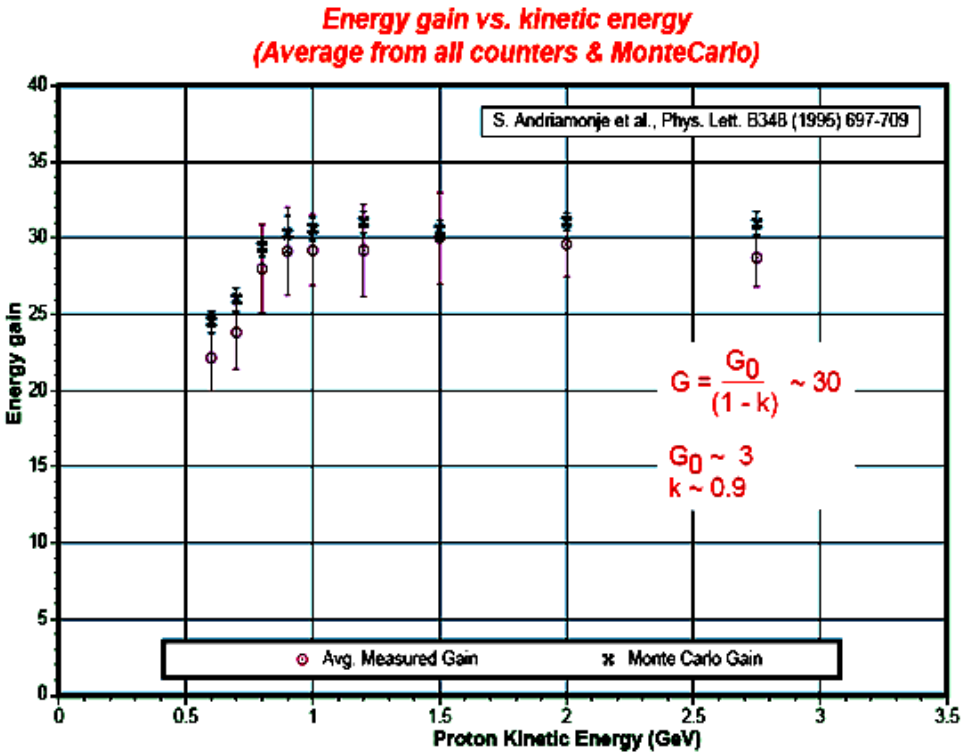

Fig. (1.8): *Variation of gain with incident proton energy. The gain is constant energies larger than 1 GeV [28].*

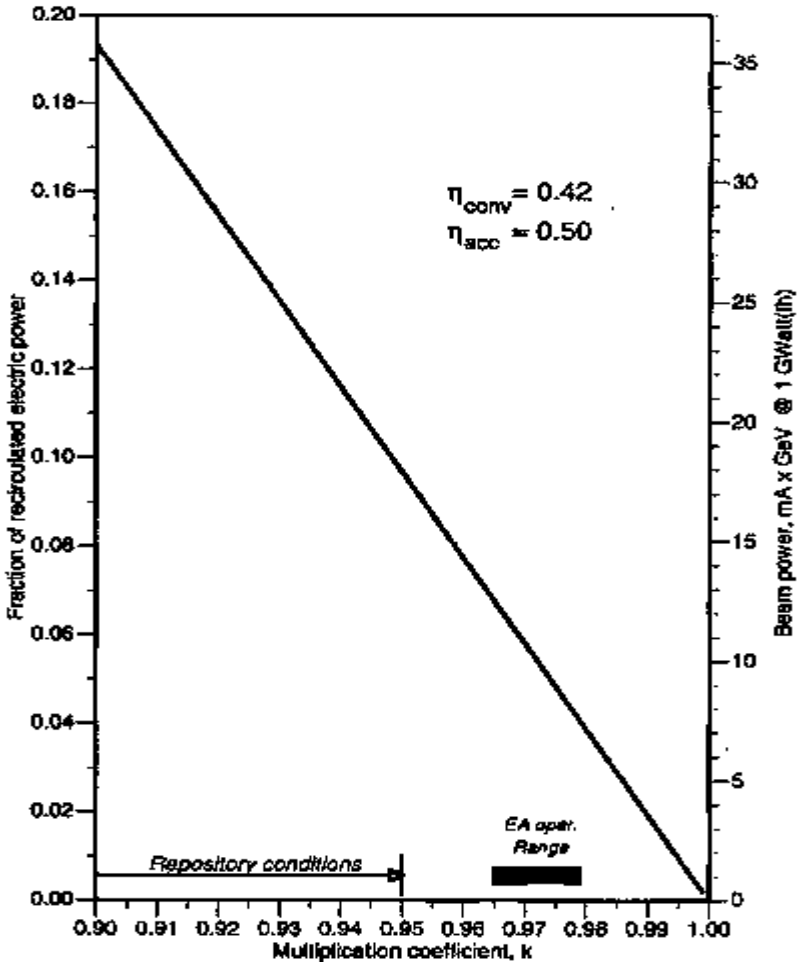

Fig. (1.9): *Fraction of energy recirculated to run the accelerator, assuming 42% energy conversion and 50% accelerator efficiency. The relevant figure is the beam power (GeV × mA) over 1 GeV [28].*

the core by natural convection in molten lead, through a heat exchanger to a secondary circuit. The presence of lead results in a harder neutron spectrum than is the case in usual, sodium-cooled fast reactors. As shown in Figure (1.10), this is opens up the very important ability of the device to fission practically all actinides with a reasonable probability.

The use of lead as a heat carrying medium has important safety implications. In comparison with Sodium (which has been used extensively in critical fast reactors, Lead is chemically inert and it has a low vapour pressure even at a high temperature. Its high density allows the use of cooling by natural convection which avoids using pumps. This is a safety feature: no pumps, no failure. The nuclear properties are also remarkable: lead being a doubly-closed shell nucleus (the nuclear equivalent of a noble gas, it has a very low absorption by neutrons.

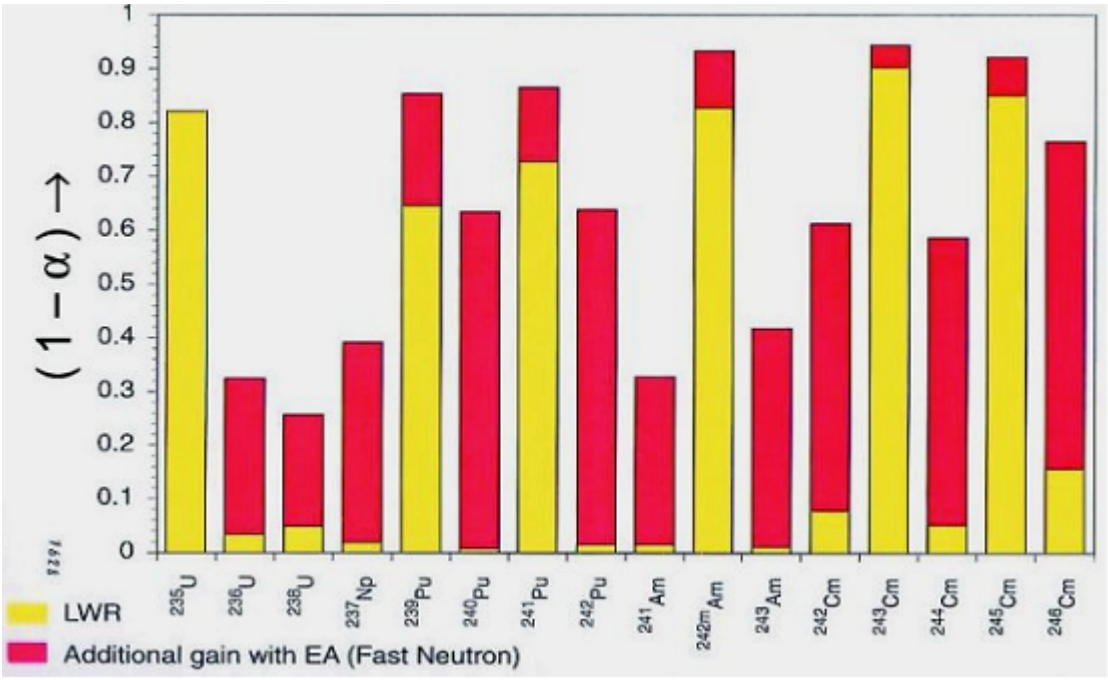

Fig (1.10): *Probability of fission/neutron absorbed because of the Lead neutron-diffusing medium, all elements will undergo fission to some degree. the opens the way to destroying actinide waste [29].*

The schematic principle of the Energy Amplifier is shown in Fig. (1.11). One safety problem which is specific to the EA and has been much talked about is the window separating the beam from the target. There is at CERN and other labs an

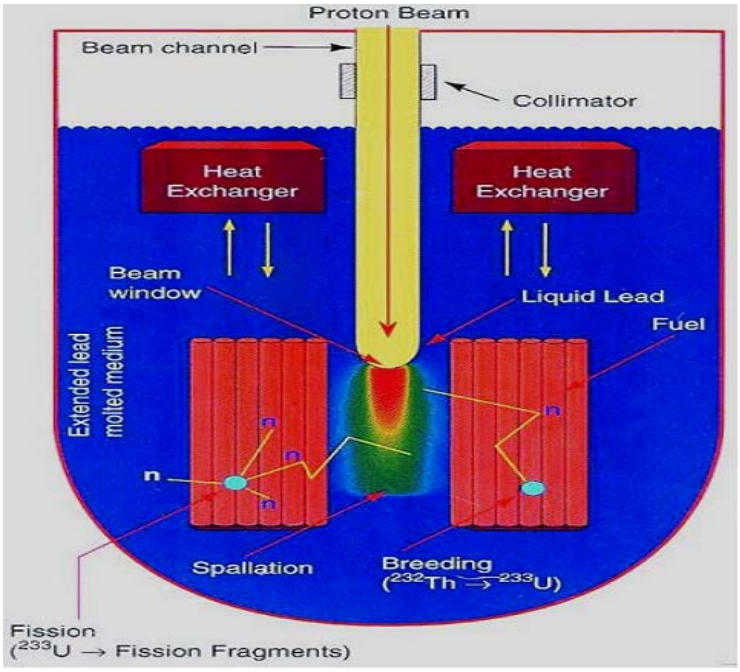

Fig. (1.11): *Schematic principle of the Energy Amplifier [29].*

extensive experience with proton beams of a fraction of a millimetre diameter and an average intensity of one microampere. The EA would admittedly involve beams of 10 000 times higher intensity, but then the beam spot would be of some 10 centimetre diameter so that the current density would actually be smaller. All this has obviously been included in the detailed simulation and there is a further plan to test experimentally at lower proton energy (where the energy loss, going as 1/E is actually greater). One has therefore confidence that the window concept is sound. One cannot argue that the window would be a weak point in the barrier insulating the reactor core from the outside world. In fact, should the window break, it would immediately be replaced by liquid lead flowing up the beam tube, preventing the beam from reaching the target and thus stopping fission processes occurring in the core [28, 29].

1.2.6 Light Water Reactor:

Today's nuclear energy system is the result of a fifty-year development during which this technology has reached industrial maturity and became a reliable resource for our electricity needs. Most of this development has been concentrated on light water reactor (LWR) concepts (pressurised water reactors and boiling water reactors) and their fuel cycle. The success of the LWR is based on the early recognition that natural fissile material were considered scarce and that nuclear energy could develop only if systems with low fissile inventories per unit power would be built in the start phase. LWRs, as initially developed for naval applications, fulfilled this criterion and used simple and relatively cheap technology that enabled a first generation of power stations to be constructed rapidly. The necessary uranium enrichment technology was available from the military development. The significant plutonium generation in LWR fuels was considered to be an asset because plutonium is an excellent fuel for fast reactors and the anticipated deployment of fast reactors around the turn of the century would have required large fissile inventories. In the early days of nuclear energy, however, the back-end of the fuel cycle was not given the same attention as the reactors, and the concept of geologic disposal of radioactive waste was not yet questioned by the public [30].

Figure (1.12) shows the radiotoxicity of uranium-oxide fuel with an average burn-up of 50 GWd/tHM as discharged from the reference LWR considered in the present study. In the figure, this radiotoxicity is compared with the radiotoxicity of the

remaining HLW after separation of 99.9% of the uranium and plutonium, assuming a cooling time of 4 years between fuel discharge and reprocessing. A decomposition of the latter into nuclide contributions is also shown. It can be seen that the radiotoxicity is dominated, first, by short-lived fission products, and later, by actinides. A few hundred-thousand years after the discharge, the radiotoxicity of the unprocessed fuel drops to the natural toxicity level for LWRs, i.e. the equilibrium radiotoxicity of the natural uranium required to fabricate the fuel.18 The separation (and intermediate storage) of uranium and plutonium would reduce the radiotoxicity of the remaining HLW in the time frame from 103 to 105 years by an order of magnitude, but it would still take some twenty-thousand years for the radiotoxicity of this waste to reach the LWR natural toxicity level. Moreover, when defining a HLW radiotoxicity reduction goal for a fuel cycle strategy involving reactors with increased resource efficiency, it should be borne in mind that the natural toxicity level decreases proportionally with the natural uranium requirement. The figure indicates that, for a pure fast reactor strategy, the natural toxicity level corresponds about to the radiotoxicity of the long-lived fission products [30].

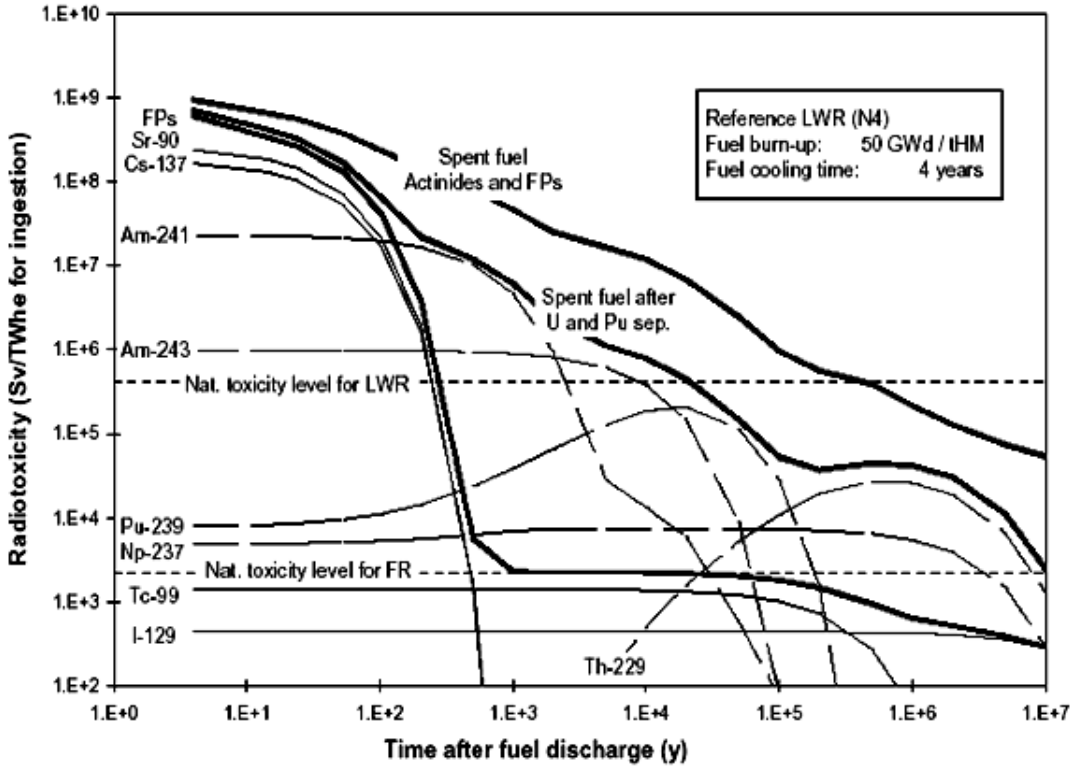

Fig. (1.12): *Radiotoxicity of LWR spent fuel [30].*

1.3 LITERATURE REVIEW:

In this work we will estimate the product of residual nuclei at medium energies from rhenium and uranium therefore it will be necessary to review the exciting literature in these issues. There are two different ways to perform experiments on is to radiate target fuels and to analyze products after end of irradiation by of-line measurement technique. This is called experiments in classical kinematic. The second method is to irradiate high hydrogen target being at rest in the laboratory frame with high energy heavy ions of the target elements. In this case the product nuclides will leave the hydrogen target due to their high momentum and can be analyzed by modern on-line nuclear physics measurement technique. This method is called experiments in inverse kinematic. In this section we will review the previous study for nuclide production from reaction between proton and uranium and rhenium.

S.A. Karamian et al. [31] studied that the nuclides production from reaction between proton and rhenium. They studied the productivity of the spallation reactions at proton energies of 100-660 MeV for accumulation of the radioactive isotopes and isomers, and identified many radioactive products of the spallation and fission reactions, and their yields were compared with theoretical code simulation. They deduced the cross section for nuclear isomers, and discussed the possibilities to optimize the method for the long lived isomers production.

The light nuclides produced in the proton-induced spallation of ^{238}U at 1 GeV were studied by M.V. Ricciardi et al. [15]. They presented 254 light residues in the element range $7 \geq Z \leq 37$ formed in the proton-induced reaction of ^{238}U at 1 GeV. They also measured and analysed the production of nuclides with $7 \geq Z \leq 92$, and they determined the velocity distributions of the produced nuclides with high precision. They found that the nuclides are produced in a very asymmetric binary decay of heavy nuclei originating from the spallation of uranium and all the features of the produced nuclides merge with the characteristic of the fission products as their mass increases.

An experimental combining the conventional radiochemical stacked target technique and rapid measurements using a gas-jet transport system were carried out with a purpose of precise determination of charge dispersion and distribution for the

proton-induced fission of ^{238}U at two incident energies of 9.4 and 12.4 MeV by H. Baba et al. [32]. They found fundamental difference in the mass distribution characteristics between 17.9 MeV and 14.8 MeV excitations. This abrupt change of the fission characteristics strongly supports the existence of different fission mechanisms below and above around 14 MeV excitation.

Cross section for the formation of rubidium isotopes 83, 84 and 86 have been determined for targets from yttrium to uranium irradiated by protons of 0.6, 10.5 and 21 GeV by M. Lagarde-Simonoff et al. [33]. They found that the excitation energies are very similar for 0.6, 10.5 and 21 GeV protons for all nuclear reaction where the mean momentum depends only slightly on proton energy. However, the apparent value of excitation energy diminishes for targets showing a decrease of mean momentum at 10.5 and 21 GeV.

G. Friedlander et al. [34] studied the excitation functions and nuclear charge dispersion in the fission of uranium by 0.1 to 6.2 GeV protons. Independent yields were determined for Rb^{84}, Rb^{86}, Cs^{127}, Cs^{129}, Cs^{130}, $Cs,^{131}$, Cs^{132}, Cs^{134}, Cs^{136} and at same energies, Rb^{83} and Sc^{135}. in addition, the independent yield of Ba^{131} and the chain yields of Cs^{125}, Cs^{127}, Cs^{129}, La^{131}, Cs^{135}, Cs^{137}, Rb^{83} and Rb^{87} were obtained.

Thin natural uranium targets were irradiated by proton beam energy 660 MeV at Phasotron accelerator has been studied by Michel et al. [35]. Cross sections for the formation of residual nuclei $^{nat}U(p, xpyn)^{A}_{Z}Res$ are determined by methods of gamma-spectroscopy. 81 long-lived ($T_{1/2}$ > 100 days), 121 intermediate-lived (1 day < $T_{1/2}$ < 100 days) and 224 short-lived ($T_{1/2}$ < 1 day) isotopes (44 of them are in meta-stable state) were observed. The date is compared with theoretical simulations using nuclear cascade and high-energy codes including those developed within the HINDAS project and calculation provided by LANL.

The projectile fragmentation and fission, induced in collisions of ^{238}U at 1 GeV with lea, have systematically has been studied by T. Enqvist et al. [36]. They gave a complete survey on the isotopic production cross section of all elements between vanadium (Z=23) and rhenium (Z=75) down to cross section of 0.1 mb, and identified about 600 isotopes produced in fragmentation and about 600 isotopes produced in fission.

CHAPTER 2
EXPERIMENTAL TECHNIQUE

2.1 AIM OF THIS WORK:

The main goal of our work is to determine the integral cross sections for residual nuclides production by proton-induced reactions with rhenium and uranium at medium energy range from 78.2 MeV to 2590 MeV for rhenium and from 211 MeV to 2530 MeV for uranium. This study is of importance for accelerator driven systems such as spallation neutrons sources and systems for accelerator driven transmutation of nuclear waste and energy amplification. Such types of Studies provided already database for model calculations of the production of cosmogenic nuclides in extraterrestrial matter by solar and galactic cosmic ray protons [37-43].

2.2 EXPERIMENTAL WORK:

The target elements relevant in the study on rhenium and uranium for which the production such as which determent am aluminium which served as beam monitoring material. Exclusively high-purity materials were used as targets to avoid additional production of nuclei by interaction of the protons with elemental impurities. Each target was thoroughly cleaned and weighted before the irradiation. Typical targets had diameters of 15.0 mm for rhenium or uranium (99.99 % purity) ranged from 10 to 33 mg/cm^2 for aluminium (99.999% purity). Both, Re, U and Al targets were supplied by Goodfellow Metals Ltd., UK. The isotopic composition of the investigated ^{nat}U sample is 0.006% ^{234}U, (0.71% ± 0.004) ^{235}U, <0.005% ^{236}U and (99.27% ± 0.01) ^{238}U and for ^{nat}Re sample is 37.40% ^{185}Re and 62.60% ^{187}Re. The foils were arranged in small stacks in which aluminium foils were arranged in front of the Re or U targets to allow for proton flux determination via the ^{27}Al(p,3p3n)^{22}Na monitor reaction. In general, each unit consisted of three aluminium foils and three rhenium or uranium foils.

The irradiations took place at the SATURNE II synchrocyclotron of the Laboratoire National Saturne at Saclay and at the cyclotron of the Svedberg Laboratory at Uppsala. At both locations a stacked-foil technique was applied

allowing for the examination of many target elements at different energy points with a minimum requirement of beam-time. We used a modified stacked-foil technique in order to minimize interferences due to secondary particles Gloris et al. [2]. The irradiations were performed in air and lasted typically about 12 h to get sufficient fluence. The beam diameter was controlled via two wire chambers arranged in front of and behind the stacks at Saclay and by fluorescent .screen at Uppsala.

After the end of irradiation, the targets were transported to Cologne where the stacks were dismounted and the individual targets separated. A part of them stayed at Cologne for measurement, another one was transported to Zentrum für Strahlenschutz und Radioökologie (ZSR) Hannover Germany for the same purpose. The γ-spectrometric measurements were performed using several high-purity germanium (HPGe) and germanium–lithium (Ge(Li)) detectors partially equipped with automatic sample changers to be used for the short-time measurements. Each detector was connected via pre- and spectroscopy amplifiers to computer-controlled multi-channel buffers whose built-in ADC digitized the pulses into spectra of usually 4096 channels. The analysis of the g-spectra was done by the commercially available code GAMMA-W. GAMMA-W calculates net peak areas via an unfolding algorithm using a least-squares fit.

2.3 EXPERIMENTS:

Design and preparation of targets, targets irradiation, activities measuring, proton flux densities in the targets and cross section calculations.

2.3.1 Design and Preparation of Targets:

The Design of the illuminated stacks depended on the following general criteria:

- Avoidance of recoil losses and cross contamination, the loss of activated nucleons from targets due to recoil effects reduced the activities of the target and thus leads to wrong computation of cross-sections. On the other hand at the same time neighbouring targets are contaminated and thus additional or increased activities are pretended. For this reason a set is always consisting of at least three targets of the same element, by which the middle is considered for the measurement where the first one shields from the recoil process and the

third one shields the other set from cross contamination. Additionally before each target set three monitors were used which also acts as a shield.

- Thickness of the targets, the thickness of the targets depends on the manufacturer technical constraints. Targets should be as small as possible with a mass allocation in order to keep the production of secondary particle small.

The natural uranium and rhenium thin target foils were arranged in small stacks, as shown in figure (2-1). For each target element, from 3 to 8 individual targets, each preceded by 3 Al monitor foils, were irradiated. The targets were arranged in sequence of increasing atomic number along the beam. A distance of 5 cm between two stacks is enough to make influences of secondaries coming from another stack negligible due to geometrical reasons. The foils were arranged in two holders, first one for proton energy < 200 MeV and the other one for proton energy > 200 MeV, at two holders three aluminium targets were arranged in the front, followed by three uranium or rhenium targets then again three aluminium targets and then another element and so on. The alignment of the stacks was done by using supporting devices on which the stacks were fixed. The final supports consisted of Al-frames which were not hit by the primary beam and in the centre of which the stacks were hanged by thin threads. The whole arrangement was optically adjusted using a laser beam to ensure that each stack is in the beam line.

2.3.1.1 Stopping power and rang for nuclei:

Since the stacked foil technique is used, the proton energies should be calculated in all the different target foils even though the energy degradation was small for the highest initial proton energies

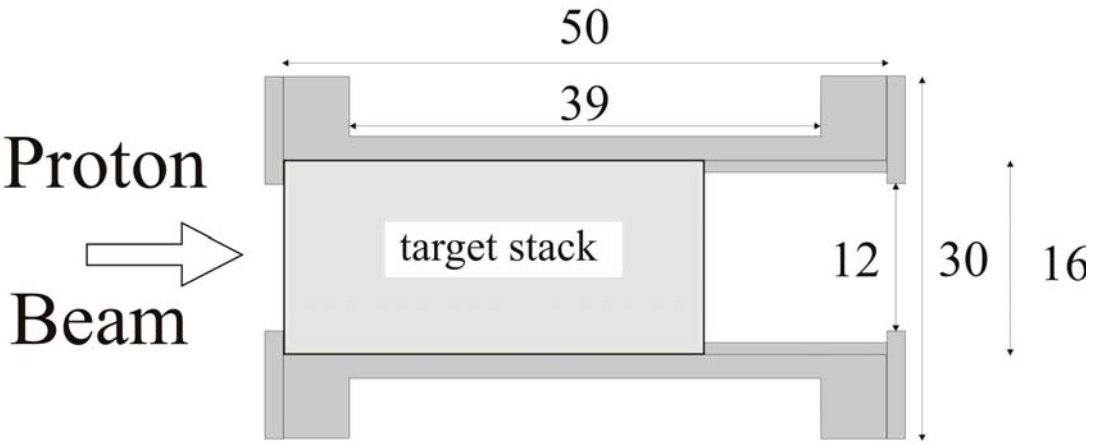

(a)

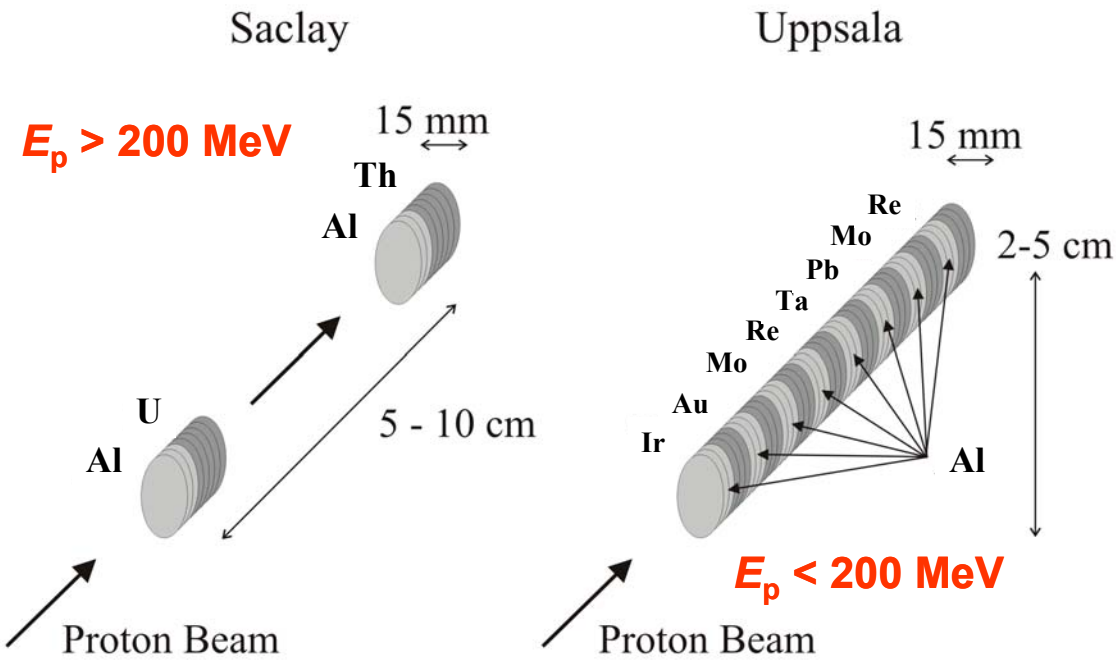

(b)

Fig. (2.1): *Overview of the (a) target holder at Uppsala (b) stacks of target foils at Saclay.*

For calculating stopping power inside the nucleus in our work we used the computer programme Stack. The total stopping power for a projectile which gets into collision with the nucleus is the sum of the electronic stopping power, S_e, due to the interaction with the target electrons, and the nuclear stopping power, S_n, due to the interaction with the target nuclei.

$$S_t = S_e + S_n \qquad (2.1)$$

Experimentally it has been found out that for high projectile energies, $S_t \approx S_n$. S_n, is in the units of eV/(10^{15}atoms/cm^2), while the projectile energy is in keV. S_n is given by

$$S_n(E) = \frac{8.462 \cdot Z_1 \cdot Z_2 \cdot M_1 \cdot S_n(\varepsilon)}{(M_1 + M_2)(Z_1^{0.23} + Z_2^{0.23}} \tag{2.2}$$

Where the reduced ion energy, ε, is defined as:

$$\varepsilon = \frac{32.53 \cdot M_1 \cdot M_2 \cdot (\frac{E}{M_1})}{Z_1 \cdot Z_2 (M_1 + M_2)(Z_1^{0.23} + Z_2^{0.23})} \tag{2.3}$$

M_1 and M_2 are the projectile and target masses (amu), and Z_1 and Z_2 is the projectile and target atomic numbers. For $\varepsilon \leq 30$ keV, then

$$S_n(\varepsilon) = \frac{\ln(1 + 1.383 \cdot \varepsilon)}{2(\varepsilon + 0.01321 \cdot \varepsilon^{0.21226} + 0.19593 \cdot \varepsilon^{0.5})} \tag{2.4}$$

If $\varepsilon > 30$ keV, the previous equation will reduced to the following formula

$$S_n(\varepsilon) = \frac{\ln \varepsilon}{2\varepsilon} \tag{2.5}$$

S can be converted to unites of MeV/(mg/cm^2) by multiplying with $0.6022/M_2$.

Experimental proton stopping power data are summarized by Anderson and Ziegler [43]. Reliable data for many elements are available over a wide range of energies. In order to obtain values for all elements the authors fit curves through the available experimental data to get coefficients for the stopping power as a function of proton energy E(keV) and for the target atomic number Z_2. S_e is assumed to be proportional to $E^{0.45}$ for $E < 25$ keV, except for $Z_2 \leq 6$, where it is proportional to $E^{0.25}$, for 25 keV $\leq E \leq$ 10 MeV, [44]. In this situation

$$\frac{1}{S_e} = \frac{1}{S_{low}} + \frac{1}{S_{high}} \tag{2.6}$$

For proton energy E_p KeV

$$S_{low} = A_1 \cdot E^{A_2} + A_3 \cdot E^{A_4} \tag{2.7}$$

and

$$S_{high} = \frac{A_5 \cdot \ln(\frac{A_6}{E} + A_7 \cdot E)}{E^{A_8}} \tag{2.8}$$

The coefficients A_i for each Z_2 are available from TRIM [45]. They are shown in table (2-1).

Table (2.1): *Coefficients for low-energy proton electronic stopping power parameterization.*

Z_2	V_f	A_1	A_2	A_3	A_4	A_5	A_6	A_7	A_8
1	1.00000	0.01217	0.0053358	1.12874	0.36420	1120.70	1.12128	2477.31	0.009771
2	1.00000	0.48900	0.0050512	0.86135	0.46741	745.38	1.04227	7988.39	0.033329
3	0.59782	0.85837	0.0050147	1.60445	0.38844	1337.30	1.04703	2659.23	0.018980
4	1.07810	0.87810	0.0051049	5.42316	0.20320	1200.62	1.02111	1401.84	0.038529
5	1.04860	1.46080	0.0048836	2.33802	0.44249	1801.27	1.03522	1784.12	0.020240
6	1.00000	2.10544	0.0049079	2.08723	0.46258	1779.22	1.01472	2324.45	0.020269
7	1.00000	0.64564	0.0050829	4.09503	0.33879	2938.49	1.04017	2911.08	0.010722
8	1.00000	0.75109	0.0050300	3.93983	0.34620	2287.85	1.01171	3997.24	0.018427
9	1.00000	1.30187	0.0051414	3.82737	0.28151	2829.94	1.02762	7831.30	0.020940
9	1.00000	1.30187	0.0051414	3.82737	0.28151	2829.94	1.02762	7831.30	0.020940
10	1.00000	4.73391	0.0044506	0.02986	1.49404	1825.36	0.97896	130.76	0.021577
11	1.00000	6.09725	0.0044292	3.19294	0.45763	1363.35	0.95182	2380.61	0.081835
12	0.71074	14.01311	0.0043646	2.26412	0.36326	2187.37	0.99098	6264.80	0.046200
13	0.90519	0.03909	0.0045417	6.96924	0.32976	1688.30	0.95944	1151.98	0.048982
14	0.97411	2.17813	0.0044455	2.60452	0.60885	1550.21	0.93302	1703.85	0.031620
15	0.97184	17.57548	0.0038346	0.07869	1.23881	2805.97	0.97284	1037.59	0.012879
16	1.00000	3.14730	0.0044716	4.97470	0.41024	4005.80	1.00110	1898.80	0.007659
17	1.00000	3.35440	0.0044740	5.92060	0.41003	4403.90	0.99623	2006.90	0.008231
18	1.00000	2.03789	0.0044775	3.07429	0.54773	3505.01	0.97575	1714.05	0.011701
19	0.36552	0.74171	0.0043051	1.15147	0.95083	917.21	0.87820	389.93	0.189258
20	0.62712	9.13157	0.0043809	5.46107	0.31327	3891.81	0.97933	6267.93	0.015196
21	0.81707	7.22475	0.0043718	6.10169	0.37511	2829.22	0.95218	6376.12	0.020398
22	0.99430	0.14700	0.0048456	6.34846	0.41057	2164.13	0.94028	5292.62	0.050263
23	1.14230	5.06114	0.0039867	2.61740	0.57957	2218.88	0.92361	6323.03	0.025669
24	1.23810	0.53267	0.0042968	0.39005	1.27254	1872.68	0.90776	64.17	0.030107
25	1.12220	0.47697	0.0043038	0.31451	1.32893	1920.54	0.90649	45.58	0.027469
26	0.92705	0.02743	0.0035443	0.03156	2.17547	1919.55	0.90099	23.90	0.025363
27	1.00470	0.16383	0.0043042	0.07345	1.85917	1918.42	0.89678	27.61	0.023184
28	1.20000	4.25623	0.0043737	1.56057	0.72067	1546.84	0.87958	302.02	0.040944
29	1.06610	2.35083	0.0043237	2.88205	0.50113	1837.72	0.89992	2376.95	0.049650
30	0.97411	3.10952	0.0038455	0.11477	1.50371	2184.69	0.89309	67.31	0.016588
31	0.84912	15.32177	0.0040306	0.65391	0.67668	3001.71	0.92484	3344.18	0.016366
32	0.95000	3.69319	0.0044813	8.60801	0.27638	2982.66	0.92760	3166.57	0.030874
33	1.09030	7.13728	0.0043134	9.42470	0.27937	2725.83	0.91597	3166.08	0.025008
34	1.04290	4.89794	0.0042937	3.77931	0.50004	2824.50	0.91028	1282.42	0.017061
35	0.49715	1.36827	0.0043024	2.56787	0.60822	6907.83	0.98170	628.01	0.006805
36	0.37755	2.23528	0.0043096	4.88562	0.47883	4972.28	0.95146	1185.23	0.009236
37	0.35211	0.42056	0.0041169	0.01695	2.36159	2252.73	0.89192	39.75	0.027757
38	0.57801	30.77977	0.0037736	0.55813	0.76816	7113.16	0.97697	1604.39	0.006527
39	0.77773	11.57598	0.0042119	7.02444	0.37764	4713.52	0.94264	2493.22	0.011270
40	1.02070	6.24058	0.0041916	5.27012	0.49453	4234.55	0.93232	2063.92	0.011844
41	1.02900	0.33073	0.0041243	1.72460	1.10621	1930.19	0.86907	27.42	0.038208
42	1.25420	0.01775	0.0041715	0.14586	1.73052	1803.62	0.86315	29.67	0.032123
43	1.12200	3.72287	0.0041768	4.62860	0.56769	1678.02	0.86202	3093.95	0.062440
44	1.12410	0.13998	0.0041329	0.25573	1.42411	1919.26	0.86326	72.80	0.032235
45	1.08820	0.28590	0.0041386	0.31301	1.34235	1954.82	0.86175	115.18	0.029342
46	1.27090	0.76002	0.0042179	3.38597	0.76285	1867.39	0.85805	69.99	0.036448
47	1.25420	6.39568	0.0041935	5.46891	0.41378	1712.61	0.85397	18493.0	0.056471
48	0.90094	3.47169	0.0041344	3.23372	0.63788	1116.36	0.81959	4766.03	0.117895
49	0.74093	2.52651	0.0042282	4.53198	0.53562	1030.85	0.81652	16252.23	0.197218
50	0.86054	7.36830	0.0041007	4.67911	0.51428	1160.00	0.82454	17964.82	0.133160
51	0.93155	7.71972	0.0043880	3.24198	0.68434	1428.11	0.83398	1786.67	0.066512
52	1.00470	16.77990	0.0041918	9.31977	0.29568	3370.92	0.90289	7431.72	0.026160
53	0.55379	4.21323	0.0042098	4.67533	0.57945	3503.93	0.89261	1468.87	0.014359
54	0.43289	4.61889	0.0042203	5.81644	0.52184	3961.24	0.90410	1473.26	0.014195
55	0.32636	0.18517	0.0036215	0.00059	3.53154	2931.30	0.88936	26.18	0.026393
56	0.51310	4.82483	0.0041458	6.09343	0.57026	2300.11	0.86359	2980.72	0.038679
57	0.69500	0.49857	0.0041054	1.97754	0.95877	786.55	0.78509	806.60	0.408824

58	0.72591	3.27544	0.0042177	5.76803	0.54054	6631.29	0.94282	744.07	0.008303
59	0.71202	2.99783	0.0040901	4.52986	0.62025	2161.15	0.85669	1268.59	0.043031
60	0.67413	2.87011	0.0040960	4.25677	0.61380	2130.43	0.85235	1704.11	0.039385
61	0.71418	10.85293	0.0041149	5.89075	0.46834	2857.17	0.87550	3654.17	0.029955
62	0.71453	3.64072	0.0041782	4.87424	0.57861	1267.70	0.82211	3508.17	0.241737
63	0.59110	17.64547	0.0040992	6.58550	0.32734	3931.30	0.90754	5156.66	0.036278
64	0.70263	7.53089	0.0040814	4.93891	0.50679	2519.67	0.85818	3314.62	0.030514
65	0.68049	5.47418	0.0040829	4.89696	0.51113	2340.07	0.85296	2342.68	0.035662
66	0.68203	4.26608	0.0040667	4.50318	0.55257	2076.39	0.84151	1666.56	0.040801
67	0.68121	6.83128	0.0040486	4.39869	0.51675	2003.00	0.83437	1410.45	0.034780
68	0.68532	1.27070	0.0040553	4.62946	0.57428	1626.28	0.81858	995.68	0.055319
69	0.68715	5.75613	0.0040491	4.35700	0.52496	2207.32	0.83796	1579.51	0.027165
70	0.61884	14.12746	0.0040596	5.83039	0.37755	3645.89	0.87823	3411.77	0.016392
71	0.71801	6.69476	0.0040603	4.93612	0.47961	2719.03	0.85249	1885.84	0.019713
72	0.83048	3.06189	0.0040511	3.58030	0.59082	2346.10	0.83713	1221.99	0.020072
73	1.12220	10.81081	0.0033008	1.37671	0.76512	2003.73	0.82269	1110.57	0.024958
74	1.23810	2.71007	0.0040961	1.22895	0.98598	1232.39	0.79066	155.42	0.047294
75	1.04500	0.52345	0.0040244	1.40380	0.85510	1461.39	0.79677	503.34	0.036789
76	1.07330	0.46160	0.0040203	1.30141	0.87043	1473.54	0.79687	443.09	0.036301
77	1.09530	0.97814	0.0040374	2.01267	0.72250	1890.81	0.81747	930.70	0.027690
78	1.23810	3.20857	0.0040510	3.66577	0.53618	3091.16	0.85602	1508.12	0.015401
79	1.28790	2.00351	0.0040431	7.48824	0.35610	4464.33	0.88836	3966.54	0.012839
80	0.78654	15.42995	0.0039432	1.12374	0.70703	4595.72	0.88437	1576.47	0.008853
81	0.66401	3.15124	0.0040524	4.09956	0.54250	3246.31	0.85772	1691.77	0.015058
82	0.84912	7.18963	0.0040588	8.69271	0.35842	4760.56	0.88833	2888.27	0.011029
83	0.88433	9.32087	0.0040540	11.54282	0.32027	4866.16	0.89124	3213.38	0.011935
84	0.80746	29.24222	0.0036195	0.16864	1.12264	5687.96	0.89812	1033.26	0.007130
85	0.43357	1.85222	0.0039973	3.15560	0.65096	3754.97	0.86383	1602.02	0.012042
86	0.41923	3.22200	0.0040041	5.90236	0.52678	4040.15	0.86804	1658.35	0.011747
87	0.43638	9.34124	0.0039661	7.92099	0.42977	5180.90	0.88773	2173.16	0.009201
88	0.51464	36.18267	0.0036003	0.58341	0.86747	6990.21	0.91082	1417.10	0.006219
89	0.73087	5.92839	0.0039695	6.40824	0.52122	4619.51	0.88083	2323.52	0.011627
90	0.81065	5.24536	0.0039744	6.79689	0.48542	4586.31	0.87794	2481.50	0.011282
91	1.95780	33.70174	0.0036901	0.47257	0.89235	5295.69	0.88930	2053.30	0.009191

The proton stopping power, $S_t(^1H)$, for energies 10 keV ≤ E_p ≤ 100 MeV, which were calculated with TRIM [45] using the parameterization in table (2.2) for various target materials, are plotted in Fig. (2.2). High-energy proton stopping powers, $S_e \approx S_t$, calculated using the parameterization in equation (2.9), for 10 MeV ≤ E_p ≤ 2 GeV are given in the lower curves in Fig. (2.2). Proton stopping powers for 1 keV ≤ E_p ≤ 10 GeV and Z_2 ≤ 92, based on a combination of theoretical calculations and experimental data (for 20 keV ≤ E_p ≤ 1 MeV), have been tabulated by Janni [46]. These values agree within 10% with those plotted in Fig. (2.2). For 10 MeV ≤ E ≤ 2 GeV, TRIM2 includes four additional coefficients, A_9 through A_{12}, shown in Table (2.2), to be used in the parameterization

$$S_e = A_9 + A_{10} \cdot \left(\frac{\ln E}{E}\right) + A_{11} \cdot \left(\frac{\ln E}{E}\right)^2 + A_{12} \cdot \left(\frac{E}{\ln E}\right) \qquad (2.9)$$

Table (2.2): *Coefficients for high-energy proton electronic stopping power parameterization.*

Z_2	A_9	A_{10}	A_{11}	A_{12}
1	4.17923×10^{-3}	1.85351×10^{2}	1.73395×10^{2}	1.03342×10^{-8}
2	7.87969×10^{-3}	3.37897×10^{2}	-1.21551×10^{4}	1.92256×10^{-8}
3	1.17242×10^{-2}	4.99690×10^{2}	-2.05489×10^{4}	2.84849×10^{-8}
4	1.53771×10^{-2}	6.39460×10^{2}	-2.52185×10^{4}	3.62232×10^{-8}
5	1.88005×10^{-2}	7.85353×10^{2}	-5.81862×10^{4}	4.55928×10^{-8}
6	2.25672×10^{-2}	9.33404×10^{2}	-6.12123×10^{4}	5.37140×10^{-8}
7	2.61772×10^{-2}	1.07594×10^{3}	-7.38496×10^{4}	6.19253×10^{-8}
8	2.96061×10^{-2}	1.20559×10^{3}	-9.10080×10^{4}	6.95374×10^{-8}
9	3.28578×10^{-2}	1.32120×10^{3}	-1.11202×10^{5}	7.64117×10^{-8}
10	3.60771×10^{-2}	1.44270×10^{3}	-1.40758×10^{5}	8.40467×10^{-8}
11	4.04266×10^{-2}	1.55387×10^{3}	-5.48654×10^{4}	8.58005×10^{-8}
12	4.27369×10^{-2}	1.71185×10^{3}	-2.09978×10^{5}	1.01158×10^{-7}
13	4.56765×10^{-2}	1.83950×10^{3}	-2.75340×10^{5}	1.10651×10^{-7}
14	4.98400×10^{-2}	1.97154×10^{3}	-2.27594×10^{5}	1.15392×10^{-7}
15	5.30531×10^{-2}	2.09546×10^{3}	-2.61762×10^{5}	1.23310×10^{-7}
16	5.62856×10^{-2}	2.21626×10^{3}	-2.91405×10^{5}	1.30771×10^{-7}
17	6.00254×10^{-2}	2.37308×10^{3}	-3.08937×10^{5}	1.40031×10^{-7}
18	6.34885×10^{-2}	2.48602×10^{3}	-3.09324×10^{5}	1.45714×10^{-7}
19	6.61386×10^{-2}	2.61892×10^{3}	-4.02448×10^{5}	1.57037×10^{-7}
20	7.06403×10^{-2}	2.71378×10^{3}	-2.83540×10^{5}	1.56347×10^{-7}
21	7.27608×10^{-2}	2.82763×10^{3}	-4.14705×10^{5}	1.67825×10^{-7}
22	7.49584×10^{-2}	2.95813×10^{3}	-5.55519×10^{5}	1.80782×10^{-7}
23	7.91888×10^{-2}	3.04568×10^{3}	-4.62426×10^{5}	1.80519×10^{-7}
24	8.16522×10^{-2}	3.14779×10^{3}	-5.50701×10^{5}	1.89345×10^{-7}
25	8.45124×10^{-2}	3.24460×10^{3}	-5.97089×10^{5}	1.95891×10^{-7}
26	8.78728×10^{-2}	3.35075×10^{3}	-6.06019×10^{5}	2.01321×10^{-7}
27	9.08265×10^{-2}	3.43834×10^{3}	-6.35674×10^{5}	2.06443×10^{-7}
28	9.44268×10^{-2}	3.53336×10^{3}	-6.11897×10^{5}	2.09676×10^{-7}
29	9.70308×10^{-2}	3.63804×10^{3}	-6.97379×10^{5}	2.18179×10^{-7}
30	1.01064×10^{-1}	3.76368×10^{3}	-6.62649×10^{5}	2.22804×10^{-7}
31	1.03813×10^{-1}	3.87169×10^{3}	-7.31501×10^{5}	2.31014×10^{-7}
32	1.08558×10^{-1}	3.99456×10^{3}	-6.28264×10^{5}	2.32273×10^{-7}
33	1.10147×10^{-1}	4.07755×10^{3}	-7.81829×10^{5}	2.42794×10^{-7}
34	1.13619×10^{-1}	4.22875×10^{3}	-8.26686×10^{5}	2.52509×10^{-7}
35	1.17630×10^{-1}	4.34695×10^{3}	-7.86689×10^{5}	2.56540×10^{-7}
36	1.20336×10^{-1}	4.46509×10^{3}	-8.70085×10^{5}	2.65922×10^{-7}
37	1.21919×10^{-1}	4.62546×10^{3}	-1.10030×10^{6}	2.84798×10^{-7}
38	1.27026×10^{-1}	4.69242×10^{3}	-9.08710×10^{5}	2.78534×10^{-7}
39	1.30043×10^{-1}	4.78771×10^{3}	-9.41457×10^{5}	2.84240×10^{-7}
40	1.32588×10^{-1}	4.87865×10^{3}	-1.01440×10^{6}	2.91492×10^{-7}
41	1.35950×10^{-1}	4.97111×10^{3}	-1.01510×10^{6}	2.95396×10^{-7}
42	1.36106×10^{-1}	5.16807×10^{3}	-1.41996×10^{6}	3.24194×10^{-7}
43	1.40468×10^{-1}	5.19156×10^{3}	-1.25960×10^{6}	3.16476×10^{-7}
44	1.43663×10^{-1}	5.27679×10^{3}	-1.26999×10^{6}	3.20349×10^{-7}
45	1.46717×10^{-1}	5.37846×10^{3}	-1.31024×10^{6}	3.26601×10^{-7}
46	1.50285×10^{-1}	5.43183×10^{3}	-1.25450×10^{6}	3.25513×10^{-7}
47	1.52977×10^{-1}	5.52331×10^{3}	-1.31881×10^{6}	3.32296×10^{-7}
48	1.55788×10^{-1}	5.66333×10^{3}	-1.42129×10^{6}	3.43645×10^{-7}
49	1.58932×10^{-1}	5.74463×10^{3}	-1.43497×10^{6}	3.47382×10^{-7}
50	1.60761×10^{-1}	5.80360×10^{3}	-1.55052×10^{6}	3.54295×10^{-7}
51	1.64200×10^{-1}	5.97036×10^{3}	-1.61215×10^{6}	3.65844×10^{-7}
52	1.68822×10^{-1}	6.05229×10^{3}	-1.47984×10^{6}	3.63253×10^{-7}
53	1.73337×10^{-1}	6.25893×10^{3}	-1.47965×10^{6}	3.74553×10^{-7}
54	1.76177×10^{-1}	6.36538×10^{3}	-1.53822×10^{6}	3.82146×10^{-7}
55	1.76210×10^{-1}	6.47955×10^{3}	-1.87545×10^{6}	4.02778×10^{-7}
56	1.81909×10^{-1}	6.52962×10^{3}	-1.62147×10^{6}	3.92193×10^{-7}
57	1.83401×10^{-1}	6.66321×10^{3}	-1.84280×10^{6}	4.08537×10^{-7}
58	1.88362×10^{-1}	6.67157×10^{3}	-1.61720×10^{6}	3.96734×10^{-7}
59	1.90072×10^{-1}	6.80044×10^{3}	-1.81380×10^{6}	4.11707×10^{-7}
60	1.93086×10^{-1}	6.85616×10^{3}	-1.81714×10^{6}	4.13253×10^{-7}
61	1.97060×10^{-1}	6.95911×10^{3}	-1.77715×10^{6}	4.15753×10^{-7}
62	1.99197×10^{-1}	7.07103×10^{3}	-1.91805×10^{6}	4.27100×10^{-7}
63	2.03901×10^{-1}	7.13989×10^{3}	-1.77658×10^{6}	4.22819×10^{-7}
64	2.06590×10^{-1}	7.20210×10^{3}	-1.81810×10^{6}	4.26463×10^{-7}
65	2.08873×10^{-1}	7.30450×10^{3}	-1.92452×10^{6}	4.36101×10^{-7}
66	2.11796×10^{-1}	7.42092×10^{3}	-1.98599×10^{6}	4.44400×10^{-7}
67	2.14077×10^{-1}	7.44650×10^{3}	-2.01829×10^{6}	4.45809×10^{-7}
68	2.17372×10^{-1}	7.64665×10^{3}	-2.12622×10^{6}	4.61611×10^{-7}
69	2.19975×10^{-1}	7.62469×10^{3}	-2.08183×10^{6}	4.56486×10^{-7}
70	2.23522×10^{-1}	7.69987×10^{3}	-2.04404×10^{6}	4.57783×10^{-7}
71	2.25289×10^{-1}	7.78858×10^{3}	-2.18576×10^{6}	4.68159×10^{-7}
72	2.27765×10^{-1}	7.89050×10^{3}	-2.27431×10^{6}	4.76889×10^{-7}
73	2.31358×10^{-1}	7.92833×10^{3}	-2.19599×10^{6}	4.73988×10^{-7}
74	2.28110×10^{-1}	8.16002×10^{3}	-2.94915×10^{6}	5.21279×10^{-7}
75	2.35299×10^{-1}	8.10728×10^{3}	-2.44245×10^{6}	4.93146×10^{-7}
76	2.38183×10^{-1}	8.18025×10^{3}	-2.49027×10^{6}	4.97212×10^{-7}
77	2.41184×10^{-1}	8.23883×10^{3}	-2.48729×10^{6}	4.98990×10^{-7}
78	2.44759×10^{-1}	8.28482×10^{3}	-2.41345×10^{6}	4.96956×10^{-7}
79	2.48248×10^{-1}	8.43317×10^{3}	-2.47420×10^{6}	5.06469×10^{-7}
80	2.50960×10^{-1}	8.47029×10^{3}	-2.46266×10^{6}	5.07107×10^{-7}
81	2.53520×10^{-1}	8.59960×10^{3}	-2.55377×10^{6}	5.18382×10^{-7}
82	2.57190×10^{-1}	8.70207×10^{3}	-2.51461×10^{6}	5.21905×10^{-7}
83	2.60218×10^{-1}	8.80265×10^{3}	-2.55391×10^{6}	5.28151×10^{-7}
84	2.62536×10^{-1}	8.92190×10^{3}	-2.65304×10^{6}	5.39186×10^{-7}
85	2.65692×10^{-1}	9.03749×10^{3}	-2.69021×10^{6}	5.46553×10^{-7}
86	2.71675×10^{-1}	9.15297×10^{3}	-2.62905×10^{6}	5.43040×10^{-7}
87	2.74509×10^{-1}	9.16992×10^{3}	-2.58884×10^{6}	5.40957×10^{-7}
88	2.77425×10^{-1}	9.28632×10^{3}	-2.65660×10^{6}	5.49344×10^{-7}
89	2.79628×10^{-1}	9.38802×10^{3}	-2.78260×10^{6}	5.59200×10^{-7}
90	2.82865×10^{-1}	9.45968×10^{3}	-2.78437×10^{6}	5.61524×10^{-7}
91	2.85549×10^{-1}	9.47397×10^{3}	-2.78465×10^{6}	5.59993×10^{-7}
92	2.87219×10^{-1}	9.60975×10^{3}	-2.99558×10^{6}	5.75858×10^{-7}

When a charged particle penetrates in matter it will interact with the electrons and nuclei present in the material through the electromagnetic force. If the charged particle is a proton, an alpha particle or any other particle with strong interactions it can also undergo nuclear interactions, but such nuclear interactions will be less

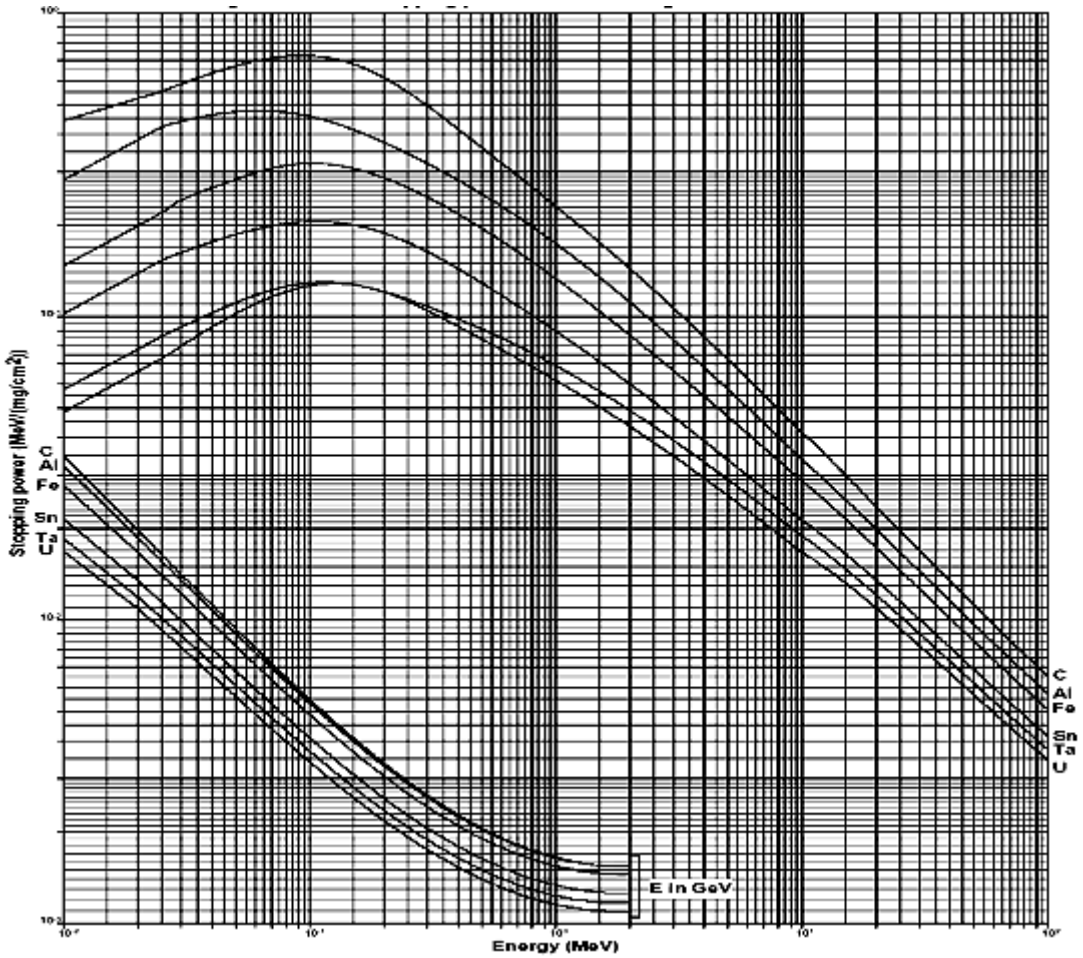

Fig. (2.2): *Proton stopping powers in various targets for 10 keV<E<2 GeV*

frequent [47]. If the particle has an energy of 1 MeV or more, as is typical in nuclear phenomena, the energy is large compared to the binding energy of the electrons in the atom. To a first approximation, matter can be seen as a mixture of free electrons and nuclei at rest. The charged particle will feel the electromagnetic fields of the electrons and the nuclei, and in this way undergo elastic collisions with these objects. The interactions with electrons and with the nuclei in matter will give rise to very different effects. Let us assume for the sake of definiteness that the charged article is a proton. If the proton collides with a nucleus, it will transfer some of its energy to the nucleus, and its direction will be changed. The proton is much lighter than most nuclei, and the collision with a nucleus will cause little energy loss. It is easy to show, using non-relativistic kinematics and energy-momentum conservation that the maximum energy transfer in the elastic collision of a proton of mass 'm' with nucleus of mass M is given by:

$$\Delta E_{max} = \frac{1}{2} m v^2 \left(\frac{4mM}{(m+M)^2} \right) \tag{2.10}$$

If the mass of the proton m is much smaller than the mass of the nucleus M, we therefore have

$$\Delta E_{max} \approx \frac{1}{2} m v^2 \left(4\frac{m}{M} \right) \qquad (m << M) \tag{2.11}$$

The energy loss of a high-energy charged particle in matter is given by the Bethe-Bloch equation.

$$\frac{dE}{dx} = \rho \frac{Z_{nucl}}{A_{nucl}} [0.307(MeV \cdot cm^2 / g)] \frac{Z^2}{\beta^2} [\frac{1}{2} \ln(\frac{2m_e v^2 \gamma T_{max}}{I^2}) - \beta^2 - \frac{\delta}{2}] \tag{2.12}$$

Where,

dE/dx energy loss of particle per unit length.

Z charge of the particle divided by the proton charge.

c velocity of light.

β v/c velocity of the particle divided by velocity of light.

γ relativistic gamma factor $\gamma = \sqrt{1 - \frac{v^2}{c^2}}$.

ρ density of the martial.

Z_{nucl} dimensionless charge of the nuclei.

A_{nucl} atomic number of nuclei.

I mean excitation energy in eV. Parameter usually determined experimentally. It is typically around (10 eV times Z_{nucl}).

T_{max} maximum energy transfer to the electron. For all particles except the electron itself this is to a good approximation given by $\approx 2m_e c^2 \beta^2 \gamma^2$. For electrons T_{max} is the energy of the incoming electron.

δ density correction to ionisation energy loss, important only for very high energy.

For the purpose of a qualitative discussion the Bethe-Bloch equation can be approximated as:

$$\frac{dE}{dx} \approx \rho(2MeVcm^2/g)\frac{Z^2}{\beta^2} \qquad (2.13)$$

For all particles the energy loss decreases with increasing energy and eventually reaches a constant, energy-independent value. That value is approximately the same for all particles of unit charge see Figure (2.3). For alpha particles the velocity is usually much less than the velocity of light and the energy loss is much larger. However, the Bethe-Bloch equation is valid only if the velocity of the particle is much larger than the velocity of the electrons in the atoms, and for alpha particles this conditions is usually not satisfied. For particle velocities that are small compared to the typical electron velocities in the atoms, the energy loss increases with the energy, and reach a maximum when the particle velocity is equal to the typical electron velocity. After this maximum, the energy loss decreases according to the Bethe-Bloch equation.

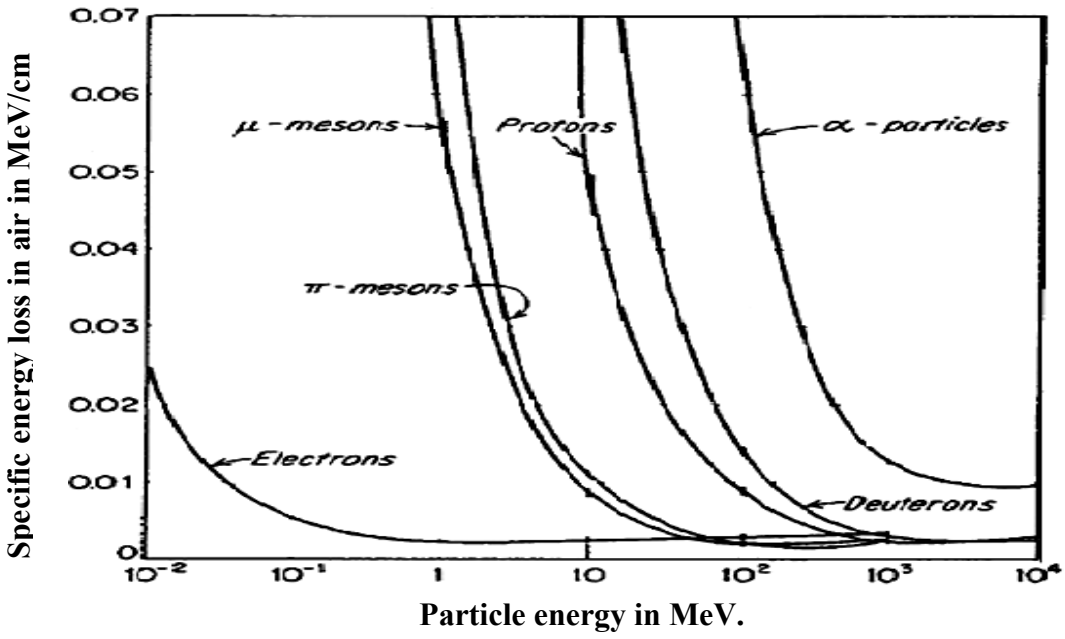

Fig. (2.3): *Variation of the specific energy loss in air versus the energy of the charged particles.*

Since particles lose energy when travelling in a medium, they will eventually have lost all their kinetic energy and come to rest. The distance travelled by the particles is referred to as the range. As the particle penetrates in the medium, its energy loss per unit length will change. The energy loss of a particle as a function of its distance of penetration is illustrated in Figure (2.4). The energy loss increases towards the end of the range. Close to the end it reaches a maximum and then abruptly drops to zero [48].

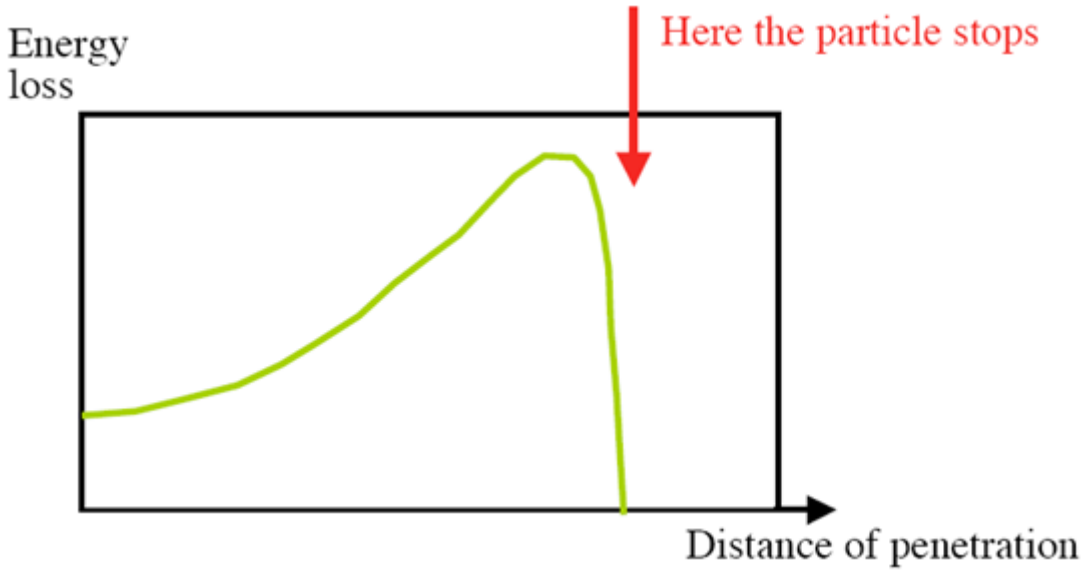

Fig. (2.4): *Schematic representation of the energy loss of particles along their range in matter.*

2.3.1.2 Computer Program Stack:

Since we applied a stacked foil technique we had to calculate the proton energies in all the different target foils. Although the energy degradation was small for the highest initial proton energies we performed such calculations for all irradiations. This was done by a computer program stack version 4.0.

The input file for the program Stack Version 4.0 contains all the information about all foils in the stack, like the atomic and mass numbers, thickness, masses and radii of the foils. Subsequently the program is run and we get the values of energies which pass through each target. Observation shows that after passing through each target the proton beam losses its energy du to collision with the target nuclei by making processes like reaction, absorption and scattering with the target nuclei and with atomic electrons. The following figure (2.5) show that, the relation between

proton energy and target number in the stack for all irradiation experiments. From these figures we can see that, the proton energy decreases with increasing the target number in the stack.

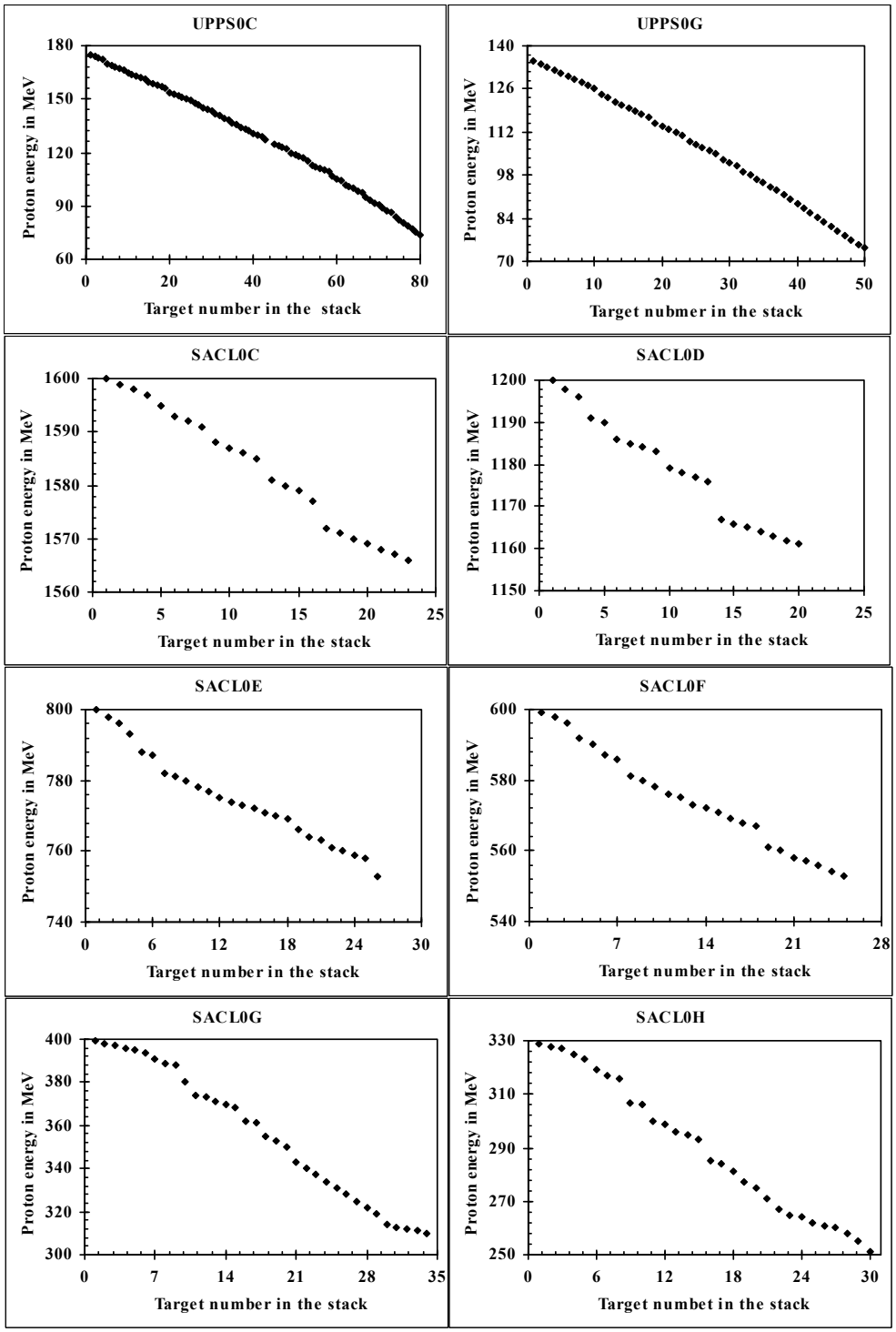

Fig. (2.5): *Relation between proton energy and target number in the stack for all irradiation experiments.*

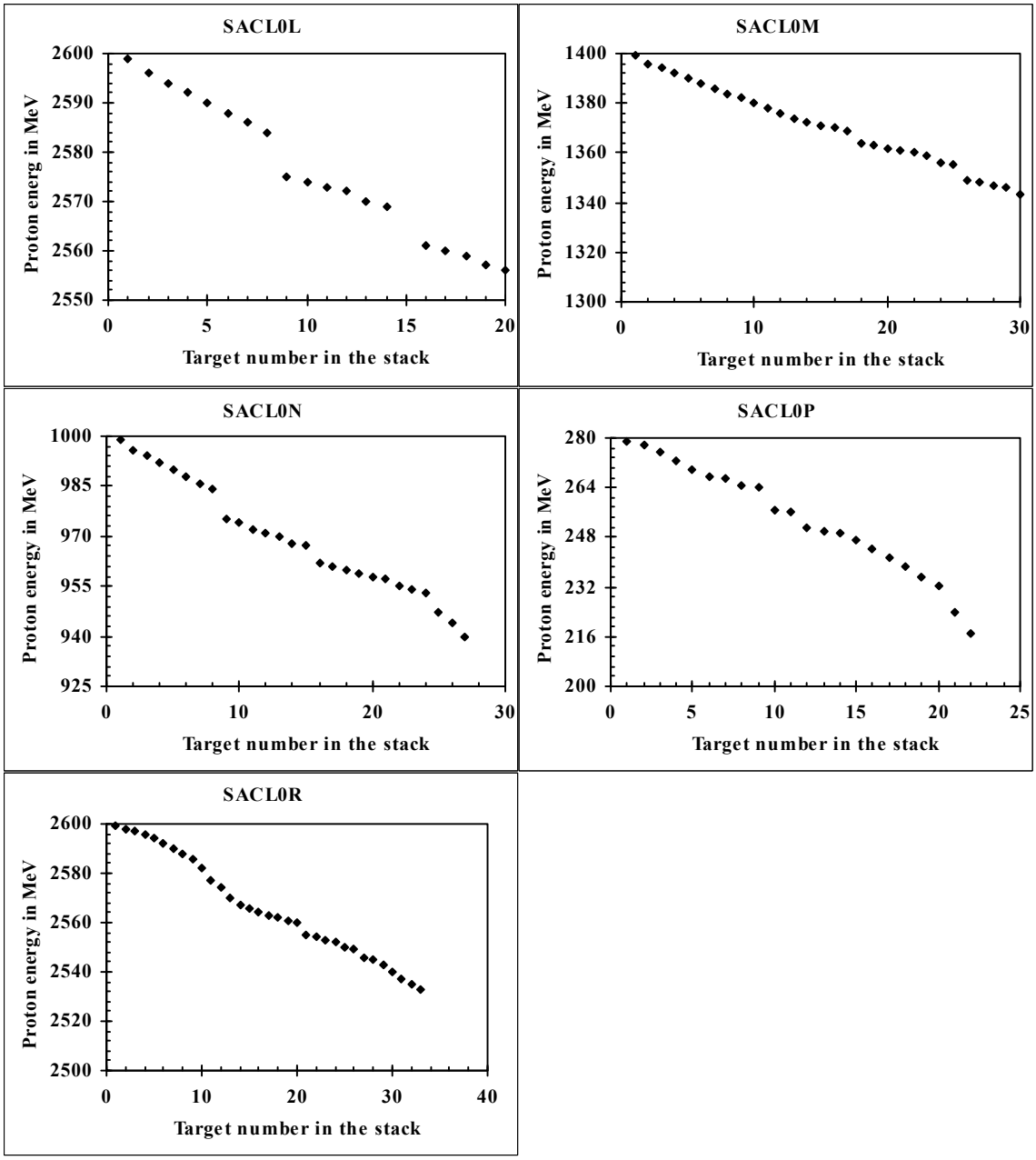

Fig. (2.5): *Continued*

2.3.1.3 Proton Energies Uncertainties:

For calculating the uncertainty of the proton energy in a target three sources have to be considered. First, the protons leaving the accelerator have an energy uncertainty ΔE_A. Second, the protons are slowed down in the target foil from an initial energy $E_{n;i}$ to the final energy $E_{n;f}$ resulting in an energy spread with a half-width $\Delta E_{loss} = (E_{n;i} - E_{n;f})/2$. Third, due to the statistical nature of the slowing down process there is an energy straggling which can be described according to Ref. [49] by a

Gaussian distribution with a width (straggling) parameter α_i. Consequently, the uncertainty of proton energy E_n in the *n*th target foil of a stack is given by:

$$\Delta E_n = \sqrt{\Delta E_B^2 + \Delta E_{loss}^2 + (\sum_{i=1}^{n} \alpha_i)^2} \qquad (2.10)$$

In general, this resulted in energy uncertainties of less than 1% in all targets. Theses uncertainties are given in the numerical database.

2.3.2 Targets Irradiation:

The irradiations took place at the SATURNE II synchrocyclotron of the Laboratoire National Saturne at Saclay and at the cyclotron of the Svedberg Laboratory at Uppsala. At both locations a stacked-foil technique was applied allowing for the examination of many target elements at different energy points with a minimum requirement of beam-time. We used a modified stacked-foil technique in order to minimize interferences due to secondary particles. The irradiations were performed in air and lasted typically about 12 h to get sufficient flounce. The beam diameter was controlled via two wire chambers arranged in front of and behind the stacks. In this work, we report about results of a total of 13 irradiation experiments performed and observed in table (2.3).

Table (2.3): *Overview of the name of irradiation experiment, where $E_{p,i}$ is the praimary energy, $E_{p,f}$ is the starting energy, t_{EoI} is the time at end of irradiation, t_{irr} is the time of irradiation and ξ is the mass per unit.*

Eperiment	$E_{p,i}$ (MeV)	$E_{p,f}$ (MeV)	t_{EoI}	t_{irr} (s)	ξ (g/cm^2)
UPPSOC	175.9±1.0	72.7	19.01.1994 / $23^{\underline{10}}$	25200	28.4
UPPSOG	136.1±0.5	74.2	21.02.1995 / $21^{\underline{30}}$	12000	16.0
SACLOC	1600	1565	14.10.1993 / $08^{\underline{53}}$	60180	22.9
SACLOD	1200	1161	15.10.1993 / $08^{\underline{07}}$	74040	21.1
SACLOE	800	752	19.05.1994 / $08^{\underline{00}}$	86940	29.5
SACLOF	600	545	20.05.1994 / $11^{\underline{00}}$	91260	31.0
SACLOG	400	309	06.10.1994 / $08^{\underline{04}}$	121200	39.7
SACLOH	330	228	07.10.1994 / $07^{\underline{58}}$	76200	38.5
SACLOL	2600	2525	11.07.1995 / $07^{\underline{17}}$	72180	48.5
SACLOM	1400	1341	04.10.1995 / $14^{\underline{07}}$	70980	37.4
SACLON	1000	938	05.10.1995 / $09^{\underline{00}}$	60480	38.1
SACLOP	280	188	22.05.1996 / $09^{\underline{54}}$	55500	31.1
SACLOR	2600	2541	23.05.1996 / $09^{\underline{05}}$	63600	37.7

Thirteen irradiation experiments were performed at the SATURNE II synchrocyclotron of the Laboratoire National Saturne at Saclay and at the cyclotron of the Svedberg Laboratory at Uppsala. Table (2.4) has the parameters for all experiments.

Table (2.3): *Irradiation experiments at Uppsala and Saclay.*

Irradiation target name	Target mass in mg	Atomic weight in amu	Proton energy in MeV	Flux density in $cm^{-2}s^{-1}$
REUG431	471.5	186.207	7.82E+01	1.37E+11
REUC751	509.02	186.207	8.19E+01	9.31E+10
REUG361	517.97	186.207	9.00E+01	1.455E+11
REUC683	516.91	186.207	9.34E+01	1.03E+11
REUG311	475.32	186.207	9.80E+01	1.51E+11
REUC603	464.5	186.207	1.05E+02	1.11E+11
REUG251	524.07	186.207	1.08E+02	1.55E+11
REUG191	485.32	186.207	1.15E+02	1.58E+11
REUG101	508.79	186.207	1.24E+02	1.61E+11
REUC453	521.15	186.207	1.25E+02	1.22E+11
REUG041	512.1	186.207	1.31E+02	1.62E+11
REUC381	517.65	186.207	1.34E+02	1.25E+11
REUC291	461.85	186.207	1.45E+02	1.29E+11
REUC221	520.33	186.207	1.53E+02	1.31E+11
REUC141	472.41	186.207	1.62E+02	1.32E+11
REUC071	503.35	186.207	1.69E+02	1.34E+11
RESH222	493.63	186.207	2.51E+02	9.89E+08
RESG222	505.44	186.207	3.31E+02	1.52E+09
RESF222	516.36	186.207	5.58E+02	2.79E+09
RESE222	476.43	186.207	7.63E+02	2.91E+09
RESD203	503.41	186.207	1.17E+03	3.80E+09
RESC203	513.99	186.207	1.57E+03	7.50E+09
RESL222	524.11	186.207	2.59E+03	2.64E+09
UUSM272	631.9	238.0289	2.11E+02	7.11E+09
UUSK272	554.1	238.0289	1.00E+03	1.71E+09
UUSL272	651	238.0289	1.40E+03	1.76E+09
UUSN272	628.05	238.0289	2.53E+03	1.62E+10

2.3.2.1 Uppsala Proton Accelerator:

The (Theodor) Svedberg (1884-1971) professor in physical chemistry at Uppsala University from 1912 to 1949 , was awarded the Nobel Prize in chemistry in 1926 for his research on dispersed systems (colloidal solutions). He invented the ultracentrifuge, which was used in the discovery that proteins consist of

macromolecules. Towards the end of the 1930's The Svedberg and his colleagues built their first accelerator, a neutron generator. In 1945, a donation from the Gustaf Werner Corporation gave the opportunity to build a much larger accelerator, a synchrocyclotron. The Gustaf Werner Institute with the synchrocyclotron as the main research instrument was founded in 1949 and continued to act as a base for research in high-energy physics and radiation biology until 1986 when The Svedberg Laboratory was established. Intensive discussions concerning the type and size of accelerators Swedish research in nuclear and high-energy physics should have at its disposal took place in early 1980's, One result of this process was that a decision was taken to bring the magnets of the so-called ICE-ring (Initial Cooling Experiment) from CERN to Uppsala. The accelerator ring was rebuilt as a cooler and storage ring and given the acronym CELSIUS (Cooling with Electrons and Storing of Ions from the Uppsala Synchrocyclotron). Figure (2.6) shows that the overview of the institute.

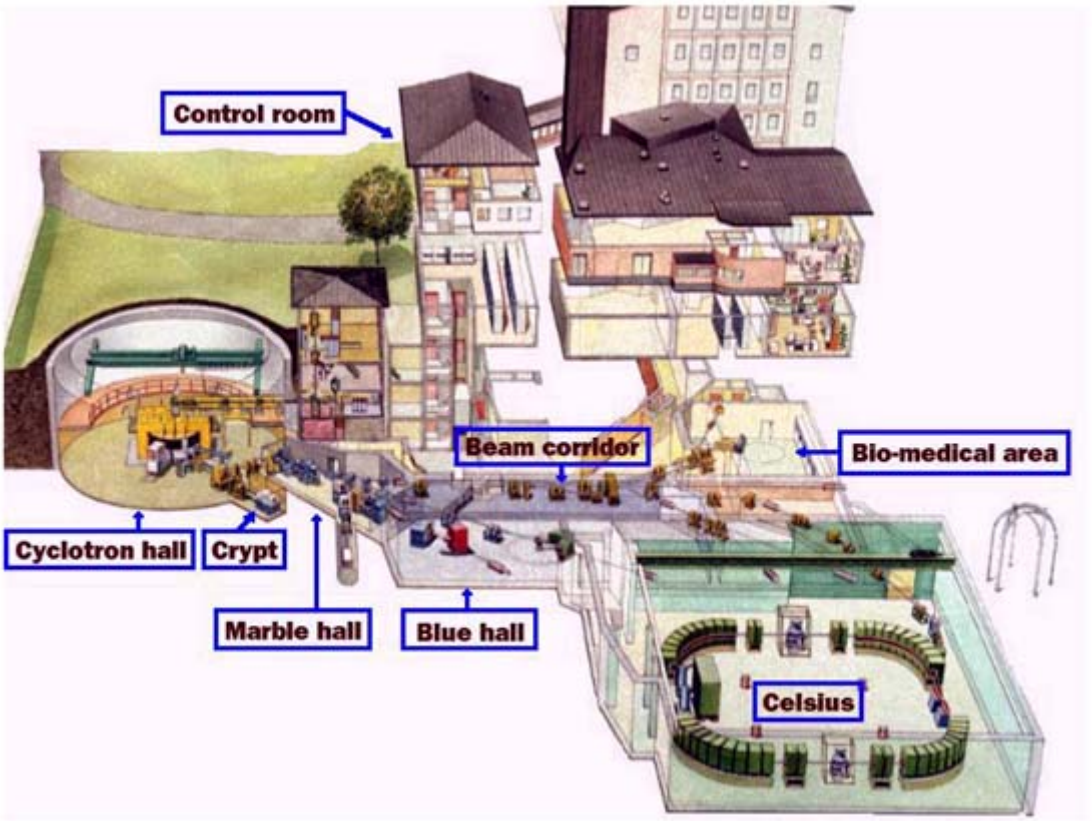

Fig. (2.6): An overview of Uppsala proton accelerator TSL.

The Svedberg Laboratory (TSL) in Uppsala is a cyclotron facility with a reputed mission in proton radiotherapy, interdisciplinary research and commercial irradiations [50, 51]

2.3.3 Measurements of Activities:

The activities at the end of irradiation were calculated by performing γ-spectrometry with six high purity germanium (HPGe) and germanium-lithium (Ge(Li)) detectors. According the following equation we can calculate the activities:

$$A_{BOC} = \frac{N_p(E_\gamma) \cdot 100}{Eff(E_\gamma) \cdot I_\gamma(E_\gamma) \cdot TOC} \tag{2.11}$$

Where,

A_{BOC}	activity at the began of count.	N_p	net peak area of peak at E_γ.
$Eff(E_\gamma)$	absolute efficiency.	I_γ	intensity of emitted γ-ray.
TOC	time of counting.	E_γ	gamma energy.

2.3.3.1 γ-Spectrometry:

After the irradiation the stacks were transported to Zentrum für Strahlenschutz und Radioökologie (ZSR) Hannover Germany for offline gamma-spectroscopy. Gamma-quanta are usually emitted by the decay of a nucleus and possess energy characteristic of the nucleus and can be detected by means of suitable detectors over their interaction with the subject. Semiconductor crystals, e.g. Si (Li), Ge(Li) or HPGe (High Purity Germanium) are used to form the core of the detectors. The interaction of gamma-rays with the detector core produces free charge carriers. Although a large number of possible interaction mechanisms are known for interaction of gamma-rays with matter, only photo-electric absorption, Compton scattering and pair production, these three types play major roles in radiation measurements. The charge produced with complete absorption of a photon in the crystal is proportional to the energy of the quantum. It can be converted into impulses via amplifiers. These again can be digitized with analogue-digital converters (ADC) and be assigned according to their sizes in different channels of a multi-channel buffers (MCB).

The detectors are connected via spectroscopic amplifier to the computer controlled multi-channel buffer (MCB). The built in ADC (analogue digital converter)

digitalized the received pulses into spectra of usually 4096 channels as shown in figure (2.7). The amplification was chosen for the registration of gamma-quanta with

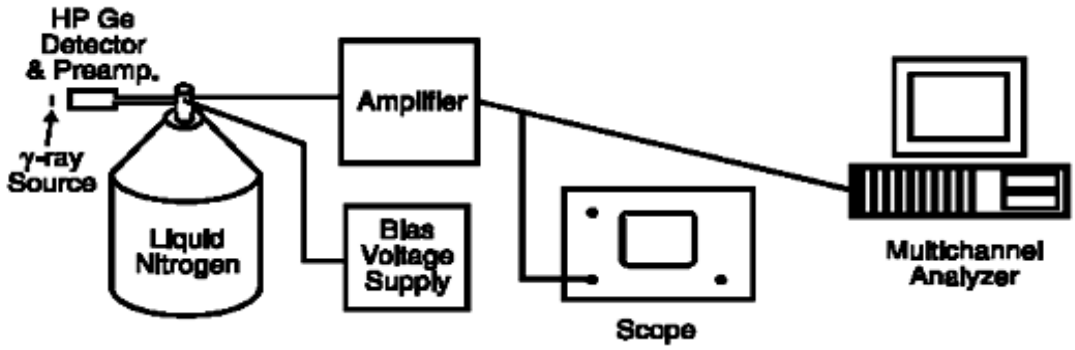

Fig. (2.7): *Germanium detector and associated counting equipment.*

energies between some keV to about 2 MeV. Typical resolution ranged from about 1 keV at 122 keV of ^{57}Co to about 2 keV at 1332 keV of ^{60}Co. The ADC measured the counting time C_t, and also the life time L_t during the impulses were actually digitized, so that from these information the dead time could be computed by $t_D = t_C - t_L$. The spectra is viewed in the computer screen and it is stored together with information of the illuminated sample, e.g. name of the detector, measuring geometry, energy calibration as well as measuring time and life time in a standard format for further processing. The cooling medium for all detectors is liquid nitrogen. In liquid nitrogen (LN_2) cooled detectors, the detector elements are housed in a clean vacuum chamber which is attached to or inserted in a LN_2 Dewar. The detector is in thermal contact with the liquid nitrogen which cools it to down to 77 °K or -200 °C. A cross sectional view of a typical liquid nitrogen cryostat is shown in Figure. (2.8).

To avoid problems with too high dead times and pile-up effects the distances between sample and detector window were varied between 5 and 50 cm. thus it was possible to keep the dead time below 10% with no detectable pile-up effects. The large distances were used especially for the short time measurements shortly after the irradiations because of the high activities of the samples. In this geometric no lead shielding of the detector was possible but interferences with background γ-lines were negligible anyway due to the short counting times as well as due to the high Compton background caused by the measured samples themselves. There are many kind of detectors and distances were used as shown in table (2.4).

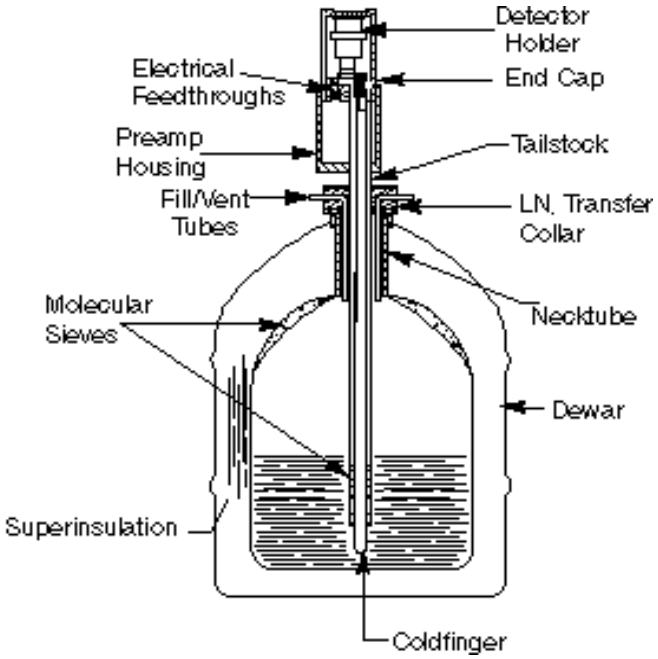

Fig. (2.8): *A cross sectional view of a typical liquid nitrogen cryostat.*

Table (2.4): *Detectors and distances were used.*

Detectors	Distance in cm	Detectors	Distance in cm
GELIN4	5 13 15 20	GE_NEU	6
GE__02	5 5.5 10 15	CA30	5 10 20
GE__01	5 10 15	CQ30	5 10 20
GE_IMM	5 15	ORS2	10 20 50

2.3.3.2 Calibration of energy:

Gamma ray spectrometry serves to identify radionuclides and to measure their activities. It is then necessary to identify the energies of all -rays of interest. This requires the energy calibration of the detector to permit measurement of detected -ray energies which is usually done as a function of their pulse height. The calibration is carried out for various gamma energies. The absolute calibration of the all γ-spectrometers was performed for each geometry used by calibrated radionuclides

sources of ^{241}Am, ^{133}Ba, ^{57}Co, ^{60}Co, ^{137}Cs,^{152}Eu, and ^{226}Ra with certified accuracies of $\leq$ 2 % supplied by PTB Braunschweig, Germany. Energy calibration was done using least squares fit to a 2nd order polynomial for the energies of the calibrated radionuclide sources.

2.3.3.3 Calibration of efficiency:

For the measurement of activity of the radionuclide, knowledge of the detector efficiency is necessary. The efficiency of a detector is measured and calculated for the purpose to investigate that how much a detector is sensitive to radiations. All radiation give rise to pulse height for each quantum of radiation which interacts with the active volume of the detector. For primary charged radiation such as alpha and beta interaction excitation or ionization take place. And after travelling small distance within the matter they are stopped. Uncharged radiation such as gamma rays travel large distances and after interaction within the active volume they give rise to a pulse height. The amount of emitted gamma rays form the source to the radiation detected by the detector is known as the efficiency of the detector. Radioactive nuclide emits photons in discrete pattern, so peaks at photon specific energies occur in the spectrum. For calculation of efficiency standard point sources ^{241}Am, ^{133}Ba, ^{57}Co, ^{60}Co, ^{137}Cs, ^{152}Eu, ^{22}Na and ^{226}Ra were used. These sources emit –lines at specific energies. In spectrum these peaks gives net peak areas. Calculated peak areas are proportional to the number of radioactive atoms that have been decayed during the measurement [52]. Efficiencies are subdivided in two groups.

Absolute efficiency which is given by:

$$\varepsilon_{abs} = \frac{\text{number of pulse recorded}}{\text{number of radiation quanta emitted by the source}}$$

The Second in known as the intrinsic efficiency by:

$$\varepsilon_{int} = \frac{\text{number of pulses recorded}}{\text{number of quanta incident on the det ector}}$$

These both efficiencies are related to each other by $\varepsilon_{int} = \varepsilon_{abs}(4\pi/\Omega)$ where Ω is the solid angle of the detector seen form the actual source position. If we neglect the

coincidence detection probability of two gamma rays, then we can calculate the factor of probability by the product of two probabilities:

- The energy emitted during the decay of gamma ray.
- The registration of this gamma ray in the spectrum.

The counting efficiency which is defined by:

$$\text{Probability of detection} = \frac{\text{number of detected photons}}{\text{number of emitted photons}}$$

depends on the detector, sample properties, and the relative distance between the detector and the source. For a given detector the efficiency is a function of a sample shape, size, composition, the distance between the source and the detector, and the photon energy. For calculating the efficiencies standard sources were measured at different distances. These sources have known activities and half lives from which the efficiencies were calculated by:

$$\varepsilon_{ff}(E_\gamma) = \frac{N_p \cdot 100}{I_\gamma(E_\gamma) \cdot t_D \cdot A_{ref}} \cdot \frac{1}{e^{-\lambda \cdot t_c}} \qquad (2.12)$$

Where,

N_p net peak area recorded by the detector.

I_γ intensity of the gamma line in %.

t_D time of decay.

A_{ref} activity of standard source at the reference data.

t_c time of counting for measurement.

λ decay constant.

The efficiencies were repeatedly checked for all geometry for the different detectors. The absolute efficiency of the different detectors was calculated at the specific energy of the standard sources for each geometry and measuring distances.

But, the γ–spectra of irradiated targets have different γ–energies. So, we need some fitting function to calculate the absolute efficiency for any considered γ–energy. We used for this purpose the so-called Gray and Ahmad fit function [53] for calculating the absolute efficiency at any interesting γ–energy in the energy range below 300 keV. For γ–energies above 300 keV a linear-class fitting function was used. This linear function is defined by:

$$\varepsilon_{ff}(E_\gamma) = e^{1+k\cdot\ln(E_\gamma)} \tag{2.13}$$

2.3.3.4 Fit function:

Efficiency functions were obtained by fitting a double-logarithmic linear function to the experimental efficiency data above 300 keV. Below this energy a fit function according to Gray and Ahmad [53] was chosen. These authors constructed two linear classes of Ge(Li) detector efficiency functions and assessed their range of applicability using a large number of independent efficiency data sets. We use that class that is defined by:

$$E_{ff}(E_\gamma) = \frac{1}{E_\gamma}\sum_{i=1}^{8} a_i \cdot \left(\ln\frac{E_\gamma}{E_\circ}\right)^{i-1} \tag{2.14}$$

Where,

E_γ energy in MeV. a_i Gray fit parameters.

E_o energy of the calibrated source.

This equation 2.14 determines the absolute efficiency. Application of this fit produce 8 parameters which we use to calculate the detector absolute efficiency at different energies. The efficiency of any detector is always less than 1, i.e., 100% which one can also see for example from Fig. (2.9). This is because of the size of the detector and the feint solid angle covered by the detector in given geometry. The decrease of the efficiency with increasing gamma energy is due to the decreasing probability of gamma quanta to deposit it is total energy in the detector. The decrease of the efficiency fig (2.9) at low energies is due to absorption of gamma quanta in the detector cap and in the death germanium material and at the end we get the resulting efficiency.

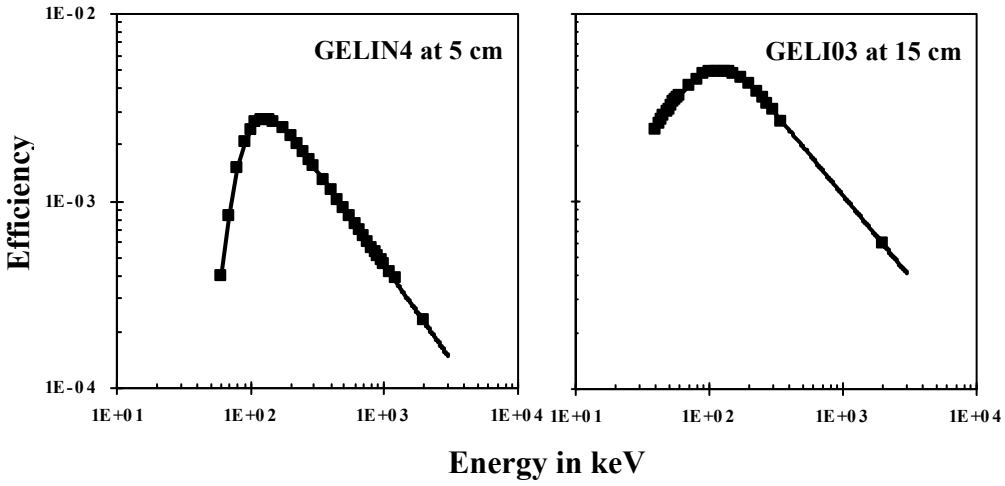

Fig. (2.9): *Comparison of experimental efficiency (■) and Absolute efficiency with Gray-Ahmad fitted function (—).*

2.3.3.5 Uncertainty of the efficiency calibration:

Results of physical measurements are likely subject to errors, e.g. failure of correction for removal of background. Results of measurements of radioactivity and many other properties are subject to two types of uncertainties known as random and systematic uncertainties. Errors in principle can be avoided, but uncertainties can not be avoided. In principle a measured can not be completely described without an infinite number of information. Suppose we have a measured Y which is determined by N other quantities. i.e.,

$$Y= f (X_1, X_2,\ldots, X_N) \tag{2.15}$$

X_i are the input quantities and may depends on other quantities and correction factors for systematic effects. The correction factors can also be considered as other sources of variability such as different observers, instruments, samples, laboratories, and times in which observations are made. Where f is a functional relation describing the model of evaporation. If we represent measured Y as an estimation y by:

$$y= f (x_1, x_2,\ldots, x_N) \tag{2.16}$$

Then we can write this estimation as an average of:

$$y = \overline{Y} = \frac{i}{n}\sum_{i=1}^{n} Y_i = \frac{1}{n}\sum_{i=1}^{N} f(X_{1,k}, X_{2,k},...,.X_{N,k}) \tag{2.17}$$

Due to this reason we take y as arithmetic mean or average of n independent determinations Yk of Y. Here each determination has the same uncertainty and each being based on a complete set of observed values of N input quantities obtained at the same time. So, we can write the combined standard uncertainty in y as:

$$u^2(y) = \sum_{i=1}^{N} \left(\frac{\partial f}{\partial X_i}\right)^2 \cdot u^2(x_i) \tag{2.18}$$

Now the overall uncertainty in the mean of a series of measurements, resulting in $y = \sum_{i=1}^{n} x_i$ can be added in quadrate i.e., $u^2(y) = \sum_{i=1}^{n} u^2(x_i)$ [54]. It is readily verified that linear additions add more weight to the overall uncertainty than quadrate additions. So from the above statement we can write the combined standard uncertainty in efficiency as

$$\left[\frac{u(\varepsilon_{ff})}{\varepsilon_{ff}}\right]^2 = \left[\frac{u(N_p)}{N_p}\right]^2 + \left[\frac{u(I_\gamma)}{I_\gamma}\right]^2 + \left[\frac{u(ToC)}{ToC}\right]^2 + \left[\frac{u(A_{BoC})}{A_{BoC}}\right]^2 \tag{2.19}$$

and as u(BoC) << ToC, so we neglect this term in the above equation. The $u(A_{BoC})$ is calculated as:

$$\left[\frac{u(A_{BoC})}{A_{BoC}}\right]^2 = \left[\frac{u(A_{DoC})}{A_{DoC}}\right]^2 + (BoC + DoC)^2 \cdot u^2(\lambda) \tag{2.20}$$

The uncertainty in the net peak area we get by evaluating the spectrum by code Gamma-W [55].

2.3.3.6 γ-spectroscopy evaluation:

The analysis of the γ-spectra themselves, the unambiguous identification of nuclides and the selection of activities used in the final calculation of cross-section turned out to be the most time-consuming step in the experiments. The γ-spectra of uranium and rhenium targets irradiated with medium-energy protons are extremely complex exhibiting for example 445, 550, 597 and 707 peaks for uranium and 271, 286, 325 and 329 peaks for rhenium in a 4096 channel spectrum covering λ-energies up to about 2MeV figure (2.10-2.11). The complexity of the spectra has two reasons.

After short decay times the spectra are dominated by a large number of radionuclides which have extremely complex decay schemes. After their decay the spectra stay rather complex because some long-lived radionuclides which are produced with large cross-sections also have very complex decay schemes or decay to short-lived daughter nuclides.

The analysis of the γ-spectra was done by the commercially available code GAMMA-W [56, 55]. GAMMA-W calculates net peak areas via an unfolding algorithm using a least-squares fit [57, 58]. For an evaluation, regions of a spectrum are defined in which all peaks are unfolded simultaneously after the background has been calculated according to Refs. [58, 59]. Peak shapes are assumed to be Gaussian with a low-energy tailing. For each detector and measuring geometry, parameters were determined and supplied to the code which describes as function of energy or channel numbers the full-width at half-maximum of full-energy peaks and their tailings.

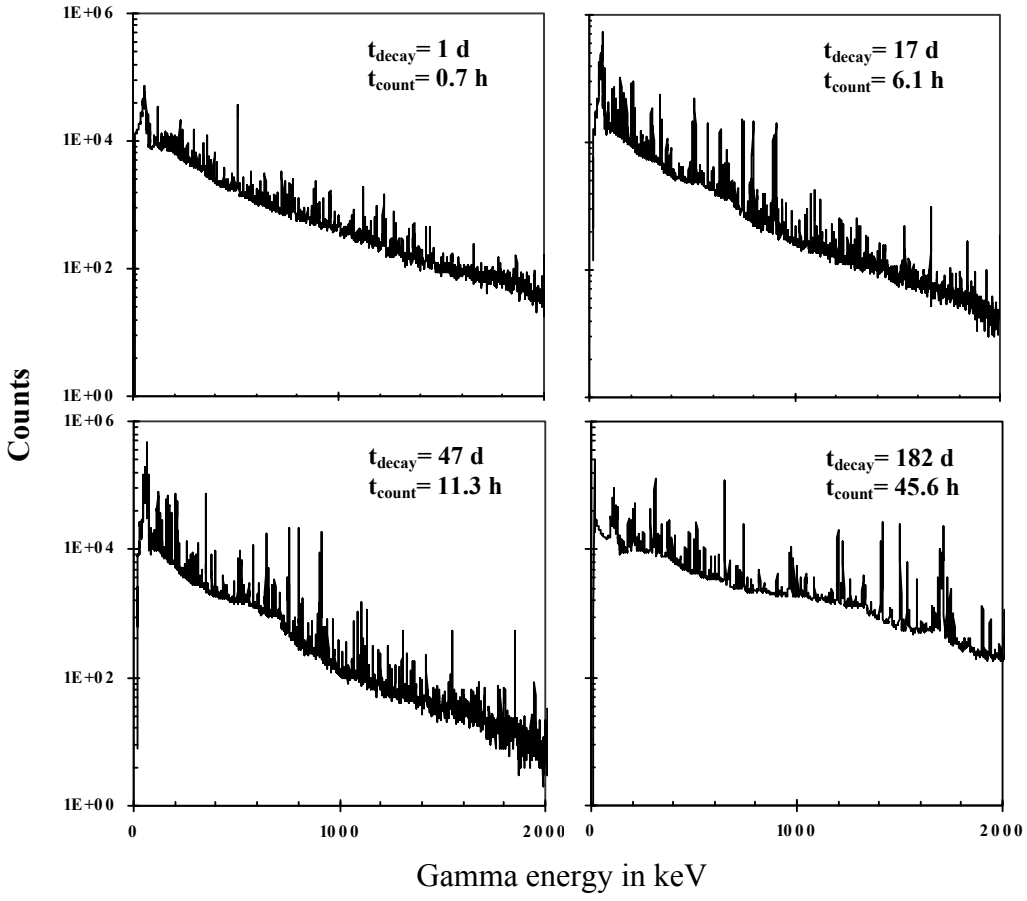

Fig. (2.10): *Examples of γ-spectra for rhenium sample irradiated with 2590 MeV*

The whole evaluation procedure can be done either in an automatic mode or interactively by the user. Although GAMMA-W is a sophisticated and successful code [60], detailed tests showed in our case that for such complex spectra as shown in Figure (2.10-2.11) the automatic mode is not reliable enough with respect to the necessary regioning of the spectrum, peak recognition, background determination, multiplet deconvolution and net-peak area calculation. Thus, we analyzed each spectrum interactively, making sure to get a maximum of information out of each spectrum. Proceeding in this way means, however, to give up the reproducibility of a spectrum analysis in contrast to the automatic and strict application of a mathematical algorithm. Therefore, repeated spectra analyses were performed independently by different persons. The results obtained in this way always were in excellent agreement within the limits of uncertainties of the unfolding procedure.

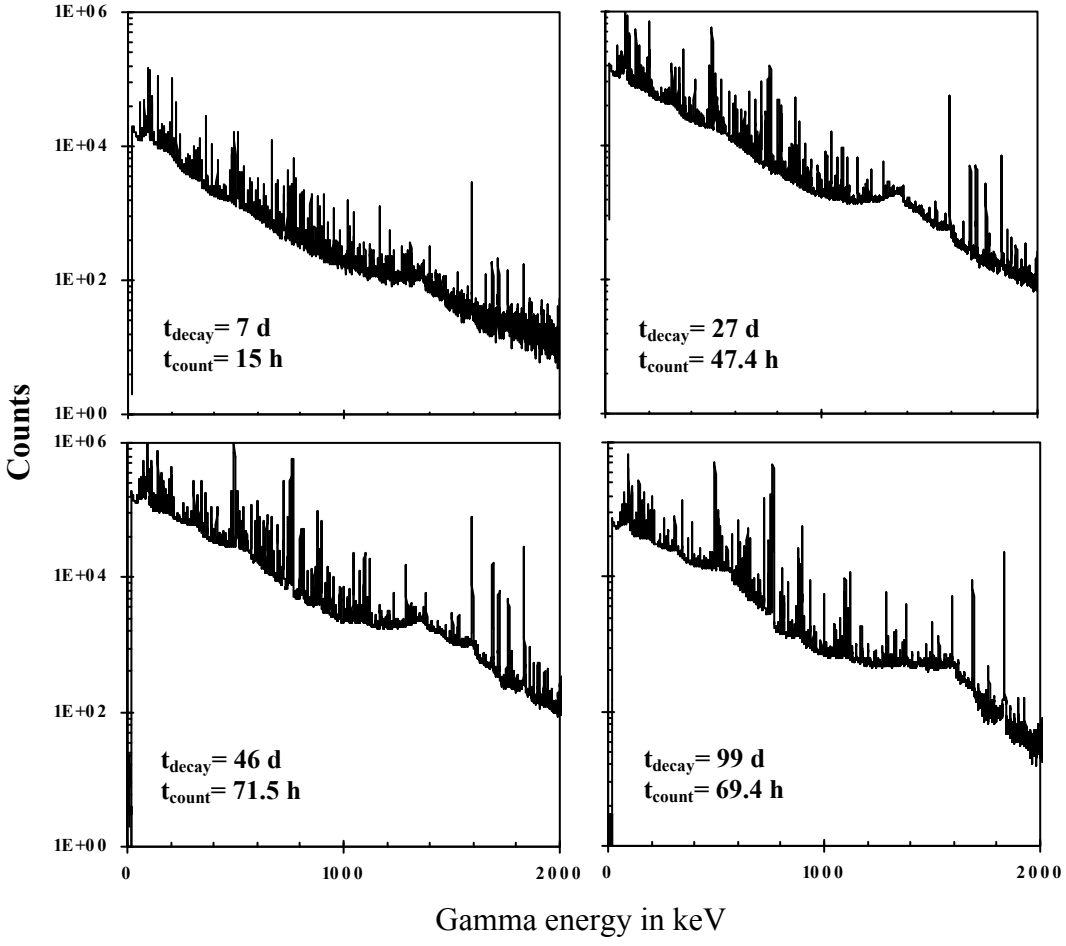

Fig. (2.11): *Examples of γ-spectra for uranium sample irradiated with 2530 MeV.*

2.3.3.7 Radionuclide identification:

Besides the spectrum analysis, an automatic and unambiguous identification of product nuclides turned out to be rather complicated. Most codes - and also GAMMA-W - offer such capabilities, but a general applicable algorithm that can be used with some confidence for complex spectra seems not to exist. By using the output (net peak area file) of the analyzing code GAMMA-W, the identification of radionuclides had to be done. The identification process starts with the spectra having the longest decay times. First such lines are selected which can be unambiguously identified. Then, successively going back in time the identified nuclides are searched for in the preceding spectra by calculating their respective activities and looking whether these activities should be detectable in the spectrum under consideration. Applying this algorithm decreases the number of possible nuclides in a spectrum. For quality control, from measured activities, we calculated the half-life times $T_{1/2}$ for considered radionuclides and compared it with its real value $T_{1/2}$ from recent evaluations to ensure that the identification of radionuclides were correct.

The identification of radionuclides was only performed for γ-energies above 95 keV. Below this energy it was impossible to get quantitative results due to the variety of overlapping X-rays and γ-rays of the produced radionuclides as well as from the lead X-rays themselves. Nuclear data for the identification step were taken from the compilation of Reus and Westmeier [61]. Although this publication is relatively old, it has the advantage that for radio-nuclides having short-lived daughters also the γ-lines of the daughters are listed as decay properties of the parent nuclide. This allows an uncomplicated evaluation procedure in contrast to other types of compilations. Consequently, abundance data may sometimes become larger than unity and do not represent the real physical decay properties of the respective radionuclide. In spite of its age, the data of this compilation are in good agreement with those of a more recent compilation [62] for most radionuclides. Only in some cases there were some deviations that had to be corrected according to more recent databases, e.g. one γ-line from ^{114m}In the energy of which had to be changed 191.6 keV to 190.3 keV [63].

2.3.3.8 Selection of reliable data:

After nuclide identification and calculation of their activities had been done, the last step before calculating cross sections is to gather all activities calculated from the spectra in one file sorted by nuclide. By this way we get a survey over all measurements for each nuclide and its γ-lines allowing for half-life control as well as for checking of consistency of activities determined using different γ-lines of a nuclide. By selecting activities that are judged to be reliable cross section are calculated as described latter.

This judgment is performed on the basis of objective and subjective criteria. Objective criteria are e.g. the agreement of the activities derived from different γ-lines of a nuclide and constancy of the activity calculated for the end of irradiation from several measurements (our half-life control). Subjective criteria are based on the experience and knowledge of the evaluator about the entire spectrometric method and their characteristic properties, about spectrometric interferences and about the physics of the underlying problem. From calculation of the activities at the end of irradiation we calculate the activity at end of irradiation, which are further used in calculating the cross sections.

2.3.4 Proton Flux Densities in the Targets:

The flux densities were determined via the monitor reaction $^{27}Al(p,3p3n)^{22}Na$ using cross sections as described in detail in [64, 65]. For this purpose our each unit in the stacks consisted of three aluminium foils and one uranium foil or rhenium foil for the SATURNE II synchrocyclotron of the Laboratoire National Saturne at Saclay and the cyclotron of the The Svedberg Laboratory at Uppsala.

The flux densities were determined via standard monitor reaction $^{27}Al(p,3p3n)^{22}Na$. For calculating flux density, cross-section data for relevant energies from [64] were considered. The use of aluminium as a target material has some advantages. This can be produced economically in highly pure form, so that no reactions from the impurities are required to be considered. Using the guarded Al target in the middle the flux densities were determined by measuring the 22Na activity via the gamma-energy line at 1274.5 keV. The measurements were done

between 3-5 months after the irradiation. The activities were measured via the equation (2.11) and the flux density will take the following form:

$$\Phi = \frac{A(EOI) \cdot M}{m \cdot N_A \cdot \sigma \cdot \exp^{(\lambda \cdot TOI)}} \tag{2.21}$$

Where,

A(EOI) activity of ^{22}Na at end of irradiation.

σ monitor cross section for the ^{27}Al(p,3p3n)^{22}Na reaction.

λ decay constant of ^{22}Na. m mass of aluminium target in g.

N_A Avogadro number. TOI time of irradiation.

In figure (2.26), we can present the excitation function for the monitor reaction ^{27}Al(p,3p3n)^{22}Na. The excitation function is composed of maxima followed by a sharp decline which is in accordance of the theory, addition a good agreement with the data from Ref. [66, 67].

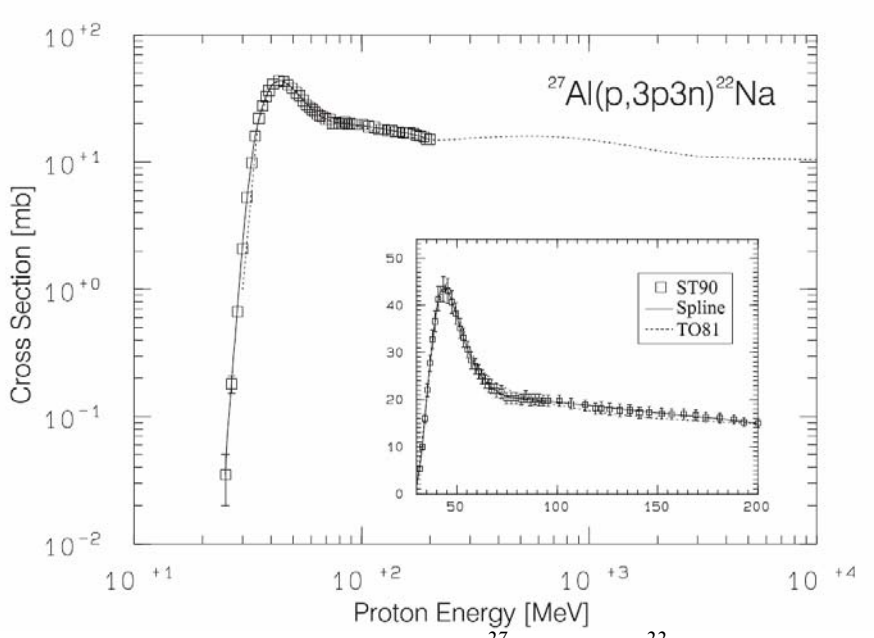

Fig. (2.12): *Monitor excitation function for the ^{27}Al(p,3p3n)^{22}Na reaction.*

The uncertainty of the flux density is mainly determined by the uncertainties of the efficiencies and of the activity of ^{22}Na. The uncertainty of flux density u(Φ) was calculated by the following equation:

$$u(\Phi) = \frac{\Phi \cdot u(A(EOI))}{A(EOI)} \tag{2.22}$$

Where, u(A(EOI)) is the uncertainty of the activity of ^{22}Na at the end of irradiation EOI, Φ is the flux density, and A(EOI) is the activity of ^{22}Na at the end of irradiation. No uncertainties were attributed to the monitor cross sections. Moreover, we do not consider an uncertainty in the monitor cross section due to an uncertainty of the proton energy because the monitor excitation functions does not vary in the energy region covered.

2.3.5 Cross Section Calculations:

For completeness we give a short survey on the calculational procedure by which cross-sections were derived. In a measured γ-spectrum we obtain a number C of counts in a net full-energy peak at γ-energy E_γ where a nuclide emits γ-quanta with an abundance $I_\gamma(E_\gamma)$ which are detected with efficiency $\varepsilon_\gamma(E_\gamma)$. C is related to the activity A of this nuclide between the beginning of counting (BOC) and the end of counting (EOC) according to:

$$C = \int_{t_{BOC}}^{t_{EOC}} dt\, \varepsilon_\gamma(E_\gamma)\, I_\gamma(E_\gamma)\, A(t) \tag{2.23}$$

Integration of Eq. (2.23) yields for the activity at the end of irradiation (EOI):

$$A(t_{EOI}) = \frac{C \cdot \lambda}{I_\lambda\, \varepsilon_\lambda (1 - \exp^{(-\lambda t_c)})} \exp^{(\lambda t_d)} \tag{2.24}$$

with $t_c = t_{EOC} - t_{BOC}$ being the counting time, $t_d = t_{BOC} - t_{EOI}$ the decay time between end of irradiation (EOI) and beginning of counting (BOC), and $\lambda = \ln 2/T_{1/2}$ the decay constant of the nuclide with half-life $T_{1/2}$. The production and decay of the nuclide during the time of irradiation t_{irr} of a sample consisting of N_T target atoms with projectiles of flux density Φ is for negligible burn-up of the targets described by:

$$A(t) = N_T\, \sigma\, \Phi (1 - \exp^{(-\lambda t)}), \qquad 0 \le t \le t_{irr} \tag{2.25}$$

With the cross-section s to be determined. Combing Eqs. (2.24) and (2.25) yields:

$$\sigma = \frac{C\lambda}{I_\lambda \varepsilon_\lambda \Phi N_T} \frac{\exp^{(\lambda t_d)}}{(1-\exp^{(-\lambda t_c)})(1-\exp^{(-\lambda t_{irr})})} \tag{2.26}$$

2.3.5.1 Cross section uncertainties:

Many sources of uncertainties are considered during the calculation of cross section and sometime they result considerable changes. The uncertainty in the cross section of the produced nuclide in our work we calculated as:

$$u(\sigma) = \sqrt{(\frac{u(A_{EOI})}{A_{EOI}})^2 + (\frac{u(m)}{m})^2 + (\frac{u(\Phi)}{\Phi})^2} \tag{2.27}$$

Where m is the mass of the target and Φ is the flux of the monitoring cross section reaction. There are many sources of uncertainties of the cross-sections and some may result in considerable uncertainties. The following sources of uncertainties were considered:

Uncertainty of the determination of net peak areas: The uncertainty of each single net-peak area is determined by the spectrum-evaluation code. It takes into account the Poisson uncertainties of the counts in the individual channels as well as the uncertainty of the background determination, propagating them according to the law of error propagation through the unfolding procedure. Sometimes a peak cannot be attributed unambiguously to a single nuclide. If the contributions were not negligible and the activity of one of the contributing nuclides can be determined using another line or in a later spectrum, the interfering lines were corrected using this activity. If it seemed that the contributions of other nuclides to a peak are very small, no correction was applied. Due to this procedure we assume a maximum inaccuracy of 2% due to contributions of other nuclides but it must be pointed out that on the average this uncertainty should be smaller.

Uncertainty of half-lives: Half-lives were taken from Ref. [61]. Since on the one hand this publication is rather old but since on the other there are no large deviations to newer ones as e.g. [68, 69], we assume typically an uncertainty of 1% for this quantity. Larger uncertainties in any time dependent terms in calculating

cross-sections via Eq. (2.26) would result in observable disagreements between different measurements due to the exponential dependence on time. Uncertainties of the half-lives were considered to be of the order of 1% for the nuclides measured. Larger uncertainties would have shown up during the half-life control.

Uncertainty of γ-abundances: Abundances were also taken from Ref. [61]. Since we used normally the strongest γ-lines which were rather well-known even in 1983, we assume a global uncertainty of 2%.

Uncertainty of efficiency: The calibration standards used had a certified accuracy of ≤ 2%. By measurements using different detectors they could be verified with a total uncertainty of the full-energy- peak efficiency of 5%.

Uncertainty of number of irradiated nuclei: Each foil was weighted with an absolute uncertainty of ± 0.4 μg. In case of the aluminium catcher foils with typical weights of 60 μg, this resulted in an inaccuracy of about 1%, while the uncertainty for the heavier lead foils with weights of about 230 or 460 mg becomes negligible.

Uncertainty of flux density: The flux densities were determined via the monitor reaction $^{27}Al(p,3p3n)^{22}Na$ using cross-sections as described in detail in Refs. [64, 65]. The uncertainty of flux density is mainly determined by the uncertainties of efficiency and of the mass of the catcher foil which sum up to be about 6%. No uncertainties were attributed to the monitor cross-sections. Moreover, we do not consider an uncertainty in the monitor cross-section due to an uncertainty of the proton energy because the monitor excitation function does not vary in the energy region covered.

Uncertainty of irradiation time, decay time and counting time: For time scales determined by the half-lives of nuclides observed within this work, we assume that uncertainties of the above-mentioned quantities are negligible.

γ-γ-coincidences: γ-γ-coincidences have to be taken into account at very small distances between sample and detector. Since distances from the detector down to 5 cm were used to get a sufficient counting statistics, it would have been necessary to correct them in some cases. But this was not done since the effects were visible only for some special nuclides. In these cases they caused an uncertainty in the

determination of activity using different γ-lines of ≤ 5%. Consequently, we took this uncertainty as a general uncertainty due to γ-γ-coincidences in case of coincident γ-rays.

Constancy of flux density over irradiation time: The beam intensities were continuously monitored and recorded. Using these protocols we took into account interruptions of the irradiations using the following replacement in Eq. (2.26)

$$\frac{1}{1-\exp^{(-\lambda t_{irr})}} \rightarrow \sum_{i=1}^{n} \frac{\exp(\lambda(t_{EOI}-t_{EOI,i}))}{1-\exp^{(-\lambda t_{irr,i})}} \tag{2.28}$$

Because the flux density itself may not be constant during irradiation we replaced F in Eq. (2.26) by:

$$\Phi \rightarrow \frac{1}{t_{EOI}-t_{BOI}} \int_{t_{BOI}}^{t_{EOI}} dt^{*}\, \Phi(t^{*}) \tag{2.29}$$

With $\Phi(t^{*})$ being the relative measurements of the beam current. Using these replacements the uncertainties due to fluctuations in the beam intensity become negligible. Moreover, they would affect only the cross-sections for very short-lived nuclides.

Recoil losses and recoil contaminations: By measuring the inner foils of each mini-stack only, both recoil losses and recoil contamination can be neglected.

Dead-time and pile-up losses in γ-spectrometry: The dead-time of the detector systems was automatically corrected. Pile-up effects were not seen because the distances between samples and detector were varied in the way that the counting rates were low enough to avoid both pile-up and failure of the automatic dead-time correction.

Absorption of γ-quanta in the sample: While absorption of g-quanta in the aluminium catcher foils played no role, it did in the lead foils. Since we evaluated our spectra for energies down to 95 keV we had to apply corrections for this effect. This was done using the tables for photon cross sections of Storm and Israel [70]. Based on these data we calculated in dependence of the mass of the foil and the energy-

dependent absorption coefficient m for each single peak in a spectrum the fraction r of g-quanta which leave the foil and can be registered by the detector by Eq. (2.30). By dividing each net-peak area by $r'(E_\gamma)$ we took into account this effect. In the worst case all these uncertainties except for that of the net peak counts summed up

$$r(E_\lambda) = \frac{1}{\xi}\int_0^{\xi} d\xi^* \exp^{(-\mu\xi^*)} = \frac{1-\exp^{(-\mu\xi)}}{\mu\xi} \qquad (2.30)$$

quadratically. As a general tendency, we obtained smaller uncertainties for longer-lived radionuclides than for short-lived ones. In most cases, however, the total uncertainties were less than 10%.

2.3.5.2 Cumulative and independent cross sections:

While calculating the cross section of a residual, two types of cross section are taken into account. One is independent and the other is cumulative. Eqs. (2.25) and (2.26) are strictly valid only for the so-called independently produced radionuclides because the only production mechanism assumed is the nuclear reaction leading to the produced nuclide. But in the majority of cases a further production by β^-, β^+, EC or α-decays of a radioactive precursor has to be taken into account. Since there are sometimes ambiguities existing about the terms independent and cumulative cross-sections we have to give some clarifications. A cross-section for the production of a nuclide is denoted as independent if the nuclide can only be produced directly via the nuclear reaction between the projectile and the target nucleus and not via subsequent β^-, β^+, EC or α-decays. Such independent cross-sections are obtained if:

- either the nuclide is shielded by stable nuclides against β-decay or by a long-lived progenitor (e.g. ^{60}Co by ^{60}Fe with $T_{1/2}=1.5\times10^6$ a, or ^{194}Au by ^{194}Hg with $T_{1/2}$=520 a);
- or the cross-section for the production of a progenitor is also measured so that the productionvia decay can be corrected for.

In all other cases the cross-sections are cumulative since they include also the production via decay of precursors. If we consider, e.g. the production of a nuclide D (daughter) on the one hand by the nuclear reaction and on the other by decay of a

radioactive precursor M (other) then the solution of the differential equation corresponding to Eq. (2.25) for the activity $A_D(t)$ of D for times $t > t_{irr}$ is given by:

$$A_D(t) = N_T \Phi \begin{pmatrix} (\sigma_D + \sigma_M \frac{\lambda_M}{\lambda_M - \lambda_D})(1 - \exp^{(-\lambda_D t_{irr})}) \exp^{(-\lambda_D t)} \\ + \sigma_M \frac{\lambda_D}{\lambda_M - \lambda_D}(1 - \exp^{(-\lambda_M t_{irr})}) \exp^{(-\lambda_M t)} \end{pmatrix} \quad (2.31)$$

Where, σ_D, σ_M are the independent cross sections for the mother M and the daughter D, respectively. Provided that the half-life of M is short compared to that one of D ($\lambda_M >> \lambda_D$), we can neglect the second term in Eq. (2.31) for large t_d. This yield:

$$\sigma_{D,com} = \sigma_D + \sigma_M \frac{\lambda_M}{\lambda_M - \lambda_D} \quad (2.32)$$

With the cumulative cross-section $\sigma_{D;cum}$ of the nuclide D calculated according to Eq. (2.26).

2.3.5.3 Corrections for γ-interferences:

From the very complex spectra we dealt with in this work, the cross-sections for some nuclides could only be determined after the correction of interfering γ-lines from another nuclide which could not be resolved by our detectors. Assume that $A_1(t_{EOI})$ and $A_2(t_{EOI})$ are the activities of two nuclides at the end of irradiation which have interfering γ-lines with $I_{\gamma 1}$ and $I_{\gamma 2}$ being the abundances of the corresponding γ-quanta. Then first a wrong activity $A^*_1(t_{EOI})$ is calculated according to Eq. (2.24) in our evaluation procedure under the assumption that the peak is only caused by nuclide 1. If $A_2(t_{EOI})$ is known, e.g. from other γ-lines of nuclide 2, we can calculate the correct value of $A_1(t_{EOI})$ to be:

$$A_1(t_{EOI}) = A_1^*(t_{EOI}) - A_2(t_{EOI}) \frac{\lambda_1 I_{\gamma 1}(1 - \exp^{(-\lambda_2 t_c)})}{\lambda_2 I_{\gamma 2}(1 - \exp^{(-\lambda_1 t_c)})} \cdot \exp^{(-(\lambda_2 - \lambda_1) t_d)} \quad (2.33)$$

Although it is in principle possible to apply this scheme to more than only one interfering γ-line we limit ourselves to one correction term since the resulting uncertainty of the corrected activity quickly becomes rather high if the correction is large.

2.3.5.4 Corrections for γ-self-attenuation in the targets:

Because of the high density of 19.05 g/cm^3 of the uranium targets, self absorption of γ-quanta in the uranium foils played an important role. So, we must correct the measured activities. We used the XCOM code [71] to calculate the energy-dependent mass absorption coefficient (μ_ρ) for each single peak in a spectrum. The total attenuation coefficient for uranium as calculated by the XCOM code is plotted against photon energy in Fig. (2.13).

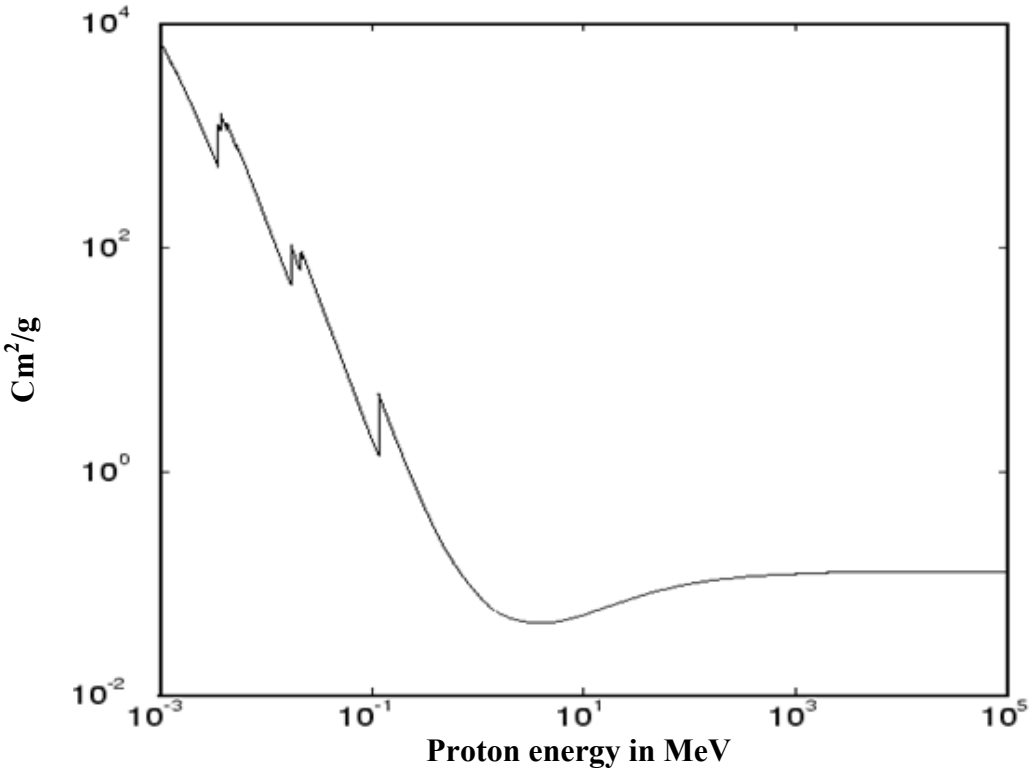

Fig. (2.13): *The total attenuation coefficient of uranium as calculated by the XCOM code as a function of the photon energy.*

For the calculation of the self-attenuation in a target foil with subdivided a foil into *n* different thin layers of thickness *d*. For the calculation of the self-attenuation in the target foil, we then used the formula (2.34) to calculate the fraction *f* which gets out of the target foil as the average of the fraction from each thin layer *i*.

$$f = \frac{1}{n+1} \cdot \sum_{i=0}^{n} e^{-\mu_\rho \frac{\rho \cdot d \cdot i}{n+1}} \qquad (2.34)$$

(1- f*)* is the part which has been absorbed by the target, μ_ρ the energy-dependent mass absorption coefficient, ρ the density of the absorber and d its thickness. By dividing each net-peak area by f we took into account this effect.

2.3.5.5 Correction for radioactive progenitors:

If the condition $\lambda_M \gg \lambda_D$ under which we derived the cumulative cross section $\sigma_{D,cum}$ of D is full-filled and we were able to measure σ_M then we can of course derive the independent cross section σ_D for the production of D from Eq. (2.32). However, there are some cases in which $\lambda_M \gg \lambda_D$ is not satisfied e.g. for ^{95g}Nb with a half-life of 34.97 d which is produced also by the β^--decay of ^{95}Zr ($T_{1/2}$ = 64.03 d). For such cases we proceed as follows. Assume a mother nuclide M of known activity A_M decaying with decay constant λ_M into the daughter D with λ_D for which wrong activities A_D^* are calculated according to Eq. (2.24). Solving the system of coupled differential equations describing the decay of the mother and the decay and the build-up of the daughter after the end of irradiation (t = 0) we calculate the corrected activity A_D according to equ.(2.35) and obtain the independent cross section of the daughter via Eq.(2.36) .

$$A_D(t_{EOI}) = \left(A_D^*(t_{EOI}) + A_M(t_{EOI}) \frac{\lambda_D}{\lambda_D - \lambda_M} \left(1 - \frac{\lambda_D}{\lambda_M} \frac{1 - \exp^{(-\lambda_M t_c)}}{1 - \exp^{(-\lambda_D t_c)}} \cdot \right. \right. \\ \left. \left. \exp^{(-(\lambda_M - \lambda_D) t_D)} \right) \right) \qquad (2.35)$$

$$\sigma_D = \left(\frac{A_D^*(t_{EOI})}{N_T \Phi (1 - \exp^{(-\lambda_D t_{irr})})} - \sigma_M \left(1 - \frac{\lambda_D}{\lambda_D - \lambda_M} \left(1 - \frac{1 - \exp^{(-\lambda_M t_{irr})}}{1 - \exp^{(-\lambda_D t_{irr})}}\right)\right) \right) \qquad (2.36)$$

2.3.5.6 Half-life control:

After calculating the activity a plot was made between the activity at the begin of counting versus time of decay, which is the time that has been spanned before the specific measurement after the irradiation. Linear function available in Microsoft Excel ® of the form y = a exp(− λx) was used. Here λ is the decay constant. Thus the half-life was calculated by the formula $T_{1/2} = \ln(2)/\lambda$. After measuring the half-life of the corresponding nuclide, it was compared with the original half-life of the nuclide. If they agree then the identification of the corresponding nuclide is assumed to be

correct see for example figure (2.14). This procedure is continued for all the nuclides assumed. Half- lives those did not agree are not considered any more.

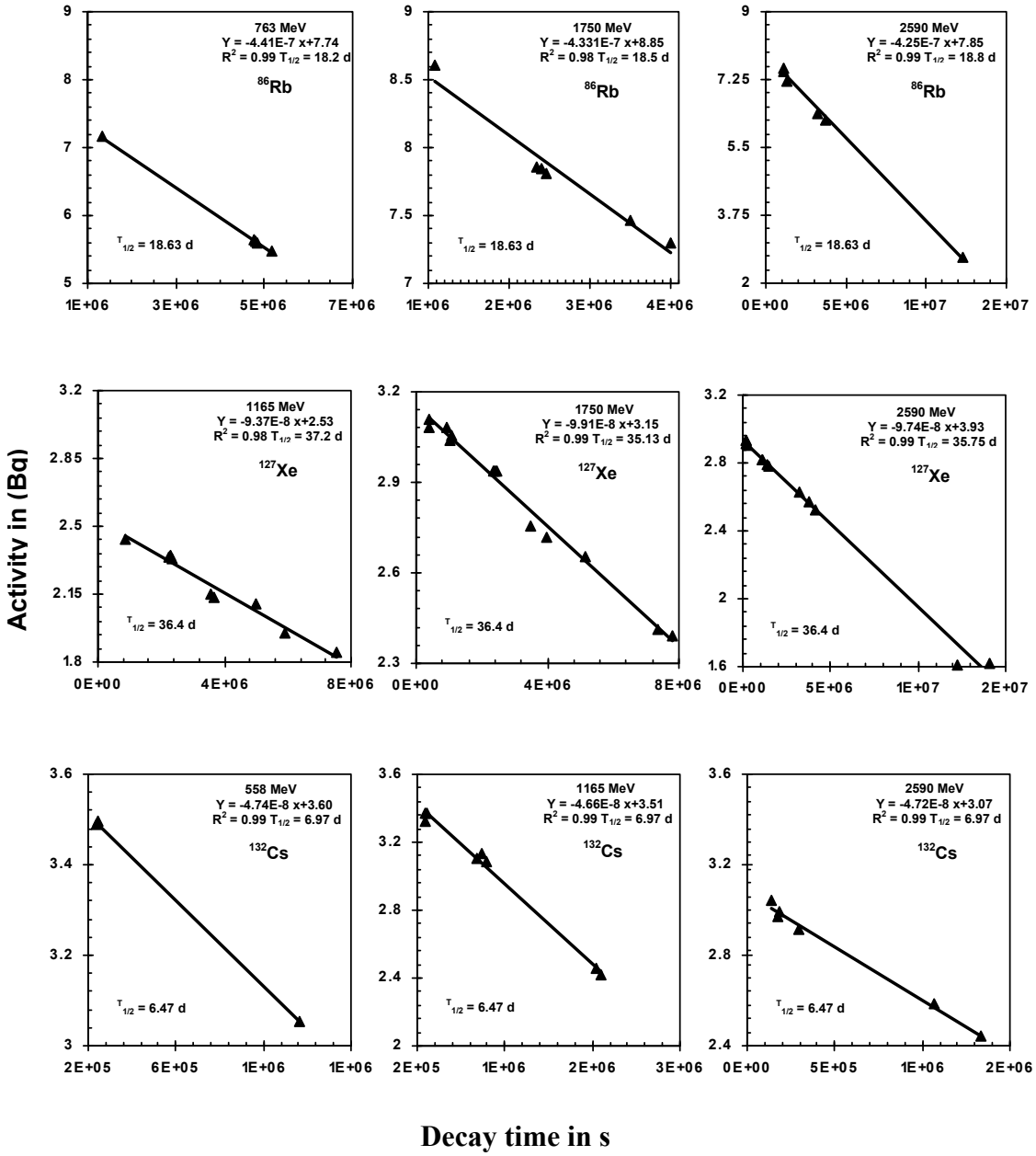

Fig. (2.14): *Apparent half-life for ^{86}Rb, ^{127}Xe and ^{132}Cs.*

CHAPTER 3
MODEL CALCULATION

The interaction of high energy protons with atomic nuclei has attracted the attention for many years [72]. But the main emphasis was put on coherent elastic and inelastic scattering and on the understanding of these processes in terms of multiple scattering series [73] (or more recently in terms of scattering by relativistic scalar and vector average fields) [74]. In recent years however, there has been among physicists an increasing interest in the more violent (and mainly incoherent) processes which are taking place in these reactions. The target nucleus can undergo some transformations. In some cases, it loses a few nucleons (the so-called spallation). If the excitation energy is sufficiently high, it can presumably disintegrate into malay pieces. It is a general belief that, in a first approximation, the interaction process between an incoming proton with energy of a few hundreds of MeV or more can be grossly divided in two steps. In the first rapid step, the incoming nucleon makes a few (mainly) incoherent scatterings with nucleons of the target, depositing in this way some fraction of its energy. The second step, which supposedly starts after the incoming proton has left the target, involves the propagation and the dissipation of the energy gained by the nucleus. Generally, the ultimate fate of the nucleus is its fragmentation. The mass yield has been measured in many circumstances and exhibits a so-called U-shape [75]: the small fragments and those of size comparable with the original nucleus are the more represented. But, any fragment between the nucleon and the target has been observed. Not very much is known about the second step and only several idealizations have been proposed. Let us summarize the most important ones.

- *Spallation models* [76]: the energy is evacuated by the nucleons hit in the first step, which leave the nucleus without interaction. Possibly, the remaining nucleus releases some energy gained by its axcitation.

- *Thermal models* [77, 78]: the energy is shared by the whole nucleus which decays in fragments according the phase space constituted by the possible partitions of the target. These models involve at least one free parameter which can be considered as the freeze-out density.

- *Cold fragmentation* [79]. Those models share with the previous ones the idea of equipopulation of a phase space. But here, the phase space is restricted to the possible fragmentations including neither the relative motion between the fragments nor the intrinsic excitation of the fragments.

- *Condensation models* [80-82]. As thermal models, the latter assume a therrealization of the system, but the separation into fragments is determined by the proximity of the critical point of the underlying gas-liquid transition.

- *Percolation models* [83-85]. In the latter, it is assumed that the eventual fragmentation of the nucleus is determined by the geometry of the "damage" made to the nucleus after the initial step which, in turn, is believed to be largely correlated to the number of nucleons hit during the first step.

3.1 TALYS CODE:

With the advent of fast computers, software that simulates nuclear reactions is able to play an increasingly important role in nuclear data. It is possible to provide an exact computational scheme for sophisticated nuclear models, not only new ones but also those that have been lying on the shelf for decades and only now become amenable for numerical implementation. Large scale comparisons with measurements are within reach. TALYS is a nuclear reaction program created at NRG Petten, the Netherlands and CEA Bruyères-le-Châtel, France. The idea to make TALYS was born in 1998, when it was decided to implement the combined knowledge of nuclear reactions into one single software package. The objective was to provide a complete and accurate simulation of nuclear reactions in the 1 keV-200 MeV energy range, through an optimal combination of reliable nuclear models, flexibility and user-friendliness. There are two main purposes of TALYS, which are strongly connected. First, it is a *nuclear physics* tool that can be used for the analysis of nuclear reaction experiments. The interplay between experiment and theory gives us insight in the fundamental interaction between particles and nuclei, and precise measurements enable us to constrain our models and their parameters. In return, when the resulting nuclear models are believed to have sufficient predictive power, the prediction can even give an indication of the reliability of measurements. The many examples of TALYS presented in various other contributions to this conference confirm that

software project would be nowhere without the existing experimental database. After the nuclear physics stage comes the second function of TALYS, namely as a nuclear data tool: After fine-tuning the adjustable parameters of the various reaction models using available experimental data, TALYS can *generate* nuclear data for all open reaction channels, interpolating between and extrapolating beyond experimental data, on a user-defined energy and angle grid beyond the resonance region. The associated nuclear data libraries that can be constructed provide essential information for existing and new nuclear technologies. Figure (3.1) shows the nuclear models implemented in TALYS [86].

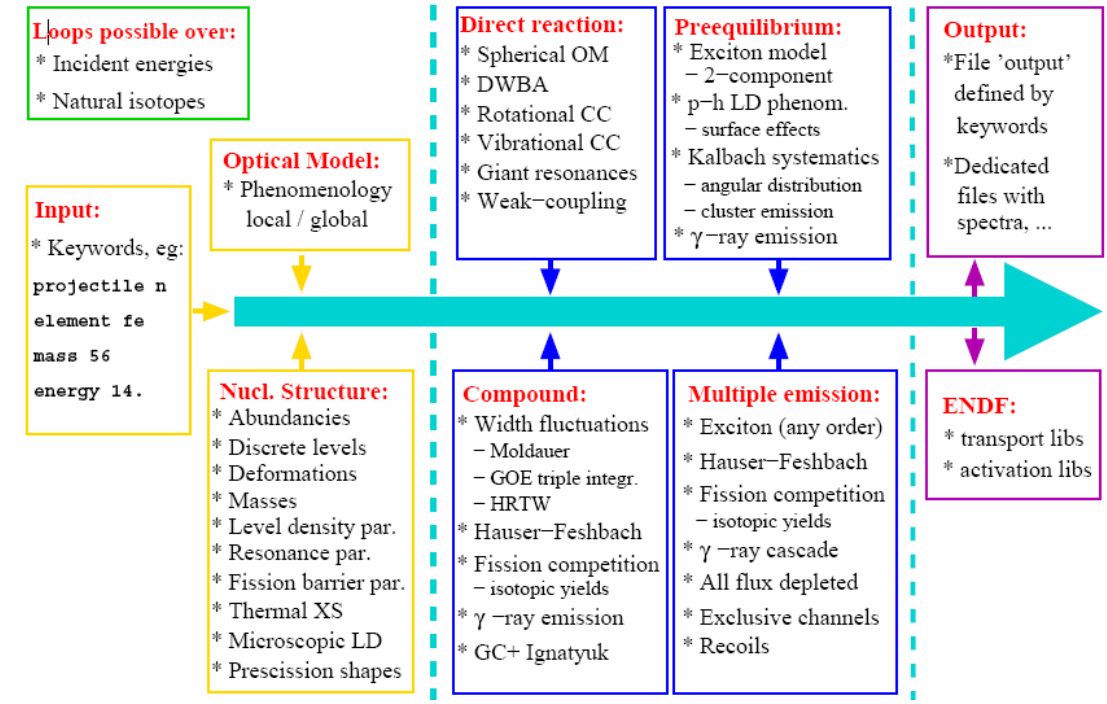

Fig. (3.1):- *flowchart of TALYS.*

TALYS is a nuclear reaction program which simulates nuclear reactions that involve neutrons, gamma-rays, protons, deuterons, tritons, helions and alpha-particles, in the 1 keV - 200 MeV energy range. A suite of nuclear reaction models has been implemented into a single code system; enable to evaluate basically all nuclear reactions beyond the resonance range. An overview is given of the main nuclear models used, such as newly developed optical models, various compound nucleus, fission, gamma-ray strength, level density and pre-equilibrium models, all driven by a comprehensive database of nuclear structure parameters. The predictive power of the code is demonstrated by comparing calculated results with a very diverse set of

experimental observables. The TALYS code combines a compound nucleus model in the form of Hauser Feshbach calculations [87] with a pre-equilibrium model according to the exciton model by Kalbach [88]. The transmission coefficients are calculated by an optical model making use of the recent parameterization by Koning and Delaroche [89]. The level densities are used in form of a back-shifted Fermi-gas model according to Gilbert-Cameron [90] taking into account the Ignatyuk formalism [91]. The competition between particle emission, gamma-de-excitation and fission is calculated at each energy step of the proceeding reaction. Fission is treated according to the Brosa model [92] as incorporated earlier into fission modelling by Duijvenstijn [93].

3.2 INCL4+ABLA CODE:

The most successful model used to describe spallation reactions is the intranuclear cascade (INC) plus evaporation model. A new version of the Liáge intranuclear cascade (INC) model is proposed for the description of spallation reactions. Compared to the previous version, it incorporates new features: (i) it can accommodate a diffuse nuclear surface, (ii) the treatment of the Pauli blocking effect is improved, removing unphysical features linked with the use of statistical blocking factors, (iii) collisions between moving spectator nucleons are explicitly suppressed, (iv) pion dynamics is improved, especially concerning the delta lifetime, (v) it can accommodate light ions as incoming projectiles, (vi) the remnant angular momentum is included in the output of the model. Another important feature is the self-consistent determination of the stopping time, i.e., the time at which the INC calculation is terminated and coupled to evaporation. The predictions of the model, used with the Schmidt evaporation code, are tested against a large body of experimental data, in the 200-MeV–2-GeV range for incident energy per nucleon, including total reaction cross sections, neutron, proton, pion, and composite double differential cross sections, particle multiplicities, residue mass and charge distributions, and residue recoil velocity distributions. Good agreement is generally obtained without additional varying parameters. It is shown that the introduction of a diffuse surface considerably improves the description of the total reaction cross sections, of the intensity of the quasielastic peak in proton and neutron double differential cross sections and of the residue production yield for isotopes close to the target. High energy neutron spectra

are found to be sensitive to details of the deuteron structure in deuteron-induced reactions. The shape of the fragmentation peaks in residue mass spectra is shown to be closely related to the shape of the distribution of the excitation energy left after the cascade stage. The longitudinal residue recoil velocity and its fluctuations display typical random-walk characterics, which are interpreted as a direct consequence of the independence of successive binary collisions occurring during the cascade process and therefore provide a strong support of the basic hypotheses of the INC model [94, 95].

Recently we proposed an advanced version of the Liège intranuclear cascade model (INCL4) [95], which, coupled which the K.-H. Schmidt evaporation-fission (ABLA) model [96, 97], gives a very accurate description of a large set of data (of different kinds) for proton and deuteron-induced reactions in the 200 MeV to 2 GeV range of incident energy per nucleon. The INCL4 model is basically a multiple-scattering semi-classical model, which handles nucleon degrees of freedom explicitly. Therefore the model of Ref. [95] can accommodate emission of light clusters in the evaporation stage only. This deficiency is not a serious problem as far as global particle multiplicities are concerned. To fix the ideas, rough analyses of experimental data indicate that in a proton-induced reaction on a heavy target in the GeV range, the ratio of the number of nucleons appearing in the form of clusters emitted during the cascade stage to the total number of emitted nucleons, whatever their origin, lies between 5 and 10%. However, the lack of cascade light cluster emission appears more serious in view of technological applications. Indeed light clusters correspond to gaseous elements (H, He), which are liable to create voids or other damages in materials. Therefore it is of utmost interest for the designers of (solid) spallation sources to have at their disposal a good model for the production of these elements. This motivates the present work in which we extent the INCL4 model in order to incorporate light cluster emission in the cascade stage. The INCL4 model is described in detail elsewhere [95].

CHAPTER 4

RESULTS AND DISCUSSION

In this work, we have made the first comprehensive measurements for the proton-induced residual nuclei distribution for rhenium and uranium targets. A total of 7146 cross sections were determined by means of gamma-spectrometry for an energy range between 78.2 MeV and 2590 MeV for rhenium and between 211 MeV and 2530 MeV for uranium. The experimental data were compared with previously obtained experimental data and with calculated excitation functions using the codes INCL4+ABLA and TALYS which are based on theoretical models.

4.1 CROSS SECTIONS FOR RHENIUM:

We present here final cross sections for proton-induced reactions on natural rhenium which are independent (ind.) or cumulative (cum.). We determined a total of about 5252 cross sections for the independent production of ^{186}Re, ^{184}Re, ^{184m}Re, ^{156}Tb, ^{106m}Ag, ^{86}Rb, ^{84}Rb, ^{58}Co and ^{46}Sc and cumulative production of ^{185}Os, ^{183}Os, ^{182}Os, ^{183}Re, ^{182}Re, ^{181}Re, ^{183}Ta, ^{175}Hf, ^{173}Hf, ^{171}Lu ^{170}Lu, ^{169}Lu, ^{169}Yb, ^{166}Tm, ^{155}Tb, ^{153}Tb, ^{152}Tb, ^{151}Tb, ^{149}Gd, ^{147}Gd, ^{146}Gd, ^{148}Eu, ^{147}Eu, ^{145}Eu, ^{139}Ce, ^{137m}Ce, ^{135}Ce, ^{132}Cs, ^{131}Ba, ^{129}Cs, ^{127}Xe, ^{125}Xe, ^{121}Te, ^{119}Te, ^{95}Nb, ^{88}Y, ^{87}Y, ^{85}Sr, ^{75}Se, ^{65}Zn, ^{60}Co ^{59}Fe, ^{57}Ni, ^{51}Cr, ^{7}Be from natural Rhenium for 24 individual energies between 78.2 MeV and 2590 MeV. By using the flux densities of the proton beams, which we calculated it via monitor reaction ^{27}Al(p,3p3n)^{22}Na, we measured and calculated the activity at the end of irradiation for the production of residual radionuclides. After that we calculated the cross sections for these residual radionuclides and compared our results with those of previous experimental work to ensure that the flux densities which we calculated are correct. By this way, we made quality control for our flux density because; it plays the essential role in calculating the cross sections for the targets.

4.1.1 Rhenium: Results from this and Previous Work:

The measured cross sections of the nuclear reactions ^{nat}Re(p,xn)^{185}Os, ^{nat}Re(p,xn)^{182}Os, ^{nat}Re(p,xn)^{183}Os, ^{nat}Re(p,pxn)^{186}Re, ^{nat}Re(p,pxn)^{184}Re,

^{nat}Re(p,pxn)^{184m}Re, ^{nat}Re(p,pxn)^{183}Re, ^{nat}Re(p,pxn)^{182}Re, ^{nat}Re(p,pxn)^{181}Re and ^{nat}Re(p,3pxn)^{183}Ta are presented in graphical form in figure (4-1).

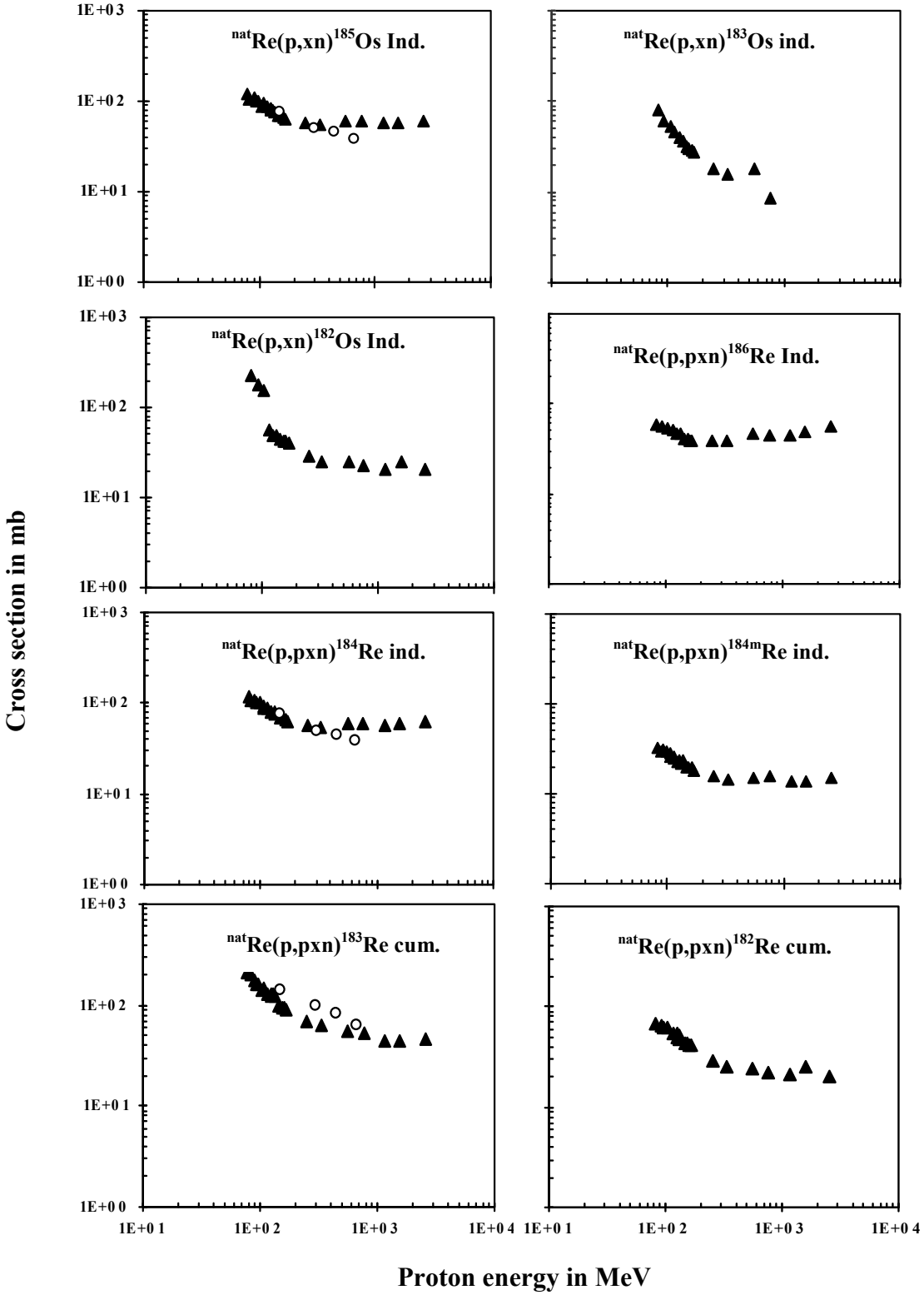

Fig. (4-1): *Cross section as function of proton energy for this work (▲) and Karamian et al. (○) [31] for target near products, part one. The uncertainties of the experimental data are generally smaller than the symbol sizes.*

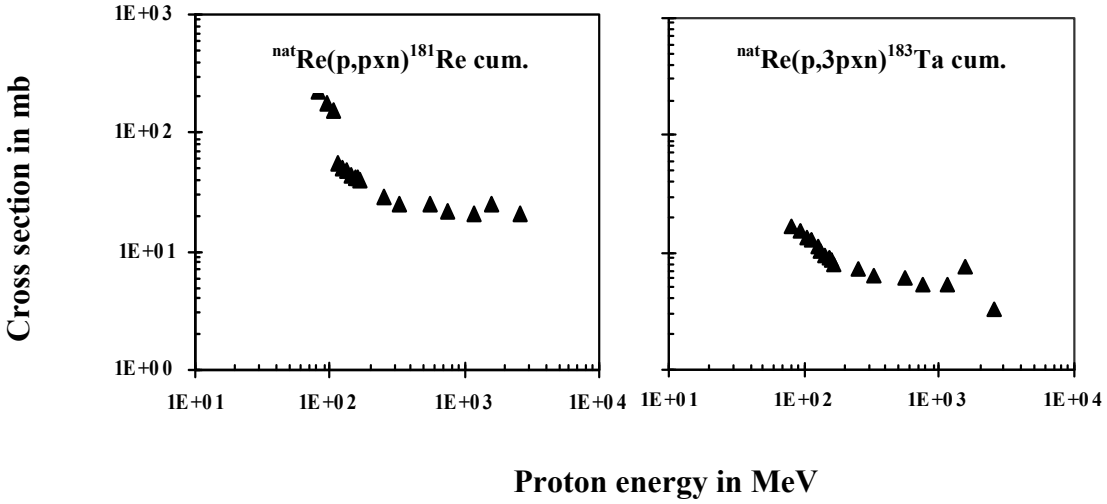

Fig. (4-1): *Continued.*

The excitation functions are compared with the previous work [31] for reactions ^{nat}Re(p,xn)^{185}Os, ^{nat}Re(p,pxn)^{184}Re and ^{nat}Re(p,pxn)^{183}Re. A literature search was performed with EXFOR databases maintained by OECD/NEA Data Bank and National Nuclear Data Center. The survey resulted in only one reference for ^{nat}Re irradiated by proton energies 150 MeV, 300 MeV, 450 MeV and 600 MeV. It means that, our work is the first experiment in which comprehensively 24 individual energies between 78.2 MeV and 2590 MeV were investigated.

Figure (4-1) shows that, the cross sections as functions of proton energy decrease with increasing proton energy from 78.2 MeV to 331 MeV and then the excitation functions look little bit constant to 2590 MeV. A good agreement with Karamian et al. [31] for reactions ^{nat}Re(p,xn)^{185}Os and ^{nat}Re(p,pxn)^{184}Re at proton energies 150 MeV, 300 MeV and 450 MeV and at 600 MeV our data is little bit higher. For reaction ^{nat}Re(p,pxn)^{183}Re at 300 MeV and 450 MeV the previous experimental data is higher than our results.

The excitation functions for Spallation products of nuclear reactions ^{nat}Re(p,4pxn)^{175}Hf, ^{nat}Re(p,4pxn)^{173}Hf, ^{nat}Re(p,5pxn)^{171}Lu, ^{nat}Re(p,5pxn)^{170}Lu, ^{nat}Re(p,5pxn)^{169}Lu, ^{nat}Re(p,6pxn)^{169}Yb, ^{nat}Re(p,7pxn)^{166}Tm, ^{nat}Re(p,11pxn)^{156}Tb, ^{nat}Re(p,11pxn)^{153}Tb, ^{nat}Re(p,11pxn)^{152}Tb, ^{nat}Re(p,12pxn)^{149}Gd, ^{nat}Re(p,13pxn)^{148}Eu, ^{nat}Re(p,12pxn)^{147}Gd, ^{nat}Re(p,13pxn)^{147}Eu, ^{nat}Re(p,12pxn)^{146}Gd, ^{nat}Re(p,13pxn)^{145}Eu, ^{nat}Re(p,18pxn)^{139}Ce, ^{nat}Re(p,18pxn)^{137m}Ce, ^{nat}Re(p,18pxn)^{135}Ce, ^{nat}Re(p,21pxn)^{132}Cs,

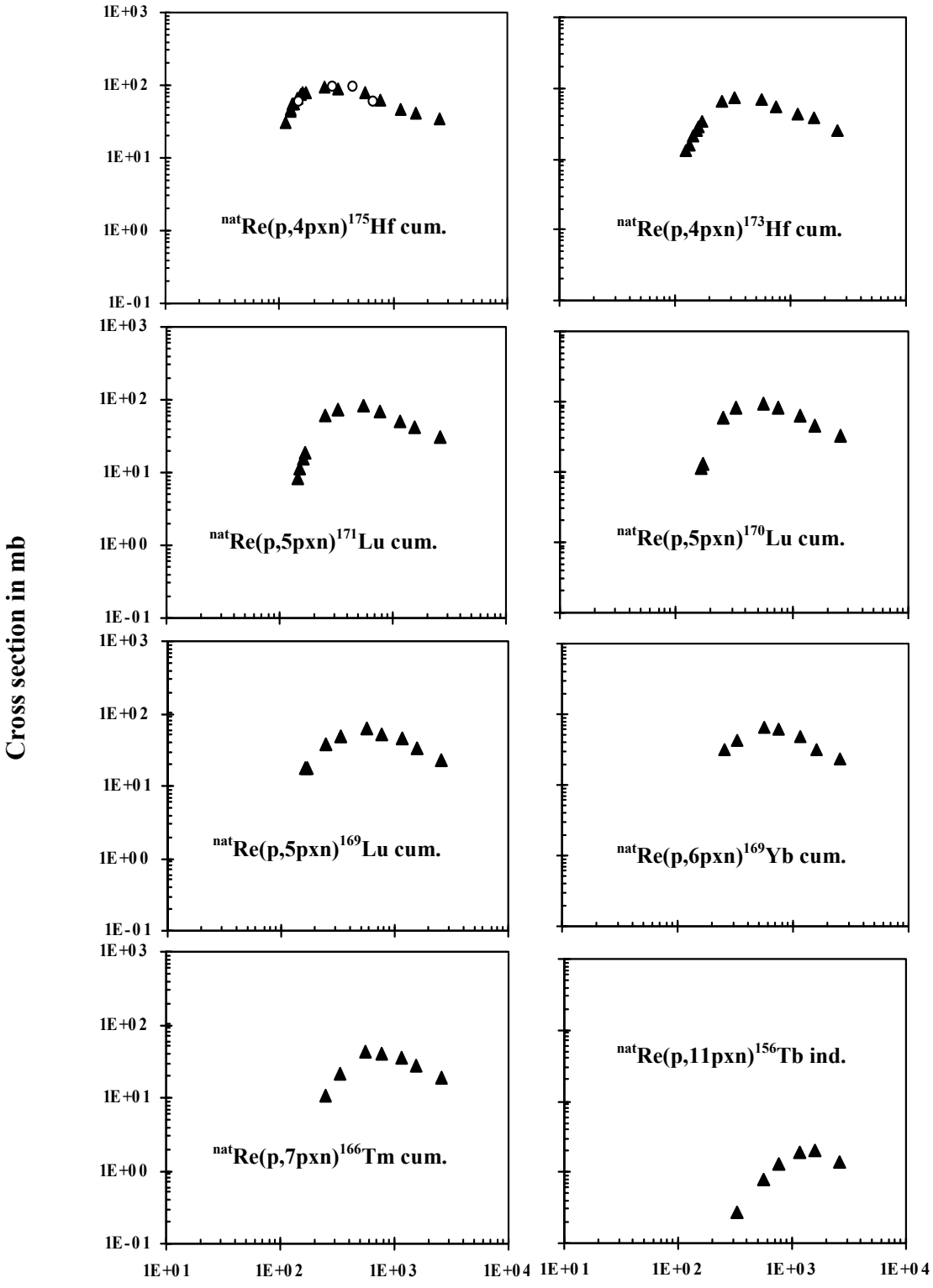

Fig. (4.2): *Cross section as function of proton energy for this work (▲) and Karamian et al. (○) [31] for spsllation products, part one. The uncertainties of the experimental data are generally smaller than the symbol sizes.*

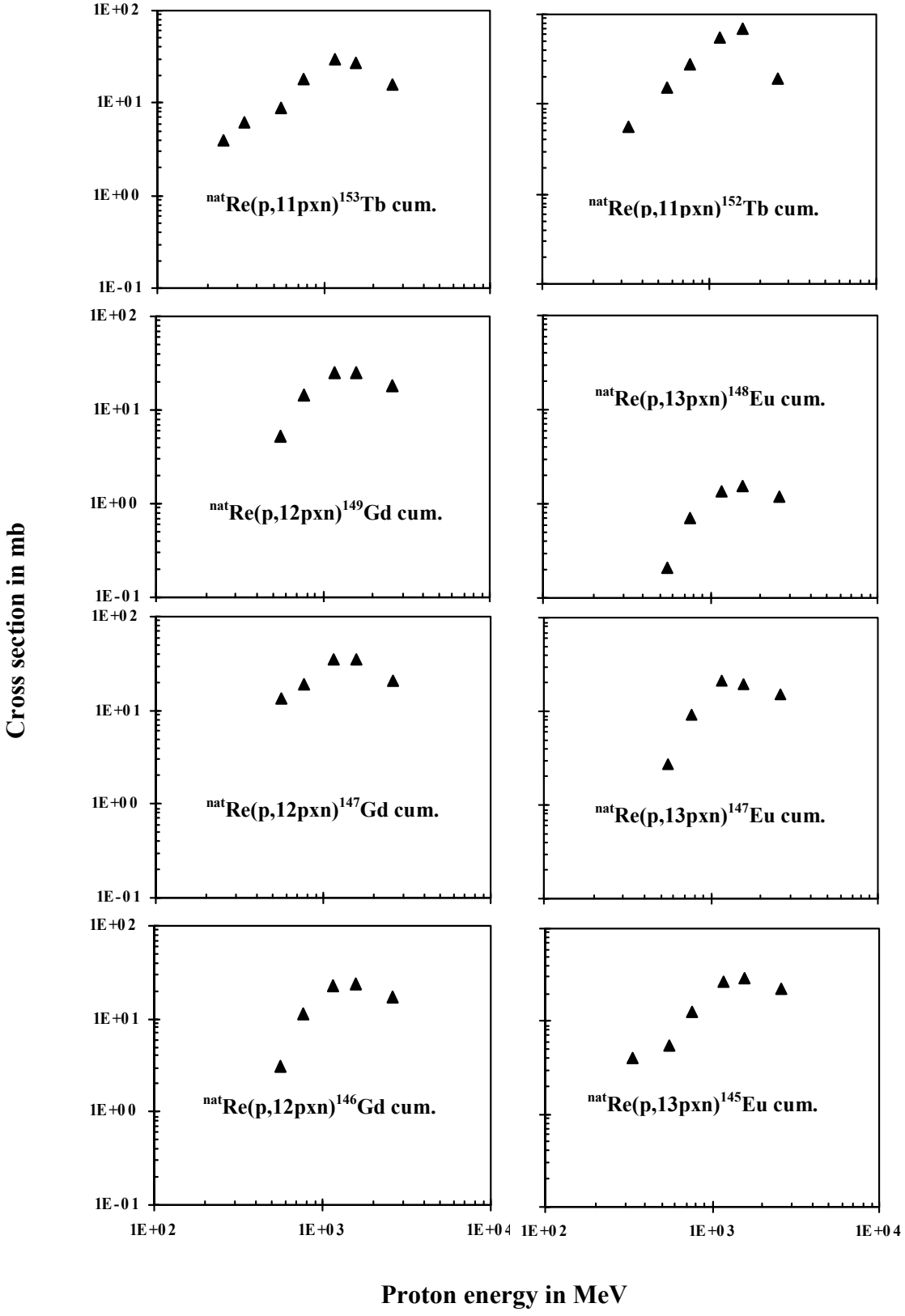

Fig. (4-2): *Continued.*

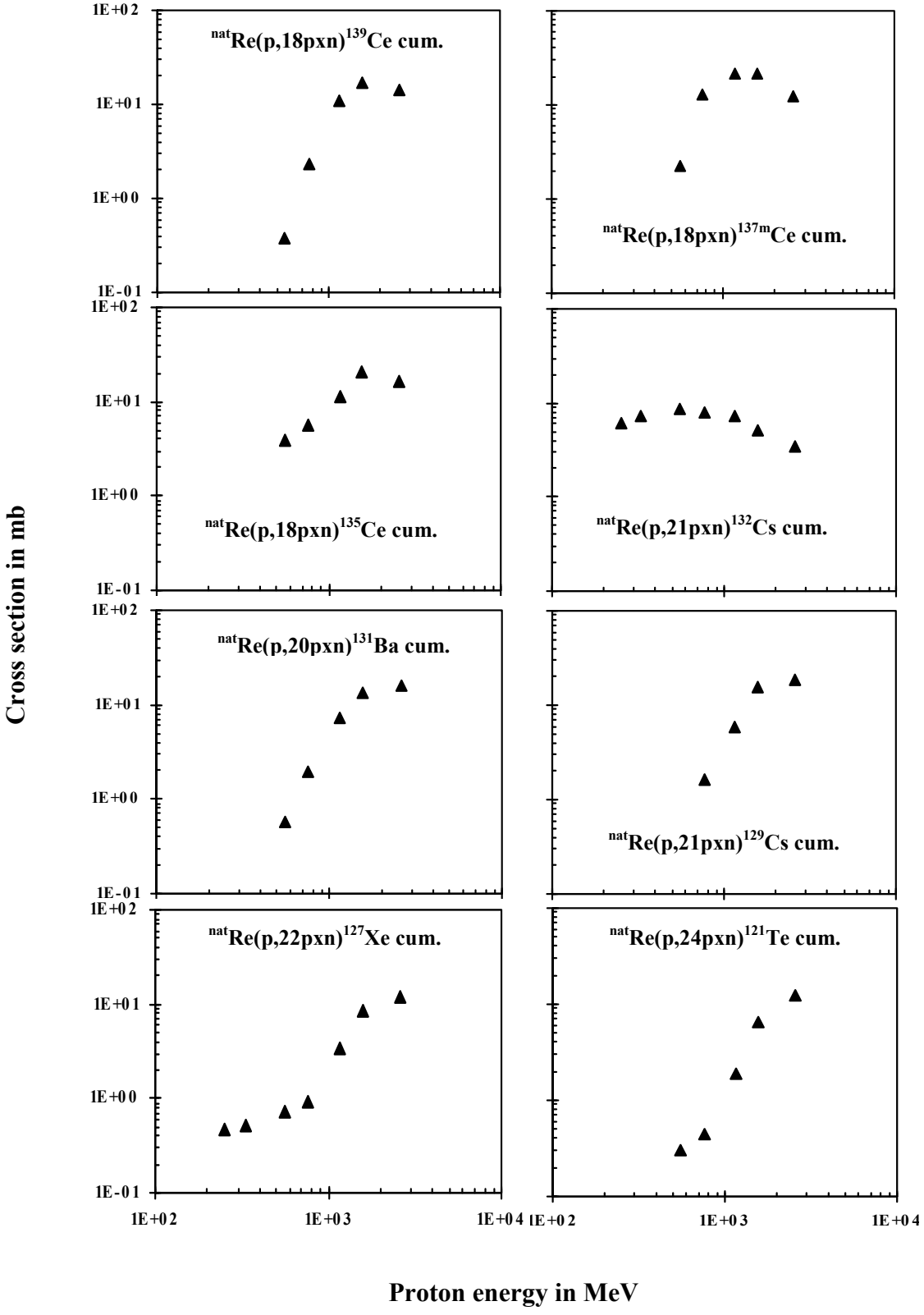

Fig. (4-2): *Continued.*

^{nat}Re(p,20pxn)^{131}Ba, ^{nat}Re(p,21pxn)^{129}Cs, ^{nat}Re(p,22pxn)^{127}Xe and ^{nat}Re(p,24pxn)^{121}Te are drawn in figure (4-2). The cross sections increase with increasing proton energy to a maximum and then go down, except for the last four reactions which increase continuously with increasing proton energy. It is clear also a very good agreement in the frist reactions ^{nat}Re(p,4pxn)^{175}Hf with previous work [31].

Figure (4-3) shows that, the relation between cross section and proton energy for fission products of the nuclear reactions ^{nat}Re(p,f)^{95}Nb, ^{nat}Re(p,f)^{88}Y, ^{nat}Re(p,f)^{87}Y, ^{nat}Re(p,f)^{86}Rb, ^{nat}Re(p,f)^{85}Sr, ^{nat}Re(p,f)^{84}Rb, ^{nat}Re(p,X)^{75}Se, ^{nat}Re(p,X)^{65}Zn, ^{nat}Re(p,X)^{59}Fe, ^{nat}Re(p,X)^{46}Sc and ^{nat}Re(p,X)^{7}Be. The cross section increases with increasing proton energy for all reactions. For the reaction ^{nat}Re(p,f)^{86}Rb the cross section increase with increasing proton energy to a maximum and then the cross section goes down.

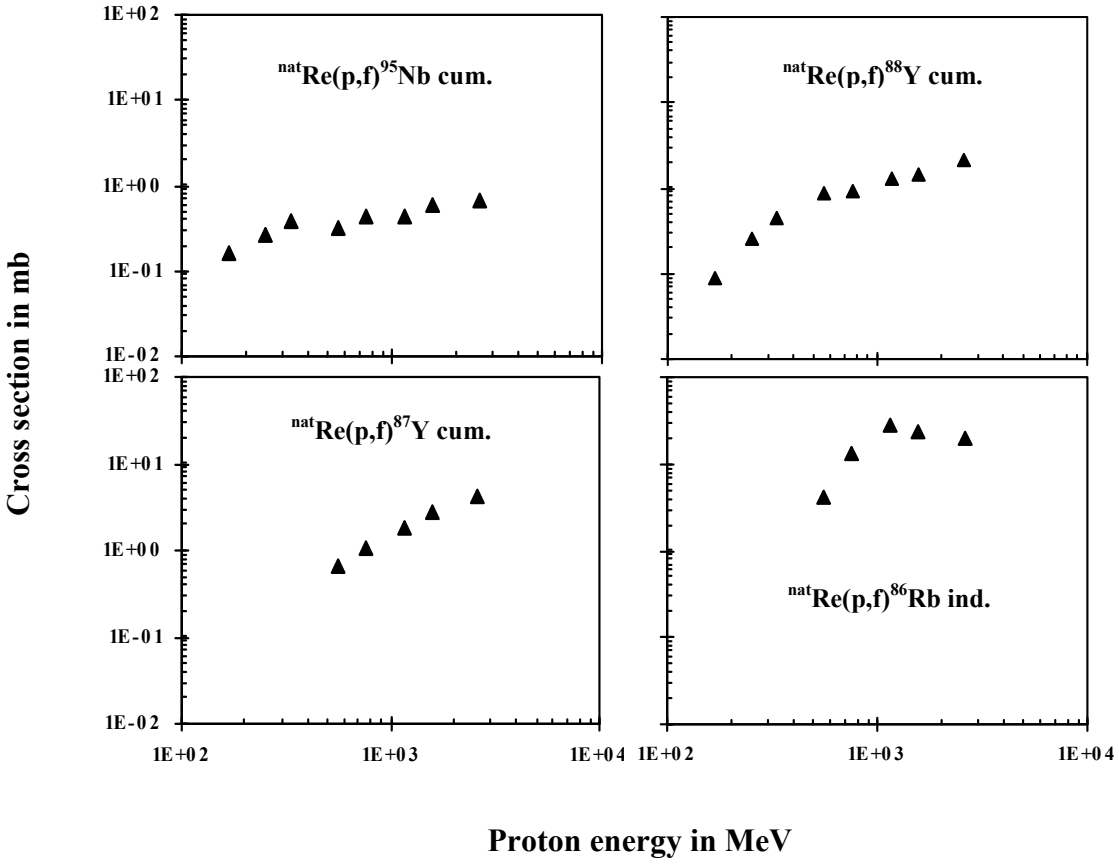

Fig. (4-3): *Cross section as function of proton energy for his work (▲) for fission products. The uncertainties of the experimental data are generally smaller than the symbol sizes.*

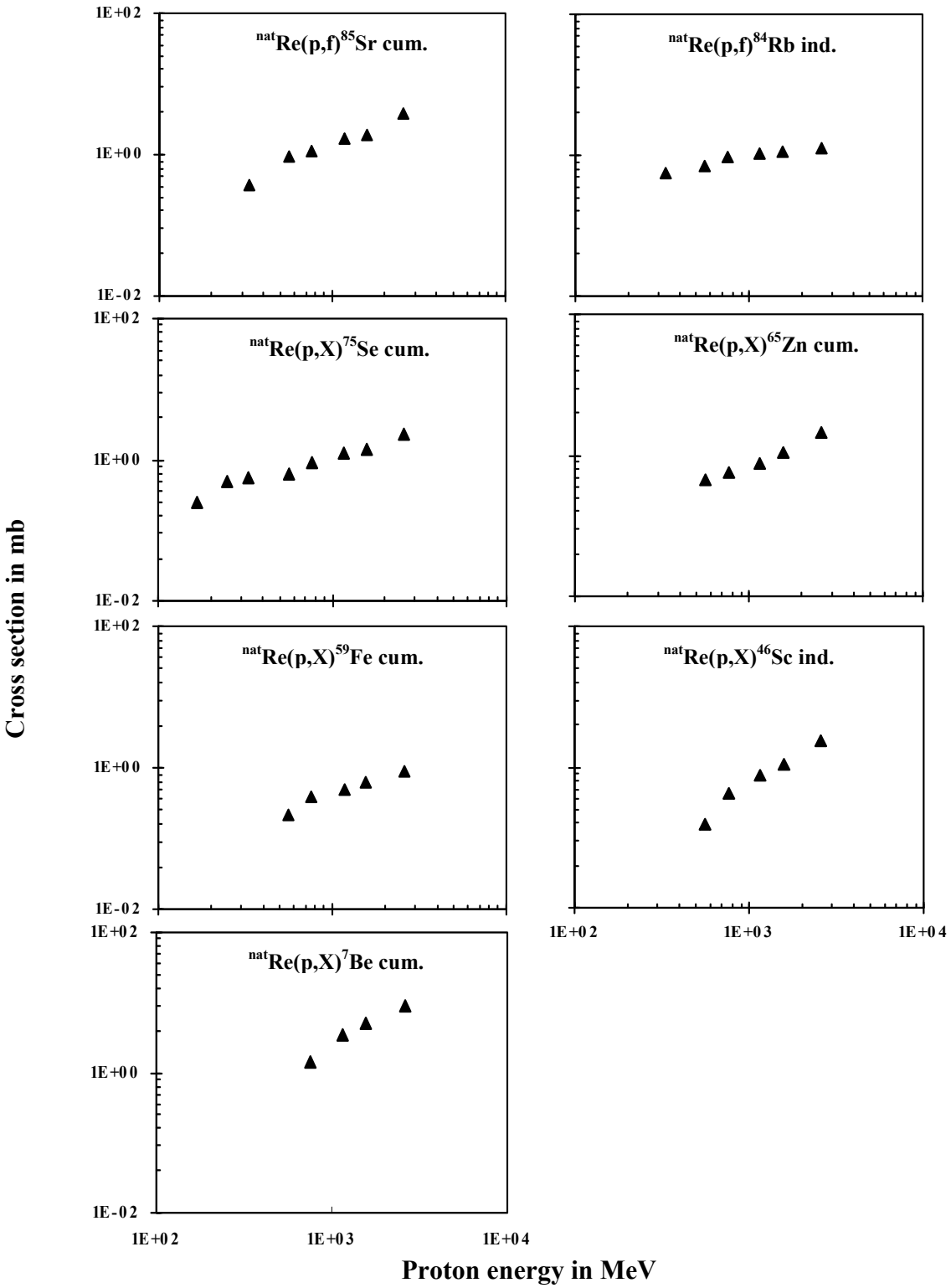

Fig. (4-3): *Continued.*

Figure (4.1) shows there are only very scarce previous data on the production of radioactive residual nuclides from rhenium by proton-induced reactions. The work of Karamian et al. [31] gives results only for a few products such as ^{185}Os, ^{184}Re, ^{183}Re and ^{175}Hf. Except for these data; we do not see any other experimental data from previous work.

The phenomenology of the excitation functions of residual nuclide production by proton-induced reactions from rhenium can be seen, for instance, from the data in figure (4.1) for (p,xn)- and (p,pxn)-reactions. The experimental data show generally a continuous decline from low energies above 80 MeV. They behave in different ways at high energies; namely, (p,pxn)-reactions tend to show more expressed plateaux at higher energies then the pure (p,xn)-reactions. This decline is typical in a way that at low energies the decline is determined by compound nucleus reactions in statistical equilibrium, while at higher energies the pre-equilibrium production forms the respective plateau. In particular for (p,pxn)-reactions, the plateau is due to the effect that these reactions are mainly reactions at the surface of the nucleus leaving away a residual nucleus which just has relatively low excitation energy.

The phenomenology of the excitation functions changes drastically if we go to hafnium (Hf), terbium (Tb) and thulium (Tm) isotopes as displayed in figure (4.2). Here, we have the shapes typically for deep-spallation reactions which increase at relatively high energies above 100 MeV. They show a maximum around a few hundred MeV and then decline to higher energies when the number of exit channels increases.

These transitions of the shapes are going on for the data of figure (4.2) where the terbium (Tb), europium (Eu) and gadolinium (Gd) isotopes are shown. One of observes an increasing shift of the maxima to higher energies and also higher apparent threshold energies of the excitation functions. The decline at higher energies is scarcely to be seen for terbium (Tb) isotope and also is not really seen for the cerium (Ce) isotopes in the continuation of figure (4.2). Moreover, the barium (Ba), xenon (Xe) and tellurium (Te) isotopes only show a continuous increase above a relatively high threshold up to the highest energies investigated. There is exclusively one reaction which does not follow this behaviour. This is ^{nat}Re(p, 21pxn)^{132}Cs which

exhibits still the behaviour of low-energy product and in this way indicates the approach of a fission region.

The fission products are finally really seen in figure (4.3) where niobium (Nb), yttrium (Y) and Rubidium (Rb) isotopes are displayed. These fission products have relatively low thresholds. The data indicate that for ^{95}Nb we are having a threshold well below 100 MeV. The same is true for ^{88}Y. For fission products such as ^{86}Rb we see the same shape of the excitation function as for spallation products. These different shapes depend finally on the type of fission process which produces a fission product.

In principle, the two types of fission possible from heavy elements at medium energies is one that is occurring after a peripheral collision of the incoming protons with the target nucleus leading to a compound nucleus after the fast cascade which has relatively low excitation energy and then undergoes fission. In this way, the neutron excess is preserved; that means that the fission products are neutron-rich product and on the right side of valley of stability.

On the other hand, we have a second process of fission and that is after a relatively long intranuclear cascade in the initial phase of the reaction. Then, a residual nucleus remains which has relatively high proton excess and which undergoes fission. The proton excess is conserved in the fission. Such cases can be seen exemplarily in Fig. 4.3 were we having isotopes from ^{85}Sr down to ^{46}Sc. All these nuclides which are produced by fission after a long initial cascade process show a continuous increase over the entire range of energies investigated.

There is one nucleus in the proton-induced production of residual nuclide from rhenium, namely ^{7}Be, which shows an extraordinary behaviour with respect to the absolute height of the cross section. As was seen also in other reaction of medium-energy protons with heavy elements, ^{7}Be is produced by fragmentation reaction. The yield of ^{7}Be, if one looks for its dependence on the target masses, does not vary very much over the entire periodic system. There is generally an increase of the ^{7}Be production relative to light fission products.

4.1.2 Comparison with TALYS Code:

In this section we present the comparison between our results and the theoretical data calculated by TALYS code. The cross sections are plotted in figure (4-4) against proton energy for target near products of nuclear reactions $^{nat}Re(p,xn)^{185}Os$, $^{nat}Re(p,xn)^{182}Os$, $^{nat}Re(p,xn)^{183}Os$, $^{nat}Re(p,pxn)^{186}Re$, $^{nat}Re(p,pxn)^{184}Re$ and $^{nat}Re(p,pxn)^{183}Re$. It is clear that very good agreement between our results and TALYS code for all reactions at energy range from 78.2 MeV to 169 MeV except for the reaction $^{nat}Re(p,pxn)^{184}Re$ the our results are slightly smaller than the calculated values.

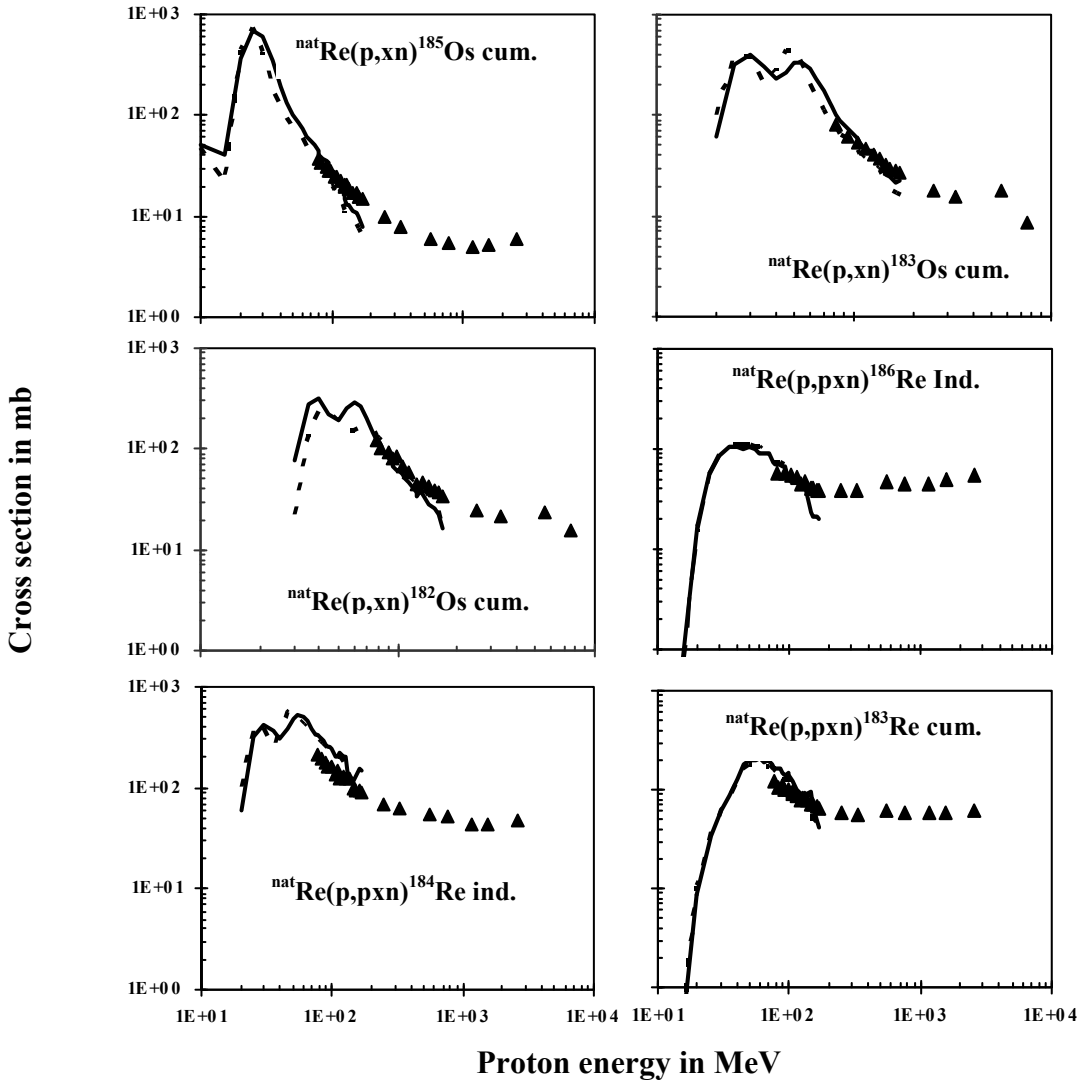

Fig. (4-4): *Cross section as function of proton energy for this work (▲), TALYS 0.72 (·····) and TALYS 1.0 (—) for target near products. The uncertainties of the experimental data are generally smaller than the symbol sizes.*

In figure (4-4) we can see that there are no experimental results to compare with TALYS code below 78.2 MeV because natural rhenium samples irradiated form 78.2 MeV. Also there are no calculated data above 169 MeV to compare with the experimental results due to the TALYS code calculate the cross section for proton energy only up 200 MeV.

The TALYS excitation functions are compared with experimental results in figure (4-5) for target near products of nuclear reaction $^{nat}Re(p,pxn)^{182}Re$ and $^{nat}Re(p,pxn)^{181}Re$. For reaction $^{nat}Re(p,pxn)^{181}Re$ the calculated excitation function is good agreement with our results at 81.9 MeV and it looks slightly higher than the experimental excitation function at 93.4 MeV and 105 MeV. In general the experimental results are smaller than the calculated values from 81.9 MeV to 2590 MeV for reaction $^{nat}Re(p,pxn)^{182}Re$ and from 115 MeV to 2590 MeV for reaction $^{nat}Re(p,pxn)^{181}Re$.

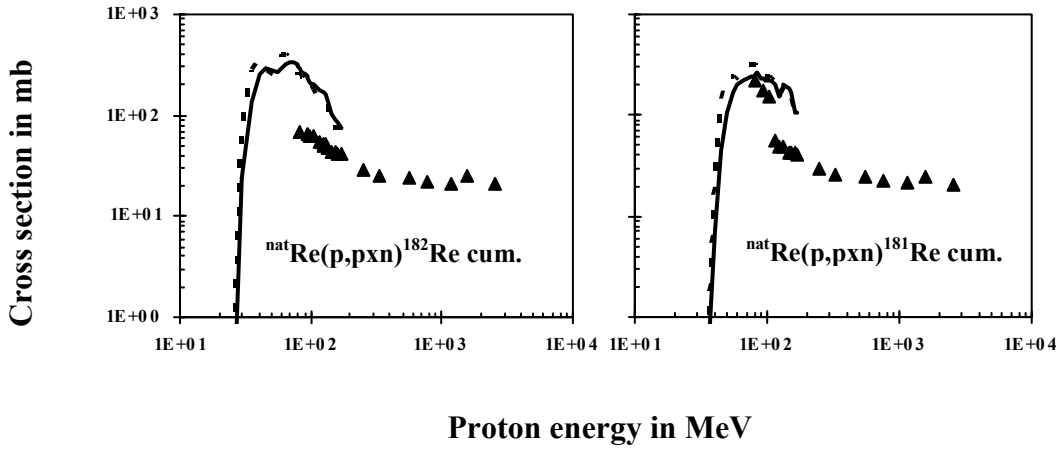

Fig. (4-5): *Cross section as function of proton energy for this work (▲), TALYS 0.72 (·····) and TALYS 1.0 (—) for spallatin products. The uncertainties of the experimental data are generally smaller than the symbol sizes.*

Figure (4-6) show that, the relation between cross section and proton energy for spallation products of nuclear reactions $^{nat}Re(p,4pxn)^{175}Hf$, $^{nat}Re(p,4pxn)^{173}Hf$, $^{nat}Re(p,5pxn)^{171}Lu$, $^{nat}Re(p,5pxn)^{170}Lu$, $^{nat}Re(p,5pxn)^{169}Lu$, $^{nat}Re(p,6pxn)^{169}Yb$ and $^{nat}Re(p,7pxn)^{166}Tm$. A good agreement between calculated values and experimental results for reaction $^{nat}Re(p,4pxn)^{175}Hf$, while at 125MeV and 134 Mev there is very

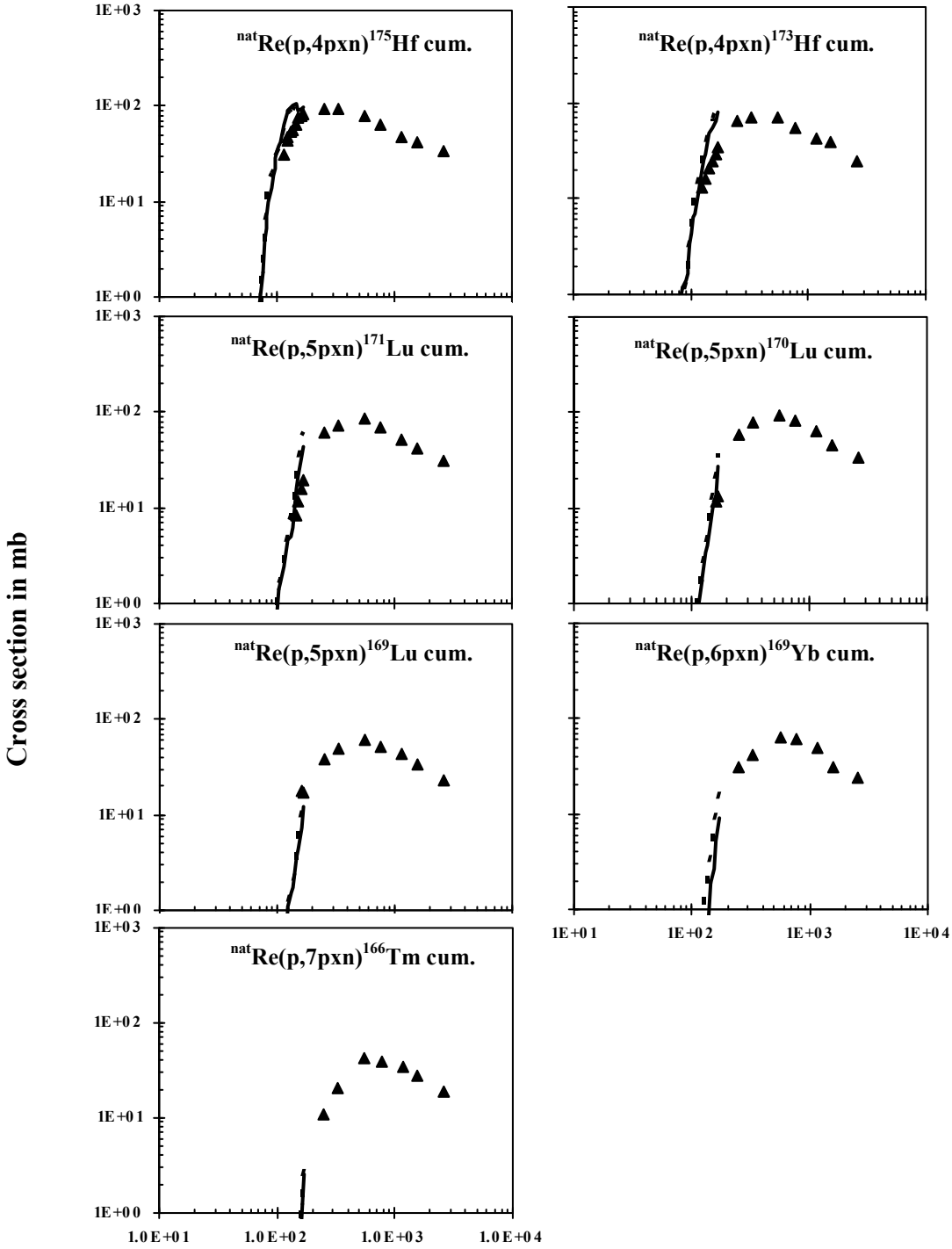

Fig. (4-6): *Cross section as function of proton energy for this work (▲), TALYS 0.72 (·····) and TALYS 1.0 (—) for spallatin products. The uncertainties of the experimental data are generally smaller than the symbol sizes.*

good agreement for reaction $^{nat}Re(p,4pxn)^{173}Hf$ and then the TALYS excitation function slightly higher than the experimental excitation function. For reactions $^{nat}Re(p,5pxn)^{171}Lu$, $^{nat}Re(p,5pxn)^{170}Lu$ very good agreement between the calculated

and experimental results. There are no results to compare in the last three reactions in previous figure due to the same reason which explained above.

Next we make a comparison between the experimental data for rhenium and the results of calculation performed by the TALYS code. Actually, there are two types of theoretical data plotted in the figurers, one from the original TALYS [] version and one from the later version of the TALYS code. The TALYS calculations start at 10 MeV, far below the energy range investigated experimentally in this thesis allow completing the excitation functions to lower energies.

On the other hand, they allow seeing at least for the energies between 80 MeV and 200 MeV how well this model is capable of modelling the production of residual nuclide. We see in figure (4.4) the (p,xn) and (p,pxn) reactions, where the calculations show us the low-energy parts of the excitation functions which are not investigated experimentally in this thesis. The low-energy parts are very much dominating the excitation functions. On the other hand, we see that the transition to the range of energies investigated in this thesis shows generally smooth transitions. The deviations between the experimental and the theoretical data at higher energies are due to the fact that one is approaching the limits of the applicability of the TALYS code. These deviations should be not a cause to judge negatively about the performance of the TALYS code which is working quite well below 200 MeV.

There are, however, a few reactions given in figure (4.5), i.e. the production of ^{182}Re and ^{181}Re from rhenium, where the TALYS calculations evidently overestimate the experimental data. It appears that here further improvement of the theoretical calculations are needed.

For the spallation products starting with the hafnium isotopes in figure (4.6), the TALYS calculations can only describe the increases from threshold up to 200 MeV. As this figure shows, TALYS is performing very well for these (p,4pxn)- to (p,7pxn)-reactions. However, we are again at the limit of Talys calculations for the higher energies and for those nuclides which are further a way from the target nucleus. We have two relay on other model calculations to describe the excitation functions at higher energies. Such a model is INCL4+ABLA which provides the necessary theoretical framework.

4.1.3 Comparison with INCL4+ABLA:

A comparison of the experimental data with the results of the model calculation for INCL4+ABLA and Bertini/Dresner will be discussed in this section. The excitation functions for target near products are plotted in figure (4-7). It is clear that, the cross section decreases with increasing proton energy. The reaction $^{nat}Re(p,xn)^{185}Os$

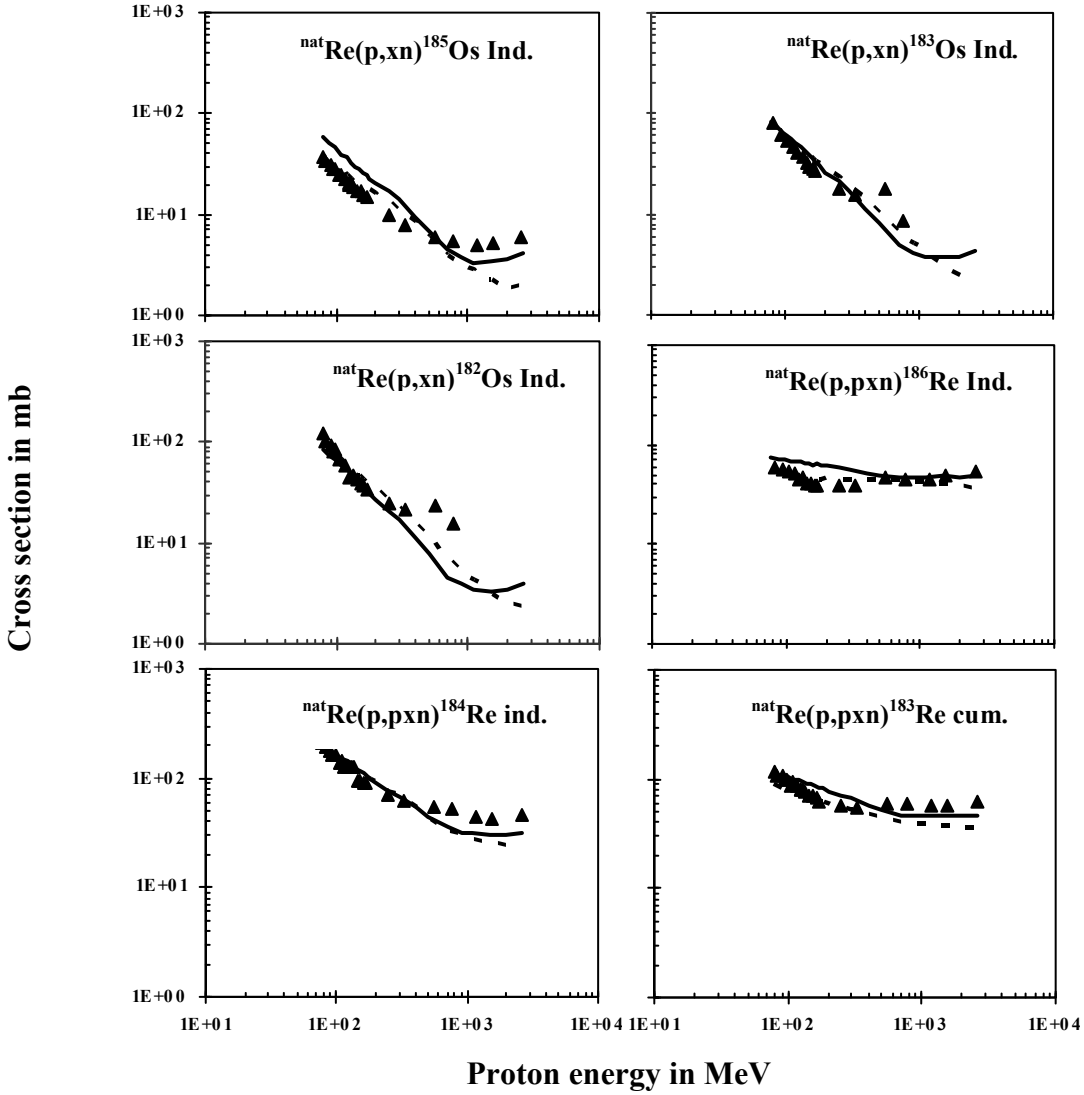

Fig. (4-7): *Cross section as function of proton energy for this work (▲), Bertini/Dresner (····) and INCL4+ABLA (—) for target near products. The uncertainties of the experimental data are generally smaller than the symbol sizes.*

shows very good agreement between experimental data and theoretical results at 558 MeV. The INCL4+ABLA and Bertini/Dresner results below 558 MeV slightly smaller than experimental data and above 558 MeV the INCL4+ABLA results are

higher than our work. From 78.2 MeV to 162 MeV very good agreement between experimental excitation function and Bertini/Dresner excitation function and then the calculated results slightly higher than our results up to 558 MeV.

The comparison between experimental cross section and calculated codes, INCL4+ABLA and Bertini/Dresner, for nuclear reactions $^{nat}Re(p,xn)^{182}Os$, $^{nat}Re(p,xn)^{183}Os$ and $^{nat}Re(p,xn)^{184}Re$ observed very good agreement up to 331 MeV and then our results little bit higher than the calculated data.

For nuclear reaction $^{nat}Re(p,pxn)^{186}Re$ the Bertini/Dresner calculations are in very good agreement with our measurements. The INCL4+ABLA excitation function is in quite good with the measured excitation function up to 331 MeV and then very good agreement at 558 MeV, 763 MeV, 1165 MeV, 1570 MeV and 2590 MeV. Very good agreement between calculated results and our experimental date for reaction $^{nat}Re(p,pxn)^{183}Re$.

Figure (4-8) gives the comparison between the experimental cross section as function in proton energy and theoretical results for reactions $^{nat}Re(p,pxn)^{182}Re$ and $^{nat}Re(p,pxn)^{181}Re$. It is clear that, the calculated cross sections, INCL4+ABLA and

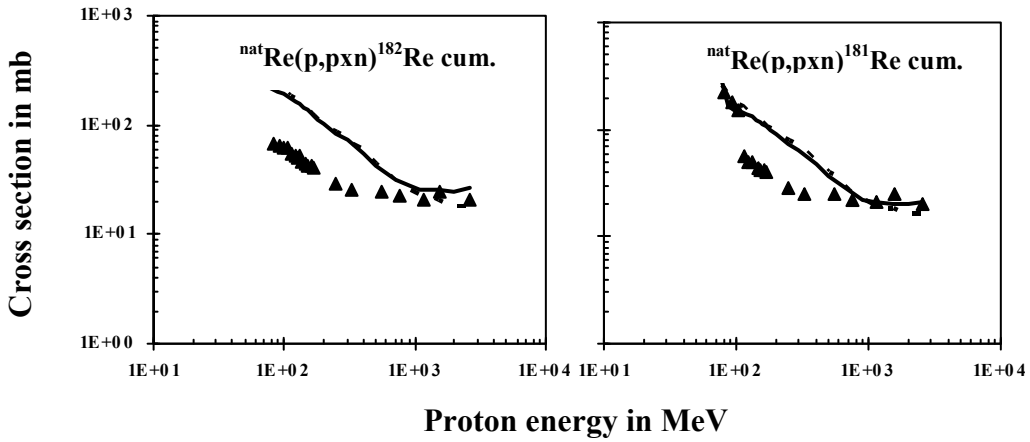

Fig. (4-8): *Cross section as function of proton energy for this work (▲), Bertini/Dresner (····) and INCL4+ABLA (—) for target near products. The uncertainties of the experimental data are generally smaller than the symbol sizes.*

Bertini/Dresner, are higher than the measured data and then tend to quite good for the lift reaction. For the ^{181}Re product the measured excitation function is in very good agreement with INCL4+ABLA and Bertini/Dresner codes except proton energy range

from 115 Mev to 331 MeV the experimental cross sections are smaller than the calculated cross sections.

Excellent agreement between experimental results and calculated data, INCL4+ABLA and Bertini/Dresner, is observed in figure (4-9a) for the nuclear reactions $^{nat}Re(p,4pxn)^{175}Hf$, $^{nat}Re(p,4pxn)^{173}Hf$, $^{nat}Re(p,5pxn)^{171}Lu$ and $^{nat}Re(p,5pxn)^{170}Lu$, and good agreement for nuclear reaction $^{nat}Re(p,5pxn)^{169}Lu$ and $^{nat}Re(p,6pxn)^{169}Yb$.

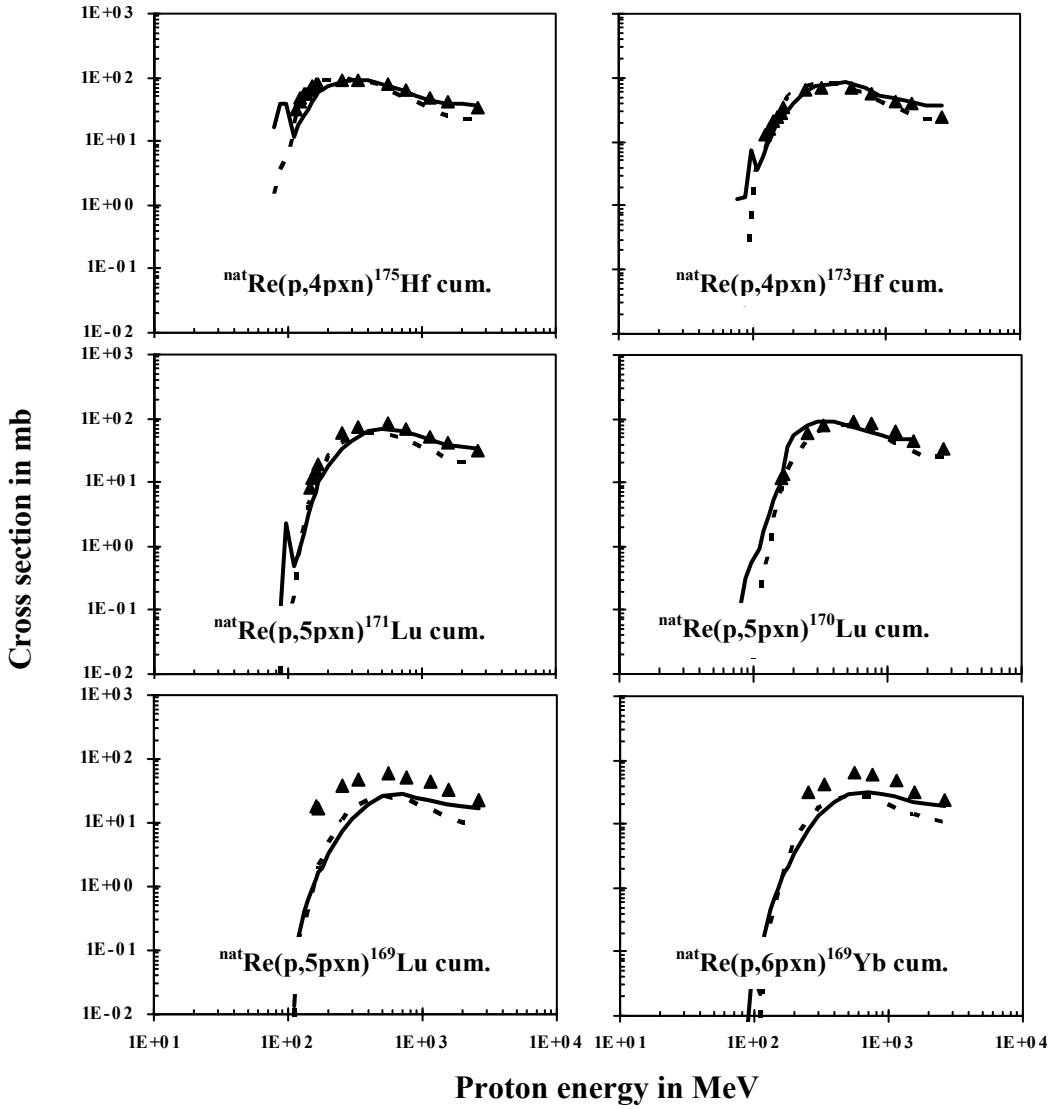

Fig. (4-9a): *Cross section as function of proton energy for this work (▲), Bertini/Dresner (····) and INCL4+ABLA (—) for target-near products. The uncertainties of the experimental data are generally smaller than the symbol sizes.*

In figure (4-9b) one can see that, the experimental results are higher than calculated results for reaction $^{nat}Re(p,11pxn)^{156}Tb$ and good agreement for reaction $^{nat}Re(p,12pxn)^{149}Gd$, $^{nat}Re(p,12pxn)^{146}Gd$, $^{nat}Re(p,13pxn)^{148}Eu$ and $^{nat}Re(p,13pxn)^{147}Eu$.

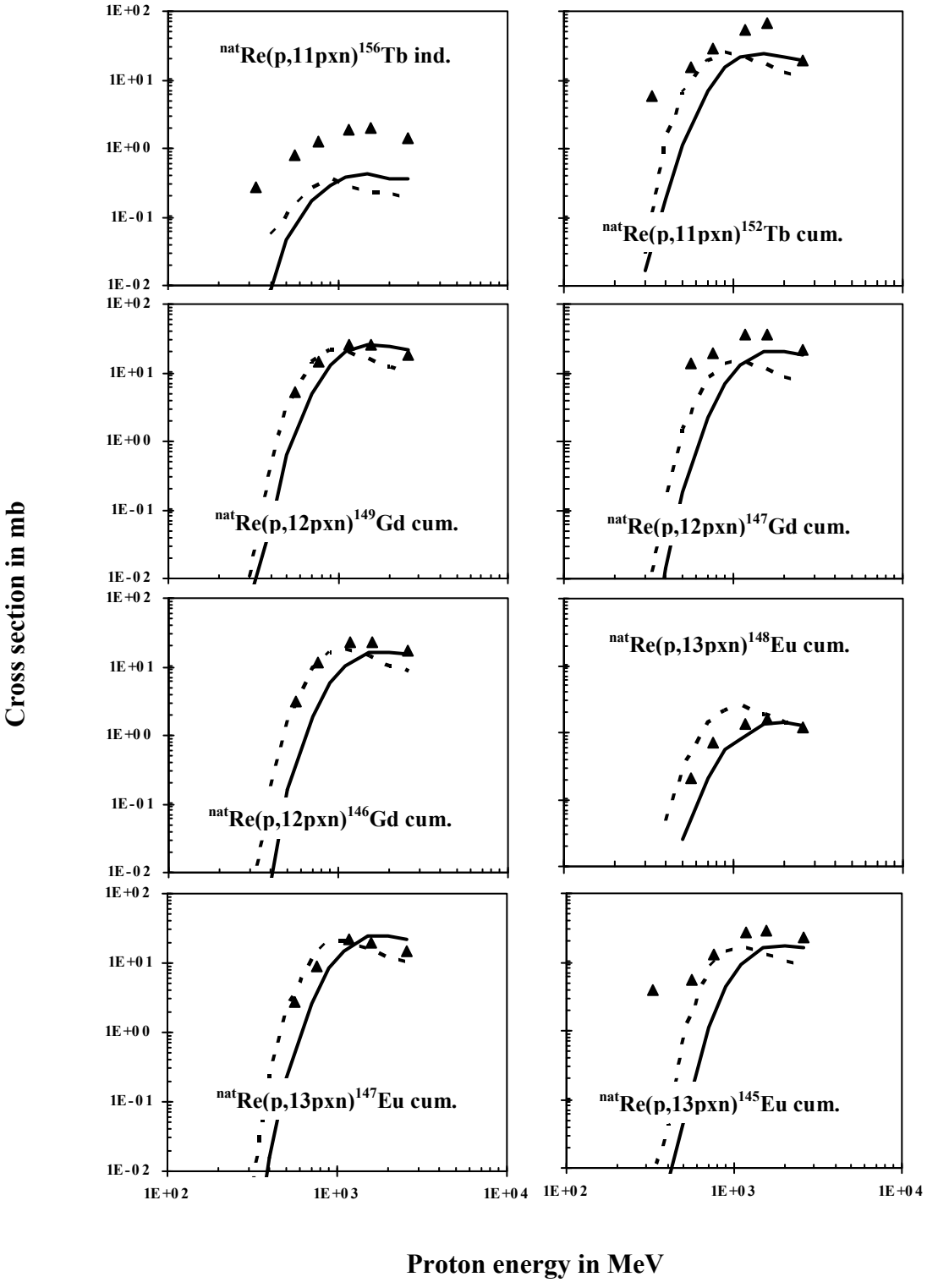

Fig. (4-9b): *Continued.*

From Figure (4-9b) it is evident that, the experimental excitation functions are higher than calculated excitation functions for reactions ^{nat}Re(p,11pxn)^{152}Tb and ^{nat}Re(p,12pxn)^{147}Gd except at proton energy 2590 MeV. For reaction ^{nat}Re(p,13pxn)^{145}Eu it easy to observe that, good agreement at proton energies 558 MeV and 763 MeV and.

Quite good agreement between measured results and Bertini/Dresner calculated results for all nuclear reactions in figure (4-9c) except for reaction ^{nat}Re(p,22pxn)^{127}Xe the calculated data is smaller than our results. For reactions ^{nat}Re(p,18pxn)^{135}Ce, ^{nat}Re(p,21pxn)^{129}Cs and ^{nat}Re(p,24pxn)^{121}Te the INCL4+ABLA results are smaller than our results.

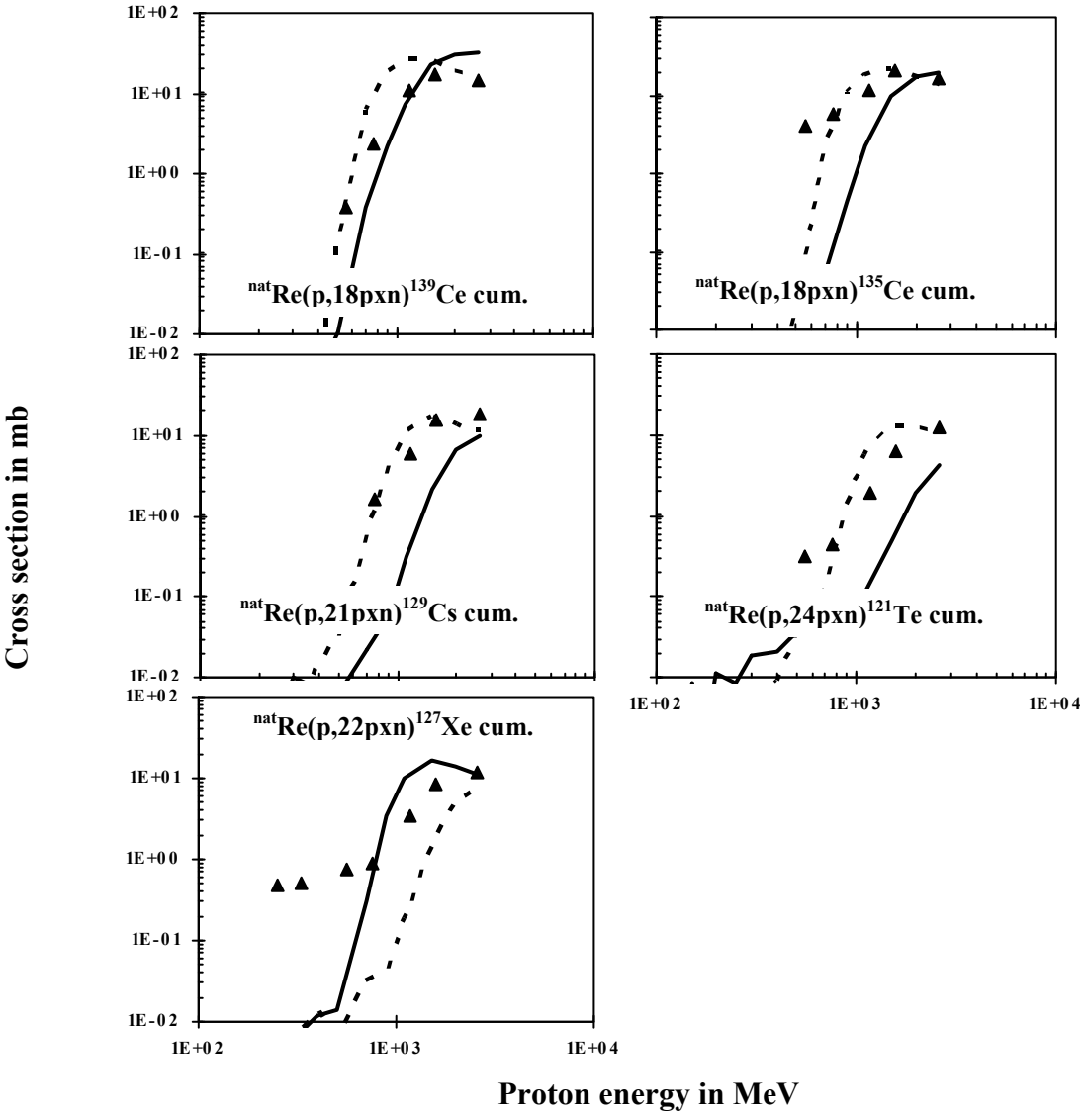

Fig. (4-9c): *Continued.*

It is clear that from figure (4-10), the Experimental excitation functions are generally higher than INCL4+ABLA and Bertini/Dresner excitation functions for all nuclear reactions

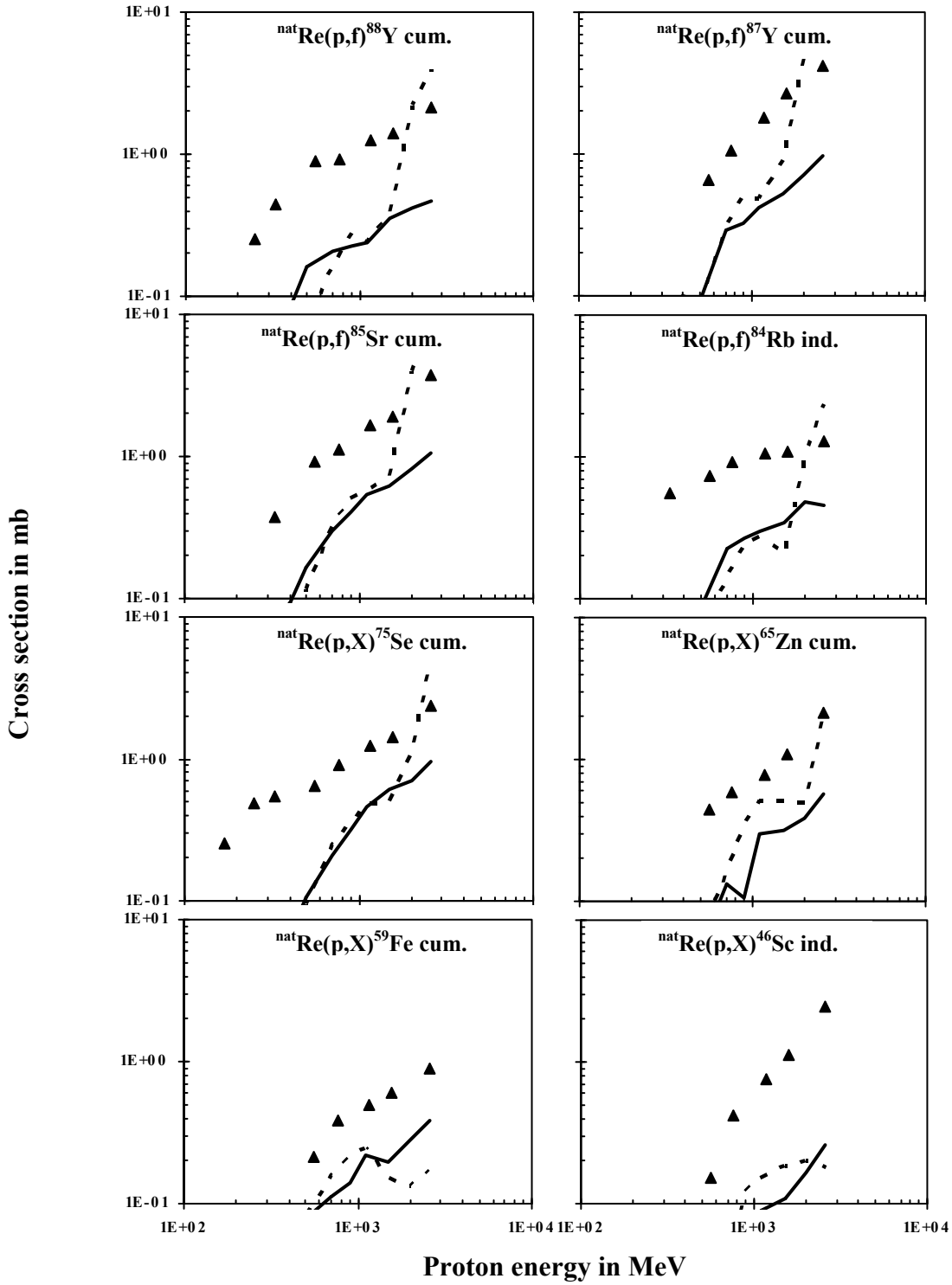

Fig. (4-10): *Cross section as function of proton energy for this work (▲), Bertini/Dresner (····) and INCL4+ABLA (—) for fission products. The uncertainties of the experimental data are generally smaller than the symbol sizes.*

In section 4.1.3 we have plotted two different theoretical model calculations and compared them with experimental data. The doted lines describe so called Bertini/Dresner model calculations, while the solid lines describe INCL4+ABLA calculations.

For the (p,nx) and (p,pxn) reactions in figure (4.7) both models behave reasonably well. There are just slight different between them as for instance seen for the production of ^{185}Os above 1 GeV. The Bertini/Dresner calculations strongly underestimate the experimental data, while INCL4+ABLA data follow at least the shape of the excitation functions at higher energy so that the absolute values are slightly underestimated. Certain problems occur still for the (p,pxn) reactions, as e.g. for ^{182}Re and ^{181}Re in figure (4.8), where in both cases the theory overestimates the low-energy production considerably. The behaviour of the model calculations tends to be more promising if we go to the spallation products, figures (4.9a), (4.9b) and (4.9c).

In general, both versions of the intranuclear cascade modelling of residual nuclide production at medium energies describe the experimental data reasonably well. The discontinuity seen in the theoretical data of the INCL4+ABLA calculations at slightly above 100 MeV are numerical artefact of the calculations are due to extension of these models below energies where they appear to be namely below 200 MeV.

There remain still a few nuclides which are not very well described as can be seen in figure (4.9b). There, the production of radionuclide between ^{156}Tb and ^{145}Eu is shown, two nuclides which are produced by deep spallation. Here we see that, in particular the independent production of ^{156}Tb is grossly underestimated. The same is true to some degree for ^{152}Tb.

Generally, the absolute heights of the excitation functions and the shapes of the excitation functions are reasonably well reproduced by theory. It appears, however, that the emission of protons and neutrons in the de-excitation process is not well balanced here. This observation is also continued in figure (4.9c), where we see occasionally relatively good shapes for the INCL4+ABLA calculations and a not as good behaviour of Bertini/Dresner calculations, where a general shift to higher

energies is observed: This can only be explained by a lack of balance in the neutron and proton emission calculations. The performance of the high-energy codes changes dramatically if one goes into the fission area. In figure (4.10) fission products from ^{88}Y down to ^{46}Sc are shown and here the performance of both theories, Bertini/Dresner and INCL4+ABLA, is dramatically worse. We have underestimates of up to nearly one order of magnitude for the different isotopes and we see that Bertini/Dresner and INCL4+ABLA show different behaviour, in particular, for the yttrium (Y), scandium (Sc), rubidium (Rb) and selenium (Se) isotopes in a way that Bertini/Dresner predicts a much higher production at higher energies than INCL4+ABLA.

At higher energies, the Bertini/Dresner calculations describe the absolute quantity of the experimental data in most cases. The shape of the Bertini/Dresner calculations is in contrast with the observed shape of the excitation functions. The INCL4+ABLA calculations reproduce quite well the general shapes of excitation functions, but in generally, strongly underestimate them.

4.1.4 Phenomenology of Residual Nuclides Production by Proton-induced reaction on Rhenium:

Important differences between medium energy reactions on medium and heavy mass target elements can be seen in detail when looking for the dependence of cross sections on mass differences between target and product nuclides for different energies. For eight energies 162 MeV, 251 MeV, 331 MeV, 558 MeV, 763 MeV, 1115 MeV, 1570 MeV and 2590 MeV for example are plotted in figure (4-11) the measured cross sections against product masses. Since we did not measure the production of stable nuclides and since we did not sum up cross sections measured for isobaric products, these plots just give an impression of the isobaric yields. However, results of the cross sections give good approximations of the mass yield curves because the cumulative cross sections of nuclides close to the valley of stability sum up a lot of the total production. For figure (4-11) one recognizes the typical patterns of spallation reactions. The mass yields decrease exponentially with increasing mass differences, the slopes of the half-logarithmic linear envelopes becoming smaller with increasing proton energies. The fragmentation product ^{7}Be falls out of the spallation

systematics. The measured cross sections indicate that the mass yield curve rises again at small product masses due to the influence of fragmentation. For ^{7}Be also an alternative production mode, namely evaporation as well as preequilibrium emission have also been discussed [98. 99].

With the rising interest in accelerator-driven technologies intermediate-energy nuclear reactions with heavy target elements were systematically investigated and a new feature of spallation reactions was observed. The intermediate residuals at the end of intra-nuclear cascade could deexcite in addition to evaporation of nucleons and light complex particles via fission. Already at about 200 MeV the fission channel is open. This plot also allows a crude estimate of the isobaric yields of products which would be the upper envelope of the experimental data. One can clearly distinguish two major reaction modes. The products at about half the target mass are clearly attributable to fission processes. Fission products show up as peaks in the mass distributions which become higher and broader with increasing proton energy. The radionuclides observed in the vicinity of the target are produced by reactions involving a compound nucleus in statistical equilibrium, by pre-equilibrium reactions and by spallation processes. From 558 MeV, deep spallation, muli-fragmentation and β^{+}-, EC-, and α-decay of neutron poor precursors become increasingly more important. As a consequence the two product mass regions merge, fission becoming less important and deep spallation filling the gape in product masses. Moreover, there is a significant increase of cross section for nuclides with low masses, probably due to multi-fragmentation as a production process.

For describing the phenomenology of the mass distribution of products from rhenium in figure (4.11) we present them for energies between 162 and 2590 MeV. It appears that these mass distributions are considerably changing from lower energies to higher energies. At a low energy of 162 MeV, we just observed products close to the target nuclei. Already at 251 MeV, the first fission product show up at about half the mass of the target nuclei and also some deep spallation products above mass 100 are seen. At 331 MeV, and more pronounced at 558 MeV, we have a clear distinction between the fission products at about half the mass of the target nuclei and also more spallation products. The shapes of the mass distribution for the spallation products can be approximated by an exponential decrease of the cross sections.

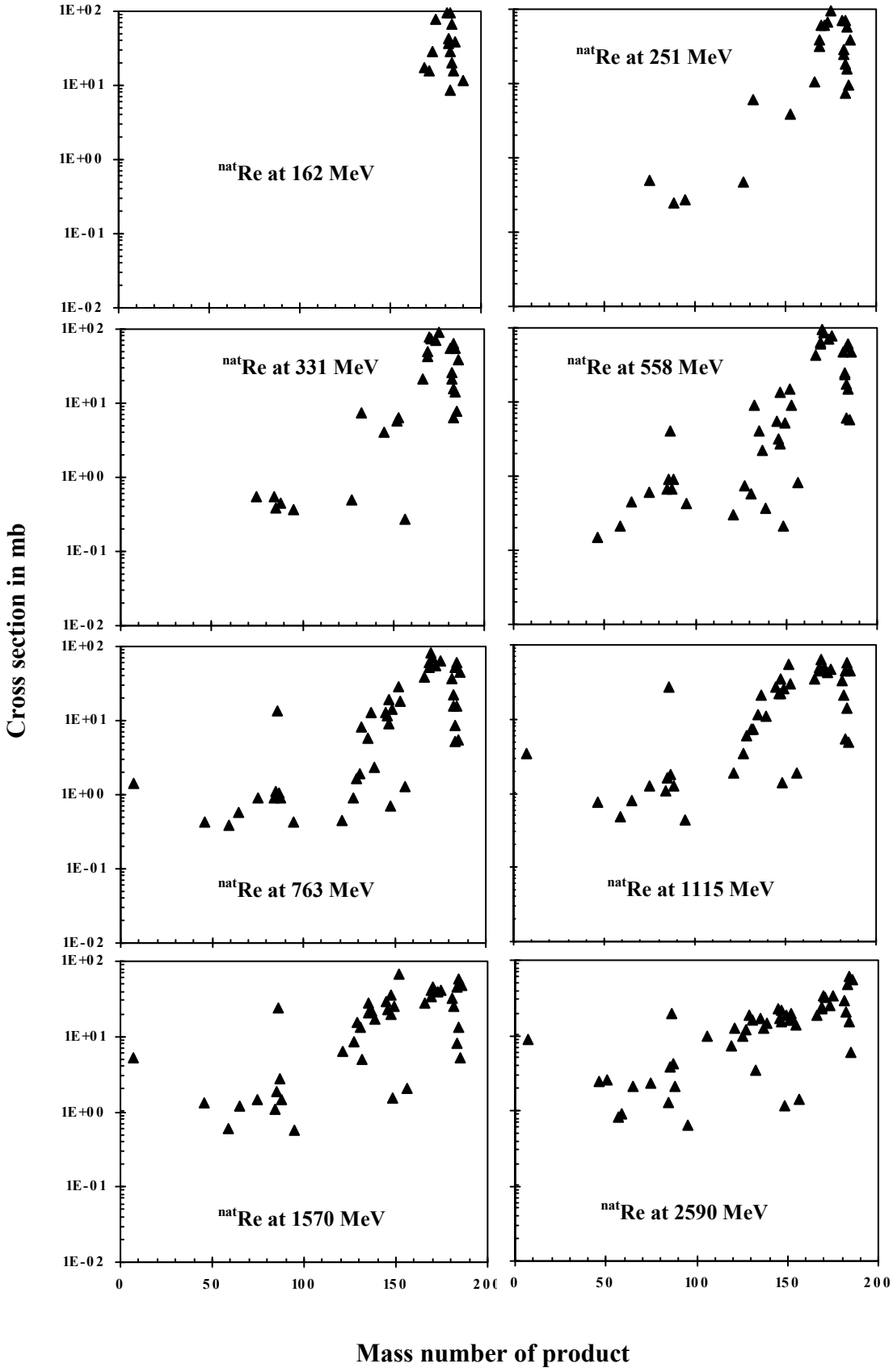

Fig. (4-11): *Cross sections for the production of residual nuclides from rhenium as function of the product mass numbers.*

The fission products show a broad maximum and demonstrate fission as a dominant production mode of residual nuclide from rhenium. Starting with several 63 MeV and pertaining up to 2590 MeV we observe increased cross section for the production of ^{7}Be pointing to the fact that the production of light complex particles such as ^{7}Be does neither fit into spallation systematic nor into the fission systematic of the production of residual nuclide.

4.2 CROSS SECTIONS FOR URANIUM:

We present here final cross sections for proton-induced reactions on natural uranium which are independent (ind.) or cumulative (cum.). We determined a total of about 1894 cross sections for the independent production of ^{232}Pa, ^{230}Pa, ^{136}Cs, ^{124}Sb, ^{122}Sb, ^{110m}Ag, ^{96}Tc, ^{86}Rb, ^{84}Rb, ^{74}As, ^{54}Mn, ^{127}Sb, ^{120m}Sb, ^{106m}Ag, and ^{58}Co and cumulative production of ^{237}U, ^{233}Pa, ^{127}Xe, ^{121}Te, ^{113}Sn, ^{111}In, ^{106}Ag, ^{97}Ru, ^{89}Zr, ^{88}Y, ^{87}Y, ^{83}Rb, ^{85}Zn, ^{52}Mn, ^{51}Cr, ^{102}Rh, ^{141}Ce, ^{140}Ba, ^{139}Ce, ^{137}Cs, ^{132}Te, ^{131}I, ^{126}Sb, ^{125}Sn, ^{115}Cd, ^{111}Ag, ^{103}Ru, ^{99}Mo, ^{95}Zr, ^{91}Y, ^{22}Na, ^{115m}Cd, ^{95m}Tc, ^{95m}Nb, ^{95}Nb, ^{60}Co, and ^{48}V from natural uranium for 4 individual energies between 211 MeV and 2530 MeV ± 2.

4.2.1 Comparison: Uranium Results with Previous Work:

The experimental cross sections of the nuclear reactions ^{nat}U(p, pxn)^{237}U, ^{nat}U(p, 2pxn)^{233}Pa , ^{nat}U(p, 2pxn)^{232}Pa and ^{nat}U(p, 2pxn)^{230}Pa are presented in graphical form in figure (4-12) in comparison with the previous results Titarenko et al. [100], Blanchard et al. [101]. Comparing the experimental excitation functions with the excitation functions of the previous work calculation, it was found that, all cross sections measured in this study are very good agreement with previous work.

The measured excitation functions of the nuclear reactions ^{nat}U (p,f)^{127}Xe, ^{nat}U(p,f)^{121}Te, ^{nat}U(p,f)^{113}Sn, ^{nat}U(p,f)^{111}In, ^{nat}U(p,f)^{105}Ag, ^{nat}U(p,f)^{97}Ru, ^{nat}U(p,f)^{89}Zr, ^{nat}U(p,f)^{88}Y, ^{nat}U(p,f)^{87}Y, ^{nat}U(p,f)^{83}Rb, ^{nat}U(p,f)^{65}Zn and ^{nat}U(p,f)^{52}Mn are plotted in figure (4-13). The experimental cross sections for neutron poor products are also compared with previous work Titarenko et al. [100], Blanchard et al. [101] and Friedlander et al. [102] in figure (4-13). Very good agreement at 211 MeV and quite good agreement for reaction ^{nat}U (p, f)^{127}Xe. For reaction ^{nat}U(p, f)^{113}Sn we notice that, a good agreement between our results and Titarenko [100]. It is clear that,

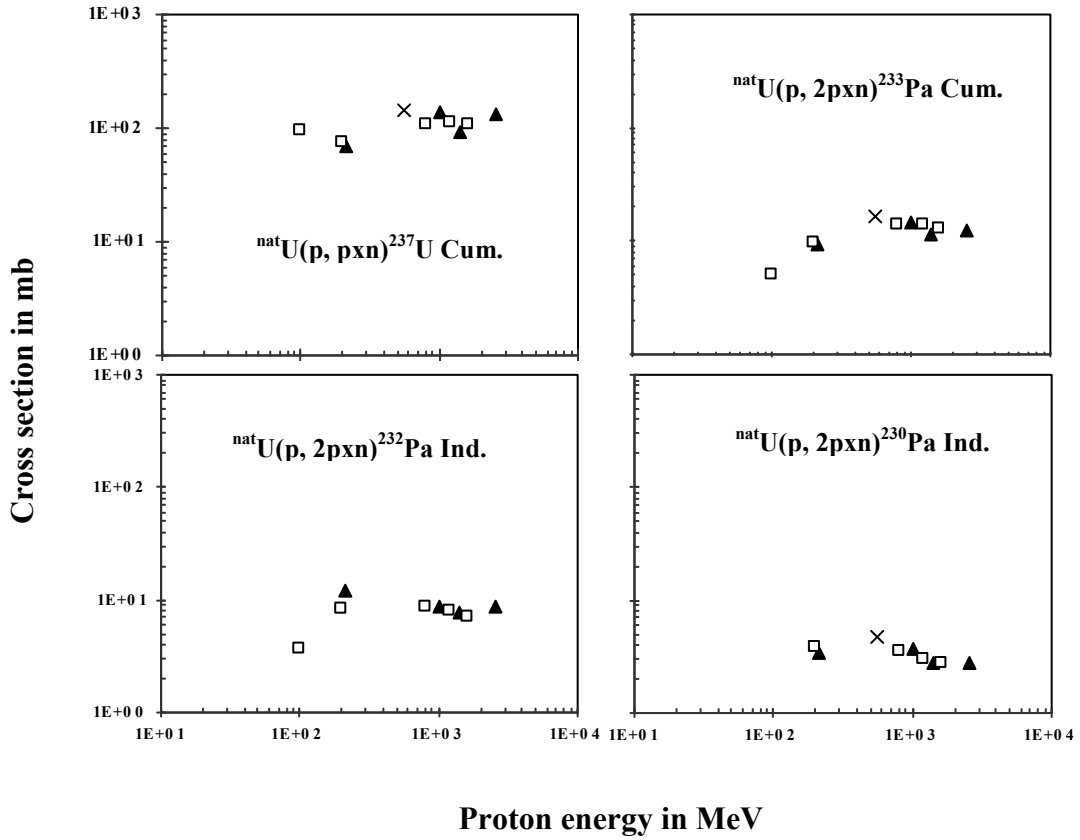

Fig. (4-12): *Cross section as function of proton energy for this work (▲), Titarenko et al. (□) [100] and Blanchard et al. (×) [101] for target near products. The uncertainties of the experimental data are generally smaller than the symbol sizes.*

the experimental excitation function and previous work for reactions $^{nat}U(p, f)^{105}Ag$, $^{nat}U(p, f)^{89}Zr$, $^{nat}U(p, f)^{88}Y$, $^{nat}U(p, f)^{87}Y$, $^{nat}U(p, f)^{83}Rb$ and $^{nat}U(p, f)^{65}Zn$ has the same behaviour except at 1400 MeV the measured cross sections are little bit smaller than the previous work. For reaction $^{nat}U(p, f)^{121}Te$ the previous results are higher than our results, and little bit agreement for reaction $^{nat}U(p, f)^{111}In$ except at 1000 MeV. At 1000 MeV, 1400 and 2530 MeV there are no previous results to compare with our results for reactions $^{nat}U(p, f)^{97}Ru$ and $^{nat}U(p, f)^{52}Mn$.

Figure (4-14) show that, the cross section as function of proton energy of nuclear reactions $^{nat}U(p,f)^{136}Cs$, $^{nat}U(p,f)^{124}Sb$,$^{nat}U(p,f)^{122}Sb$, $^{nat}U(p,f)^{110m}Ag$, $^{nat}U(p,f)^{106m}Ag$, $^{nat}U(p,f)^{102}Rh$, $^{nat}U(p,f)^{96}Tc$, $^{nat}U(p,f)^{86}Rb$, $^{nat}U(p,f)^{84}Rb$, $^{nat}U(p,f)^{74}As$ and $^{nat}U(p,f)^{54}Mn$.

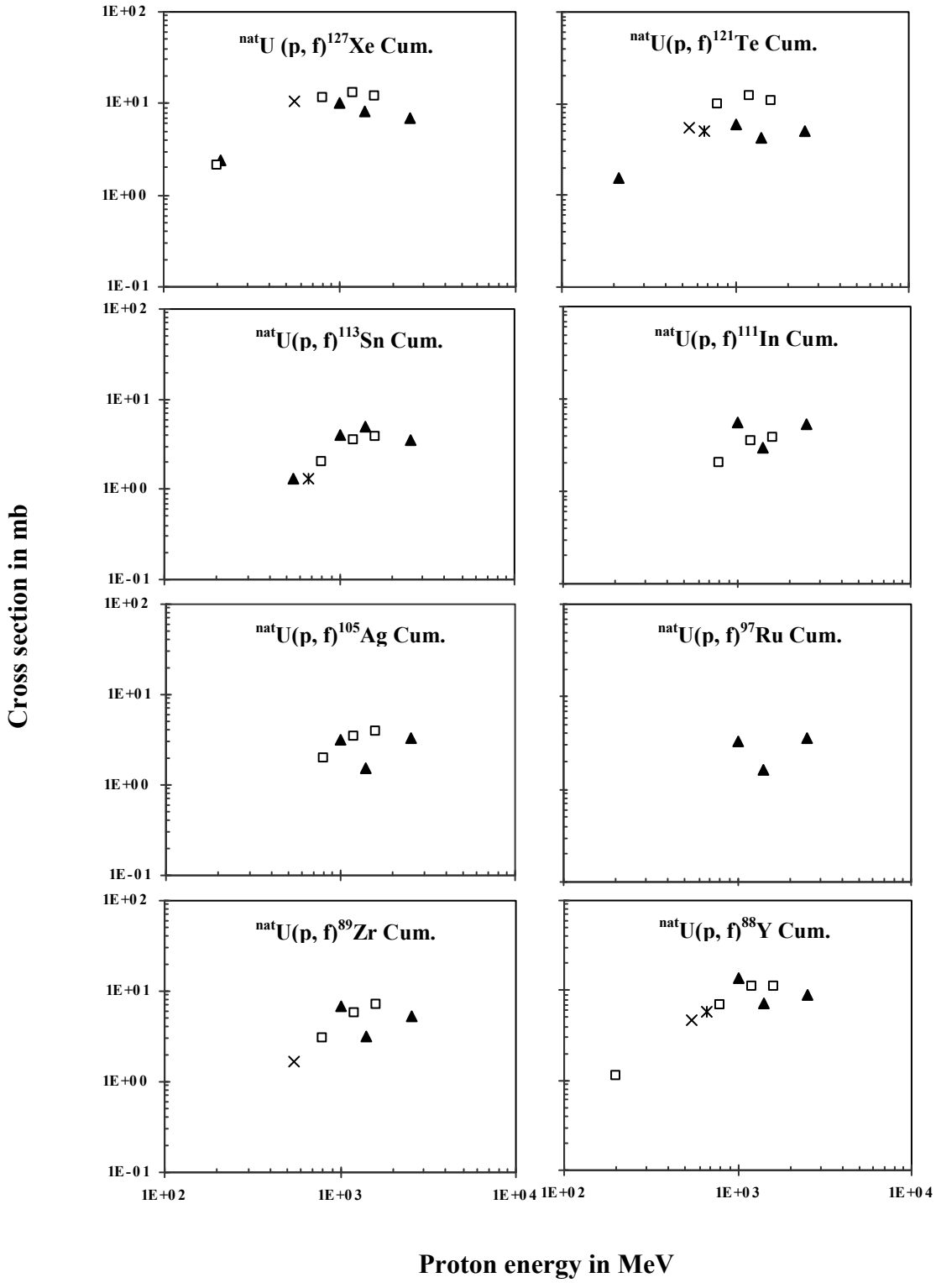

Fig. (4-13): *Cross section as function of proton energy for this work (▲), Titarenko et al. (□) [100], Blanchard et al. (×) [101], Friedlander et al. (○) [102] (○) and Michel et al. (✳) [35] for neutron poor products. The uncertainties of the experimental data are generally smaller than the symbol sizes.*

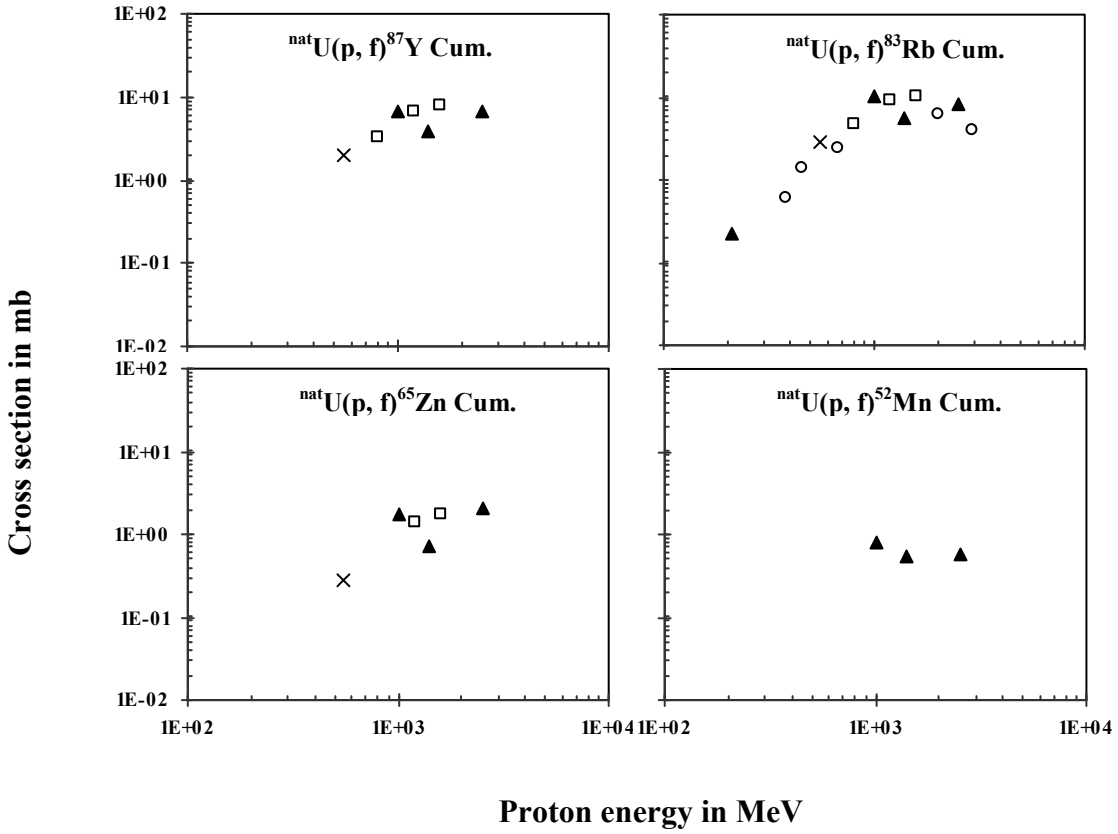

Fig. (4-13): *Continued.*

The experimental excitation functions are compared also with previous work Titarenko et al. [100], Blanchard et al. [101], Friedlander et al. [102], Hicks et al. [103], Davies et al. [104] and Uosif et al. [105]. From figure (4-14) we can see that, excellent agreement between the measured cross section and previous work for reactions $^{nat}U(p,f)^{136}Cs$, $^{nat}U(p,f)^{124}Sb$,$^{nat}U(p,f)^{122}Sb$, $^{nat}U(p,f)^{110m}Ag$ and $^{nat}U(p,f)^{86}Rb$. Good agreement for reactions $^{nat}U(p,f)^{106m}Ag$ and $^{nat}U(p,f)^{96}Tc$ and quite good agreement for reactions $^{nat}U(p,f)^{84}Rb$, $^{nat}U(p,f)^{74}As$ and $^{nat}U(p,f)^{54}Mn$. For the last reaction $^{nat}U(p,f)^{102}Rh$ no experimentally obtained data was available.

The comparison between measured cross section and previous work are drawn in figure (4-15) for nuclear reactions $^{nat}U(p,f)^{141}Ce$, $^{nat}U(p,x)^{140}Ba$, $^{nat}U(p,f)^{139}Ce$ $^{nat}U(p,f)^{137}Cs$, $^{nat}U(p,f)^{132}Te$, $^{nat}U(p,f)^{131}I$, $^{nat}U(p,f)^{127}Sb$, $^{nat}U(p,f)^{126}Sb$, $^{nat}U(p,f)^{125}Sn$, $^{nat}U(p,f)^{115}Cd$, $^{nat}U(p,f)^{111}Ag$, $^{nat}U(p,f)^{103}Ru$, $^{nat}U(p,f)^{99}Mo$, $^{nat}U(p,f)^{95}Zr$ and $^{nat}U(p,f)^{91}Y$. Also our results are compared with previous work Titarenko et al. [100], Blanchard et al. [101], Friedlander et al. [102], Hicks et al. [103], Davies et al. [104], Uosif et al. [105] and Baba et al. [106].

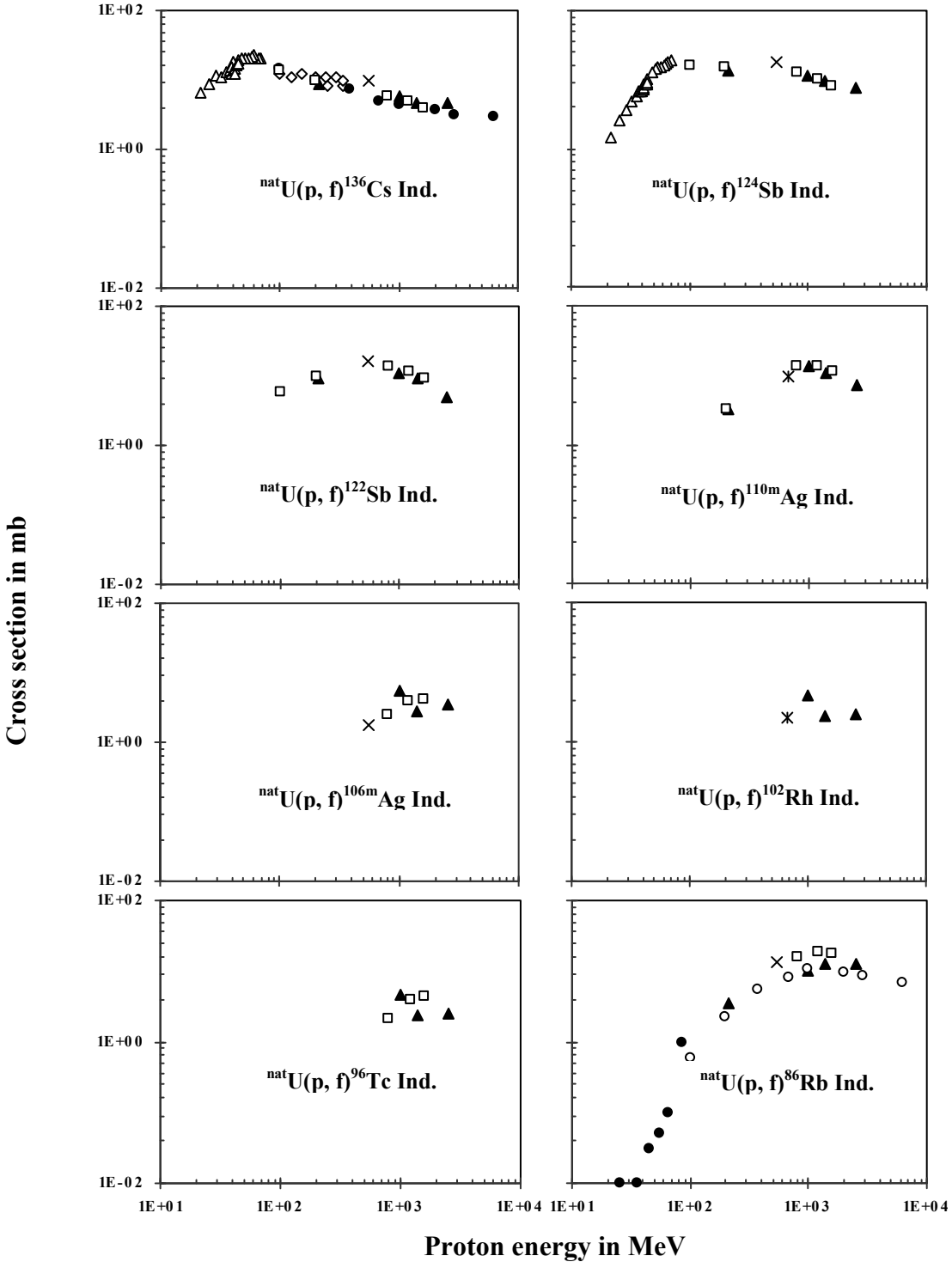

Fig. (4-14): *Cross section as function of proton energy for this work (▲), Titarenko et al. (□) [100], Blanchard et al. (×) [101], Friedlander et al. (○) [102], Hicks et al. (◊) [103], Davies et al [104]. (●), Uosif et al. (Δ) [105] and Michel et al. (✳) [35] for intermediate products. The uncertainties of the experimental data are generally smaller than the symbol sizes.*

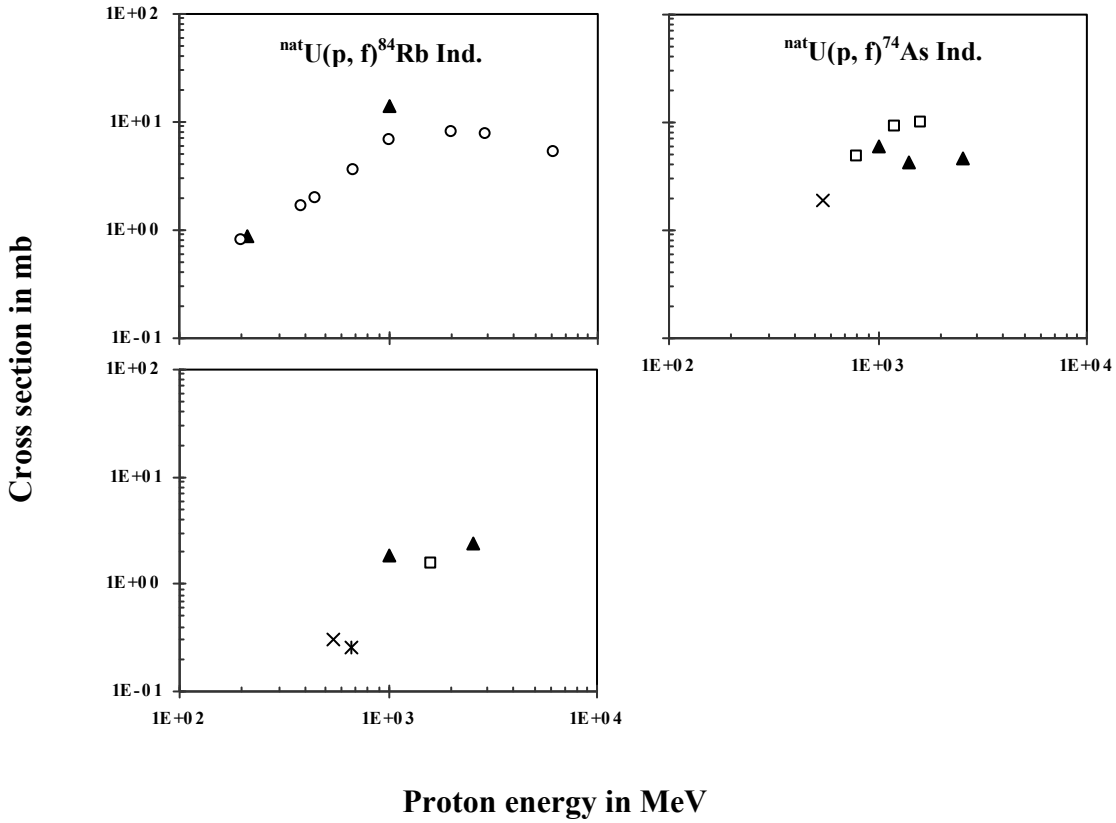

Fig. (4-14): *Continued.*

Figure (4-15) clears that, excellent agreement with earlier results for reactions $^{nat}U(p,f)^{131}I$, $^{nat}U(p,f)^{127}Sb$, $^{nat}U(p,f)^{126}Sb$, $^{nat}U(p,f)^{125}Sn$, $^{nat}U(p,f)^{115}Cd$, $^{nat}U(p,f)^{111}Ag$, $^{nat}U(p,f)^{103}Ru$ and $^{nat}U(p,f)^{95}Zr$, and good agreement for the reactions $^{nat}U(p,f)^{141}Ce$, $^{nat}U(p,f)^{139}Ce$, $^{nat}U(p, f)^{132}Te$ and $^{nat}U(p,f)^{99}Mo$. For reaction $^{nat}U(p,x)^{140}Ba$ very good agreement except at 2530 MeV the measured cross section is higher than the previous work, also at 211 MeV very good agreement between experimental excitation function and Friedlander [102] for reaction $^{nat}U(p, f)^{137}Cs$ while at proton energies 1000 MeV, 1400 MeV and 2530 MeV our cross sections are higher than the earlier. For reaction $^{nat}U(p, f)^{91}Y$ unfortunately, there are no available earlier results to compare.

For the target element uranium, we are starting with figure (4.12) where we have very few radionuclides in the vicinity of the target mass 238, namely ^{237}U, Pa-233, Pa-232, and Pa-230. All these excitation functions, for which at least new and relevant data by Titarenko et al. [100] and Blanchard et al. [101] do exist, show

relatively flat and constant behavior as a function of energy. There are no detailed structures to be seen.

Structured excitation functions can later be seen in figure (4.13) where we are already in the area of the fission products. It has to be noticed that we practically do not see deep spallation products for uranium, we just see a few nuclides which are close to target nuclide and then we see very extensively the fission products. For the excitation function of the fission products in figure (4.13) one generally sees good agreement between the results form this work and those from the work of Blanchard et al. [102], Friedlander et al. [102] and Titarenko et al. [100].

The excitation functions of the fission products start already at higher product mass numbers compared to the fission products from rhenium. So, we see that already ^{127}Xe has a pronounced fission production with a threshold of the order of 100 MeV. After a slight maximum around 1 GeV it tends to decline at higher energies. The same is true for practically all nuclides given in figure (4.13).

There are, however, also other fission products and some of them are displayed in figure (4.14). Here we have the neutron-rich radionuclides ^{136}Cs, ^{124}Sb, and ^{86}Rb. In particular, the first radionuclides, ^{136}Cs and ^{124}Sb, have fission threshold well below 100 MeV. For these cases there we have a number of data from other authors which allow together with our new ones to judge about the complete excitation functions for the production of these nuclides.

In most cases, the agreement between the different measurements of different laboratories can be considered as reasonably good for all nuclides which we have measured in this work. Also the production of ^{86}Rb is showing a general agreement between the experimental data. For this nuclide the fission threshold is at only 20 MeV. The excitation function shows a maximum which is shifted to higher energies compared to ^{136}Sc and ^{124}Sb. The observation we are making for these fission products and also for those given in figure (4.14 continued) and (4.15) is that, we have again two classes of fission products which have been to be clearly distinguished. One is the class of nuclide with high neutron excesses being in the neutron-rich part of the valley of stability and the other one which comprises nuclide in the neutron poor side of the valley of stability. For the neutron-rich nuclides, one observes relatively low

fission thresholds and the maximum of the excitation functions are already at low particle energies around 100 MeV. For the neutron poor nuclides, we are observing high thresholds and maxima around 1 GeV.

The neutron-rich low-energy fission products tend to show a slight but continuous decrease at higher energies behind the maximum, while the neutron poor products show fewer tendencies to decrease at higher energy. For the fission products which are far away from the uranium one observes slightly declining excitation function.

4.2.2 Comparison with TALYS Code:

Figure (4-16) gives a comparison for nuclear reactions $^{nat}U(p,pxn)^{237}U$, $^{nat}U(p,2pxn)^{233}Pa$, $^{nat}U(p,2pxn)^{232}Pa$ and $^{nat}U(p,2pxn)^{230}Pa$ from natural uranium and systematic survey on the capability of the TALYS code. It is clear that, up to 211 MeV, there are no available experimental cross sections to compare with TALYS code because the sample starts irradiation for 4 individual energies between 211 MeV and 2530 MeV.

For uranium, we can do the same comparison with theoretical calculations which we have performed for the target element rhenium. We start first with the TALYS calculations which only allow us seeing information for the target-near products. The fission products from uranium are not described by the TALYS model. In figure (4.16) we are seeing the TALYS calculations without a direct comparison with experimental data because in this thesis only cross sections at higher energies could be measured. So, the TALYS calculations just allow us to get estimates of the entire excitation functions below the measured values. The breaking down of the theoretical cross sections in case of Pa-233, Pa-232 and Pa-230 is again a numerical artefact and not an indication for a bad performance of the model. Generally for the data of this work, we can not judge about the behavior of TALYS because of the lack of experimental data in the energy range covered by the TALYS calculations.

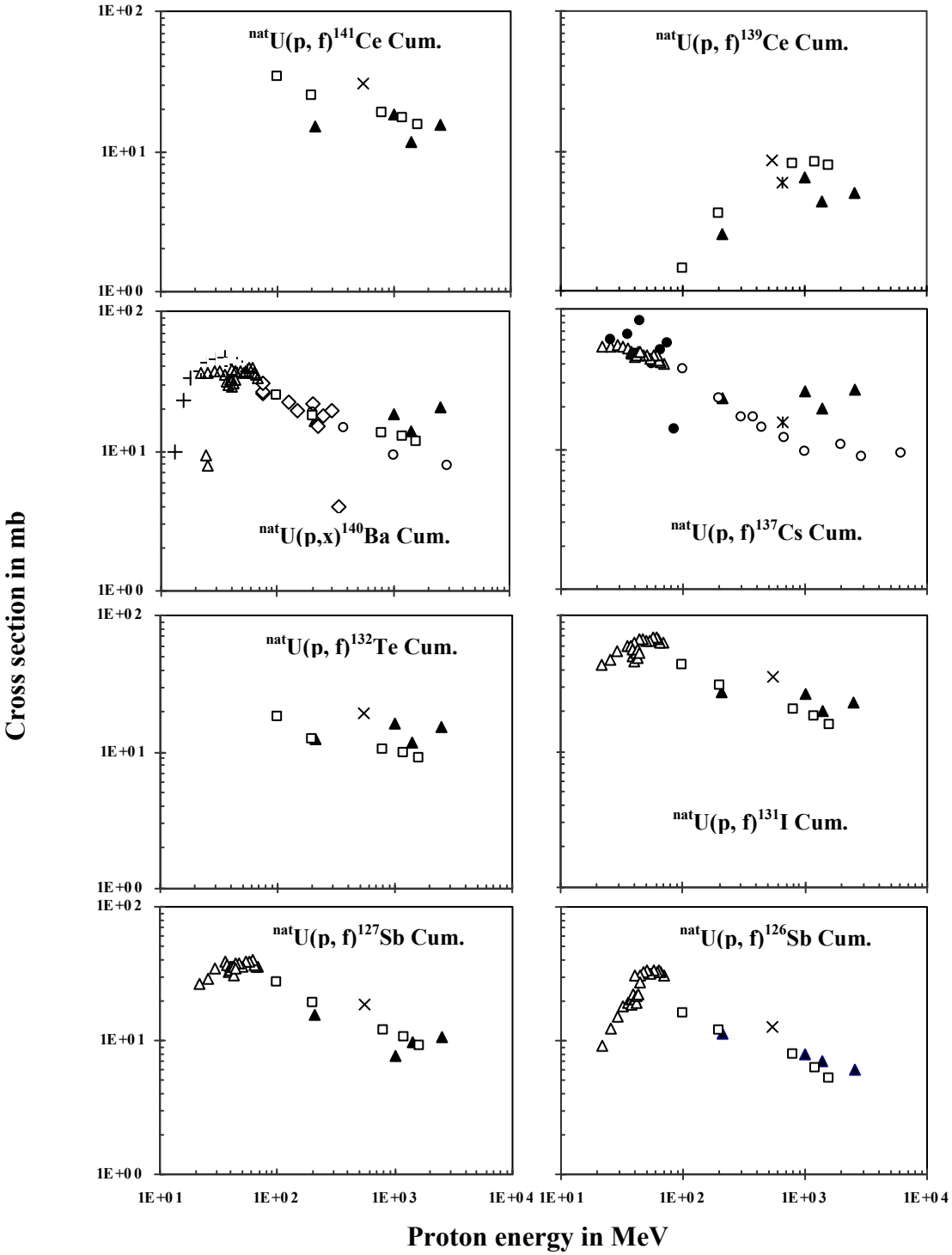

Fig. (4-15): *Cross section as function of proton energy for this work (▲), Titarenko et al. (□) [100], Blanchard et al. (×) [101], Friedlander et al. (○) [102], Hicks et al. (◊) [103], Davies et al. (●)[104], Uosif et al. (Δ) [105], Baba et al. (+) [106] and Michel et al. (∗) [107] for neutron-rich products. The uncertainties of the experimental data are generally smaller than the symbol sizes.*

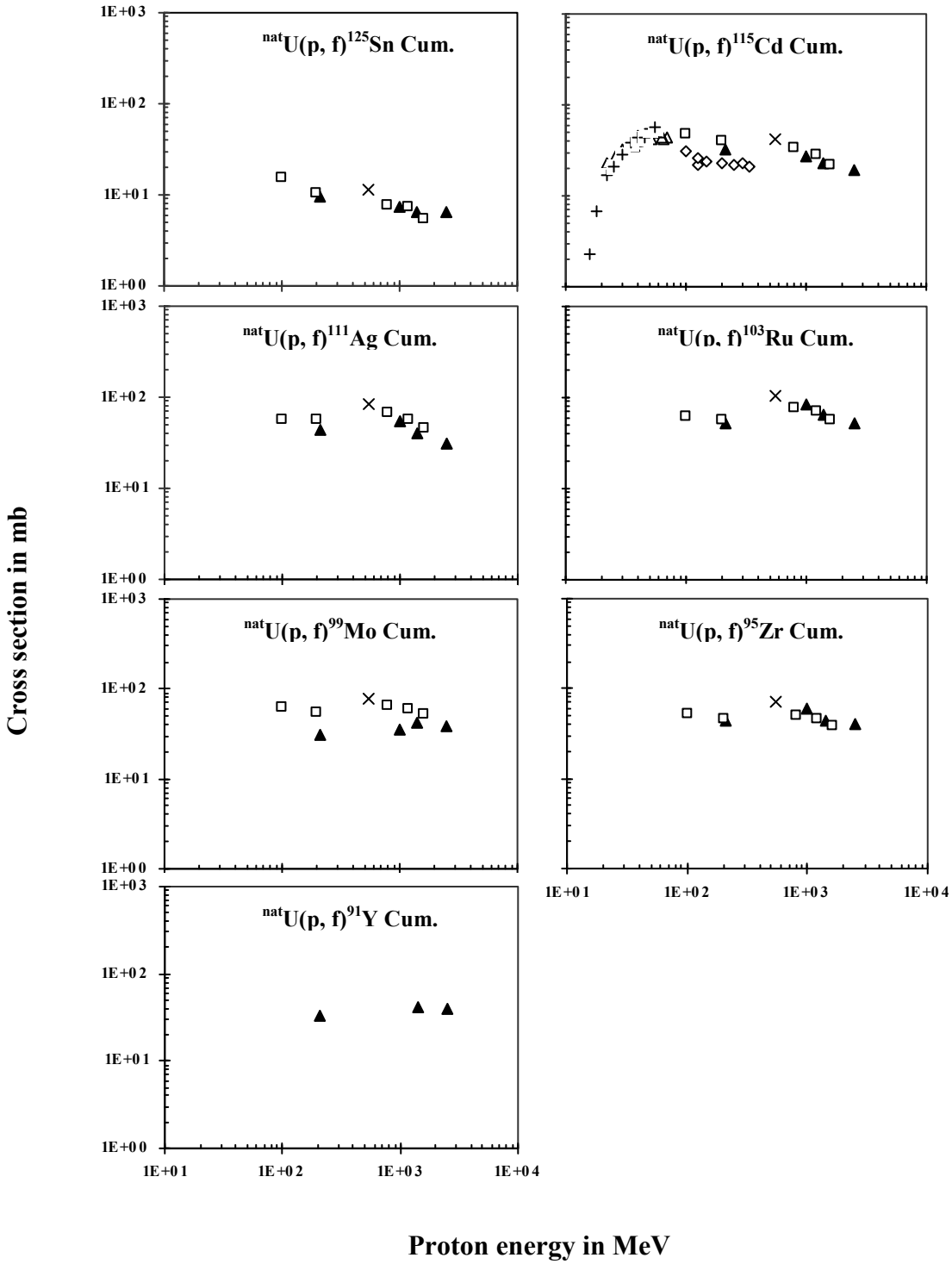

Fig. (4-15): *Continued.*

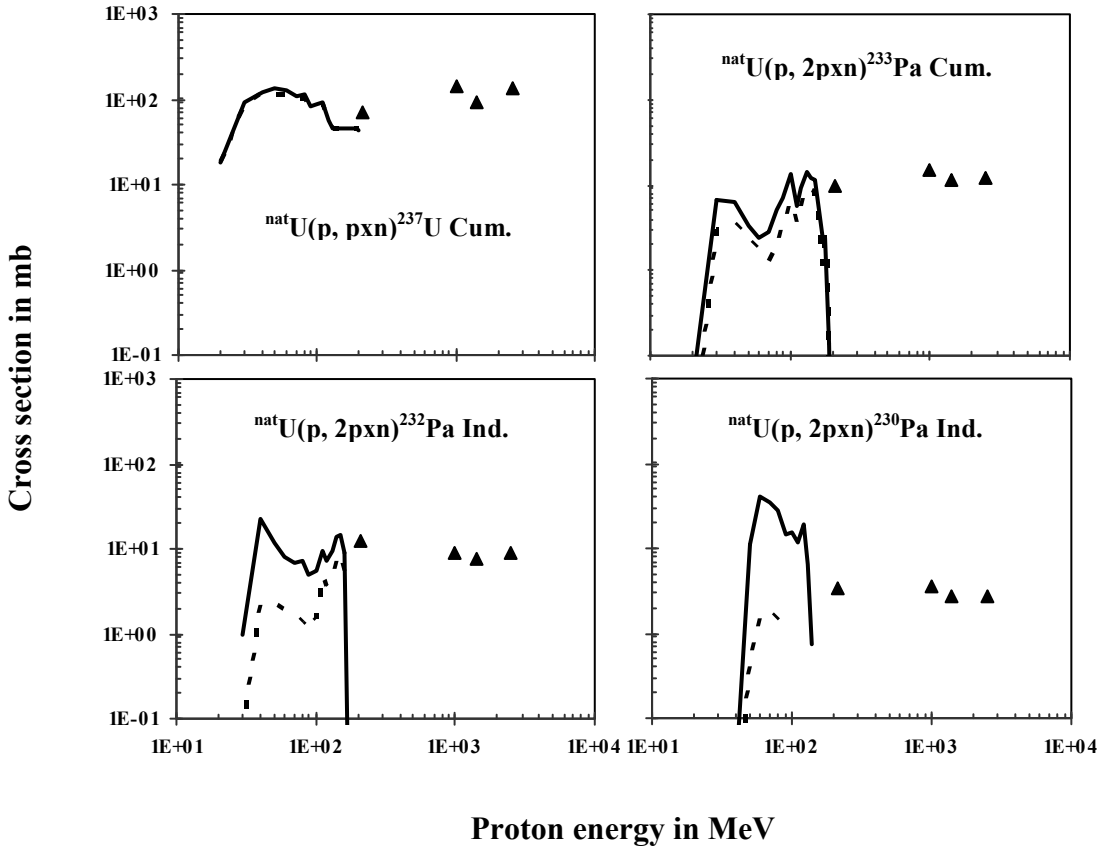

Fig. (4-16): *Cross section as function of proton energy for this work (▲), TALYS 0.72 (·····) and TALYS 1.0 (—) for target near products. The uncertainties of the experimental data are generally smaller than the symbol sizes.*

4.2.3 Comparison with INCL4+ABLA:

In this section we present the comparison between experimental cross section and calculated INCL4+ABLA code. Comparing the measured excitation function with the results of the INCL4+ABLA for nuclear reactions $^{nat}U(p,pxn)^{237}U$, $^{nat}U(p,2pxn)^{233}Pa$, $^{nat}U(p,2pxn)^{232}Pa$ and $^{nat}U(p,2pxn)^{230}Pa$ are given in figure (4-17). Good agreement between measured cross section and calculated results for nuclear reaction $^{nat}U(p, pxn)^{237}U$, and very good agreement for reaction $^{nat}U(p, 2pxn)^{233}Pa$ at proton energies 211 MeV and 1400 MeV but at 1000 MeV and 2530 Mev the experimental cross sections are slightly higher than the calculated cross sections. Figure (4-17) gives that also, the calculated excitation functions by using INCL4+ABLA are smaller than the measured excitation functions for nuclear reactions $^{nat}U(p,2pxn)^{232}Pa$ and $^{nat}U(p,2pxn)^{230}Pa$.

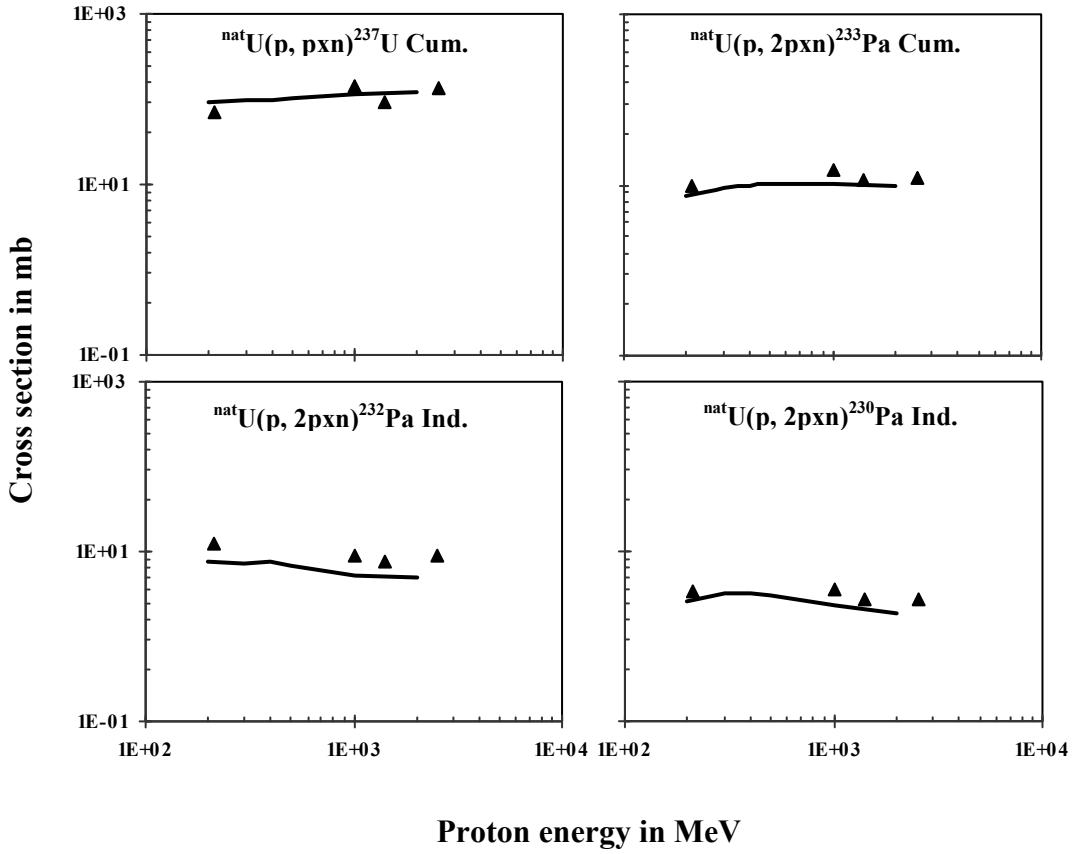

Fig. (4-17): *Cross section as function of proton energy for this work (▲) and INCL4+ABLA (—) for target near products. The uncertainties of the experimental data are generally smaller than the symbol sizes.*

Comparing experimental cross sections with calculated cross sections for reactions ^{nat}U (p,f)^{127}Xe, ^{nat}U(p,f)^{121}Te, ^{nat}U(p,f)^{113}Sn, ^{nat}U(p,f)^{111}In, ^{nat}U(p,f)^{105}Ag, ^{nat}U(p,f)^{97}Ru,^{nat}U(p,f)^{89}Zr, ^{nat}U(p,f)^{88}Y, ^{nat}U(p,f)^{87}Y, ^{nat}U(p,f)^{83}Rb, ^{nat}U(p,f)^{65}Zn, ^{nat}U(p,f)^{52}Mn and ^{nat}U(p,f)^{51}Cr are plotted in figure (4-18). It is evident from figure (4-18) that, very agreement between measured excitation functions and calculated excitation functions for reactions ^{nat}U (p,f)^{127}Xe, ^{nat}U(p,f)^{113}Sn and ^{nat}U(p,f)^{83}Rb. For reactions ^{nat}U(p,f)^{111}In, ^{nat}U(p,f)^{105}Ag and ^{nat}U(p,f)^{65}Zn excellent agreement at 1000 MeV, while at 1400 MeV and 2530 MeV the experimental cross sections are smaller than the calculated cross sections and for reaction ^{nat}U(p,f)^{121}Te very good agreement at 211 MeV between INCL4+ABLA cross section and our cross section but at 1000MeV, 1400 MeV and 2530 MeV the measured cross sections are higher than the experimental cross sections. Our results are in good agreement with INCL4+ABLA results for reactions ^{nat}U(p,f)^{97}Ru and ^{nat}U(p,f)^{89}Zr, and little bit agreement for reactions ^{nat}U(p,f)^{88}Y and ^{nat}U(p,f)^{87}Y. It is clear also that, the

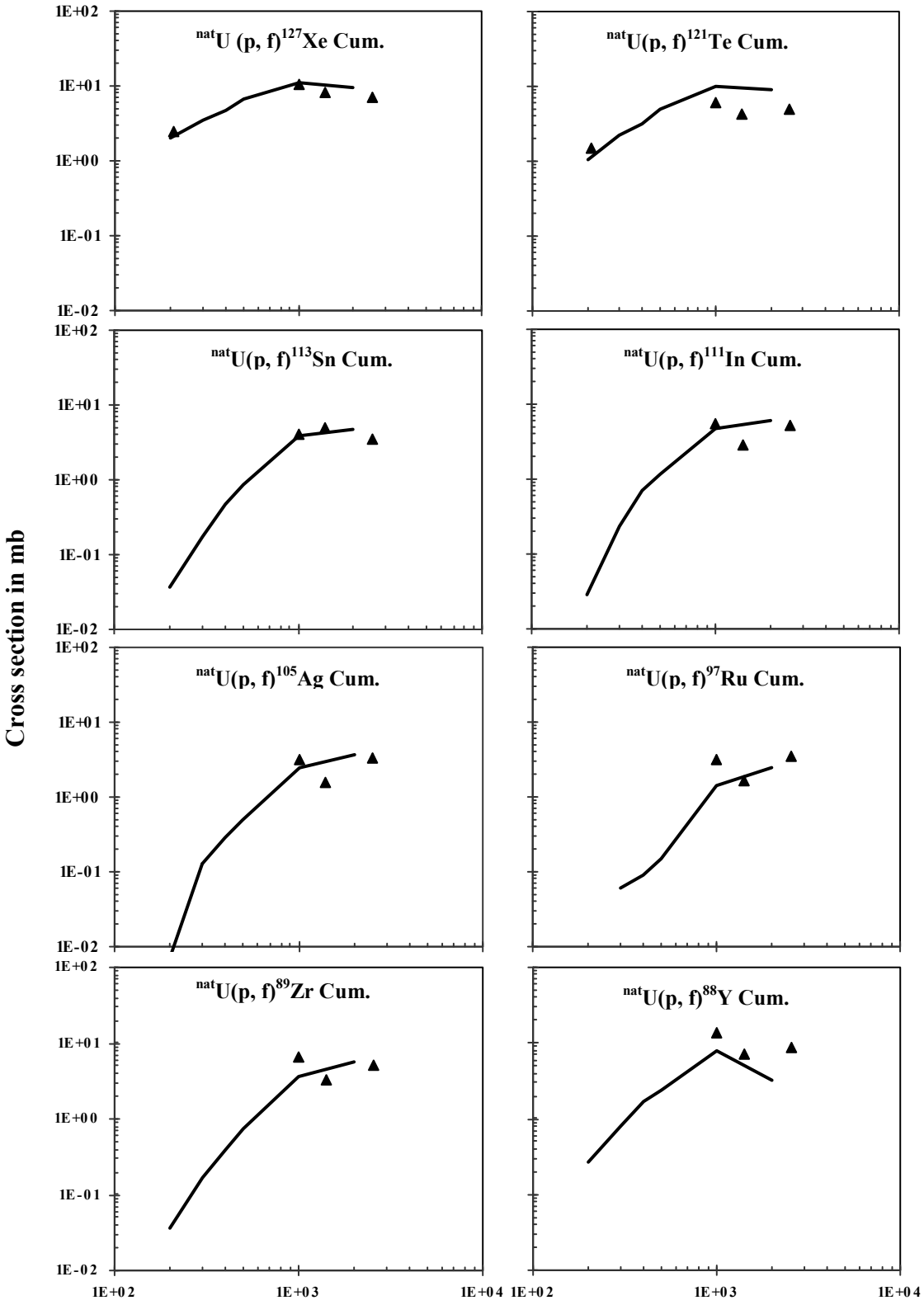

Fig. (4-18): *Cross section as function of proton energy for this work (▲) and INCL4+ABLA (—) for neutron poor products, part one. The uncertainties of the experimental data are generally smaller than the symbol sizes.*

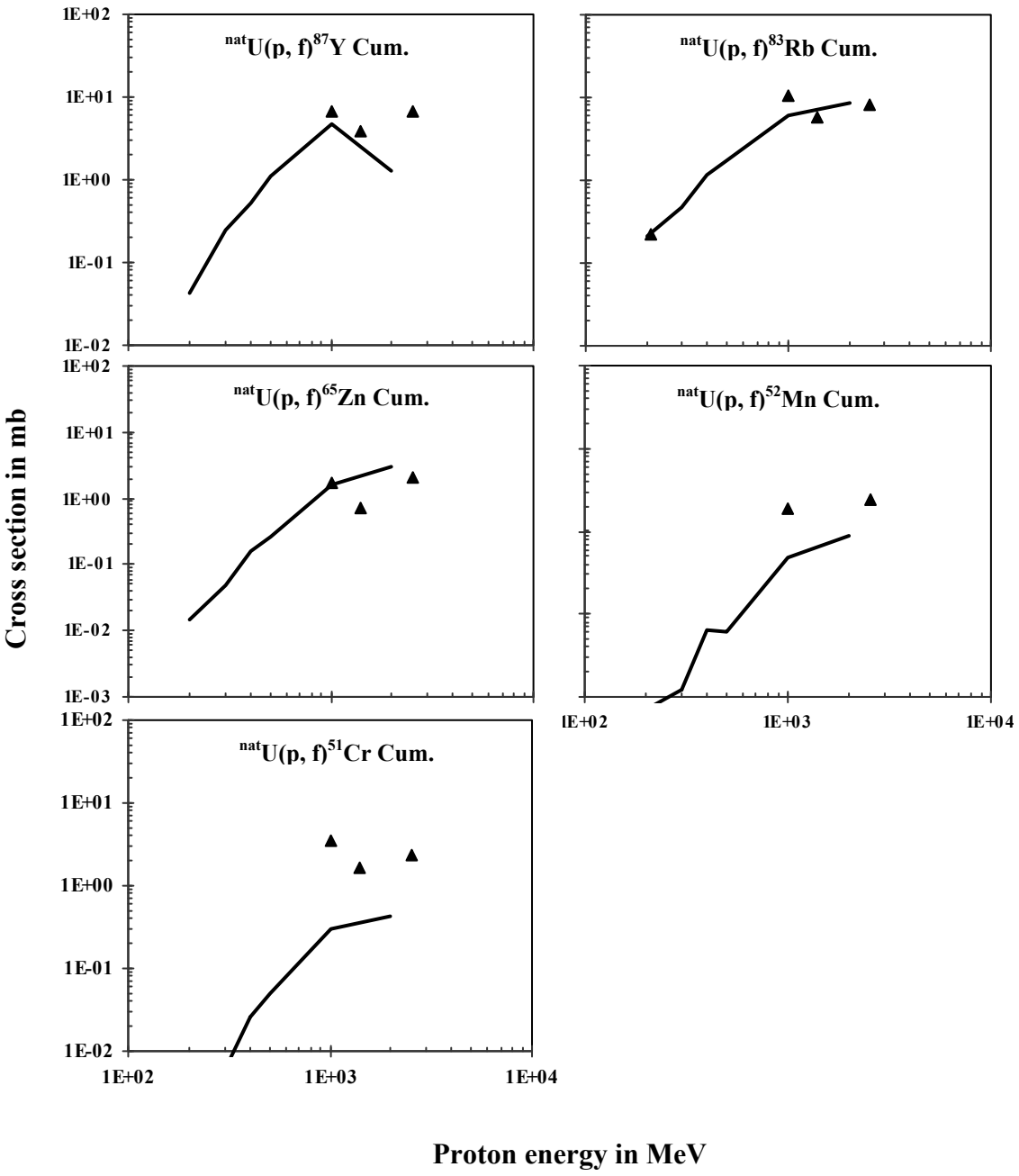

Fig. (4-18): *Continued.*

measured excitation functions are higher than the calculated excitation functions for reactions $^{nat}U(p,f)^{52}Mn$ and $^{nat}U(p,f)^{51}Cr$.

Figure (4-19) show that comparing between experimental cross section and INCL4+ABLA cross sections for reactions $U(p,f)^{136}Cs$, $U(p,f)^{124}Sb$, $^{nat}U(p,f)^{122}Sb$, $^{nat}U(p,f)^{110m}Ag$, $^{nat}U(p,f)^{106m}Ag$, $^{nat}U(p,f)^{102}Rh$, $^{nat}U(p,f)^{96}Tc$, $^{nat}U(p,f)^{86}Rb$, $^{nat}U(p,f)^{84}Rb$, $^{nat}U(p,f)^{74}As$ and $^{nat}U(p,f)^{54}Mn$. Man can see that excellent agreement between measured excitation functions and INCL4+ABLA excitation functions for

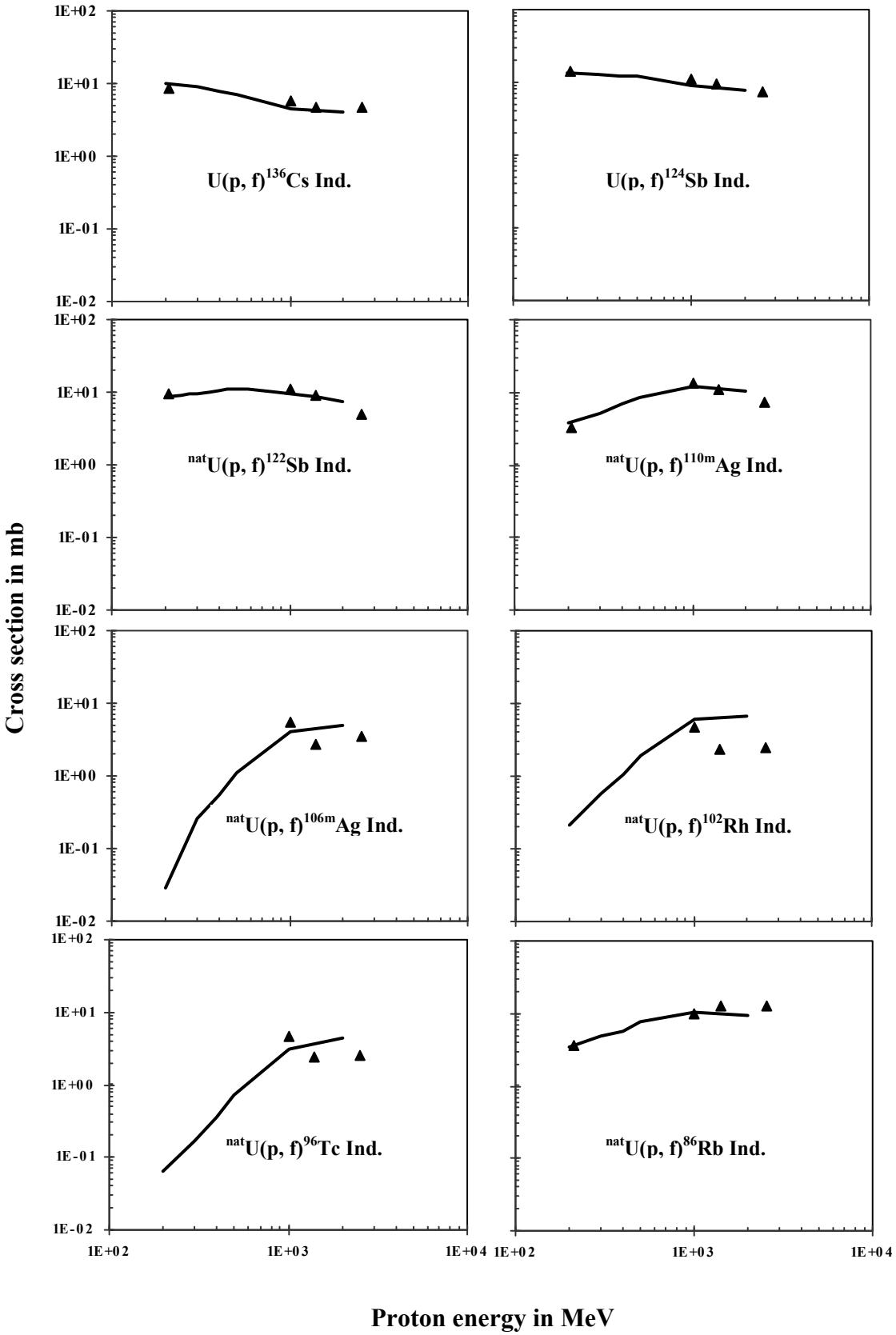

Fig. (4-19): *Cross section as function of proton energy for this work (▲) and INCL4+ABLA (—) for intermediate products, part one. The uncertainties of the experimental data are generally smaller than the symbol sizes.*

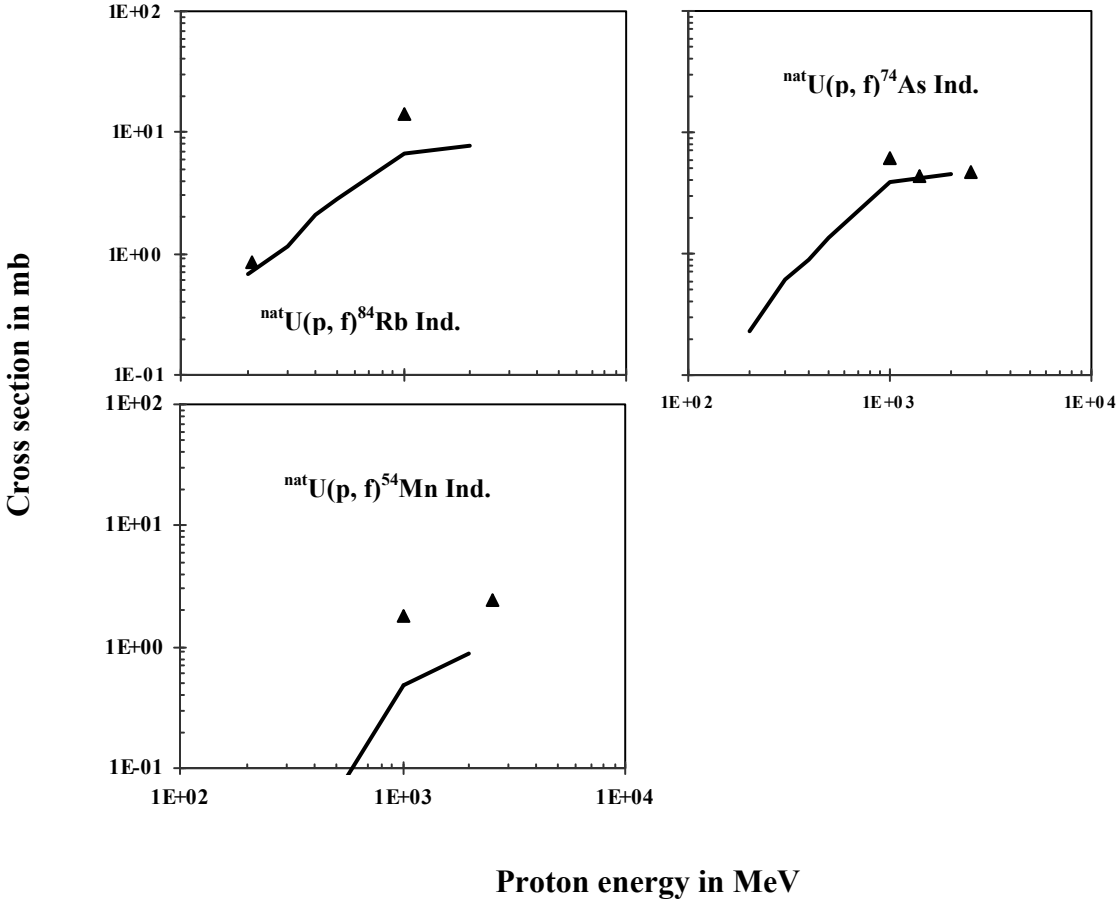

Fig. (4-19): *Continued.*

reactions U(p,f)^{136}Cs, U(p,f)^{124}Sb, ^{nat}U(p,f)^{122}Sb, ^{nat}U(p,f)^{110m}Ag, ^{nat}U(p,f)^{86}Rb and ^{nat}U(p,f)^{74}As. Good agreement between measured cross section and calculated cross sections for reactions ^{nat}U(p,f)^{106m}Ag, ^{nat}U(p,f)^{102}Rh and ^{nat}U(p,f)^{96}Tc at 1000 MeV but at 1400 MeV and 2530 MeV the experimental cross sections are little bit smaller than the theoretical cross sections. For reaction ^{nat}U(p,f)^{84}Rb very good agreement at 211 MeV between measured and calculated cross section but in ^{nat}U(p,f)^{54}Mn we can notice that, the theoretical excitation function is smaller than experimental excitation function.

From figure (4-20) we can see that, the experimental cross sections as functions of proton energy in comparison with INCL4+ABLA model calculation for reactions ^{nat}U(p,f)^{141}Ce, ^{nat}U(p,f)^{140}Ba, ^{nat}U(p,f)^{139}Ce, ^{nat}U(p,f)^{137}Cs, ^{nat}U(p,f)^{132}Te, ^{nat}U(p,f)^{131}I, ^{nat}U(p,f)^{127}Sb, ^{nat}U(p,f)^{126}Sb, ^{nat}U(p,f)^{125}Sn, ^{nat}U(p,f)^{115}Cd, ^{nat}U(p,f)^{111}Ag, ^{nat}U(p,f)^{103}Ru, ^{nat}U(p,f)^{99}Mo, ^{nat}U(p,f)^{95}Zr and ^{nat}U(p,f)^{91}Y.

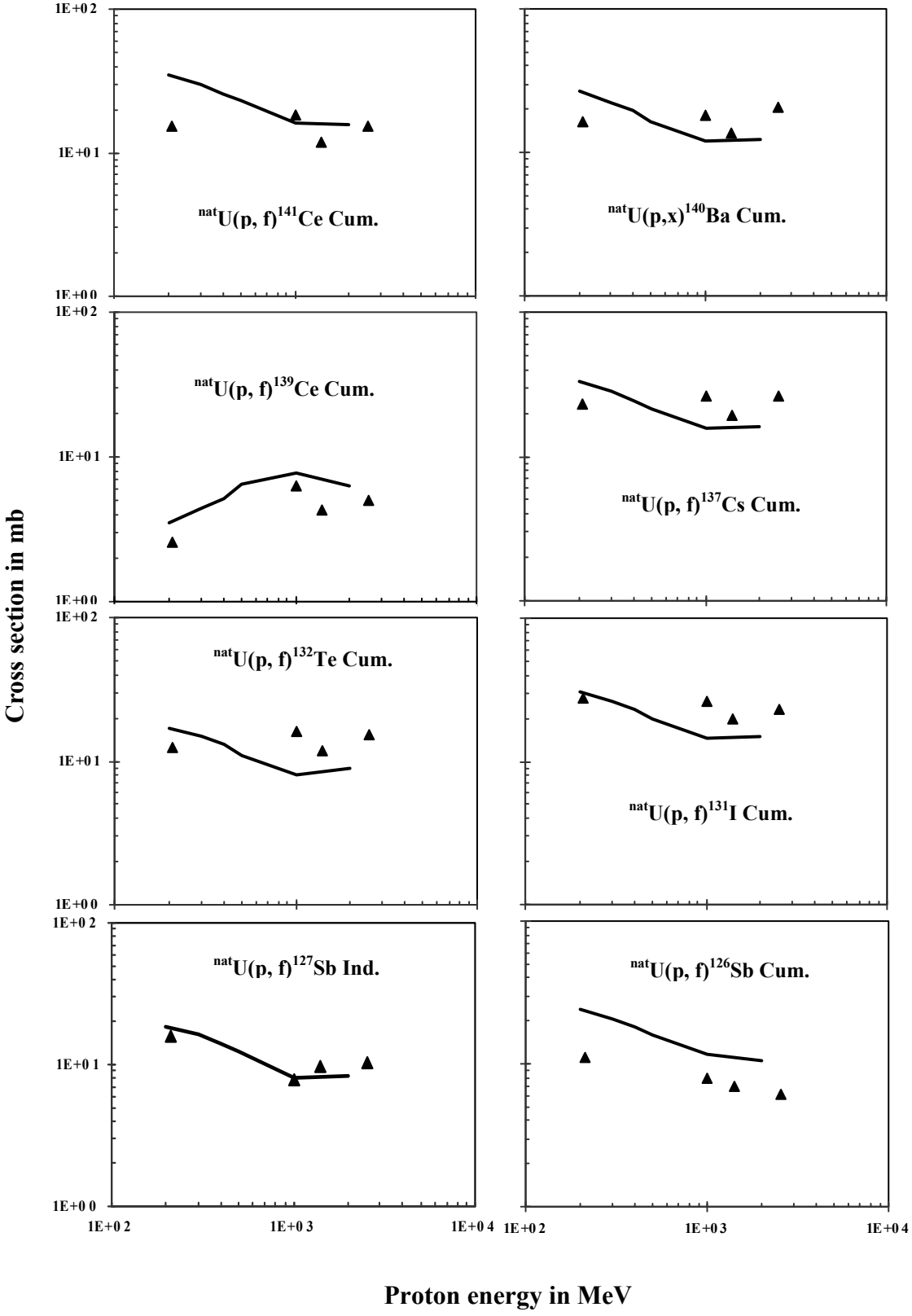

Fig. (4-20): *Cross section as function of proton energy for this work (▲) and INCL4+ABLA (—) for neutron-rich products, part one. The uncertainties of the experimental data are generally smaller than the symbol sizes.*

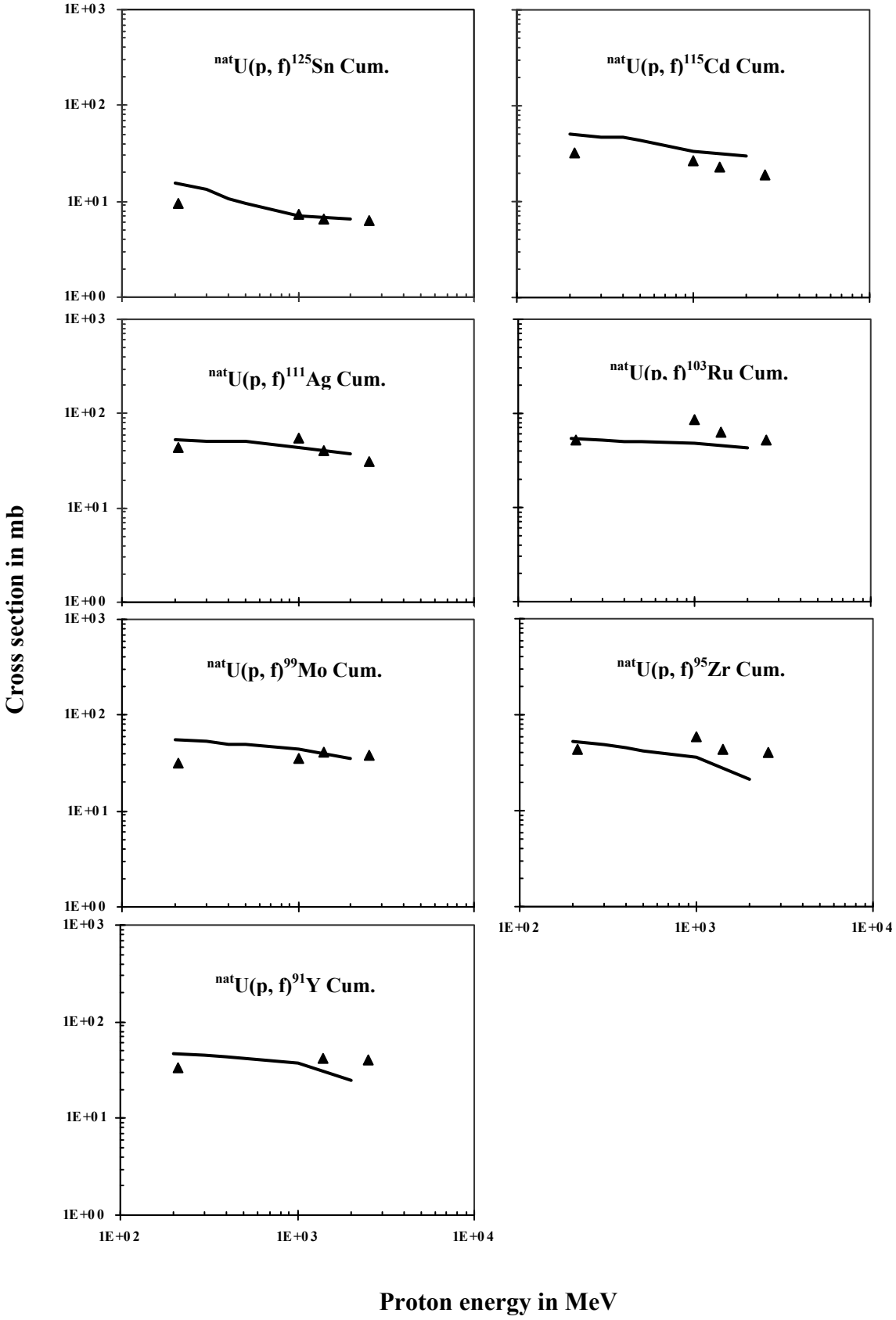

Fig. (4-20): *Continued.*

It is evident from figure (4-20) that, very good agreement between INCL4+ABLA code cross section and measured cross section for reactions $^{nat}U(p,f)^{127}Sb$, $^{nat}U(p,f)^{125}Sn$, $^{nat}U(p,f)^{115}Cd$, $^{nat}U(p,f)^{111}Ag$, $^{nat}U(p,f)^{103}Ru$, $^{nat}U(p,f)^{99}Mo$, $^{nat}U(p,f)^{95}Zr$ and $^{nat}U(p,f)^{91}Y$. Good agreement between calculated cross section and measured cross section for reaction $^{nat}U(p,f)^{141}Ce$ at 1000 MeV and 2530 MeV, while at 211 MeV and 1400 MeV the experimental cross sections are smaller than the theoretical cross sections. For reaction $^{nat}U(p,f)^{140}Ba$ we can notice also good agreement at 1400 MeV but at 211 MeV our result is smaller than calculated and vice versa at proton energies 1000 MeV and 2530 MeV. Good agreement between theoretical and measured cross section at 211 MeV for reaction $^{nat}U(p, f)^{131}I$ but at 1000 MeV, 1400 MeV and 2530 MeV we can see that comparing the experimental cross sections with the results of the model calculation it was found that the our cross section in this study are higher than the results of the model calculation. For reactions $^{nat}U(p,f)^{137}Cs$ and $^{nat}U(p,f)^{132}Te$ the measured cross section is little bit smaller than calculated cross section at 211 MeV, while at proton energies 1000 MeV, 1400 MeV and 2530 MeV vice versa could be noticed. The INCL4+ABLA excitation functions are higher than the experimental excitation functions for reactions $^{nat}U(p,f)^{139}Ce$ and $^{nat}U(p,f)^{126}Sb$.

The INCL4+ABLA calculations also allow describing the target near products as shown in figure (4.17). All these excitation functions are characterized by more or less constant behaviours as a function of energy. These products are more or less confined to peripheral reactions and low excitation energies.

More promising is the comparison of the INCL4+ABLA calculation with the fission products. For uranium, in general, the INCL4+ABLA calculations reproduced the experimental data very well. That is true for all radionuclide starting with ^{127}Xe and going down to ^{86}Rb (Fig. 4-18, 4-19, 4-20). The distinction between the different fission products from uranium namely the low-energy and the high-energy products does not show different performance of the model used. However, for lower mass fission products, as e.g. ^{54}Mn in figure (4.19), we are getting already a significant underestimation of the experimental data. In general, one can say that, the performance of the INCL4+ABLA with respect the fission products from uranium is much better that was observed from rhenium.

4.2.4 Phenomenology of Residual Nuclides Production by Proton-Induced reaction on Uranium:

In Figure (4-21) our experimental cross sections are plotted versus product masses. Already at about 200 MeV the fission channel is open. This plot also allows a crude estimate of the isobaric yields of products which would be the upper envelope of the experimental data. One can clearly distinguish two major reaction modes. Products are observed in the vicinity of the target masses and at about half the target mass with a clear gap between them. This gap still ranges from mass 140 to 230, 140 to 200, 140 to 230 and 150 to 200 at 211 MeV, 1000 MeV, 1400 MeV and 2530 MeV, respectively. The products at about half the target mass are clearly attributable to fission processes. Fission products show up as peaks in the mass distributions which become higher and broader with increasing proton energy. The radionuclides observed in the vicinity of the target are produced by reactions involving a compound nucleus in statistical equilibrium, by pre-equilibrium reactions and by spallation processes.

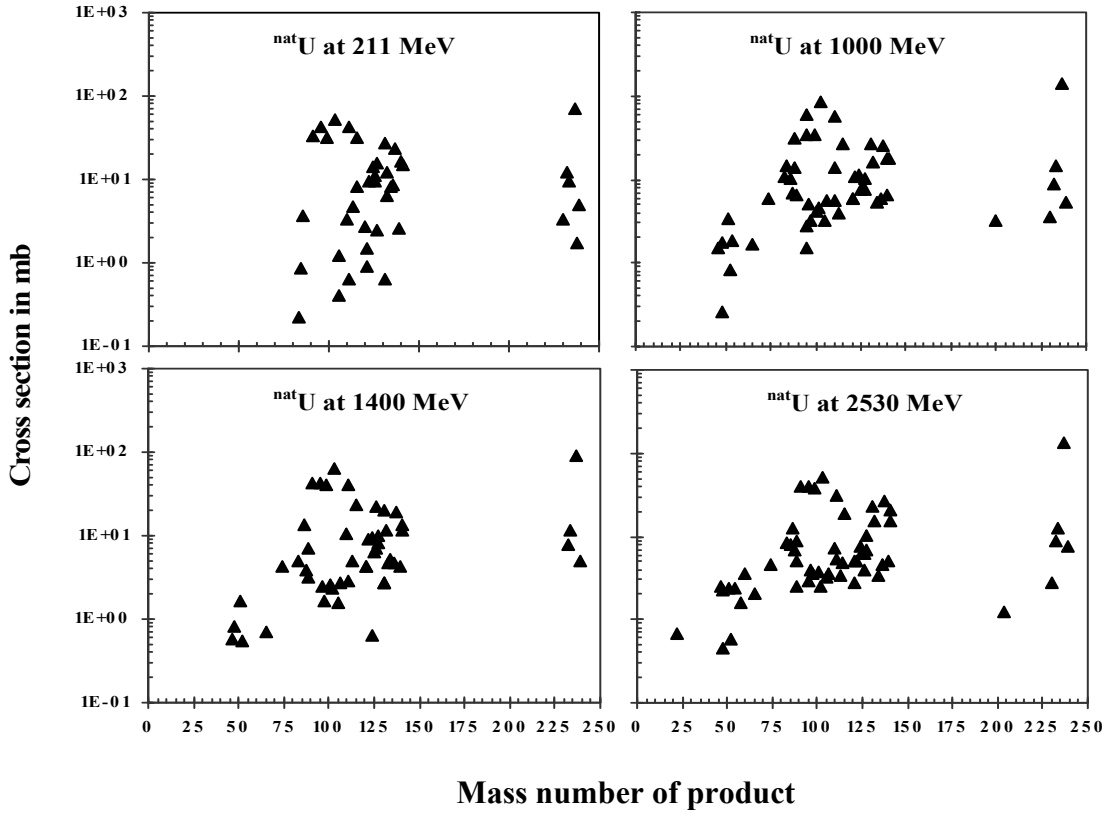

Fig. (4-21): *Cross sections for the production of residual nuclides from uranium as function of the product mass numbers.*

So, finally we go to the mass distribution of the observed radionuclides from uranium. In figure (4.21) we are having these mass distributions at four energies. We see that the range of target-near products is very strongly confined and that then we are only observing fission products. Very dominating is fission for uranium, but this fission does not appear here as a simple symmetric fission process. There are indications that the heavy peak of the fission products in the low-energy uranium fission distribution pertains for intermediate energies so that there is a certain preference for masses between 125 and 150. Except for that, we also see a relative asymmetric maximum in the distribution of the fission product at masses around 100, pointing to the importance of the second mode of fission, namely that of fission of residual nuclide after long intra-nuclear cascade.

The part of the mass distribution at masses between 125 and 150 is pointing to low-energy fission and production after a short cascade with low excitation energies in which the fissioning nucleus remembers a relatively high neutron excess. The experimental cross sections with uncertainty and type of reaction for natural rhenium and uranium are given in appendix (I) and appendix (II).

CONCLUSION

The context of this work describes residual nuclides produced from rhenium and uranium by proton-induced reaction. This was a part of the 5th frame work of the European Commission project HINDAS (High and intermediate Data for Accelerator Driven System). The aim of this project is to provide reliable nuclear reaction data for the feasibility studies of accelerator driven system. Our new experimental data for the production of residual readionuclides will increase the data libraries and will contribute to develop new and improved simulation codes.

The irradiations took place at the SATURNE II synchrocyclotron of the Laboratoire National Saturne at Saclay for uranium target with proton energy range from 211 MeV to 2530 MeV, and at the cyclotron of the Svedberg Laboratory at Uppsala for rhenium target with proton energy range from 78.2 MeV to 2590 MeV. At both locations a stacked-foil technique was applied allowing for the examination of many target elements at different energy points with a minimum requirement of beam-time. The foils were arranged in small stacks in which aluminium foils were arranged in front of the rhenium or uranium targets to allow for proton flux determination via the ^{27}Al(p,3p3n)^{22}Na monitor reaction. γ-spectrometric measurements were performed using several high-purity germanium (HPGe) and germanium–lithium (Ge(Li)) detectors partially equipped with automatic sample changers to be used for the short-time measurements. Residual nuclides were measured in Center of Radiation Protection and Radioecology [Zentrum für Strahlenschutz und Radioökologie (ZSR)] Hannover Germany. The spectrums were evaluated by commercially available software GAMMA-W.

Cross sections were determined for fifty four residual nuclides $^{185,\ 183,\ 182}$Os, $^{186,\ 184,\ 184m,\ 183,\ 182,\ 181}$Re, ^{183}Ta, $^{175,\ 173}$Hf, $^{171,\ 170.\ 169}$Lu, ^{169}Yb, ^{166}Tm, $^{156,\ 155,\ 153,\ 152,\ 151}$Tb, $^{149,\ 147,\ 146}$Gd, $^{148,\ 147,\ 145}$Eu, $^{139,\ 137m,\ 135}$Ce, ^{131}Ba, $^{132,\ 129}$Cs, $^{127,\ 125}$Xe, $^{121,\ 119}$Te, ^{106m}Ag, ^{95}Nb, $^{88,\ 87}$Y, ^{85}Sr, $^{86,\ 84}$Rb, ^{75}Se, ^{65}Zn, ^{57}Ni, $^{60,\ 58}$Co, ^{59}Fe, ^{51}Cr, ^{46}Sc and ^{7}Be are generated by proton interactions with natural rhenium.

Fifty two residual nuclides ^{237}U, $^{233,\ 232,\ 230}$Pa, $^{141,\ 139}$Ce, ^{140}Ba, $^{137,\ 136}$Cs, ^{127}Xe, ^{131}I, $^{132,\ 121}$Te, $^{127,\ 126,\ 124,\ 122,\ 120m}$Sb, $^{125,\ 113}$Sn, ^{111}In, $^{115,\ 115m}$Cd, $^{111,\ 110m,\ 106,\ 106m}$Ag, ^{102}Rh, $^{103,\ 97}$Ru, $^{96,\ 95m}$Tc, ^{99}Mo, $^{95,\ 95m}$Nb, $^{95,\ 89}$Zr, $^{91,\ 88,\ 87}$Y, $^{86,\ 84,\ 83}$Rb, ^{74}As, ^{85}Zn, ^{60,}

^{58}Co, ^{54,} ^{52}Mn, ^{51}Cr, ^{48}V, ^{22}Na, are generated by proton interactions with natural uranium target and cross sections could be determined. The experimental obtained data were compared with previously obtained experimental data and codes INCL4+ABLA, TALYS and Bertini/Dresner based in theoretical models. Very good agreement between different experimental work and the codes were obtained. Still in some cases there are discrepancy between the experimental obtained data and the codes which require further improvement.

REFERENCES

[1] "Analytical applications of nuclear techniques", IAEA VIENNA, (2004).

[2] R. Michel et al. Nucl. Instr. and Meth. A 463 (2001) 593.

[3] Stanley G. Prussin, "Nuclear Physics for Applications", WILY-VCH Verlag GmbH & KGaA, Weinheim, (2007).

[4] Norman K. Glendenning, "Direct Nuclear reactions", World Scientific publishing Co. Pte. Ltd., (2004).

[5] C. Keller, "Radiochemistry", Haleted Press, JOHN WILEY & SON, (1988).

[6] Weston M. Stacey, "Nuclear Reactor Physics", WILY-VCH Verlag GmbH & KGaA, Weinheim, (2007).

[7] Choppin R. Gregory, "Raidochemistry and Nuclear Chemistry", Buttreworth-Heinemann, (2002).

[8] James E. Turner, "Atoms, Radiations, and Radiation protection", WILY-VCH Verlag GmbH & KGaA, Weinheim, (2007).

[9] John R. Lamarsh, "Introduction to nuclear Reaction Theory", Addison-Weseley-Pub. Company, (1966).

[10] H. Semat and J.R. Albright, "Introduction to Atomic and Nuclear Physics", 5th Edition, Chapman and Hall Ltd. London, (1973).

[11] Ian Hore-Lacy, "Nuclear Electricity", 6th Edition, Uranium Information Center & Minerals Council of Australia, (2000).

[12] Henri Becquerel, "on radioactivity", a new Property of Matter, Nobel Lecture, (1903).

[13] http://www.nea.fr/pub/activities/ar2000/trends-in-nuclear-power.

[14] Pierre Marmier and Eric Sheldon, "Physics of nuclei and particles", Academic Press, New York and London, (1969).

[15] M.V. Ricciardi et al., Phys. Rev. C 73 (2006) 014607.

[16] S.R. Hashemi-Nezhad et al., Nucl. Instr. and Meth. A 482 (2002) 547.

[17] R. Klapisch, Europhysics, 31, 6, (2000).

[18] ADS Nuclear Energy, Nuclear Science Issue Briefing Paper August (2003).

[19] Transmutation of Nuclear Waste, A report of one day workshop held by U. K's academic physics community in Nov. 2002, The Engineering and Physical Science Research Council, May (2003).

[20] Y. Kadi and Revol, “Design of an Accelerator Driven System for the Destruction of Nuclear Waste”, European Organization for Nuclear Research, GERN, Geneva, Switzerland, (2001).

[21] Adonai Herrera-Martinez et al., Annals of Nuclear Energy, 34 (2007) 564.

[22] Adonai Herrera-Martinez et al., Annals of Nuclear Energy, 34 (2007) 550.

[23] Basar Sarer et al., Energy conversion and management, In Press, (2008).

[24] Richard E. Prael and Henry Lichenstein, LA-UR-89-3014, Los Alamos national Laboratory, (1989).

[25] Frank Goldenbaum, “The Physics of Spallation Processes”, Forschunszentrum Juelich GmbH, (2004).

[26] Yacine Kadi, Nucl. Instr. and Meth. A 562 (2006) 573.

[27] Adonai Herrera-Martinez, “Transmutation of Nuclear Waste in Accelerator Driven System”, Ph. D. Thesis, Department of Engineering, Dawin College Cambridge University, (2004).

[28] R. Klapisch, Europhysics News, 31 Nr. 6 (2000).

[29] S. Andriamarieat, Phys. Lett. B 348 (1995) 697.

[30] Accelerator Driven System (ADS) and Fast Reactors (FR) in Advanced Nuclear Fuel Cycles, Acomparative Study, OECD/NEA (2002).

[31] S.A. Karamian et al., Nucl. Inst. And Meth. A 489 (2002) 448.

[32] H. Baba et al., Z. Phys. A 356 (1996) 61.

[33] M. Lagarde-Simonoff et al., Phys. Rev. C 20 (1979) 1498.

[34] G. Friedlander et al., Phys. Rev. 129 (1963) 1809.

[35] R. Michel et al. Proc. Int. Conf. Nucl. Data for science and technology, Santa Fee, AIP Conference Proceeding, Vol. 769, Melville, New York (2005) 1043.

[36] T. Enqvist et al., Nucl. Phys. A 658 (1999) 47.

[37] R. Michel et al., J. Radioanal. Chem. 59 (1980) 461.

[38] R. Michel et al., Earth Planet. Sci. Lett. 59 (1982) 33; Erratum, ibid 64 (1983) 174.

[39] R. Michel et al., J. Geophys. Res. 89 B, Suppl. (1984) 673.

[40] R. Michel, in: Intermediate Energy Nuclear Data for Applications, ed. N.P. Kocherov. INDC(NDS)-245 (IAEA, Wien, 1991) pp. 17-36.

[41] R. Michel et al., Meteoritics 26 (1991) 221.

[42] R. Michel et al., Planet. Space Sci. 43 (1995) 557.

[43] R. Michel et al., Nucl. lnstr. and Meth. B 113 (1996) 434.

[44] H.H. Andersen et al., Hydrogen Stopping Power and Range in all Elements, Vol. 3 of the Stopping and Ranges of Ions in Matter, Pergamon Press, ISBN 008-021605-6, (1977).

[45] J.F. Ziegler et al., The Stopping Power and Ranges of Ions in Solids, Vol. 1 of the Stopping and Ranges of Ions in Matter, Pergamon Press, New York, (1985).

[46] J.F. Ziegler et al., TRIM version 92.16, updated version of a computer code for calculating stopping and ranges, described by P.C. Stevenson et al., Phys. Rev. 111 Nr. 3 (1958) 886.

[47] J.F. Janni, At. Data Nucl. Data Tables, 27 (1982) 147.

[48] S. Tavernier, Measurement Techniques in Nuclear and Particle Physics, Lecture Notes for Students in: Interuniversity Programme in nuclear engineering (BNEN), Master of Biomedical engineering (UGent-VUB) and Kernfysica en Toepassingen (VUB), VUB (2007).

[49] J.F. Janni, Atomic Data and Nuclear Data Tables 27 (1982) 147.

[50] N. Bohr, Philos. Mag. 30 (1915) 851.

[51] www.tsl.uu.seltl_history.html.

[52] G.A. Tutin et al., Nucl. lnstr. and Meth. A 457 (2001) 646.

[53] G.F. Konll, Radiation detection and measurements, 2nd Edi., John Wiley&Sons, New York, USA, (1989).

[54] P.W. Gray and A. Ahmad, Nucl. Instr. Meth. Phys. Res. A 237 (1985) 577.

[55] ISO Guide to the Expression of Uncertainty in Measurements, 1995.

[56] W. Westmeier, Commercially available Code GAMMA-W ver, 1997.

[57] W. Westmeier, Gamma Manual, Ebsdorferground-Moellen, 1995.

[58] I.A. Slavic, Nucl. lnstr. and Meth. 134 (1976) 285.

[59] W. Westmeier, Nucl. lnstr. and Meth. 180 (1981) 205.

[60] W. Westmeier, Nucl. lnstr. and Meth. A 242 (1986) 437.

[61] M. Blaauw et al., Nucl. lnstr. and Meth. A 387 (1997) 416.

[62] U. Reuss and W. Westmeier, At. Data Nucl. Data Tables 29 (1983).

[63] R.R. Kinsey et al., The NUDAT/PCNUDAT Program for Nuclear Data Processing, Paper submitted to the Ninth International Symposium of Capture Gamma-Ray Spectroscopy and Related Topics, Budapest, Hungary, October 1996; data extracted from the UNDAT database version 2.22, 31. January 1996.

[64] M. Gloris, thesis, Hannover University, 1998.

[65] R. Michel et al., Nucl. lnstr. and Meth in Phys. Res. B 129 (1997) 153.

[66] R. Bodmann et al., TSL Progress Report 1994-1995 (1996) 36.

[67] G.F. Steynet et al., Appl. Rad. Isot. 41 (1990) 315.

[68] J. Tobailem, Section Efficaces des Reactions Nucleaires Induites par Protons, Deutons, Particules Alpha V -Silicium, CEA-N-1466(5), (1981) 103.

[69] G. Pfennig et al., Chart of the nuclides, Forschungszntrum Karlsruhe GmbH, 6. Auflage, (1995).

[70] J.K. Tuli, Nuclear Wallet Cards, Brookhaven National Laboratory, (1990).

[71] E. Storm et al., Nucl. Data Tables A 7 (1970) 565.

[72] Program XCOM, Version 3.1 by M.J.Berger and J.H.Hubbell, 23 June 1999.

[73] P. Schwandt, The interaction between medium energy nucleons in nuclei, ed. H.O. Meyer (AIP Editions, 1983) p. 89.

[74] G.W. Hoffmann et al., Phys. Rev. C24 (1981) 541.

[75] J.M. Cameron, Nucl. Phys. A434 (1985) 261c.

[76] G. English, N.T. Porile and E.P. Steinberg, Phys. Rev. C10 (1974) 2268.

[77] G. Rudstam, Z. Naturforsch. 21a (1966) 1027.

[78] G. Fai and J. Randrup, Nucl. Phys. A381 (1982) 557.

[79] D.H.E. Gross et al., Z. Phys. A309 (1982) 41.

[80] J. Aichelin and J. Hiifner, Phys. Lett. 136B (1984) 15.

[81] M.E. Fisher, Physica 3 (1967) 225.

[82] A.D. Panagiotou et al., Phys. Rev. Lett. 52 (1984) 496.

[83] R.W. Minich et aL, Phys. Lett. I18B (1982) 458.

[84] W. Bauer et al., Phys. Lett. 15015 (1985) 53; Nucl. Phys. A452 (1986) 699.

[85] X. Campi and J. Desbois, Seventh high energy heavy ion study, GSI Publication GSI-85-10 (1985) 707.

[86] T.S. Biro, J. Knoll and J. Richert, Nucl. Phys. A459 (1986) 692.

[87] A.J. Koning et al. in R. C. Haight et al. (eds) AIP Conf. Proc. 769, Melvillee NY (2005) 1154.

[88] H. Feshbach, A. Kerman and S. Koonin, Ann. Phys. (NY) 125 (1980) 429.

[89] H. Gruppelaar, P. Nagel and P.E. Hodgson, Riv. Nuov. Cim. 9, no. 7 (1986) 1.

[90] IAEA Report INDC (CCP)-385, 1995. A.J.Koing, J.P.Delaroche, Local and global nucleon optical models from 1 keV to 200 MeV, Nucl. Phys. A 713(2003) 231-310.

[91] Gilbert A. and Cameron A.G.W., Can.J.Phys.43 (1965) 1446.

[92] Ignatyuk A.V.,Smirenkin G.N., and Tishin A.S., Sov. J. Nucl. Phys.21, no.3 (1975) 255.

[93] Brosa U., Grossmann S. and Müller, 1990, Nuclear Scission, Phys. Rep. 197 (1990) 167.

[94] Duijvenstijn M.C., and Hambsch F-J., 1999, Proceedings of the International Conference on Fission and Properties of Neutron-Rich Nuclei, June 28- July 2(1999) St. Andrews, Scotland.

[95] A. Boudard et al., Phys. Rev. C 66 (2002) 044615.

[96] A.R. Junghans et al., Nucl. Phys. A 629 (1998) 635.

[97] J.-J. Gaimard, K.-H. Schmidt, Nucl. Phys. A 531 (1991) 709.

[98] A.R. Junghans, M. de Jong, H.G. Clerc, A.V. Ignatyuk, G.A. Kudyaev, K.-H. Schmidt, Nucl. Phys. A 629 (1998) 635.

[99] M.S. Lafleur, et al. Can. J. Chem. 44 (1966) 2749.

[100] A.Y. Konobeyev et al. Kerntechnik 60 (1995) 147.

[101] Y. Titarenko et al., ISTC Project #839, Final Technical Report, http://www-nds.iaea.org/reports/indc-ccp-434.pdf.

[102] X. Blanchard et al., in: H. Condé (ed.) Proc. 2nd Int. Conf. on Accelerator-Driven Transmutation Technologies and Applications, 3.-7.6. 1996, Kalmar, Sweden, Uppsala University, Gotab (1997) 543.

[103] G. Friedlander et al., Phys. Rev. 129 (1963) 1809.

[104] H.G. Hicks et al., Phys. Rev. 100 (1955) 1286.

[105] J.H. Davies et al., Cand. J. of Phys. 41 (1963) 762.

[106] M.A.M. Uosif et al., AIP Conference Proceedings, Vol. 769, Melville, New York (2005) p. 1547.

[107] S. Baba et al., Nucl. Phys. A 175 (1971) 177.

APPENDIX (I)

Cross section data for reaction $^{nat}Re(p,xn)^{185}Os$ cumulative.

Target	Reaction	Product	E_p in MeV	$u(E_p)$ in MeV	σ in mb	u(σ) in mb
^{nat}Re	p,xn	^{185}Os	7.800E+01	1.7E+00	3.7E+01	1.5E+00
^{nat}Re	p,xn	^{185}Os	8.200E+01	2.2E+00	3.4E+01	1.1E+00
^{nat}Re	p,xn	^{185}Os	9.000E+01	1.6E+00	3.1E+01	6.0E-01
^{nat}Re	p,xn	^{185}Os	9.300E+01	2.1E+00	2.8E+01	9.0E-01
^{nat}Re	p,xn	^{185}Os	9.800E+01	1.5E+00	2.8E+01	5.0E-01
^{nat}Re	p,xn	^{185}Os	1.100E+02	1.9E+00	2.4E+01	8.0E-01
^{nat}Re	p,xn	^{185}Os	1.100E+02	1.4E+00	2.4E+01	5.0E-01
^{nat}Re	p,xn	^{185}Os	1.200E+02	1.2E+00	2.3E+01	6.0E-01
^{nat}Re	p,xn	^{185}Os	1.200E+02	1.9E+00	2.2E+01	8.0E-01
^{nat}Re	p,xn	^{185}Os	1.200E+02	1.1E+00	2.0E+01	1.3E+00
^{nat}Re	p,xn	^{185}Os	1.300E+02	1.8E+00	2.0E+01	7.0E-01
^{nat}Re	p,xn	^{185}Os	1.300E+02	9.0E-01	2.0E+01	6.0E-01
^{nat}Re	p,xn	^{185}Os	1.300E+02	1.7E+00	1.9E+01	1.1E+00
^{nat}Re	p,xn	^{185}Os	1.500E+02	1.6E+00	1.7E+01	5.0E-01
^{nat}Re	p,xn	^{185}Os	1.500E+02	1.5E+00	1.7E+01	6.0E-01
^{nat}Re	p,xn	^{185}Os	1.600E+02	1.4E+00	1.5E+01	8.0E-01
^{nat}Re	p,xn	^{185}Os	1.700E+02	1.3E+00	1.5E+01	9.0E-01
^{nat}Re	p,xn	^{185}Os	2.500E+02	1.9E+00	9.7E+00	8.0E-01
^{nat}Re	p,xn	^{185}Os	3.300E+02	1.8E+00	8.0E+00	1.1E+00
^{nat}Re	p,xn	^{185}Os	5.600E+02	1.6E+00	5.9E+00	3.8E-01
^{nat}Re	p,xn	^{185}Os	7.600E+02	1.5E+00	5.4E+00	3.6E-01
^{nat}Re	p,xn	^{185}Os	1.200E+03	1.5E+00	4.9E+00	4.8E-01
^{nat}Re	p,xn	^{185}Os	1.600E+03	1.5E+00	5.2E+00	4.4E-01
^{nat}Re	p,xn	^{185}Os	2.600E+03	1.0E+00	6.0E+00	2.8E-01

Cross section data for reaction $^{nat}Re(p,xn)^{183}Os$ cumulative.

Target	Reaction	Product	E_p in MeV	$u(E_p)$ in MeV	σ in mb	u(σ) in mb
^{nat}Re	p,xn	^{183}Os	7.800E+01	1.7E+00	-	-
^{nat}Re	p,xn	^{183}Os	8.200E+01	2.2E+00	8.0E+01	8.1E+00
^{nat}Re	p,xn	^{183}Os	9.000E+01	1.6E+00	-	-
^{nat}Re	p,xn	^{183}Os	9.300E+01	2.1E+00	6.2E+01	3.1E+00
^{nat}Re	p,xn	^{183}Os	9.800E+01	1.5E+00	-	-
^{nat}Re	p,xn	^{183}Os	1.100E+02	2.0E+00	5.3E+01	3.6E+00
^{nat}Re	p,xn	^{183}Os	1.100E+02	1.4E+00	-	-
^{nat}Re	p,xn	^{183}Os	1.200E+02	1.2E+00	4.6E+01	2.8E+00
^{nat}Re	p,xn	^{183}Os	1.200E+02	1.9E+00	-	-
^{nat}Re	p,xn	^{183}Os	1.200E+02	1.1E+00	-	-
^{nat}Re	p,xn	^{183}Os	1.300E+02	1.8E+00	4.0E+01	2.9E+00
^{nat}Re	p,xn	^{183}Os	1.300E+02	9.0E-01	-	-
^{nat}Re	p,xn	^{183}Os	1.300E+02	1.7E+00	3.7E+01	3.2E+00
^{nat}Re	p,xn	^{183}Os	1.500E+02	1.6E+00	3.2E+01	1.7E+00
^{nat}Re	p,xn	^{183}Os	1.500E+02	1.5E+00	3.0E+01	1.6E+00
^{nat}Re	p,xn	^{183}Os	1.600E+02	1.4E+00	2.8E+01	1.8E-01
^{nat}Re	p,xn	^{183}Os	1.700E+02	1.3E+00	2.7E+01	1.9E+00
^{nat}Re	p,xn	^{183}Os	2.500E+02	1.9E+00	1.8E+01	5.0E-01
^{nat}Re	p,xn	^{183}Os	7.800E+01	1.8E+00	1.6E+01	1.5E+00

Continued.

Target	Reaction	Product	E_p in MeV	u(E_p) in MeV	σ in mb	u(σ) in mb
^{nat}Re	p,xn	^{183}Os	5.600E+02	1.6E+00	1.8E+01	1.6E+00
^{nat}Re	p,xn	^{183}Os	7.600E+02	1.5E+00	8.7E+00	2.4E+00
^{nat}Re	p,xn	^{183}Os	1.200E+03	1.5E+00	-	-
^{nat}Re	p,xn	^{183}Os	1.600E+03	1.5E+00	-	-
^{nat}Re	p,xn	^{183}Os	2.600E+03	1.0E+00	-	-

Cross section data for reaction ^{nat}Re(p,xn)^{182}Os cumulative.

Target	Reaction	Product	E_p in MeV	u(E_p) in MeV	σ in mb	u(σ) in mb
^{nat}Re	p,xn	^{182}Os	7.800E+01	1.7E+00	-	-
^{nat}Re	p,xn	^{182}Os	8.200E+01	2.2E+00	1.0E+02	2.9E+00
^{nat}Re	p,xn	^{182}Os	9.000E+01	1.6E+00	-	-
^{nat}Re	p,xn	^{182}Os	9.300E+01	2.1E+00	8.2E+01	4.5E+00
^{nat}Re	p,xn	^{182}Os	9.800E+01	1.5E+00	-	-
^{nat}Re	p,xn	^{182}Os	1.100E+02	2.0E+00	6.8E+01	4.4E+00
^{nat}Re	p,xn	^{182}Os	1.100E+02	1.4E+00	-	-
^{nat}Re	p,xn	^{182}Os	1.200E+02	1.2E+00	5.8E+01	2.6E+00
^{nat}Re	p,xn	^{182}Os	1.200E+02	1.9E+00	-	-
^{nat}Re	p,xn	^{182}Os	1.200E+02	1.1E+00	-	-
^{nat}Re	p,xn	^{182}Os	1.300E+02	1.8E+00	4.5E+01	4.2E+00
^{nat}Re	p,xn	^{182}Os	1.300E+02	9.2E-01	-	-
^{nat}Re	p,xn	^{182}Os	1.300E+02	1.7E+00	4.7E+01	3.3E+00
^{nat}Re	p,xn	^{182}Os	1.500E+02	1.6E+00	4.3E+01	6.3E+00
^{nat}Re	p,xn	^{182}Os	1.500E+02	1.5E+00	3.9E+01	1.3E+00
^{nat}Re	p,xn	^{182}Os	1.600E+02	1.4E+00	3.7E+01	1.8E+00
^{nat}Re	p,xn	^{182}Os	1.700E+02	1.3E+00	3.4E+01	2.9E+00
^{nat}Re	p,xn	^{182}Os	2.500E+02	1.9E+00	2.5E+01	2.2E+00
^{nat}Re	p,xn	^{182}Os	3.300E+02	1.8E+00	2.1E+01	4.2E+00
^{nat}Re	p,xn	^{182}Os	5.600E+02	1.6E+00	2.3E+01	3.2E+00
^{nat}Re	p,xn	^{182}Os	7.600E+02	1.5E+00	1.6E+01	3.7E+00
^{nat}Re	p,xn	^{182}Os	1.200E+03	1.5E+00	-	-
^{nat}Re	p,xn	^{182}Os	1.600E+03	1.5E+00	-	-
^{nat}Re	p,xn	^{182}Os	2.600E+03	1.0E+00	-	-

Cross section data for reaction ^{nat}Re(p,pxn)^{186}Re independent.

Target	Reaction	Product	E_p in MeV	u(E_p) in MeV	σ in mb	u(σ) in mb
^{nat}Re	p,pxn	^{186}Re	7.800E+01	1.7E+00	-	-
^{nat}Re	p,pxn	^{186}Re	8.200E+01	2.2E+00	5.8E+01	4.0E+00
^{nat}Re	p,pxn	^{186}Re	9.000E+01	1.6E+00	-	-
^{nat}Re	p,pxn	^{186}Re	9.300E+01	2.1E+00	5.7E+01	1.0E+00
^{nat}Re	p,pxn	^{186}Re	9.800E+01	1.5E+00	-	-
^{nat}Re	p,pxn	^{186}Re	1.100E+02	2.0E+00	5.4E+01	7.0E-01
^{nat}Re	p,pxn	^{186}Re	1.100E+02	1.4E+00	-	-
^{nat}Re	p,pxn	^{186}Re	1.200E+02	1.2E+00	5.2E+01	1.6E+00
^{nat}Re	p,pxn	^{186}Re	1.200E+02	1.9E+00	-	-
^{nat}Re	p,pxn	^{186}Re	1.200E+02	1.1E+00	-	-
^{nat}Re	p,pxn	^{186}Re	1.300E+02	1.8E+00	4.6E+01	4.4E+00
^{nat}Re	p,pxn	^{186}Re	1.300E+02	9.0E-01	-	-
^{nat}Re	p,pxn	^{186}Re	1.300E+02	1.7E+00	4.7E+01	1.2E+00

Continued.

Target	Reaction	Product	E_p in MeV	u(E_p) in MeV	σ in mb	u(σ) in mb
^{nat}Re	p,pxn	^{186}Re	1.450E+02	1.6E+00	4.1E+01	5.5E+00
^{nat}Re	p,pxn	^{186}Re	1.530E+02	1.5E+00	4.1E+01	4.3E+00
^{nat}Re	p,pxn	^{186}Re	1.620E+02	1.4E+00	4.0E+01	5.7E+00
^{nat}Re	p,pxn	^{186}Re	1.690E+02	1.3E+00	3.9E+01	4.2E+00
^{nat}Re	p,pxn	^{186}Re	2.510E+02	1.9E+00	3.8E+01	2.7E+00
^{nat}Re	p,pxn	^{186}Re	3.310E+02	1.8E+00	3.8E+01	1.9E+00
^{nat}Re	p,pxn	^{186}Re	5.580E+02	1.6E+00	4.8E+01	3.9E+00
^{nat}Re	p,pxn	^{186}Re	7.630E+02	1.5E+00	4.5E+01	3.2E+00
^{nat}Re	p,pxn	^{186}Re	1.165E+03	1.5E+00	4.6E+01	2.5E+00
^{nat}Re	p,pxn	^{186}Re	1.570E+03	1.5E+00	4.9E+01	3.5E+00
^{nat}Re	p,pxn	^{186}Re	2.590E+03	1.0E+00	5.5E+01	1.9E+00

Cross section data for reaction ^{nat}Re(p,pxn)^{184}Re independent.

Target	Reaction	Product	E_p in MeV	u(E_p) in MeV	σ in mb	u(σ) in mb
^{nat}Re	p,pxn	^{184}Re	7.820E+01	1.7E+00	1.2E+02	5.4E+00
^{nat}Re	p,pxn	^{184}Re	8.190E+01	2.2E+00	1.1E+02	4.1E+00
^{nat}Re	p,pxn	^{184}Re	9.000E+01	1.6E+00	1.1E+02	3.9E+00
^{nat}Re	p,pxn	^{184}Re	9.340E+01	2.1E+00	1.0E+02	5.5E+00
^{nat}Re	p,pxn	^{184}Re	9.800E+01	1.5E+00	9.9E+01	8.7E+00
^{nat}Re	p,pxn	^{184}Re	1.050E+02	2.0E+00	8.9E+01	4.1E+00
^{nat}Re	p,pxn	^{184}Re	1.080E+02	1.4E+00	9.4E+01	4.6E+00
^{nat}Re	p,pxn	^{184}Re	1.150E+02	1.2E+00	8.6E+01	3.1E+00
^{nat}Re	p,pxn	^{184}Re	1.150E+02	1.9E+00	8.8E+01	4.3E+00
^{nat}Re	p,pxn	^{184}Re	1.240E+02	1.1E+00	8.0E+01	6.0E+00
^{nat}Re	p,pxn	^{184}Re	1.250E+02	1.8E+00	8.2E+01	7.9E+00
^{nat}Re	p,pxn	^{184}Re	1.310E+02	9.0E-01	8.1E+01	3.3E+00
^{nat}Re	p,pxn	^{184}Re	1.340E+02	1.7E+00	7.7E+01	9.9E+00
^{nat}Re	p,pxn	^{184}Re	1.450E+02	1.6E+00	7.1E+01	2.6E+00
^{nat}Re	p,pxn	^{184}Re	1.530E+02	1.5E+00	6.9E+01	5.0E+00
^{nat}Re	p,pxn	^{184}Re	1.620E+02	1.4E+00	6.6E+01	3.3E+00
^{nat}Re	p,pxn	^{184}Re	1.690E+02	1.3E+00	6.3E+01	3.3E+00
^{nat}Re	p,pxn	^{184}Re	2.510E+02	1.9E+00	5.8E+01	5.3E+00
^{nat}Re	p,pxn	^{184}Re	3.310E+02	1.8E+00	5.5E+01	8.5E+00
^{nat}Re	p,pxn	^{184}Re	5.580E+02	1.6E+00	6.0E+01	3.3E+00
^{nat}Re	p,pxn	^{184}Re	7.630E+02	1.5E+00	5.9E+01	2.9E+00
^{nat}Re	p,pxn	^{184}Re	1.165E+03	1.5E+00	5.8E+01	6.7E+00
^{nat}Re	p,pxn	^{184}Re	1.570E+03	1.5E+00	5.8E+01	2.2E+00
^{nat}Re	p,pxn	^{184}Re	2.590E+03	1.0E+00	6.1E+01	2.2E+00

Cross section data for reaction ^{nat}Re(p,pxn)^{184m}Re independent.

Target	Reaction	Product	E_p in MeV	u(E_p) in MeV	σ in mb	u(σ) in mb
^{nat}Re	p,pxn	^{184m}Re	7.820E+01	1.7E+00	3.4E+01	3.8E+00
^{nat}Re	p,pxn	^{184m}Re	8.190E+01	2.2E+00	3.3E+01	3.2E+00
^{nat}Re	p,pxn	^{184m}Re	9.000E+01	1.6E+00	3.0E+01	2.4E+00
^{nat}Re	p,pxn	^{184m}Re	9.340E+01	2.1E+00	3.0E+01	2.1E+00
^{nat}Re	p,pxn	^{184m}Re	9.800E+01	1.5E+00	2.9E+01	5.3E+00
^{nat}Re	p,pxn	^{184m}Re	1.050E+02	2.0E+00	2.8E+01	2.2E+00
^{nat}Re	p,pxn	^{184m}Re	1.080E+02	1.4E+00	2.6E+01	1.3E+00

Continued.

Target	Reaction	Product	E_p in MeV	u(E_p) in MeV	σ in mb	u(σ) in mb
^{nat}Re	p,pxn	^{184m}Re	1.150E+02	1.2E+00	2.5E+01	1.8E+00
^{nat}Re	p,pxn	^{184m}Re	1.150E+02	1.9E+00	2.4E+01	1.0E+00
^{nat}Re	p,pxn	^{184m}Re	1.240E+02	1.1E+00	2.3E+01	2.2E+00
^{nat}Re	p,pxn	^{184m}Re	1.250E+02	1.8E+00	2.3E+01	2.2E+00
^{nat}Re	p,pxn	^{184m}Re	1.310E+02	9.0E-01	2.2E+01	8.0E-01
^{nat}Re	p,pxn	^{184m}Re	1.340E+02	1.7E+00	2.4E+01	2.7E+00
^{nat}Re	p,pxn	^{184m}Re	1.450E+02	1.6E+00	2.0E+01	1.2E+00
^{nat}Re	p,pxn	^{184m}Re	1.530E+02	1.5E+00	2.0E+01	2.0E+00
^{nat}Re	p,pxn	^{184m}Re	1.620E+02	1.4E+00	2.0E+01	2.0E+00
^{nat}Re	p,pxn	^{184m}Re	1.690E+02	1.3E+00	1.8E+01	1.9E+00
^{nat}Re	p,pxn	^{184m}Re	2.510E+02	1.9E+00	1.6E+01	1.3E+00
^{nat}Re	p,pxn	^{184m}Re	3.310E+02	1.8E+00	1.4E+01	8.0E-01
^{nat}Re	p,pxn	^{184m}Re	5.580E+02	1.6E+00	1.5E+01	1.2E+00
^{nat}Re	p,pxn	^{184m}Re	7.630E+02	1.5E+00	1.6E+01	1.2E+00
^{nat}Re	p,pxn	^{184m}Re	1.165E+03	1.5E+00	1.4E+01	1.0E+00
^{nat}Re	p,pxn	^{184m}Re	1.570E+03	1.5E+00	1.4E+01	6.0E-01
^{nat}Re	p,pxn	^{184m}Re	2.590E+03	1.0E+00	1.5E+01	4.0E-01

Cross section data for reaction ^{nat}Re(p,pxn)^{183}Re cumulative.

Target	Reaction	Product	E_p in MeV	u(E_p) in MeV	σ in mb	u(σ) in mb
^{nat}Re	p,pxn	^{183}Re	7.820E+01	1.7E+00	2.1E+02	3.8E+00
^{nat}Re	p,pxn	^{183}Re	8.190E+01	2.2E+00	2.0E+02	5.7E+00
^{nat}Re	p,pxn	^{183}Re	9.000E+01	1.6E+00	1.8E+02	2.9E+00
^{nat}Re	p,pxn	^{183}Re	9.340E+01	2.1E+00	1.6E+02	6.7E+00
^{nat}Re	p,pxn	^{183}Re	9.800E+01	1.5E+00	1.6E+02	6.6E+00
^{nat}Re	p,pxn	^{183}Re	1.050E+02	2.0E+00	1.4E+02	2.2E+00
^{nat}Re	p,pxn	^{183}Re	1.080E+02	1.4E+00	1.5E+02	3.3E+00
^{nat}Re	p,pxn	^{183}Re	1.150E+02	1.2E+00	1.3E+02	3.5E+00
^{nat}Re	p,pxn	^{183}Re	1.240E+02	1.1E+00	1.3E+02	1.0E+00
^{nat}Re	p,pxn	^{183}Re	1.250E+02	1.8E+00	1.3E+02	9.2E+00
^{nat}Re	p,pxn	^{183}Re	1.310E+02	9.0E-01	1.3E+02	3.0E-01
^{nat}Re	p,pxn	^{183}Re	1.340E+02	1.7E+00	1.3E+02	4.1E+00
^{nat}Re	p,pxn	^{183}Re	1.450E+02	1.6E+00	9.7E+01	5.0E+00
^{nat}Re	p,pxn	^{183}Re	1.530E+02	1.5E+00	9.5E+01	2.3E+00
^{nat}Re	p,pxn	^{183}Re	1.620E+02	1.4E+00	9.3E+01	3.0E+00
^{nat}Re	p,pxn	^{183}Re	1.690E+02	1.3E+00	9.1E+01	4.3E+00
^{nat}Re	p,pxn	^{183}Re	2.510E+02	1.9E+00	7.0E+01	3.1E+00
^{nat}Re	p,pxn	^{183}Re	3.310E+02	1.8E+00	6.2E+01	3.7E+00
^{nat}Re	p,pxn	^{183}Re	5.580E+02	1.6E+00	5.5E+01	5.4E+00
^{nat}Re	p,pxn	^{183}Re	7.630E+02	1.5E+00	5.3E+01	2.7E+00
^{nat}Re	p,pxn	^{183}Re	1.165E+03	1.5E+00	4.4E+01	2.6E+00
^{nat}Re	p,pxn	^{183}Re	1.570E+03	1.5E+00	4.3E+01	2.2E+00
^{nat}Re	p,pxn	^{183}Re	2.590E+03	1.0E+00	4.7E+01	1.3E+00

Cross section data for reaction ^{nat}Re(p,pxn)^{182}Re cumulative.

Target	Reaction	Product	Ep in MeV	u(Ep) in MeV	σ in mb	u(σ) in mb
natRe	p,pxn	182Re	7.820E+01	1.7E+00	-	-
natRe	p,pxn	182Re	8.190E+01	2.2E+00	6.9E+01	6.4E+00

Continued.

Target	Reaction	Product	E_p in MeV	u(E_p) in MeV	σ in mb	u(σ) in mb
^{nat}Re	p,pxn	^{182}Re	9.000E+01	1.6E+00	-	-
^{nat}Re	p,pxn	^{182}Re	9.340E+01	2.1E+00	6.4E+01	4.1E+00
^{nat}Re	p,pxn	^{182}Re	9.800E+01	1.5E+00	6.2E+01	9.2E+00
^{nat}Re	p,pxn	^{182}Re	1.050E+02	2.0E+00	6.1E+01	3.7E+00
^{nat}Re	p,pxn	^{182}Re	1.080E+02	1.4E+00	-	-
^{nat}Re	p,pxn	^{182}Re	1.150E+02	1.2E+00	5.5E+01	4.7E+00
^{nat}Re	p,pxn	^{182}Re	1.150E+02	1.9E+00	5.7E+01	5.9E+00
^{nat}Re	p,pxn	^{182}Re	1.240E+02	1.1E+00	5.3E+01	5.5E+00
^{nat}Re	p,pxn	^{182}Re	1.250E+02	1.8E+00	5.0E+01	5.3E+00
^{nat}Re	p,pxn	^{182}Re	1.310E+02	9.0E-01	5.2E+01	2.8E+00
^{nat}Re	p,pxn	^{182}Re	1.340E+02	1.7E+00	4.7E+01	7.6E+00
^{nat}Re	p,pxn	^{182}Re	1.450E+02	1.6E+00	4.4E+01	2.6E+00
^{nat}Re	p,pxn	^{182}Re	1.530E+02	1.5E+00	4.3E+01	8.0E+00
^{nat}Re	p,pxn	^{182}Re	1.620E+02	1.4E+00	4.2E+01	6.4E+00
^{nat}Re	p,pxn	^{182}Re	1.690E+02	1.3E+00	4.1E+01	6.9E+00
^{nat}Re	p,pxn	^{182}Re	2.510E+02	1.9E+00	2.9E+01	2.0E+00
^{nat}Re	p,pxn	^{182}Re	3.310E+02	1.8E+00	2.5E+01	1.9E+00
^{nat}Re	p,pxn	^{182}Re	5.580E+02	1.6E+00	2.5E+01	2.3E+00
^{nat}Re	p,pxn	^{182}Re	7.630E+02	1.5E+00	2.2E+01	1.7E+00
^{nat}Re	p,pxn	^{182}Re	1.165E+03	1.5E+00	2.1E+01	3.2E+00
^{nat}Re	p,pxn	^{182}Re	1.570E+03	1.5E+00	2.5E+01	1.6E+00
^{nat}Re	p,pxn	^{182}Re	2.590E+03	1.0E+00	2.1E+01	1.1E+00

Cross section data for reaction ^{nat}Re(p,pxn)^{181}Re cumulative.

Target	Reaction	Product	E_p in MeV	u(E_p) in MeV	σ in mb	u(σ) in mb
^{nat}Re	p,pxn	^{181}Re	7.820E+01	1.7E+00	-	-
^{nat}Re	p,pxn	^{181}Re	8.190E+01	2.2E+00	2.2E+02	1.0E-01
^{nat}Re	p,pxn	^{181}Re	9.000E+01	1.6E+00	-	-
^{nat}Re	p,pxn	^{181}Re	9.340E+01	2.1E+00	1.8E+02	1.1E+00
^{nat}Re	p,pxn	^{181}Re	9.800E+01	1.5E+00	-	-
^{nat}Re	p,pxn	^{181}Re	1.050E+02	2.0E+00	1.5E+02	1.0E-01
^{nat}Re	p,pxn	^{181}Re	1.080E+02	1.4E+00	-	-
^{nat}Re	p,pxn	^{181}Re	1.150E+02	1.2E+00	5.6E+01	9.3E+00
^{nat}Re	p,pxn	^{181}Re	1.150E+02	1.9E+00	-	-
^{nat}Re	p,pxn	^{181}Re	1.240E+02	1.1E+00	-	-
^{nat}Re	p,pxn	^{181}Re	1.250E+02	1.8E+00	5.0E+01	8.8E+00
^{nat}Re	p,pxn	^{181}Re	1.310E+02	9.0E-01	-	-
^{nat}Re	p,pxn	^{181}Re	1.340E+02	1.7E+00	4.9E+01	7.3E+00
^{nat}Re	p,pxn	^{181}Re	1.450E+02	1.6E+00	4.4E+01	5.7E+00
^{nat}Re	p,pxn	^{181}Re	1.530E+02	1.5E+00	4.3E+01	8.2E+00
^{nat}Re	p,pxn	^{181}Re	1.620E+02	1.4E+00	4.2E+01	7.9E+00
^{nat}Re	p,pxn	^{181}Re	1.690E+02	1.3E+00	4.1E+01	7.8E+00
^{nat}Re	p,pxn	^{181}Re	2.510E+02	1.9E+00	2.9E+01	2.0E+00
^{nat}Re	p,pxn	^{181}Re	3.310E+02	1.8E+00	2.5E+01	5.1E+00
^{nat}Re	p,pxn	^{181}Re	5.580E+02	1.6E+00	2.5E+01	6.0E-01
^{nat}Re	p,pxn	^{181}Re	7.630E+02	1.5E+00	2.2E+01	3.0E+00
^{nat}Re	p,pxn	^{181}Re	1.165E+03	1.5E+00	2.1E+01	3.6E+00
^{nat}Re	p,pxn	^{181}Re	1.570E+03	1.5E+00	2.5E+01	1.3E+00

Continued.

Target	Reaction	Product	E_p in MeV	u(E_p) in MeV	σ in mb	u(σ) in mb
^{nat}Re	p,pxn	^{181}Re	2.590E+03	1.0E+00	2.1E+01	1.3E+00

Cross section data for reaction ^{nat}Re(p,3pxn)^{183}Ta cumulative.

Target	Reaction	Product	E_p in MeV	u(E_p) in MeV	σ in mb	u(σ) in mb
^{nat}Re	p,3pxn	^{183}Ta	7.820E+01	1.7E+00	-	-
^{nat}Re	p,3pxn	^{183}Ta	8.190E+01	2.2E+00	1.6E+01	3.0E+00
^{nat}Re	p,3pxn	^{183}Ta	9.000E+01	1.6E+00	-	-
^{nat}Re	p,3pxn	^{183}Ta	9.340E+01	2.1E+00	1.5E+01	2.8E+00
^{nat}Re	p,3pxn	^{183}Ta	9.800E+01	1.5E+00	-	-
^{nat}Re	p,3pxn	^{183}Ta	1.050E+02	2.0E+00	1.4E+01	2.5E+00
^{nat}Re	p,3pxn	^{183}Ta	1.080E+02	1.4E+00	-	-
^{nat}Re	p,3pxn	^{183}Ta	1.150E+02	1.2E+00	1.3E+01	2.6E+00
^{nat}Re	p,3pxn	^{183}Ta	1.150E+02	1.9E+00	-	-
^{nat}Re	p,3pxn	^{183}Ta	1.240E+02	1.1E+00	-	-
^{nat}Re	p,3pxn	^{183}Ta	1.250E+02	1.8E+00	1.1E+01	2.1E+00
^{nat}Re	p,3pxn	^{183}Ta	1.310E+02	9.3E-01	-	-
^{nat}Re	p,3pxn	^{183}Ta	1.340E+02	1.7E+00	1.0E+01	1.7E+00
^{nat}Re	p,3pxn	^{183}Ta	1.450E+02	1.6E+00	9.3E+00	6.3E-01
^{nat}Re	p,3pxn	^{183}Ta	1.530E+02	1.5E+00	9.1E+00	1.4E+00
^{nat}Re	p,3pxn	^{183}Ta	1.620E+02	1.4E+00	8.7E+00	1.7E+00
^{nat}Re	p,3pxn	^{183}Ta	1.690E+02	1.3E+00	7.9E+00	1.8E+00
^{nat}Re	p,3pxn	^{183}Ta	2.510E+02	1.9E+00	7.3E+00	3.8E-01
^{nat}Re	p,3pxn	^{183}Ta	3.310E+02	1.8E+00	6.3E+00	6.2E-01
^{nat}Re	p,3pxn	^{183}Ta	5.580E+02	1.6E+00	6.2E+00	4.8E-01
^{nat}Re	p,3pxn	^{183}Ta	7.630E+02	1.5E+00	5.3E+00	1.0E+00
^{nat}Re	p,3pxn	^{183}Ta	1.165E+03	1.5E+00	5.4E+00	1.1E+00
^{nat}Re	p,3pxn	^{183}Ta	1.570E+03	1.5E+00	7.5E+00	3.7E-01
^{nat}Re	p,3pxn	^{183}Ta	2.590E+03	1.0E+00	3.3E+00	6.0E-01

Cross section data for reaction ^{nat}Re(p,4pxn)^{175}Hf cumulative.

Target	Reaction	Product	E_p in MeV	u(E_p) in MeV	σ in mb	u(σ) in mb
^{nat}Re	p,4pxn	^{175}Hf	1.150E+02	1.9E+00	3.1E+01	1.3E-01
^{nat}Re	p,4pxn	^{175}Hf	1.240E+02	1.1E+00	4.3E+01	2.5E+00
^{nat}Re	p,4pxn	^{175}Hf	1.250E+02	1.8E+00	4.6E+01	2.1E+00
^{nat}Re	p,4pxn	^{175}Hf	1.310E+02	9.3E-01	5.4E+01	7.6E+00
^{nat}Re	p,4pxn	^{175}Hf	1.340E+02	1.7E+00	5.6E+01	3.2E+00
^{nat}Re	p,4pxn	^{175}Hf	1.450E+02	1.6E+00	6.5E+01	3.5E+00
^{nat}Re	p,4pxn	^{175}Hf	1.530E+02	1.5E+00	7.4E+01	3.9E+00
^{nat}Re	p,4pxn	^{175}Hf	1.620E+02	1.4E+00	7.9E+01	2.6E+00
^{nat}Re	p,4pxn	^{175}Hf	1.690E+02	1.3E+00	8.1E+01	2.6E+00
^{nat}Re	p,4pxn	^{175}Hf	2.510E+02	1.9E+00	9.4E+01	2.0E+00
^{nat}Re	p,4pxn	^{175}Hf	3.310E+02	1.8E+00	9.1E+01	2.2E+00
^{nat}Re	p,4pxn	^{175}Hf	5.580E+02	1.6E+00	7.9E+01	4.9E+00
^{nat}Re	p,4pxn	^{175}Hf	7.630E+02	1.5E+00	6.4E+01	2.8E+00
^{nat}Re	p,4pxn	^{175}Hf	1.165E+03	1.5E+00	4.7E+01	2.4E+00
^{nat}Re	p,4pxn	^{175}Hf	1.570E+03	1.5E+00	4.1E+01	1.5E+00
^{nat}Re	p,4pxn	^{175}Hf	2.590E+03	1.0E+00	3.4E+01	1.2E+00

Cross section data for reaction $^{nat}Re(p,4pxn)^{173}Hf$ cumulative.

Target	Reaction	Product	E_p in MeV	u(E_p) in MeV	σ in mb	u(σ) in mb
^{nat}Re	p,4pxn	^{73}Hf	1.250E+02	1.8E+00	1.3E+01	4.7E-01
^{nat}Re	p,4pxn	^{73}Hf	1.310E+02	9.3E-01	-	-
^{nat}Re	p,4pxn	^{73}Hf	1.340E+02	1.7E+00	1.6E+01	8.3E-01
^{nat}Re	p,4pxn	^{73}Hf	1.450E+02	1.6E+00	2.1E+01	1.2E+00
^{nat}Re	p,4pxn	^{73}Hf	1.530E+02	1.5E+00	2.5E+01	2.1E+00
^{nat}Re	p,4pxn	^{73}Hf	1.620E+02	1.4E+00	2.9E+01	4.2E+00
^{nat}Re	p,4pxn	^{73}Hf	1.690E+02	1.3E+00	3.4E+01	1.4E+00
^{nat}Re	p,4pxn	^{73}Hf	2.510E+02	1.9E+00	6.6E+01	4.1E+00
^{nat}Re	p,4pxn	^{73}Hf	3.310E+02	1.8E+00	7.1E+01	2.3E+00
^{nat}Re	p,4pxn	^{73}Hf	5.580E+02	1.6E+00	6.9E+01	1.0E+00
^{nat}Re	p,4pxn	^{73}Hf	7.630E+02	1.5E+00	5.5E+01	3.2E+00
^{nat}Re	p,4pxn	^{73}Hf	1.165E+03	1.5E+00	4.2E+01	2.2E+00
^{nat}Re	p,4pxn	^{73}Hf	1.570E+03	1.5E+00	3.9E+01	2.8E+00
^{nat}Re	p,4pxn	^{73}Hf	2.590E+03	1.0E+00	2.5E+01	9.2E-01

Cross section data for reaction $^{nat}Re(p,5pxn)^{171}Lu$ cumulative.

Target	Reaction	Product	E_p in MeV	u(E_p) in MeV	σ in mb	u(σ) in mb
^{nat}Re	p,5pxn	^{171}Lu	1.450E+02	1.6E+00	2.1E+01	1.2E+00
^{nat}Re	p,5pxn	^{171}Lu	1.530E+02	1.5E+00	2.5E+01	2.1E+00
^{nat}Re	p,5pxn	^{171}Lu	1.620E+02	1.4E+00	2.9E+01	4.2E+00
^{nat}Re	p,5pxn	^{171}Lu	1.690E+02	1.3E+00	3.4E+01	1.4E+00
^{nat}Re	p,5pxn	^{171}Lu	2.510E+02	1.9E+00	6.6E+01	4.1E+00
^{nat}Re	p,5pxn	^{171}Lu	3.310E+02	1.8E+00	7.1E+01	2.3E+00
^{nat}Re	p,5pxn	^{171}Lu	5.580E+02	1.6E+00	6.9E+01	1.0E+00
^{nat}Re	p,5pxn	^{171}Lu	7.630E+02	1.5E+00	5.5E+01	3.2E+00
^{nat}Re	p,5pxn	^{171}Lu	1.165E+03	1.5E+00	4.2E+01	2.2E+00
^{nat}Re	p,5pxn	^{171}Lu	1.570E+03	1.5E+00	3.9E+01	2.8E+00
^{nat}Re	p,5pxn	^{171}Lu	2.590E+03	1.0E+00	2.5E+01	9.2E-01

Cross section data for reaction $^{nat}Re(p,5pxn)^{170}Lu$ cumulative.

Target	Reaction	Product	E_p in MeV	u(E_p) in MeV	σ in mb	u(σ) in mb
^{nat}Re	p,5pxn	^{170}Lu	1.620E+02	1.4E+00	1.1E+01	6.6E-01
^{nat}Re	p,5pxn	^{170}Lu	1.690E+02	1.3E+00	1.3E+01	3.2E-01
^{nat}Re	p,5pxn	^{170}Lu	2.510E+02	1.9E+00	6.0E+01	4.0E+00
^{nat}Re	p,5pxn	^{170}Lu	3.310E+02	1.8E+00	8.0E+01	2.5E+00
^{nat}Re	p,5pxn	^{170}Lu	5.580E+02	1.6E+00	9.3E+01	6.0E+00
^{nat}Re	p,5pxn	^{170}Lu	7.630E+02	1.5E+00	8.3E+01	6.8E+00
^{nat}Re	p,5pxn	^{171}Lu	1.165E+03	1.5E+00	6.3E+01	9.3E+00
^{nat}Re	p,5pxn	^{171}Lu	1.570E+03	1.5E+00	4.5E+01	4.2E+00
^{nat}Re	p,5pxn	^{171}Lu	2.590E+03	1.0E+00	3.3E+01	3.2E+00

Cross section data for reaction $^{nat}Re(p,5pxn)^{169}Lu$ cumulative.

Target	Reaction	Product	E_p in MeV	u(E_p) in MeV	σ in mb	u(σ) in mb
^{nat}Re	p,5pxn	^{169}Lu	1.620E+02	1.4E+00	1.8E+01	1.7E+00
^{nat}Re	p,5pxn	^{169}Lu	1.690E+02	1.3E+00	1.7E+01	9.7E-01
^{nat}Re	p,5pxn	^{169}Lu	2.510E+02	1.9E+00	3.8E+01	9.0E-01
^{nat}Re	p,5pxn	^{169}Lu	3.310E+02	1.8E+00	4.9E+01	1.2E+00
^{nat}Re	p,5pxn	^{169}Lu	5.580E+02	1.6E+00	6.0E+01	5.8E-01

Continued.

Target	Reaction	Product	E_p in MeV	u(E_p) in MeV	σ in mb	u(σ) in mb
^{nat}Re	p,5pxn	^{169}Lu	7.630E+02	1.5E+00	5.2E+01	4.2E+00
^{nat}Re	p,5pxn	^{169}Lu	1.165E+03	1.5E+00	4.4E+01	1.8E+00
^{nat}Re	p,5pxn	^{169}Lu	1.570E+03	1.5E+00	3.4E+01	1.6E+00
^{nat}Re	p,5pxn	^{169}Lu	2.590E+03	1.0E+00	2.3E+01	1.1E+00

Cross section data for reaction ^{nat}Re(p,6pxn)^{169}Yb cumulative.

Target	Reaction	Product	E_p in MeV	u(E_p) in MeV	σ in mb	u(σ) in mb
^{nat}Re	p,6pxn	^{169}Yb	2.510E+02	1.9E+00	3.2E+01	4.5E+00
^{nat}Re	p,6pxn	^{169}Yb	3.310E+02	1.8E+00	4.2E+01	5.9E+00
^{nat}Re	p,6pxn	^{169}Yb	5.580E+02	1.6E+00	6.4E+01	2.8E+00
^{nat}Re	p,6pxn	^{169}Yb	7.630E+02	1.5E+00	6.0E+01	3.1E+00
^{nat}Re	p,6pxn	^{169}Yb	1.165E+03	1.5E+00	4.8E+01	5.1E+00
^{nat}Re	p,6pxn	^{169}Yb	1.570E+03	1.5E+00	3.2E+01	3.2E+00
^{nat}Re	p,6pxn	^{169}Yb	2.590E+03	1.0E+00	2.4E+01	1.9E+00

Cross section data for reaction ^{nat}Re(p,7pxn)^{166}Tm cumulative.

Target	Reaction	Product	E_p in MeV	u(E_p) in MeV	σ in mb	u(σ) in mb
^{nat}Re	p,7pxn	^{166}Tm	2.510E+02	1.9E+00	1.1E+01	5.9E-01
^{nat}Re	p,7pxn	^{166}Tm	3.310E+02	1.8E+00	2.1E+01	9.4E-01
^{nat}Re	p,7pxn	^{166}Tm	5.580E+02	1.6E+00	4.3E+01	1.4E+00
^{nat}Re	p,7pxn	^{166}Tm	7.630E+02	1.5E+00	3.9E+01	2.6E+00
^{nat}Re	p,7pxn	^{166}Tm	1.165E+03	1.5E+00	3.5E+01	1.5E+00
^{nat}Re	p,7pxn	^{166}Tm	1.570E+03	1.5E+00	2.8E+01	3.4E+00
^{nat}Re	p,7pxn	^{166}Tm	2.590E+03	1.0E+00	1.9E+01	4.5E-01

Cross section data for reaction ^{nat}Re(p,11pxn)^{156}Tb independent.

Target	Reaction	Product	E_p in MeV	u(E_p) in MeV	σ in mb	u(σ) in mb
^{nat}Re	p,11pxn	^{156}Tb	2.510E+02	1.9E+00	9.7E+00	6.2E-01
^{nat}Re	p,11pxn	^{156}Tb	3.310E+02	1.8E+00	2.7E-01	4.0E-02
^{nat}Re	p,11pxn	^{156}Tb	5.580E+02	1.6E+00	8.0E-01	7.0E-02
^{nat}Re	p,11pxn	^{156}Tb	7.630E+02	1.5E+00	1.3E+00	3.0E-01
^{nat}Re	p,11pxn	^{156}Tb	1.165E+03	1.5E+00	1.9E+00	2.4E-01
^{nat}Re	p,11pxn	^{156}Tb	1.570E+03	1.5E+00	2.0E+00	1.9E-01
^{nat}Re	p,11pxn	^{156}Tb	2.590E+03	1.0E+00	1.4E+00	2.2E-01

Cross section data for reaction ^{nat}Re(p,11pxn)^{153}Tb cumulative.

Target	Reaction	Product	E_p in MeV	u(E_p) in MeV	σ in mb	u(σ) in mb
^{nat}Re	p,11pxn	^{153}Tb	2.510E+02	1.9E+00	3.9E+00	4.2E-01
^{nat}Re	p,11pxn	^{153}Tb	3.310E+02	1.8E+00	6.3E+00	8.0E-01
^{nat}Re	p,11pxn	^{153}Tb	5.580E+02	1.6E+00	8.9E+00	4.9E-01
^{nat}Re	p,11pxn	^{153}Tb	7.630E+02	1.5E+00	1.8E+01	2.8E+00
^{nat}Re	p,11pxn	^{153}Tb	1.165E+03	1.5E+00	3.0E+01	2.2E+00
^{nat}Re	p,11pxn	^{153}Tb	1.570E+03	1.5E+00	2.7E+01	2.0E+00
^{nat}Re	p,11pxn	^{153}Tb	2.590E+03	1.0E+00	1.6E+01	9.2E-01

Cross section data for reaction ^{nat}Re(p,11pxn)^{152}Tb cumulative.

Target	Reaction	Product	E_p in MeV	u(E_p) in MeV	σ in mb	u(σ) in mb
^{nat}Re	p,11pxn	^{152}Tb	3.310E+02	1.8E+00	5.7E+00	4.8E-01
^{nat}Re	p,11pxn	^{152}Tb	5.580E+02	1.6E+00	1.5E+01	-
^{nat}Re	p,11pxn	^{152}Tb	7.630E+02	1.5E+00	2.8E+01	5.5E+00
^{nat}Re	p,11pxn	^{152}Tb	1.165E+03	1.5E+00	5.5E+01	2.8E+00
^{nat}Re	p,11pxn	^{152}Tb	1.570E+03	1.5E+00	6.9E+01	2.1E+00
^{nat}Re	p,11pxn	^{152}Tb	2.590E+03	1.0E+00	1.9E+01	1.8E+00

Cross section data for reaction ^{nat}Re(p,12pxn)^{149}Gd cumulative.

Target	Reaction	Product	E_p in MeV	u(E_p) in MeV	σ in mb	u(σ) in mb
^{nat}Re	p,12pxn	^{149}Gd	5.580E+02	1.6E+00	5.2E+00	7.6E-01
^{nat}Re	p,12pxn	^{149}Gd	7.630E+02	1.5E+00	1.4E+01	9.5E-01
^{nat}Re	p,12pxn	^{149}Gd	1.165E+03	1.5E+00	2.6E+01	1.9E+00
^{nat}Re	p,12pxn	^{149}Gd	1.570E+03	1.5E+00	2.5E+01	1.9E+00
^{nat}Re	p,12pxn	^{149}Gd	2.590E+03	1.0E+00	1.8E+01	9.1E-01

Cross section data for reaction ^{nat}Re(p,12pxn)^{147}Gd cumulative.

Target	Reaction	Product	E_p in MeV	u(E_p) in MeV	σ in mb	u(σ) in mb
^{nat}Re	p,12pxn	^{147}Gd	5.580E+02	1.6E+00	1.4E+01	4.0E-01
^{nat}Re	p,12pxn	^{147}Gd	7.630E+02	1.5E+00	1.9E+01	1.5E+00
^{nat}Re	p,12pxn	^{147}Gd	1.165E+03	1.5E+00	3.5E+01	4.2E-01
^{nat}Re	p,12pxn	^{147}Gd	1.570E+03	1.5E+00	3.5E+01	6.5E-01
^{nat}Re	p,12pxn	^{147}Gd	2.590E+03	1.0E+00	2.1E+01	6.6E-01

Cross section data for reaction ^{nat}Re(p,12pxn)^{146}Gd cumulative.

Target	Reaction	Product	E_p in MeV	u(E_p) in MeV	σ in mb	u(σ) in mb
^{nat}Re	p,12pxn	^{146}Gd	5.580E+02	1.6E+00	3.1E+00	5.2E-01
^{nat}Re	p,12pxn	^{146}Gd	7.630E+02	1.5E+00	1.2E+01	1.1E+00
^{nat}Re	p,12pxn	^{146}Gd	1.165E+03	1.5E+00	2.3E+01	2.0E+00
^{nat}Re	p,12pxn	^{146}Gd	1.570E+03	1.5E+00	2.3E+01	1.7E+00
^{nat}Re	p,12pxn	^{146}Gd	2.590E+03	1.0E+00	1.7E+01	1.3E+00

Cross section data for reaction ^{nat}Re(p,13pxn)^{148}Eu cumulative.

Target	Reaction	Product	E_p in MeV	u(E_p) in MeV	σ in mb	u(σ) in mb
^{nat}Re	p,13pxn	^{148}Eu	5.580E+02	1.6E+00	2.1E-01	3.0E-02
^{nat}Re	p,13pxn	^{148}Eu	7.630E+02	1.5E+00	6.9E-01	1.2E-01
^{nat}Re	p,13pxn	^{148}Eu	1.165E+03	1.5E+00	1.4E+00	2.5E-01
^{nat}Re	p,13pxn	^{148}Eu	1.570E+03	1.5E+00	1.6E+00	2.7E-01
^{nat}Re	p,13pxn	^{148}Eu	2.590E+03	1.0E+00	1.2E+00	9.0E-02

Cross section data for reaction ^{nat}Re(p,13pxn)^{147}Eu cumulative.

Target	Reaction	Product	E_p in MeV	u(E_p) in MeV	σ in mb	u(σ) in mb
^{nat}Re	p,13pxn	^{147}Eu	5.580E+02	1.6E+00	2.7E+00	2.1E-01
^{nat}Re	p,13pxn	^{147}Eu	7.630E+02	1.5E+00	9.1E+00	6.2E-01
^{nat}Re	p,13pxn	^{147}Eu	1.165E+03	1.5E+00	2.2E+01	4.7E+00
^{nat}Re	p,13pxn	^{147}Eu	1.570E+03	1.5E+00	2.0E+01	1.4E+00
^{nat}Re	p,13pxn	^{147}Eu	2.590E+03	1.0E+00	1.5E+01	1.8E+00

Cross section data for reaction $^{nat}Re(p,13pxn)^{145}Eu$ cumulative.

Target	Reaction	Product	E_p in MeV	$u(E_p)$ in MeV	σ in mb	u(σ) in mb
^{nat}Re	p,13pxn	^{145}Eu	3.310E+02	1.8E+00	4.0E+00	1.5E-01
^{nat}Re	p,13pxn	^{145}Eu	5.580E+02	1.6E+00	5.5E+00	9.3E-01
^{nat}Re	p,13pxn	^{145}Eu	7.630E+02	1.5E+00	1.3E+01	1.8E+00
^{nat}Re	p,13pxn	^{145}Eu	1.165E+03	1.5E+00	2.7E+01	7.0E-01
^{nat}Re	p,13pxn	^{145}Eu	1.570E+03	1.5E+00	2.9E+01	2.2E+00
^{nat}Re	p,13pxn	^{145}Eu	2.590E+03	1.0E+00	2.2E+01	1.7E+00

Cross section data for reaction $^{nat}Re(p,18pxn)^{139}Ce$ cumulative.

Target	Reaction	Product	E_p in MeV	$u(E_p)$ in MeV	σ in mb	u(σ) in mb
^{nat}Re	p,18pxn	^{139}Ce	5.580E+02	1.6E+00	3.7E-01	6.0E-02
^{nat}Re	p,18pxn	^{139}Ce	7.630E+02	1.5E+00	2.4E+00	8.0E-02
^{nat}Re	p,18pxn	^{139}Ce	1.165E+03	1.5E+00	1.1E+01	7.0E-01
^{nat}Re	p,18pxn	^{139}Ce	1.570E+03	1.5E+00	1.7E+01	8.7E-01
^{nat}Re	p,18pxn	^{139}Ce	2.590E+03	1.0E+00	1.4E+01	1.3E+00

Cross section data for reaction $^{nat}Re(p,18pxn)^{137m}Ce$ cumulative.

Target	Reaction	Product	E_p in MeV	$u(E_p)$ in MeV	σ in mb	u(σ) in mb
^{nat}Re	p,18pxn	^{137m}Ce	5.580E+02	1.6E+00	2.3E+00	-
^{nat}Re	p,18pxn	^{137m}Ce	7.630E+02	1.5E+00	1.3E+01	2.5E+00
^{nat}Re	p,18pxn	^{137m}Ce	1.165E+03	1.5E+00	2.1E+01	5.7E-01
^{nat}Re	p,18pxn	^{137m}Ce	1.570E+03	1.5E+00	2.1E+01	3.1E+00
^{nat}Re	p,18pxn	^{137m}Ce	2.590E+03	1.0E+00	1.2E+01	1.3E+00

Cross section data for reaction $^{nat}Re(p,18pxn)^{135}Ce$ cumulative.

Target	Reaction	Product	E_p in MeV	$u(E_p)$ in MeV	σ in mb	u(σ) in mb
^{nat}Re	p,18pxn	^{135}Ce	5.580E+02	1.6E+00	4.0E+00	9.4E-01
^{nat}Re	p,18pxn	^{135}Ce	7.630E+02	1.5E+00	5.7E+00	7.2E-01
^{nat}Re	p,18pxn	^{135}Ce	1.165E+03	1.5E+00	1.2E+01	2.6E+00
^{nat}Re	p,18pxn	^{135}Ce	1.570E+03	1.5E+00	2.1E+01	3.0E+00
^{nat}Re	p,18pxn	^{135}Ce	2.590E+03	1.0E+00	1.7E+01	1.5E+00

Cross section data for reaction $^{nat}Re(p,21pxn)^{132}Cs$ cumulative.

Target	Reaction	Product	E_p in MeV	$u(E_p)$ in MeV	σ in mb	u(σ) in mb
^{nat}Re	p,21pxn	^{132}Cs	2.510E+02	1.9E+00	6.1E+00	1.7E-01
^{nat}Re	p,21pxn	^{132}Cs	3.310E+02	1.8E+00	7.4E+00	1.5E-01
^{nat}Re	p,21pxn	^{132}Cs	5.580E+02	1.6E+00	8.8E+00	2.2E+00
^{nat}Re	p,21pxn	^{132}Cs	7.630E+02	1.5E+00	8.0E+00	7.9E-01
^{nat}Re	p,21pxn	^{132}Cs	1.165E+03	1.5E+00	7.2E+00	1.1E+00
^{nat}Re	p,21pxn	^{132}Cs	1.570E+03	1.5E+00	5.0E+00	4.2E-01
^{nat}Re	p,21pxn	^{132}Cs	2.590E+03	1.0E+00	3.4E+00	3.2E-01

Cross section data for reaction $^{nat}Re(p,20pxn)^{131}Ba$ cumulative.

Target	Reaction	Product	E_p in MeV	$u(E_p)$ in MeV	σ in mb	u(σ) in mb
^{nat}Re	p,20pxn	^{131}Ba	5.580E+02	1.6E+00	5.3E-01	6.0E-02
^{nat}Re	p,20pxn	^{131}Ba	7.630E+02	1.5E+00	1.9E+00	4.3E-01
^{nat}Re	p,20pxn	^{131}Ba	1.165E+03	1.5E+00	7.2E+00	1.4E+00
^{nat}Re	p,20pxn	^{131}Ba	1.570E+03	1.5E+00	1.3E+01	1.0E+00

Continued.

Target	Reaction	Product	E_p in MeV	u(E_p) in MeV	σ in mb	u(σ) in mb
^{nat}Re	p,20pxn	^{131}Ba	2.590E+03	1.0E+00	1.6E+01	3.0E-01

Cross section data for reaction ^{nat}Re(p,21pxn)^{129}Cs cumulative.

Target	Reaction	Product	E_p in MeV	u(E_p) in MeV	σ in mb	u(σ) in mb
^{nat}Re	p,21pxn	^{129}Cs	7.630E+02	1.5E+00	1.7E+00	3.0E-01
^{nat}Re	p,21pxn	^{129}Cs	1.165E+03	1.5E+00	5.9E+00	7.4E-01
^{nat}Re	p,21pxn	^{129}Cs	1.570E+03	1.5E+00	1.5E+01	1.1E+00
^{nat}Re	p,21pxn	^{129}Cs	2.590E+03	1.0E+00	1.9E+01	1.8E+00

Cross section data for reaction ^{nat}Re(p,22pxn)^{127}Xe cumulative.

Target	Reaction	Product	E_p in MeV	u(E_p) in MeV	σ in mb	u(σ) in mb
^{nat}Re	p,22pxn	^{127}Xe	2.510E+02	1.9E+00	4.8E-01	2.0E-03
^{nat}Re	p,22pxn	^{127}Xe	3.310E+02	1.8E+00	5.1E-01	7.0E-02
^{nat}Re	p,22pxn	^{127}Xe	5.580E+02	1.6E+00	7.4E-01	9.4E-01
^{nat}Re	p,22pxn	^{127}Xe	7.630E+02	1.5E+00	9.1E-01	9.0E-02
^{nat}Re	p,22pxn	^{127}Xe	1.165E+03	1.5E+00	3.5E+00	2.7E-01
^{nat}Re	p,22pxn	^{127}Xe	1.570E+03	1.5E+00	8.4E+00	5.2E-01
^{nat}Re	p,22pxn	^{127}Xe	2.590E+03	1.0E+00	1.2E+01	1.0E+00

Cross section data for reaction ^{nat}Re(p,24pxn)^{121}Te cumulative.

Target	Reaction	Product	E_p in MeV	u(E_p) in MeV	σ in mb	u(σ) in mb
^{nat}Re	p,24pxn	^{121}Te	5.580E+02	1.6E+00	3.1E-01	3.0E-02
^{nat}Re	p,24pxn	^{121}Te	7.630E+02	1.5E+00	4.4E-01	8.0E-02
^{nat}Re	p,24pxn	^{121}Te	1.165E+03	1.5E+00	1.9E+00	7.0E-02
^{nat}Re	p,24pxn	^{121}Te	1.570E+03	1.5E+00	6.5E+00	1.6E+00
^{nat}Re	p,24pxn	^{121}Te	2.590E+03	1.0E+00	1.2E+01	1.5E+00

Cross section data for reaction ^{nat}Re(p,f)^{95}Nb cumulative.

Target	Reaction	Product	E_p in MeV	u(E_p) in MeV	σ in mb	u(σ) in mb
^{nat}Re	p,f	^{95}Nb	2.510E+02	1.9E+00	3.7E-01	6.0E-02
^{nat}Re	p,f	^{95}Nb	3.310E+02	1.8E+00	3.7E-01	1.1E-01
^{nat}Re	p,f	^{95}Nb	5.580E+02	1.6E+00	3.1E-01	8.0E-02
^{nat}Re	p,f	^{95}Nb	7.630E+02	1.5E+00	4.3E-01	5.0E-02
^{nat}Re	p,f	^{95}Nb	1.165E+03	1.5E+00	4.3E-01	2.0E-02
^{nat}Re	p,f	^{95}Nb	1.570E+03	1.5E+00	5.7E-01	1.6E-01
^{nat}Re	p,f	^{95}Nb	2.590E+03	1.0E+00	6.6E-01	2.6E-01

Cross section data for reaction ^{nat}Re(p,f)^{88}Y cumulative.

Target	Reaction	Product	E_p in MeV	u(E_p) in MeV	σ in mb	u(σ) in mb
^{nat}Re	p,f	^{88}Y	2.510E+02	1.9E+00	2.5E-01	2.0E-02
^{nat}Re	p,f	^{88}Y	3.310E+02	1.8E+00	4.4E-01	5.0E-02
^{nat}Re	p,f	^{88}Y	5.580E+02	1.6E+00	8.8E-01	1.6E-01
^{nat}Re	p,f	^{88}Y	7.630E+02	1.5E+00	9.2E-01	9.0E-02
^{nat}Re	p,f	^{88}Y	1.165E+03	1.5E+00	1.3E+00	2.5E-01
^{nat}Re	p,f	^{88}Y	1.570E+03	1.5E+00	1.4E+00	1.3E-01
^{nat}Re	p,f	^{88}Y	2.590E+03	1.0E+00	2.1E+00	2.8E-01

Cross section data for reaction $^{nat}Re(p,f)^{87}Y$ cumulative.

Target	Reaction	Product	E_p in MeV	$u(E_p)$ in MeV	σ in mb	u(σ) in mb
^{nat}Re	p,f	^{87}Y	5.580E+02	1.6E+00	6.6E-01	2.3E-01
^{nat}Re	p,f	^{87}Y	7.630E+02	1.5E+00	1.1E+00	3.6E-01
^{nat}Re	p,f	^{87}Y	1.165E+03	1.5E+00	1.8E+00	4.0E-02
^{nat}Re	p,f	^{87}Y	1.570E+03	1.5E+00	2.7E+00	3.3E-01
^{nat}Re	p,f	^{87}Y	2.590E+03	1.0E+00	4.2E+00	3.1E-01

Cross section data for reaction $^{nat}Re(p,f)^{86}Rb$ independent.

Target	Reaction	Product	E_p in MeV	$u(E_p)$ in MeV	σ in mb	u(σ) in mb
^{nat}Re	p,f	^{86}Rb	5.580E+02	1.6E+00	4.1E+00	4.9E-01
^{nat}Re	p,f	^{86}Rb	7.630E+02	1.5E+00	1.3E+01	2.7E-01
^{nat}Re	p,f	^{86}Rb	1.165E+03	1.5E+00	2.7E+01	5.6E+00
^{nat}Re	p,f	^{86}Rb	1.570E+03	1.5E+00	2.4E+01	2.2E+00
^{nat}Re	p,f	^{86}Rb	2.590E+03	1.0E+00	1.9E+01	2.2E+00

Cross section data for reaction $^{nat}Re(p,f)^{85}Sr$ cumulative.

Target	Reaction	Product	E_p in MeV	$u(E_p)$ in MeV	σ in mb	u(σ) in mb
^{nat}Re	p,f	^{85}Sr	3.310E+02	1.8E+00	3.8E-01	3.0E-02
^{nat}Re	p,f	^{85}Sr	5.580E+02	1.6E+00	9.2E-01	2.7E-01
^{nat}Re	p,f	^{85}Sr	7.630E+02	1.5E+00	1.1E+00	8.0E-02
^{nat}Re	p,f	^{85}Sr	1.165E+03	1.5E+00	1.7E+00	2.3E-01
^{nat}Re	p,f	^{85}Sr	1.570E+03	1.5E+00	1.9E+00	3.5E-01
^{nat}Re	p,f	^{85}Sr	2.590E+03	1.0E+00	3.8E+00	4.6E-01

Cross section data for reaction $^{nat}Re(p,f)^{84}Rb$ independent.

Target	Reaction	Product	E_p in MeV	$u(E_p)$ in MeV	σ in mb	u(σ) in mb
^{nat}Re	p,f	^{84}Rb	3.310E+02	1.8E+00	5.6E-01	2.0E-01
^{nat}Re	p,f	^{84}Rb	5.580E+02	1.6E+00	7.2E-01	1.1E-01
^{nat}Re	p,f	^{84}Rb	7.630E+02	1.5E+00	9.2E-01	9.0E-02
^{nat}Re	p,f	^{84}Rb	1.165E+03	1.5E+00	1.1E+00	1.2E-01
^{nat}Re	p,f	^{84}Rb	1.570E+03	1.5E+00	1.1E+00	1.2E-01
^{nat}Re	p,f	^{84}Rb	2.590E+03	1.0E+00	1.3E+00	2.1E-01

Cross section data for reaction $^{nat}Re(p,f)^{75}Se$ cumulative.

Target	Reaction	Product	E_p in MeV	$u(E_p)$ in MeV	σ in mb	u(σ) in mb
^{nat}Re	p,f	^{75}Se	2.510E+02	1.9E+00	4.9E-01	7.0E-02
^{nat}Re	p,f	^{75}Se	3.310E+02	1.8E+00	5.5E-01	1.3E-01
^{nat}Re	p,f	^{75}Se	5.580E+02	1.6E+00	6.4E-01	1.0E-01
^{nat}Re	p,f	^{75}Se	7.630E+02	1.5E+00	9.1E-01	9.0E-02
^{nat}Re	p,f	^{75}Se	1.165E+03	1.5E+00	1.2E+00	2.6E-01
^{nat}Re	p,f	^{75}Se	1.570E+03	1.5E+00	1.4E+00	1.4E-01
^{nat}Re	p,f	^{75}Se	2.590E+03	1.0E+00	2.4E+00	1.1E-01

Cross section data for reaction $^{nat}Re(p,f)^{65}Zn$ cumulative.

Target	Reaction	Product	E_p in MeV	$u(E_p)$ in MeV	σ in mb	u(σ) in mb
^{nat}Re	p,f	^{65}Zn	5.580E+02	1.6E+00	4.5E-01	3.0E-02
^{nat}Re	p,f	^{65}Zn	7.630E+02	1.5E+00	5.8E-01	7.0E-02
^{nat}Re	p,f	^{65}Zn	1.165E+03	1.5E+00	7.8E-01	7.0E-02

Continued.

Target	Reaction	Product	E_p in MeV	u(E_p) in MeV	σ in mb	u(σ) in mb
^{nat}Re	p,f	^{65}Zn	1.570E+03	1.5E+00	1.1E+00	4.0E-02
^{nat}Re	p,f	^{65}Zn	2.590E+03	1.0E+00	2.1E+00	2.8E-01

Cross section data for reaction ^{nat}Re(p,f)^{59}Fe cumulative.

Target	Reaction	Product	E_p in MeV	u(E_p) in MeV	σ in mb	u(σ) in mb
^{nat}Re	p,f	^{59}Fe	5.580E+02	1.6E+00	2.1E-01	2.0E-02
^{nat}Re	p,f	^{59}Fe	7.630E+02	1.5E+00	3.8E-01	3.0E-02
^{nat}Re	p,f	^{59}Fe	1.165E+03	1.5E+00	4.9E-01	6.0E-02
^{nat}Re	p,f	^{59}Fe	1.570E+03	1.5E+00	6.1E-01	6.0E-02
^{nat}Re	p,f	^{59}Fe	2.590E+03	1.0E+00	8.9E-01	1.0E-01

Cross section data for reaction ^{nat}Re(p,f)^{58}Co independent.

Target	Reaction	Product	E_p in MeV	u(E_p) in MeV	σ in mb	u(σ) in mb
^{nat}Re	p,f	^{58}Co	5.580E+02	1.6E+00	2.3E+00	1.6E-01
^{nat}Re	p,f	^{58}Co	7.630E+02	1.5E+00	1.9E+00	5.0E-02
^{nat}Re	p,f	^{58}Co	1.165E+03	1.5E+00	1.6E+00	1.3E-01
^{nat}Re	p,f	^{58}Co	1.570E+03	1.5E+00	2.3E+00	7.5E-01
^{nat}Re	p,f	^{58}Co	2.590E+03	1.0E+00	2.6E+00	3.6E-01

Cross section data for reaction ^{nat}Re(p,f)^{60}Co cumulative.

Target	Reaction	Product	E_p in MeV	u(E_p) in MeV	σ in mb	u(σ) in mb
^{nat}Re	p,f	^{60}Co	7.630E+02	1.5E+00	1.2E-01	4.0E-02
^{nat}Re	p,f	^{60}Co	1.165E+03	1.5E+00	1.4E-01	2.0E-03
^{nat}Re	p,f	^{60}Co	1.570E+03	1.5E+00	4.1E-01	1.9E-01
^{nat}Re	p,f	^{60}Co	2.590E+03	1.0E+00	3.2E-01	1.7E-01

Cross section data for reaction ^{nat}Re(p,f)^{46}Sc independent.

Target	Reaction	Product	E_p in MeV	u(E_p) in MeV	σ in mb	u(σ) in mb
^{nat}Re	p,f	^{46}Sc	5.580E+02	1.6E+00	1.5E-01	2.0E-02
^{nat}Re	p,f	^{46}Sc	7.630E+02	1.5E+00	4.2E-01	1.6E-01
^{nat}Re	p,f	^{46}Sc	1.165E+03	1.5E+00	7.5E-01	1.1E-01
^{nat}Re	p,f	^{46}Sc	1.570E+03	1.5E+00	1.1E+00	1.0E-01
^{nat}Re	p,f	^{46}Sc	2.590E+03	1.0E+00	2.4E+00	1.9E-01

Cross section data for reaction ^{nat}Re(p,f)^{7}Be cumulative.

Target	Reaction	Product	E_p in MeV	u(E_p) in MeV	σ in mb	u(σ) in mb
^{nat}Re	p,f	^{7}Be	7.630E+02	1.5E+00	1.4E+00	2.4E-01
^{nat}Re	p,f	^{7}Be	1.165E+03	1.5E+00	3.5E+00	3.9E-01
^{nat}Re	p,f	^{7}Be	1.570E+03	1.5E+00	5.1E+00	5.4E-01
^{nat}Re	p,f	^{7}Be	2.590E+03	1.0E+00	8.9E+00	6.0E-01

Cross section data for different reactions at proton energy 2.590E+03 MeV ±1.0E+00.

Target	Reaction	Product	Type of yield	σ in mb	u(σ) in mb
^{nat}Re	p,11pxn	^{155}Tb	Cumulative	1.4E+01	2.2E+00
^{nat}Re	p,11pxn	^{151}Tb	Cumulative	1.6E+01	2.4E+00
^{nat}Re	p,22pxn	^{125}Xe	Cumulative	1.0E+01	3.2E-01
^{nat}Re	p,24pxn	^{119}Te	Cumulative	7.3E+00	1.7E+00

Continued.

Target	Reaction	Product	Type of yield	σ in mb	u(σ) in mb
^{nat}Re	p,29pxn	^{106m}Ag	Independent	1.0E+01	4.7E-01
^{nat}Re	p,f	^{57}Ni	Cumulative	8.3E-01	5.0E-02
^{nat}Re	p,f	^{51}Cr	Cumulative	2.6E+00	3.4E-01

APPENDIX (II)

Cross section data for reaction $^{nat}U(p,pxn)^{237}U$ cumulative.

Target	Reaction	Production	E_p in MeV	σ in mb	u (σ) in mb
^{nat}U	p,pxn	^{237}U	2.110E+02	6.9E+01	5.2E+00
^{nat}U	p,pxn	^{237}U	1.000E+03	1.4E+02	5.0E+00
^{nat}U	p,pxn	^{237}U	1.400E+03	9.1E+01	5.6E+00
^{nat}U	p,pxn	^{237}U	2.530E+03	1.3E+02	3.8E+00

Cross section data for reaction $^{nat}U(p,2pxn)^{233}Pa$ cumulative.

Target	Reaction	Production	E_p in MeV	σ in mb	u (σ) in mb
^{nat}U	p,2pxn	^{233}Pa	2.110E+02	9.5E+00	3.2E-01
^{nat}U	p,2pxn	^{233}Pa	1.000E+03	1.5E+01	9.7E-01
^{nat}U	p,2pxn	^{233}Pa	1.400E+03	1.1E+01	1.1E+00
^{nat}U	p,2pxn	^{233}Pa	2.530E+03	1.2E+01	1.1E+00

Cross section data for reaction $^{nat}U(p,2pxn)^{232}Pa$ independent.

Target	Reaction	Production	E_p in MeV	σ in mb	u (σ) in mb
^{nat}U	p,2pxn	^{232}Pa	2.110E+02	1.2E+01	1.5E+00
^{nat}U	p,2pxn	^{232}Pa	1.000E+03	8.9E+00	7.3E-01
^{nat}U	p,2pxn	^{232}Pa	1.400E+03	7.6E+00	4.5E-01
^{nat}U	p,2pxn	^{232}Pa	2.530E+03	8.8E+00	2.4E-01

Cross section data for reaction $^{nat}U(p,2pxn)^{230}Pa$ independent.

Target	Reaction	Production	E_p in MeV	σ in mb	u (σ) in mb
^{nat}U	p,2pxn	^{230}Pa	2.110E+02	3.4E+00	2.4E-01
^{nat}U	p,2pxn	^{230}Pa	1.000E+03	3.7E+00	3.9E-01
^{nat}U	p,2pxn	^{230}Pa	1.400E+03	2.8E+00	1.9E-01
^{nat}U	p,2pxn	^{230}Pa	2.530E+03	2.8E+00	1.6E-01

Cross section data for reaction $^{nat}U(p,f)^{141}Ce$ cumulative.

Target	Reaction	Production	E_p in MeV	σ in mb	u (σ) in mb
^{nat}U	p,f	^{141}Ce	2.110E+02	1.5E+01	1.5E-01
^{nat}U	p,f	^{141}Ce	1.000E+03	1.8E+01	5.7E-01
^{nat}U	p,f	^{141}Ce	1.400E+03	1.2E+01	7.7E-01
^{nat}U	p,f	^{141}Ce	2.530E+03	1.5E+01	1.2E+00

Cross section data for reaction $^{nat}U(p,f)^{139}Ce$ cumulative.

Target	Reaction	Production	E_p in MeV	σ in mb	u (σ) in mb
^{nat}U	p,f	^{139}Ce	2.110E+02	2.6E+00	2.2E-01
^{nat}U	p,f	^{139}Ce	1.000E+03	6.4E+00	1.5E-01
^{nat}U	p,f	^{139}Ce	1.400E+03	4.3E+00	8.0E-02
^{nat}U	p,f	^{139}Ce	2.530E+03	5.1E+00	1.8E-01

Cross section data for reaction $^{nat}U(p,f)^{140}Ba$ cumulative.

Target	Reaction	Production	E_p in MeV	σ in mb	u (σ) in mb
^{nat}U	p,f	^{140}Ba	2.110E+02	1.6E+01	1.8E+00
^{nat}U	p,f	^{140}Ba	1.000E+03	1.8E+01	4.1E+00
^{nat}U	p,f	^{140}Ba	1.400E+03	1.4E+01	1.8E+00
^{nat}U	p,f	^{140}Ba	2.530E+03	2.1E+01	9.7E-01

Cross section data for reaction $^{nat}U(p,f)^{131}Ba$ cumulative.

Target	Reaction	Production	E_p in MeV	σ in mb	u (σ) in mb
^{nat}U	p,f	^{131}Ba	2.110E+02	6.3E-01	1.5E-01
^{nat}U	p,f	^{131}Ba	1.000E+03	-	-
^{nat}U	p,f	^{131}Ba	1.400E+03	2.8E+00	3.8E-01
^{nat}U	p,f	^{131}Ba	2.530E+03	-	-

Cross section data for reaction $^{nat}U(p,f)^{137}Cs$ cumulative.

Target	Reaction	Production	E_p in MeV	σ in mb	u (σ) in mb
^{nat}U	p,f	^{137}Cs	2.110E+02	2.3E+01	2.1E+00
^{nat}U	p,f	^{137}Cs	1.000E+03	2.6E+01	4.6E-01
^{nat}U	p,f	^{137}Cs	1.400E+03	1.9E+01	1.7E+00
^{nat}U	p,f	^{137}Cs	2.530E+03	2.7E+01	2.1E+00

Cross section data for reaction $^{nat}U(p,f)^{136}Cs$ independent.

Target	Reaction	Production	E_p in MeV	σ in mb	u (σ) in mb
^{nat}U	p,f	^{136}Cs	2.110E+02	8.7E+00	5.3E-01
^{nat}U	p,f	^{136}Cs	1.000E+03	5.9E+00	3.4E-01
^{nat}U	p,f	^{136}Cs	1.400E+03	4.7E+00	2.7E-01
^{nat}U	p,f	^{136}Cs	2.530E+03	4.7E+00	2.8E-01

Cross section data for reaction $^{nat}U(p,f)^{134}Cs$ independent.

Target	Reaction	Production	E_p in MeV	σ in mb	u (σ) in mb
^{nat}U	p,f	^{134}Cs	2.110E+02	8.0E+00	4.6E-01
^{nat}U	p,f	^{134}Cs	1.000E+03	5.5E+00	7.0E-01
^{nat}U	p,f	^{134}Cs	1.400E+03	5.1E+00	7.2E-01
^{nat}U	p,f	^{134}Cs	2.530E+03	3.4E+00	3.6E-01

Cross section data for reaction $^{nat}U(p,f)^{127}Xe$ cumulative.

Target	Reaction	Production	E_p in MeV	σ in mb	u (σ) in mb
^{nat}U	p,f	^{127}Xe	2.110E+02	2.4E+00	1.4E-01
^{nat}U	p,f	^{127}Xe	1.000E+03	1.0E+01	4.9E-01
^{nat}U	p,f	^{127}Xe	1.400E+03	8.3E+00	2.0E-01
^{nat}U	p,f	^{127}Xe	2.530E+03	7.0E+00	5.0E-01

Cross section data for reaction $^{nat}U(p,f)^{131}I$ cumulative.

Target	Reaction	Production	E_p in MeV	σ in mb	u (σ) in mb
^{nat}U	p,f	^{131}I	2.110E+02	2.7E+01	1.3E+00
^{nat}U	p,f	^{131}I	1.000E+03	2.7E+01	9.4E-01
^{nat}U	p,f	^{131}I	1.400E+03	2.0E+01	7.0E-01
^{nat}U	p,f	^{131}I	2.530E+03	2.3E+01	8.9E-01

Cross section data for reaction $^{nat}U(p,f)^{124}I$ independent.

Target	Reaction	Production	E_p in MeV	σ in mb	u (σ) in mb
^{nat}U	p,f	^{124}I	2.110E+02	-	-
^{nat}U	p,f	^{124}I	1.000E+03	-	-
^{nat}U	p,f	^{124}I	1.400E+03	2.3E+01	2.8E-01
^{nat}U	p,f	^{124}I	2.530E+03	4.0E+00	9.7E-01

Cross section data for reaction $^{nat}U(p,f)^{132}Te$ cumulative.

Target	Reaction	Production	E_p in MeV	σ in mb	u (σ) in mb
^{nat}U	p,f	^{132}Te	2.110E+02	1.2E+01	2.4E-01
^{nat}U	p,f	^{132}Te	1.000E+03	1.6E+01	1.5E+00
^{nat}U	p,f	^{132}Te	1.400E+03	1.2E+01	6.2E-01
^{nat}U	p,f	^{132}Te	2.530E+03	1.5E+01	1.0E+00

Cross section data for reaction $^{nat}U(p,f)^{121}Te$ cumulative.

Target	Reaction	Production	E_p in MeV	σ in mb	u (σ) in mb
^{nat}U	p,f	^{121}Te	2.110E+02	1.5E+00	2.9E-01
^{nat}U	p,f	^{121}Te	1.000E+03	6.0E+00	6.9E-01
^{nat}U	p,f	^{121}Te	1.400E+03	4.2E+00	5.2E-01
^{nat}U	p,f	^{121}Te	2.530E+03	5.0E+00	3.9E-01

Cross section data for reaction $^{nat}U(p,f)^{121m}Te$ cumulative.

Target	Reaction	Production	E_p in MeV	σ in mb	u (σ) in mb
^{nat}U	p,f	^{121m}Te	2.110E+02	9.0E-01	2.0E-02
^{nat}U	p,f	^{121m}Te	1.000E+03	5.8E+00	2.6E-01
^{nat}U	p,f	^{121m}Te	1.400E+03	4.3E+00	3.8E-01
^{nat}U	p,f	^{121m}Te	2.530E+03	2.8E+00	9.0E-02

Cross section data for reaction $^{nat}U(p,f)^{127}Sb$ cumulative.

Target	Reaction	Production	E_p in MeV	σ in mb	u (σ) in mb
^{nat}U	p,f	^{127}Sb	2.110E+02	1.6E+01	7.1E-01
^{nat}U	p,f	^{127}Sb	1.000E+03	7.8E+00	9.0E-01
^{nat}U	p,f	^{127}Sb	1.400E+03	9.8E+00	2.0E-01
^{nat}U	p,f	^{127}Sb	2.530E+03	1.0E+01	7.6E-01

Cross section data for reaction $^{nat}U(p,f)^{126}Sb$ cumulative.

Target	Reaction	Production	E_p in MeV	σ in mb	u (σ) in mb
^{nat}U	p,f	^{126}Sb	2.110E+02	1.1E+01	8.2E-01
^{nat}U	p,f	^{126}Sb	1.000E+03	8.0E+00	1.0E+00
^{nat}U	p,f	^{126}Sb	1.400E+03	7.0E+00	1.1E+00
^{nat}U	p,f	^{126}Sb	2.530E+03	6.1E+00	8.0E-01

Cross section data for reaction $^{nat}U(p,f)^{124}Sb$ independent.

Target	Reaction	Production	E_p in MeV	σ in mb	u (σ) in mb
^{nat}U	p,f	^{124}Sb	2.110E+02	1.4E+01	5.0E-01
^{nat}U	p,f	^{124}Sb	1.000E+03	1.1E+01	1.4E-01
^{nat}U	p,f	^{124}Sb	1.400E+03	9.5E+00	1.9E-01
^{nat}U	p,f	^{124}Sb	2.530E+03	7.5E+00	9.1E-01

Cross section data for reaction $^{nat}U(p,f)^{122}Sb$ independent.

Target	Reaction	Production	E_p in MeV	σ in mb	u (σ) in mb
^{nat}U	p,f	^{122}Sb	2.110E+02	9.4E+00	2.6E-01
^{nat}U	p,f	^{122}Sb	1.000E+03	1.1E+01	8.9E-01
^{nat}U	p,f	^{122}Sb	1.400E+03	9.1E+00	3.9E-01
^{nat}U	p,f	^{122}Sb	2.530E+03	5.0E+00	2.1E-01

Cross section data for reaction $^{nat}U(p,f)^{125}Sn$ cumulative.

Target	Reaction	Production	E_p in MeV	σ in mb	u (σ) in mb
^{nat}U	p,f	^{125}Sn	2.110E+02	9.5E+00	4.5E-01
^{nat}U	p,f	^{125}Sn	1.000E+03	7.4E+00	7.5E-01
^{nat}U	p,f	^{125}Sn	1.400E+03	6.4E+00	9.0E-01
^{nat}U	p,f	^{125}Sn	2.530E+03	6.4E+00	6.2E-01

Cross section data for reaction $^{nat}U(p,f)^{113}Sn$ cumulative.

Target	Reaction	Production	E_p in MeV	σ in mb	u (σ) in mb
^{nat}U	p,f	^{113}Sn	2.110E+02	-	-
^{nat}U	p,f	^{113}Sn	1.000E+03	4.0E+00	1.6E-01
^{nat}U	p,f	^{113}Sn	1.400E+03	5.0E+00	1.1E+00
^{nat}U	p,f	^{113}Sn	2.530E+03	3.5E+00	2.5E-01

Cross section data for reaction $^{nat}U(p,f)^{111}In$ cumulative.

Target	Reaction	Production	E_p in MeV	σ in mb	u (σ) in mb
^{nat}U	p,f	^{111}In	2.110E+02	-	-
^{nat}U	p,f	^{111}In	1.000E+03	5.6E+00	6.2E-01
^{nat}U	p,f	^{111}In	1.400E+03	2.9E+00	2.6E-01
^{nat}U	p,f	^{111}In	2.530E+03	5.3E+00	4.6E-01

Cross section data for reaction $^{nat}U(p,f)^{115}Cd$ cumulative.

Target	Reaction	Production	E_p in MeV	σ in mb	u (σ) in mb
^{nat}U	p,f	^{115}Cd	2.110E+02	3.2E+01	7.8E-01
^{nat}U	p,f	^{115}Cd	1.000E+03	2.7E+01	1.8E+00
^{nat}U	p,f	^{115}Cd	1.400E+03	2.3E+01	1.7E+00
^{nat}U	p,f	^{115}Cd	2.530E+03	1.9E+01	1.3E+00

Cross section data for reaction $^{nat}U(p,f)^{111}Ag$ cumulative.

Target	Reaction	Production	E_p in MeV	σ in mb	u (σ) in mb
^{nat}U	p,f	^{111}Ag	2.110E+02	4.4E+01	2.5E+00
^{nat}U	p,f	^{111}Ag	1.000E+03	5.5E+01	2.7E+00
^{nat}U	p,f	^{111}Ag	1.400E+03	4.1E+01	5.0E+00
^{nat}U	p,f	^{111}Ag	2.530E+03	3.2E+01	1.3E+00

Cross section data for reaction $^{nat}U(p,f)^{110m}Ag$ independent.

Target	Reaction	Production	E_p in MeV	σ in mb	u (σ) in mb
^{nat}U	p,f	^{110m}Ag	2.110E+02	3.3E+00	2.7E-01
^{nat}U	p,f	^{110m}Ag	1.000E+03	1.4E+01	5.2E-01
^{nat}U	p,f	^{110m}Ag	1.400E+03	1.1E+01	5.6E-01
^{nat}U	p,f	^{110m}Ag	2.530E+03	7.2E+00	5.5E-01

Cross section data for reaction $^{nat}U(p,f)^{106m}Ag$ independent.

Target	Reaction	Production	E_p in MeV	σ in mb	u (σ) in mb
^{nat}U	p,f	^{106m}Ag	2.110E+02	-	-
^{nat}U	p,f	^{106m}Ag	1.000E+03	5.5E+00	1.1E+00
^{nat}U	p,f	^{106m}Ag	1.400E+03	2.7E+00	2.2E-01
^{nat}U	p,f	^{106m}Ag	2.530E+03	3.6E+00	5.7E-01

Cross section data for reaction $^{nat}U(p,f)^{105}Ag$ cumulative.

Target	Reaction	Production	E_p in MeV	σ in mb	u (σ) in mb
^{nat}U	p,f	^{105}Ag	2.110E+02	-	-
^{nat}U	p,f	^{105}Ag	1.000E+03	3.2E+00	2.9E-01
^{nat}U	p,f	^{105}Ag	1.400E+03	1.5E+00	2.3E-01
^{nat}U	p,f	^{105}Ag	2.530E+03	3.3E+00	3.7E-01

Cross section data for reaction $^{nat}U(p,f)^{102}Rh$ independent.

Target	Reaction	Production	E_p in MeV	σ in mb	u (σ) in mb
^{nat}U	p,f	^{102}Rh	2.110E+02	-	-
^{nat}U	p,f	^{102}Rh	1.000E+03	4.6E+00	3.4E-01
^{nat}U	p,f	^{102}Rh	1.400E+03	2.4E+00	8.0E-02
^{nat}U	p,f	^{102}Rh	2.530E+03	2.5E+00	2.8E-01

Cross section data for reaction $^{nat}U(p,f)^{101m}Rh$ cumulative.

Target	Reaction	Production	E_p in MeV	σ in mb	u (σ) in mb
^{nat}U	p,f	^{101m}Rh	2.110E+02	-	-
^{nat}U	p,f	^{101m}Rh	1.000E+03	4.2E+00	3.3E-01
^{nat}U	p,f	^{101m}Rh	1.400E+03	2.6E+00	4.2E-01
^{nat}U	p,f	^{101m}Rh	2.530E+03	3.7E+00	2.9E-01

Cross section data for reaction $^{nat}U(p,f)^{103}Ru$ cumulative.

Target	Reaction	Production	E_p in MeV	σ in mb	u (σ) in mb
^{nat}U	p,f	^{103}Ru	2.110E+02	5.2E+01	3.3E+00
^{nat}U	p,f	^{103}Ru	1.000E+03	8.5E+01	5.3E+00
^{nat}U	p,f	^{103}Ru	1.400E+03	6.4E+01	3.4E+00
^{nat}U	p,f	^{103}Ru	2.530E+03	5.2E+01	3.2E+00

Cross section data for reaction $^{nat}U(p,f)^{97}Ru$ cumulative.

Target	Reaction	Production	E_p in MeV	σ in mb	u (σ) in mb
^{nat}U	p,f	^{97}Ru	2.110E+02	-	-
^{nat}U	p,f	^{97}Ru	1.000E+03	3.2E+00	8.0E-02
^{nat}U	p,f	^{97}Ru	1.400E+03	1.6E+00	3.4E-01
^{nat}U	p,f	^{97}Ru	2.530E+03	3.5E+00	5.8E-01

Cross section data for reaction $^{nat}U(p,f)^{96}Tc$ independent.

Target	Reaction	Production	E_p in MeV	σ in mb	u (σ) in mb
^{nat}U	p,f	^{96}Tc	2.110E+02	-	-
^{nat}U	p,f	^{96}Tc	1.000E+03	5.0E+00	8.2E-01
^{nat}U	p,f	^{96}Tc	1.400E+03	2.5E+00	6.3E-01
^{nat}U	p,f	^{96}Tc	2.530E+03	3.9E+00	4.1E-01

Cross section data for reaction $^{nat}U(p,f)^{95m}Tc$ cumulative.

Target	Reaction	Production	E_p in MeV	σ in mb	u (σ) in mb
^{nat}U	p,f	^{95m}Tc	2.110E+02	-	-
^{nat}U	p,f	^{95m}Tc	1.000E+03	1.5E+00	3.7E-01
^{nat}U	p,f	^{95m}Tc	1.400E+03	-	-
^{nat}U	p,f	^{95m}Tc	2.530E+03	2.9E+00	3.8E-01

Cross section data for reaction $^{nat}U(p,f)^{99}Mo$ cumulative.

Target	Reaction	Production	E_p in MeV	σ in mb	u (σ) in mb
^{nat}U	p,f	^{99}Mo	2.110E+02	3.1E+01	5.2E-01
^{nat}U	p,f	^{99}Mo	1.000E+03	3.5E+01	2.0E+00
^{nat}U	p,f	^{99}Mo	1.400E+03	4.2E+01	8.1E-01
^{nat}U	p,f	^{99}Mo	2.530E+03	3.8E+01	1.2E+00

Cross section data for reaction $^{nat}U(p,f)^{95}Zr$ cumulative.

Target	Reaction	Production	E_p in MeV	σ in mb	u (σ) in mb
^{nat}U	p,f	^{95}Zr	2.110E+02	4.3E+01	1.3E+00
^{nat}U	p,f	^{95}Zr	1.000E+03	5.9E+01	1.6E+00
^{nat}U	p,f	^{95}Zr	1.400E+03	4.3E+01	5.7E-01
^{nat}U	p,f	^{95}Zr	2.530E+03	4.0E+01	1.0E+00

Cross section data for reaction $^{nat}U(p,f)^{89}Zr$ cumulative.

Target	Reaction	Production	E_p in MeV	σ in mb	u (σ) in mb
^{nat}U	p,f	^{89}Zr	2.110E+02	-	-
^{nat}U	p,f	^{89}Zr	1.000E+03	6.7E+00	5.1E-01
^{nat}U	p,f	^{89}Zr	1.400E+03	3.2E+00	1.1E-01
^{nat}U	p,f	^{89}Zr	2.530E+03	5.2E+00	2.6E-01

Cross section data for reaction $^{nat}U(p,f)^{88}Zr$ cumulative.

Target	Reaction	Production	E_p in MeV	σ in mb	u (σ) in mb
^{nat}U	p,f	^{88}Zr	2.110E+02	-	-
^{nat}U	p,f	^{88}Zr	1.000E+03	3.1E+01	9.3E-01
^{nat}U	p,f	^{88}Zr	1.400E+03	-	-
^{nat}U	p,f	^{88}Zr	2.530E+03	2.5E+00	3.3E-01

Cross section data for reaction $^{nat}U(p,f)^{91}Y$ cumulative.

Target	Reaction	Production	E_p in MeV	σ in mb	u (σ) in mb
^{nat}U	p,f	^{91}Y	2.110E+02	3.4E+01	1.9E+00
^{nat}U	p,f	^{91}Y	1.000E+03	-	-
^{nat}U	p,f	^{91}Y	1.400E+03	4.2E+01	6.2E+00
^{nat}U	p,f	^{91}Y	2.530E+03	4.0E+01	4.5E+00

Cross section data for reaction $^{nat}U(p,f)^{88}Y$ cumulative.

Target	Reaction	Production	E_p in MeV	σ in mb	u (σ) in mb
^{nat}U	p,f	^{88}Y	2.110E+02	-	-
^{nat}U	p,f	^{88}Y	1.000E+03	1.4E+01	4.9E-01
^{nat}U	p,f	^{88}Y	1.400E+03	7.2E+00	3.0E-01
^{nat}U	p,f	^{88}Y	2.530E+03	8.8E+00	6.6E-01

Cross section data for reaction $^{nat}U(p,f)^{87}Y$ cumulative.

Target	Reaction	Production	E_p in MeV	σ in mb	u (σ) in mb
^{nat}U	p,f	^{87}Y	2.110E+02	-	-
^{nat}U	p,f	^{87}Y	1.000E+03	6.7E+00	3.1E-01
^{nat}U	p,f	^{87}Y	1.400E+03	3.9E+00	6.3E-01
^{nat}U	p,f	^{87}Y	2.530E+03	6.8E+00	3.5E-01

Cross section data for reaction $^{nat}U(p,f)^{86}Rb$ independent.

Target	Reaction	Production	E_p in MeV	σ in mb	u (σ) in mb
^{nat}U	p,f	^{86}Rb	2.110E+02	3.6E+00	2.2E-01
^{nat}U	p,f	^{86}Rb	1.000E+03	1.0E+01	-
^{nat}U	p,f	^{86}Rb	1.400E+03	1.3E+01	9.0E-01
^{nat}U	p,f	^{86}Rb	2.530E+03	1.3E+01	8.1E-01

Cross section data for reaction $^{nat}U(p,f)^{84}Rb$ independent.

Target	Reaction	Production	E_p in MeV	σ in mb	u (σ) in mb
^{nat}U	p,f	^{84}Rb	2.110E+02	8.6E-01	1.2E-01
^{nat}U	p,f	^{84}Rb	1.000E+03	1.4E+01	2.1E-01
^{nat}U	p,f	^{84}Rb	1.400E+03	-	-
^{nat}U	p,f	^{84}Rb	2.530E+03	-	-

Cross section data for reaction $^{nat}U(p,f)^{83}Rb$ cumulative.

Target	Reaction	Production	E_p in MeV	σ in mb	u (σ) in mb
^{nat}U	p,f	^{83}Rb	2.110E+02	2.2E-01	3.0E-03
^{nat}U	p,f	^{83}Rb	1.000E+03	1.1E+01	1.9E-01
^{nat}U	p,f	^{83}Rb	1.400E+03	4.9E+00	3.0E-01
^{nat}U	p,f	^{83}Rb	2.530E+03	8.2E+00	3.0E-01

Cross section data for reaction $^{nat}U(p,f)^{74}As$ independent.

Target	Reaction	Production	E_p in MeV	σ in mb	u (σ) in mb
^{nat}U	p,f	^{74}As	2.110E+02	-	-
^{nat}U	p,f	^{74}As	1.000E+03	6.0E+00	2.5E-01
^{nat}U	p,f	^{74}As	1.400E+03	4.3E+00	3.6E-01
^{nat}U	p,f	^{74}As	2.530E+03	4.6E+00	1.7E-01

Cross section data for reaction $^{nat}U(p,f)^{65}Zn$ cumulative.

Target	Reaction	Production	E_p in MeV	σ in mb	u (σ) in mb
^{nat}U	p,f	^{65}Zn	2.110E+02	-	-
^{nat}U	p,f	^{65}Zn	1.000E+03	1.7E+00	6.0E-02
^{nat}U	p,f	^{65}Zn	1.400E+03	7.1E-01	1.1E-01
^{nat}U	p,f	^{65}Zn	2.530E+03	2.1E+00	1.5E-01

Cross section data for reaction $^{nat}U(p,f)^{60}Co$ cumulative.

Target	Reaction	Production	E_p in MeV	σ in mb	u (σ) in mb
^{nat}U	p,f	^{60}Co	2.110E+02	-	-
^{nat}U	p,f	^{60}Co	1.000E+03	4.7E+00	1.3E+00
^{nat}U	p,f	^{60}Co	1.400E+03	2.1E+00	6.4E-01
^{nat}U	p,f	^{60}Co	2.530E+03	3.5E+00	3.4E-01

Cross section data for reaction $^{nat}U(p,f)^{58}Co$ independent.

Target	Reaction	Production	E_p in MeV	σ in mb	u (σ) in mb
^{nat}U	p,f	^{54}Mn	2.110E+02	-	-
^{nat}U	p,f	^{54}Mn	1.000E+03	1.8E+00	2.4E-01
^{nat}U	p,f	^{54}Mn	1.400E+03	-	-
^{nat}U	p,f	^{54}Mn	2.530E+03	2.4E+00	3.6E-01

Cross section data for reaction $^{nat}U(p,f)^{52}Mn$ cumulative.

Target	Reaction	Production	E_p in MeV	σ in mb	u (σ) in mb
^{nat}U	p,f	^{52}Mn	2.110E+02	-	-
^{nat}U	p,f	^{52}Mn	1.000E+03	8.1E-01	1.0E-01
^{nat}U	p,f	^{52}Mn	1.400E+03	5.4E-01	4.0E-02
^{nat}U	p,f	^{52}Mn	2.530E+03	5.8E-01	1.7E-01

Cross section data for reaction $^{nat}U(p,f)^{51}Cr$ cumulative.

Target	Reaction	Production	E_p in MeV	σ in mb	u (σ) in mb
^{nat}U	p,f	^{51}Cr	2.110E+02	-	-
^{nat}U	p,f	^{51}Cr	1.000E+03	3.5E+00	4.1E-01
^{nat}U	p,f	^{51}Cr	1.400E+03	1.6E+00	2.8E-01
^{nat}U	p,f	^{51}Cr	2.530E+03	2.4E+00	9.0E-01

Cross section data for reaction $^{nat}U(p,f)^{48}V$ cumulative.

Target	Reaction	Production	E_p in MeV	σ in mb	u (σ) in mb
^{nat}U	p,f	^{48}V	1.000E+03	2.7E-01	1.0E-01
^{nat}U	p,f	^{48}V	2.530E+03	4.5E-01	9.0E-02

Cross section data for reaction $^{nat}U(p,f)^{48}Sc$ independent.

Target	Reaction	Production	E_p in MeV	σ in mb	u (σ) in mb
^{nat}U	p,f	^{48}Sc	1.000E+03	1.7E+00	2.0E-01
^{nat}U	p,f	^{48}Sc	1.400E+03	8.0E-01	1.4E-01
^{nat}U	p,f	^{48}Sc	2.530E+03	2.3E+00	4.0E-02

Cross section data for reaction $^{nat}U(p,f)^{46}Sc$ independent.

Target	Reaction	Production	E_p in MeV	σ in mb	u (σ) in mb
^{nat}U	p,f	^{46}Sc	1.000E+03	1.5E+00	2.3E-01
^{nat}U	p,f	^{46}Sc	1.400E+03	5.7E-01	6.0E-02
^{nat}U	p,f	^{46}Sc	2.530E+03	2.5E+00	2.1E-01

Cross section data for different reactions and different energies.

Target	Reaction	Production	E_p in MeV	Type of yield	σ in mb	u (σ) in mb
^{nat}U	p,f	^{132}Cs	2.110E+02	independent	6.3E+00	1.7E-01
^{nat}U	p,f	^{120}Sb	2.110E+02	independent	2.8E+00	3.2E-01
^{nat}U	p,f	^{115m}Cd	2.110E+02	cumulative	8.1E+00	2.0E-01
^{nat}U	p,f	^{95}Nb	1.000E+03	cumulative	3.5E+01	4.0E+00
^{nat}U	p,f	^{95m}Nb	1.000E+03	cumulative	2.7E+00	3.2E-01
^{nat}U	p,f	^{85}Sr	2.530E+03	cumulative	7.8E+00	5.5E-01
^{nat}U	p,f	^{58}Co	2.530E+03	independent	1.6E+00	2.4E-01
^{nat}U	p,f	^{22}Na	2.530E+03	cumulative	6.8E-01	5.0E-02